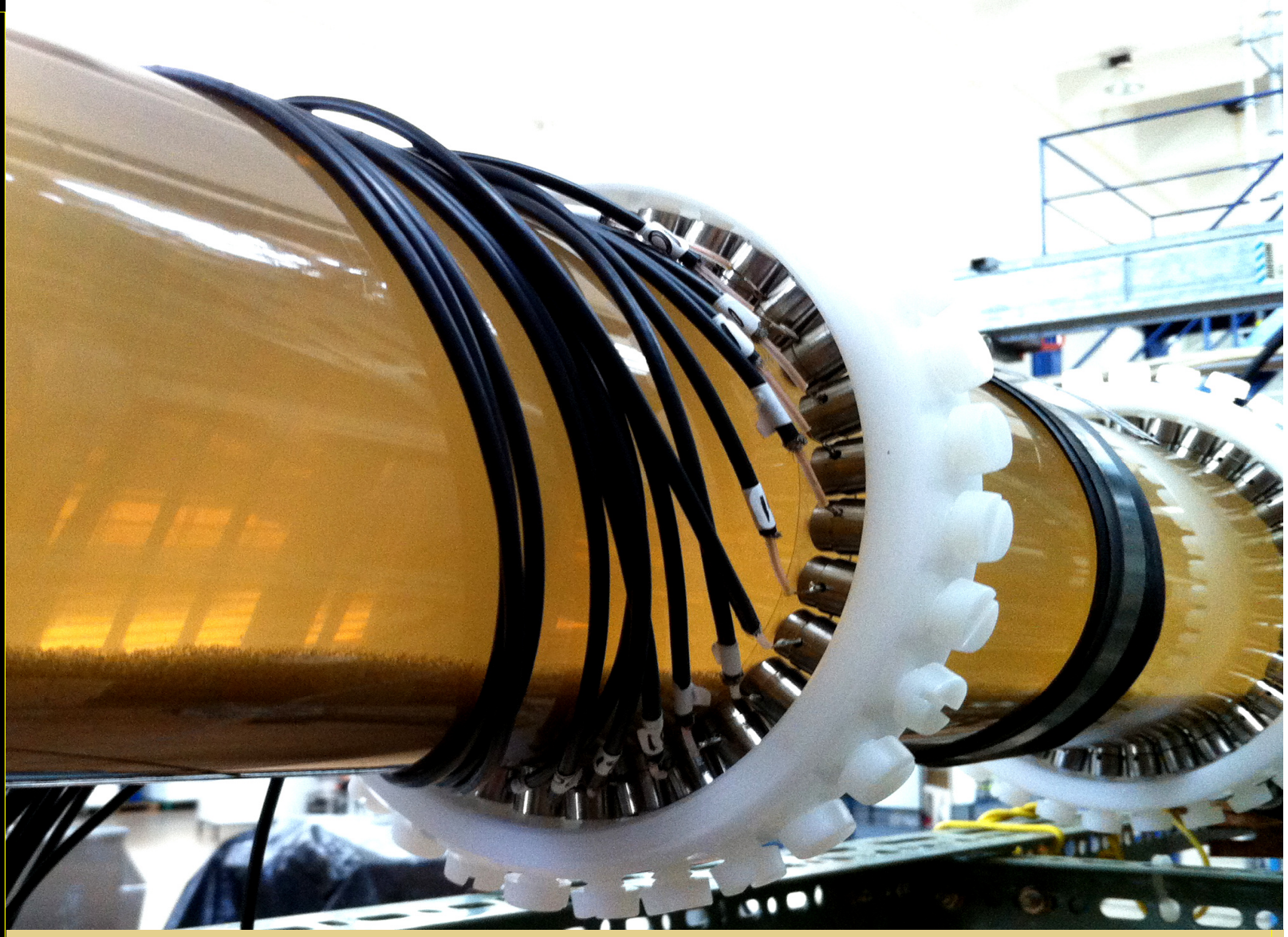

Rui César Costa da Silva

Solid/Liquid Suspension flow in pipes: modelling and experimental investigation

Escoamento de Suspensões Sólido-Líquido em tubagens: modelização e investigação experimental

Tese de Doutoramento em Engenharia Química, orientado pelo Prof. Dr. Fernando Augusto Pinto Garcia e pelo Prof. Dr. Pedro Manuel Gens Azevedo Matos Faia e apresentada ao Departamento de Engenharia Química da Faculdade de Ciências e Tecnologia da Universidade de Coimbra

Dezembro de 2014

· U C ·

Universidade de Coimbra

RUI CÉSAR COSTA DA SILVA

SOLID/LIQUID SUSPENSION FLOW IN PIPES: MODELLING AND EXPERIMENTAL INVESTIGATION

ESCOAMENTO DE SUSPENSÕES SÓLIDO-LÍQUIDO EM TUBAGENS: MODELIZAÇÃO E INVESTIGAÇÃO EXPERIMENTAL

Doctoral Thesis in the scientific area of Chemical Engineering and submitted to the Department of Chemical Engineering, Faculty of Sciences and Technology, University of Coimbra

SUPERVISORS:
Prof. Dr. Fernando Augusto Pinto Garcia
Prof. Dr. Pedro Manuel Gens Azevedo Matos Faia

HOST INSTITUTIONS:
CIEPQPF - Research Centre for Chemical Processes Engineering and Forest Products, Department of Chemical Engineering, Faculty of Sciences and Technology of the University of Coimbra

Department of Electrical and Computer Engineering, Faculty of Sciences and Technology of the University of Coimbra

FINANCING:
FCT - Portuguese Foundation for Science and Technology
Doctoral degree grant fellowship: SFRH/BD/79247/2011

COIMBRA
2014

· U C ·

UNIVERSIDADE DE COIMBRA

: DEPARTMENT OF CHEMICAL ENGINEERING
: FACULTY OF SCIENCES AND TECHNOLOGY
: UNIVERSITY OF COIMBRA

SOLID/LIQUID SUSPENSION FLOW IN PIPES: MODELLING AND EXPERIMENTAL INVESTIGATION

ESCOAMENTO DE SUSPENSÕES SÓLIDO-LÍQUIDO EM TUBAGENS: MODELIZAÇÃO E INVESTIGAÇÃO EXPERIMENTAL

DISSERTATION BY

RUI CÉSAR COSTA DA SILVA

to be presented with due permission for the public examination in the Sala dos Capelos at University of Coimbra, Portugal, to obtain the degree of Doctor in Chemical Engineering.

Financial Support by:

POPH QUALIFICAR É CRESCER. QUADRO DE REFERÊNCIA ESTRATÉGICO NACIONAL PORTUGAL 2007.2013 GOVERNO DA REPÚBLICA PORTUGUESA UNIÃO EUROPEIA Fundo Social Europeu

DEQ-FCTUC

2014

RESUMO

Esta tese tinha como grande objectivo o estudo do escoamento de suspensões sólido-líquido recorrendo em simultâneo a testes experimentais e numéricos.

Dados experimentais sob a forma de perfis de velocidade do meio líquidos e das partículas empregando Imagens por Ressonância Magnética (IRM) e Velocimetria de Pulso Ultra-sónico (VPU), respectivamente, foram obtidos para uma gama variada de tamanhos e concentrações de partículas. Conjuntamente, um sistema de Tomografia de Impedância Eléctrica (TIE) foi desenvolvido com vista à obtenção da distribuição de partículas na conduta, sistema que utiliza a distribuição da condutividade eléctrica num determinado meio como base do seu funcionamento. A distribuição de sólidos é uma das variáveis mais importantes no escoamento de suspensões sólido-líquido.

Os estudos numéricos foram realizados utilizando o Modelo de Mistura através de Dinâmica de Fluidos Computacional (DFC) na tentativa de reproduzir os dados resultantes das experiências mencionadas acima. Adicionalmente, dados da literatura para escoamentos de suspensões sólido-líquido concentradas, para partículas neutras e pesadas, com comportamentos complexos como atenuação da turbulência e migração de partículas, foram também simulados utilizando o Modelo de Mistura.

O sistema de TIE demonstrou a capacidade de reconhecer diferentes regimes de escoamento e variações na concentração de partículas na conduta com precisão. Além disso, as imagens e perfis obtidos com as três técnicas experimentais previamente citadas foram semelhantes aos resultados numéricos obtidos com o Modelo de Mistura, validando assim a sua aplicação em estudos de escoamento de suspensões sólido-líquido. Finalmente, a atenuação da turbulência induzida pelas partículas foi caracterizada com sucesso através das modificações implementadas no Modelo de Mistura.

Palavras-Chave: Dinâmica de Fluidos Computacional; Modelo de Mistura;

Escoamento de suspensões sólido-líquido; Tomografia de Impedância Eléctrica; Imagens por Ressonância Magnética; Velocimetria de Pulso Ultra-sónico.

ABSTRACT

With this thesis the leading objective was to study the complex behaviour of solid-liquid suspensions pipeline conveying. To that regard, experimental and numerical studies were both conducted.

Experimental data was acquired in the form of velocity profiles for both the liquid and solid phases employing Magnetic Resonance Imaging (MRI) and Ultrasonic Pulse Velocimetry (UPV), respectively, for a range of experiments with several sizes and concentrations of settling particles. Moreover, in order to attain the particle distribution in the pipeline, which is one of more prominent variables in solid-liquid suspensions flow, a new Electrical Impedance Tomography (EIT) system was developed: this type of systems use the distribution of electrical conductivity in a domain has is principle of development.

The Mixture Model was implemented in the numerical studies using Computational Fluid Dynamics (CFD) simulations in an attempt to replicate the experimental data that resulted from the aforementioned experiments. Additionally, experimental data for highly concentrated buoyant and settling particles, existent in the literature, where complex phenomena like turbulence attenuation and particle migration occur, was also simulated by means of the Mixture Model.

The EIT apparatus displayed the capability of recognizing the different flow regimes and particle concentration variations in the pipeline. Furthermore, the images and profiles gathered in these experiments, with the three experimental techniques mentioned above, accurately matched the numerical results from the CFD model, thus validating it for the study of solid-liquid suspensions flows.

Keywords: Computational Fluid Dynamics; Mixture Model; Solid-liquid suspensions pipeline conveying; Electrical Impedance Tomography; Magnetic Resonance Imaging; Ultrasonic Pulse Velocimetry

ACKNOWLEDGMENTS

Aos meus orientadores, o Prof. Doutor Fernando Garcia e o Prof. Doutor Pedro Faia, gostaria de agradecer o apoio e amizade demonstrada ao longo do meu percurso. O vosso incentivo e palavras de encorajamento, quando as dificuldades se apresentaram, foram essenciais.

À Prof. Dra. Graça Rasteiro, um especial agradecimento, pelos seus conselhos e colaboração no desenvolvimento deste trabalho. Mas, acima de tudo, pela oportunidade que me proporcionou, em 2008 como bolseiro de investigação onde pude desenvolver o gosto pela investigação científica. Estar-lhe-ei para sempre grato por essa oportunidade.

Ao Prof. Dr. Fredrik Lundell e sua equipa gostaria de agradecer a estadia no KTH Mekanics e a assistência prestada na obtenção de dados experimentais para esta tese. Um especial agradecimento ao aluno e colega Masato Hirota pela paciência e ajuda prestada com as técnicas IRM e VPU.

À Fundação para a Ciência e Tecnologia (FCT) com a bolsa individual de doutoramento SFRH/BD/79247/2011 no âmbito do projecto PTDC/EQU-EQU/66670/2006.

Ao Departamento de Engenharia Química da Faculdade de Ciências e Tecnologia da Universidade de Coimbra pela disponibilização dos respectivos serviços e laboratórios. Em particular agradeço, ao Dr. Adamo e ao Sr. José Santos. A vossa ajuda foi essencial para o trabalho desenvolvido

Um especial agradecimento aos meus colegas, e amigos, Hugo Costa e Bruno Branco cuja ajuda e companheirismo foram essenciais para o desenvolvimento do sistema tomográfico. À Carla Cotas, ao Nuno Amaral, Daniela Rodrigues e ao André Ferreira agradeço o companheirismo e amizade.

Sendo impossível agradecer individualmente a todos os meus amigos de Coimbra e Barcelos, saibam que estarei sempre grato pela vossa amizade e

pelo vosso apoio.

E, como se guarda sempre o melhor para último, aos meus Pais e Irmã, a minha eterna gratidão pelo vosso constante apoio e amor.

E, aos meus Avós e Padrinhos, a quem dedico esta tese, obrigado por me ensinarem a nunca desistir.

TABLE OF CONTENTS

RESUMO ---------- **I**

ABSTRACT ---------- **III**

ACKNOWLEDGMENTS ---------- **V**

TABLE OF CONTENTS ---------- **VII**

LIST OF FIGURES ---------- **XIII**

LIST OF TABLES ---------- **XXV**

NOMENCLATURE ---------- **XXIX**

1. CHAPTER I – INTRODUCTION ---------- **2**

1.1. GENERAL INTRODUCTION ---------- 2

1.2. AIMS AND OBJECTIVES ---------- 4

1.3. THESIS OUTLINE ---------- 5

2. CHAPTER II – STATE OF THE ART ---------- **8**

2.1. SOLID-LIQUID SUSPENSIONS FLOWS ---------- 8

2.1.1. CLASSIFICATION OF SOLID-LIQUID SUSPENSIONS FLOWS ---------- 9

2.1.2. INDUSTRIAL APPLICATIONS ---------- 12

2.2. CONTROL AND MONITORING: IMPORTANCE OF NON-INVASIVE TECHNIQUES ---------- 13

2.2.1. HISTORICAL OVERVIEW ---------- 13

2.3. BASICS OF A TOMOGRAPHIC SYSTEM ---------- 17

2.4. CHOOSING A TOMOGRAPHIC SYSTEM ---------- 18

2.5. ELECTRICAL IMPEDANCE TOMOGRAPHY (EIT) ---------- 20

2.5.1. ELECTRICAL IMPEDANCE TOMOGRAPHY HARDWARE HISTORY ---------- 21

2.5.2. ELECTRICAL IMPEDANCE TOMOGRAPHY MATHEMATICAL FORMULATION ---------- 22

2.5.3. INDUSTRIAL APPLICATIONS OF ELECTRICAL TOMOGRAPHY ---------- 26

2.6. NUCLEAR MAGNETIC RESONANCE IMAGING ---------- 27

2.6.1. NMR APPLICATION IN MULTIPHASE FLOWS ---------- 30

2.7. ULTRASONIC PULSE VELOCIMETRY ---------- 34

2.7.1. UPV IN MULTIPHASE FLOWS ---- 35
2.8. SOLID-LIQUID SUSPENSIONS FLOW MODELLING ---- 37
2.8.1. EMPIRICAL CORRELATIONS ---- 37
2.8.2. SEMI-EMPIRICAL CORRELATIONS ---- 39
2.9. MECHANISTIC MODELS ---- 41
2.9.1. TWO LAYER MODEL ---- 41
2.9.2. THREE LAYER MODEL ---- 42
2.10. DETERMINISTIC MODELS ---- 43
2.10.1. SINGLE-PHASE NUMERICAL MODELS ---- 44
2.10.2. EULER-EULER NUMERICAL MODELS ---- 44
2.10.3. EULER-LAGRANGE NUMERICAL MODELS ---- 46
2.10.4. LATTICE-BOLTZMANN NUMERICAL MODELS ---- 47
2.10.5. DISCRETE ELEMENT METHOD (DEM) NUMERICAL MODELS ---- 49
2.11. TURBULENCE MODULATION ---- 51
3. CHAPTER III – EXPERIMENTAL SETUPS ---- 54
3.1. FLOW LOOP I – DEQ COIMBRA ---- 54
3.1.1. INTRODUCTION ---- 54
3.1.2. FLOW LOOP I DESCRIPTION ---- 55
3.1.3. EXPERIMENTAL CONDITIONS & PARTICLE DATA ---- 56
3.2. ELECTRICAL IMPEDANCE TOMOGRAPHY (EIT) ---- 57
3.2.1. EIT HARDWARE DESIGN ---- 57
3.2.2. FREQUENCY GENERATOR AND PHASE SHIFTER MODULE ---- 59
3.2.3. DEMODULATOR AND SIGNAL CONDITIONER MODULE ---- 62
3.2.4. MULTIPLEXING AND DEMULTIPLEXING MODULE ---- 65
3.2.5. DATA ACQUISITION MODULES ---- 67
3.2.6. INJECTION AND MEASUREMENT PROTOCOLS ---- 68
3.2.7. RECONSTRUCTION ALGORITHM & HARDWARE CONTROL ---- 72
3.3. FLOW LOOP II – KTH MEKANICS ---- 73

3.3.1. INTRODUCTION ---- 73
3.3.2. FLOW LOOP II DESCRIPTION ---- 73
3.3.3. EXPERIMENTAL CONDITIONS & PARTICLE DATA ---- 77
3.3.4. NUCLEAR MAGNETIC RESONANCE IMAGING EQUIPMENT ---- 78
3.3.5. ULTRASOUND DOPPLER VELOCIMETRY PROFILING IMAGING EQUIPMENT ---- 80
4. CHAPTER IV – CFD MODELLING ---- 84
4.1. CHOOSING A NUMERICAL MODEL ---- 84
4.2. FINITE ELEMENT METHOD IN COMSOL ---- 85
4.3. MIXTURE MODEL FORMULATION ---- 93
4.3.1. CONTINUITY EQUATION ---- 93
4.3.2. MOMENTUM EQUATION ---- 94
4.3.3. CONTINUITY EQUATION FOR A PHASE ---- 95
4.3.4. DIFFUSION VELOCITY ---- 96
4.4. CONSTITUTIVE EQUATIONS ---- 98
4.4.1. DIFFUSION VELOCITY ---- 98
4.4.2. VISCOUS STRESS ---- 99
4.4.3. TURBULENCE ---- 100
4.5. VALIDITY OF THE MIXTURE MODEL ---- 101
4.6. DRAG CORRELATIONS ---- 102
4.6.1. SCHILLER-NAUMANN CORRELATION ---- 104
4.6.2. GIDASPOW-SCHILLER-NAUMANN CORRELATION ---- 104
4.6.3. HAIDER-LEVENSPIEL CORRELATION ---- 105
4.7. TURBULENCE MODELLING ---- 105
4.7.1. HIGH REYNOLDS *K-E* TURBULENCE MODEL ---- 108
4.7.2. JONES-LAUNDER LOW REYNOLDS *K-E* TURBULENCE MODEL ---- 109
4.7.3. BOUNDARY CONDITIONS ---- 111
4.7.4. NEAR-WALL TREATMENT FOR TURBULENT FLOWS ---- 112
4.8. PARTICLE-WALL STRESSES ---- 118

4.9. TURBULENCE MODULATION ---------- 120

4.9.1. *K-E* TURBULENCE MODEL MODIFICATIONS ---------- 121

4.9.2. TURBULENCE MODULATION CLASSIFICATION ---------- 122

5. CHAPTER V – NUMERICAL STUDIES RESULTS ---------- 126

5.1. NUMERICAL STUDIES ON SOLID-LIQUID SUSPENSIONS FLOWS – BUOYANT PARTICLES ---------- 126

5.1.1. EXPERIMENTAL CONDITIONS ---------- 127

5.1.2. FLOW REGIME CONSIDERATIONS ---------- 127

5.1.3. NUMERICAL STUDIES CONDITIONS ---------- 129

5.1.4. TURBULENCE SCALES ANALYSIS – NUMERICAL RESULTS ---------- 132

5.1.5. CLOSURE COEFFICIENTS ANALYSIS – NUMERICAL RESULTS ---------- 138

5.2. NUMERICAL STUDIES OF SOLID-LIQUID SUSPENSIONS FLOWS – SETTLING PARTICLES ---------- 145

5.2.1. EXPERIMENTAL CONDITIONS ---------- 145

5.2.2. FLOW REGIME CONSIDERATIONS ---------- 146

5.2.3. NUMERICAL STUDIES WITH THE MIXTURE MODEL & HIGH REYNOLDS K-E TURBULENCE MODEL ---------- 147

5.2.4. NUMERICAL STUDIES WITH THE MIXTURE MODEL & JONES-LAUNDER (JL) LOW REYNOLDS *K-E* TURBULENCE MODEL ---------- 153

5.2.5. EFFECT OF PARTICLE–WALL SHEAR STRESS ---------- 158

5.2.6. DRAG CORRELATIONS STUDY ---------- 161

5.2.7. ADDITIONAL *K-E* TURBULENCE MODEL MODIFICATIONS ---------- 170

5.3. TURBULENCE MODULATION ANALYSIS ---------- 173

5.4. CONCLUDING REMARKS ---------- 174

6. CHAPTER VI – EXPERIMENTAL RESULTS ---------- 178

6.1. EIT PRELIMINARY TESTING ---------- 178

6.2. STATIC IMAGING ---------- 181

6.3. IMAGING IN FLOW FIELDS ---------- 183

6.4. DILUTE SOLID-LIQUID SUSPENSIONS FLOWS – KTH MEKANICS ---------- 185

6.4.1. EXPERIMENTAL CONDITIONS ---------- 185
6.4.2. FLOW REGIME CONSIDERATIONS ---------- 186
6.4.3. NUMERICAL STUDIES CONDITIONS ---------- 190
6.4.4. EXPERIMENTAL AND NUMERICAL RESULTS ---------- 194
6.4.5. TURBULENCE MODULATION ANALYSIS ---------- 230
6.5. CONCENTRATED SOLID-LIQUID SUSPENSIONS FLOWS – DEQ-FCTUC ---------- 234
6.5.1. EXPERIMENTAL CONDITIONS ---------- 234
6.5.2. FLOW REGIME CONSIDERATIONS ---------- 235
6.5.3. NUMERICAL STUDIES CONDITIONS ---------- 238
6.5.4. EXPERIMENTAL AND NUMERICAL RESULTS ---------- 241
6.5.5. TURBULENCE MODULATION ANALYSIS ---------- 261
6.6. CONCLUDING REMARKS ---------- 264
7. CHAPTER VII – CONCLUSIONS AND FUTURE WORK ---------- 266
7.1. CONCLUSIONS ---------- 266
7.2. FUTURE WORK ---------- 269
APPENDIX A – ELECTRICAL IMPEDANCE TOMOGRAPHY THEORY ---------- 272
APPENDIX B – MATLAB® AND LABVIEW® CODES ---------- 289
APPENDIX C – PARTICLE SIZE ANALYSIS ---------- 303
APPENDIX D – BUOYANT PARTICLES 3D SIMULATIONS ---------- 307
APPENDIX E – CONFERENCE AND JOURNAL PUBLICATIONS ---------- 315
BIBLIOGRAPHY ---------- 319

LIST OF FIGURES

Figure 2.1 – Illustration of particle distributions and solids concentration profiles in a pipe for solid-liquid suspensions flow regimes (adapted from (Crowe 2005)). **11**

Figure 2.2 – Scopus' results for publications per year according to keywords "industrial & tomography" and "multiphase & tomography". **15**

Figure 2.3 – Typical arrangement of an industrial process tomography system. The main components are the sensor head, sensor (detector) readout electronics, data acquisition, and a reconstruction unit which usually incorporates image processing (adapted from (Crowe 2005)). **17**

Figure 2.4 – EIT injection and measurement adjacent protocols for the first (A) and second (B) projections (adapted from (Malmivuo and Plonsey 1995)). **22**

Figure 3.1 – Schematics of the flow loop at DEQ – Coimbra. **54**

Figure 3.2 – Pilot rig at DEQ – Coimbra. **55**

Figure 3.3 – Sampling probe (SP) (Top) and Perspex® section with EIT electrode rings (Bottom) at DEQ – Coimbra. **56**

Figure 3.4 – Block diagram of the EIT design implemented in this study. **58**

Figure 3.5 – Several stages of development the EIT system: earliest stage with wire-wrap modules (Top Left); intermediate stage with several modules already in PCB layout (Top Right); last stage with the EIT system already is transport case (Bottom). **59**

Figure 3.6 – Sinusoidal voltage signal generator schematics. **60**

Figure 3.7 – Amplitude and DC component adjustment schematics. **60**

Figure 3.8 – Phase shifter schematics. **61**

Figure 3.9 – Earlier wire wrap iteration (Top) and final version (Bottom) of frequency generation and phase shifting module. **62**

Figure 3.10 – Schematics of the two units in synchronous demodulation modules: in (a) the measured voltage and the in phase reference signal, from the previous Frequency and Phase Shifting module, are multiplied; in (b) the measured voltage at the electrode is multiplied by the 90 degrees out of phase **63**

reference signal.

Figure 3.11 – Low-pass filter module schematics. **64**

Figure 3.12 – Earlier wire wrap iteration (Top) of the shift control demodulation unit and synchronous demodulation unit (a) with the low-pass filter (b) and the demodulation and signal conditioning module final version (Bottom). **64**

Figure 3.13 – Schematics for the buffer circuits modules between the frequency generation and the demodulation modules (Top Left) and between the electrodes and demodulation module (Top Right) and the final version (Bottom) of both modules. **65**

Figure 3.14 – Overall schematics of the multiplexing and demultiplexing module. **66**

Figure 3.15 – Earlier wire wrap iteration (Top) and final version (Bottom) of the multiplexing and demultiplexing module. **66**

Figure 3.16 – National Instruments® NI USB-6255 Multifunction Data Acquisition (Left) and NI USB-6509 High-Density Industrial Digital I/O (Right). **67**

Figure 3.17 – Adjacent Current driven patterns (a) first current projection (P1) (b) second current projection (P2) (adapted from (Harikumar, Prabu, and Raghavan 2013)). **69**

Figure 3.18 – Opposite current Driven pattern (a) first current projection (P1) (b) second current projection (P2) (adapted from (Harikumar, Prabu, and Raghavan 2013)). **70**

Figure 3.19 – Cross current driven pattern (a) first current projection (P1) (b) second current projection (P2) (adapted from (Harikumar, Prabu, and Raghavan 2013)). **72**

Figure 3.20 – Images of the flow loop at KTH Mekanics. **74**

Figure 3.21 – UVP probes for the 34 mm pipe utilized for the data acquisition at KTH. **75**

Figure 3.22 –UVP probes for the 50 mm pipe utilized for the data acquisition at KTH. **75**

Figure 3.23 –EIT electrode ring (Top) and pressure transducer (Bottom) for the 50 mm pipe utilized for the data acquisition at KTH. **76**

Figure 3.24 –Flow loop schematics for 34 (Top) and 50 (Bottom) mm. **77**

Figure 3.25 – Radiofrequency and magnetic pulse sequence used to obtain NMR velocity profile images for the flow of water within the pipe. Gsl is the slice selection gradient and Gfe is the frequency select gradient. **79**

Figure 3.26 – Images of the NMR apparatus provide by Aspect Imaging present at KTH Mekanics. **80**

Figure 3.27 – General set-up for the UVP probe system **81**

Figure 4.1 – Numerical models comparison for modelling particle flow (adapted from (Oevermann, Gerber, and Behrendt 2008)). **85**

Figure 4.2 – Example of finite element mesh with triangular discretization (adapted from (Singh 2009)). **91**

Figure 4.3 – Standard drag curve for motion of a sphere in a fluid (adapted from (Rhodes 2008)). **103**

Figure 4.4 – Near-Wall Region in Turbulent Flows (adapted from (Ariyaratne 2005)). **114**

Figure 4.5 – The computational domain is located a distance y_p from the wall for wall functions (adapted from (COMSOL Multiphysics 2012)). **115**

Figure 4.6 – Near Wall Treatment for Low Reynolds Number approach (adapted from (Kalitzin et al. 2005)). **117**

Figure 4.7 – Mapping of turbulence modification experiments based on (a) Pa_{St} and Re_L, and (b) Pa_{Re} and Re_L. The circle and square symbols represent air and water turbulence, respectively. The open symbols represent *k* augmentation and filled symbols show *k* attenuation (adapted from (Tanaka and Eaton 2008)). **124**

Figure 5.1 – 2D (Left) and 3D (Right) unstructured meshes **131**

Figure 5.2 – 2D turbulent kinetic energy profiles for Case 1, 2 and 3 along the pipe radius for a flow velocity of 1 m. s^{-1} (Left) and 4 m. s^{-1} (Right). **134**

Figure 5.3 – 2D turbulent dissipation rate for Case 1, 2 and 3 along the pipe radius for a flow velocity of 1 m. s^{-1} (Left) and 4 m. s^{-1} (Right). **134**

Figure 5.4 –2D mixture velocity profiles for Case 1, 2 and 3 along the pipe radius, **135**

velocity of 1 m. s^{-1} (Left) and 4 m. s^{-1} (Right).

Figure 5.5 – 2D turbulent kinetic energy (Left) and turbulent dissipation rate (Right) for Case 2 along the pipe radius for a flow velocity of 1 m. s^{-1}. **136**

Figure 5.6 – Comparison between pressure drop values from experimental data by Shook (1985) (EXP) and numerical results with the Mixture Model coupled with a High Reynolds closure (MM & HR) and calculated values from Durand-Condolios correlation (DC) for the solid-liquid flows using buoyant particles with 0.3 mm diameter and 34 % (v/v). **136**

Figure 5.7 – Normalized numerical and experimental vertical solids concentration profiles for buoyant particles with solids volumetric fraction of 34.0 % (v/v). **137**

Figure 5.8 – Experimental and numerical horizontal velocity profiles for neutrally buoyant particles with solids volumetric fractions of 34 % (v/v). **138**

Figure 5.9 – 2D Turbulent Kinetic Energy (Left) and Turbulent Dissipation Rate (Right) for an increase of 20% in the standard value of $C_{\varepsilon 1}$ (Top) and $C_{\varepsilon 2}$ (Bottom) for a flow velocity of 1 m. s^{-1}. **141**

Figure 5.10 – 2D Turbulent Kinetic Energy (Right) and Turbulent Dissipation Rate (Left) for an increase of 20% in the standard value of σ_ε (Top) and σ_k (Bottom) for a flow velocity of 1 m. s^{-1} **142**

Figure 5.11 – 2D Turbulent Kinetic Energy (Right) and Turbulent Dissipation Rate (Left) for all closure coefficients values tested for a flow velocity of 1 m. s^{-1} (Top) and 4 m. s^{-1} (Bottom). **144**

Figure 5.12 – 3D unstructured mesh employed with the Mixture Model and High Reynolds Turbulence closure for the settling particles numerical studies. **149**

Figure 5.13 – Pressure gradients comparison between Lahiri & Ghanta (2010) experimental results (EXP) and the calculated pressure gradients for the settling particles using Mixture Model with the High Reynolds *k-ε* Turbulence model (MM & k-ε) and the Durand-Condolios correlation (DC). **151**

Figure 5.14 – Normalized vertical solid concentration profiles with (a) 10 % (v/v), (b) 30 % (v/v), (c) 40 % (v/v) of settling particles comparison between the experimental data (EXP) and numerical results Mixture Model with the High **152**

Reynolds k-ε Turbulence model (MM & k-ε).

Figure 5.15 – 3D unstructured mesh employed with the Mixture Model and a Low Reynolds Turbulence closure for the settling particles numerical studies. **154**

Figure 5.16 – Pressure gradients comparison between Lahiri & Ghanta (2010) experimental results (EXP) and the calculated pressure gradients for the settling particles using Mixture Model with the Low Reynolds *k-ε* Turbulence model (MM & LR) and the Durand-Condolios correlation (DC). **155**

Figure 5.17 – Normalized vertical solid concentration profiles with (a) 10 % (v/v), (b) 30 % (v/v), (c) 40 % (v/v) of settling particles comparison between the experimental data (EXP) and numerical results Mixture Model with the Low Reynolds *k-ε* Turbulence model (MM & LR). **158**

Figure 5.18 – Comparison between 2D cross-sectional profiles for the particle concentration (Top Row), Turbulent Kinetic Energy (Middle Row) and Turbulent Dissipation Rate (Bottom Row) for the MM+HR (Left Column) and MM+HR+τ_s (Right Column) for a flow velocity of $3\ \mathrm{m.s^{-1}}$ and 40 % (v/v) particle concentration. **160**

Figure 5.19 – Adimensional numerical vs experimental vertical particle distribution profiles (a) for a flow velocity of $5\ \mathrm{m.s^{-1}}$; (b) for a flow velocity of $3\ \mathrm{m.s^{-1}}$ with a particle volumetric fraction of 40 % (v/v). **163**

Figure 5.20 – Numerical horizontal (a) and vertical (b) slip velocity profiles for flow velocities of 3 and $5\ \mathrm{m.s^{-1}}$ with a particle volumetric fraction of 40 % (v/v). **164**

Figure 5.21 – Numerical horizontal (a) and vertical (b) drag profiles for flow velocities of 3 and $5\ \mathrm{m.s^{-1}}$ with a particle volumetric fraction of 40 % (v/v). **165**

Figure 5.22 – Adimensional numerical vs experimental vertical particle distribution profiles for a flow velocity of $2\ \mathrm{m.s^{-1}}$ with a particle volumetric fraction of 30 % (v/v). **166**

Figure 5.23 – Numerical horizontal (a) and vertical (b) slip velocity for a flow velocity of $2\ \mathrm{m.s^{-1}}$ with a particle volumetric fraction of 30 % (v/v). **168**

Figure 5.24 – Numerical horizontal (a) and vertical (b) drag profiles for a flow velocity of $2\ \mathrm{m.s^{-1}}$ with a particle volumetric fraction of 30 % (v/v). **169**

Figure 5.25 – Comparison between 2D cross-sectional profiles for the particle **171**

concentration (Top Row), Turbulent Kinetic Energy (Middle Row) and Turbulent Dissipation Rate (Bottom Row) for the Mixture Model with a Low Reynolds Turbulence closure (Left Column) and incorporating the Hsu modifications (MM+LR+HSU) (Right Column) for a flow velocity of 5 $m.s^{-1}$ and 40 % (v/v) particle concentration.

Figure 5.26 – Comparison between 2D cross-sectional profiles for the particle concentration (Top Row), Turbulent Kinetic Energy (Middle Row) and Turbulent Dissipation Rate (Bottom Row) for the Mixture Model with a Low Reynolds Turbulence closure (Left Column) and incorporating the Hsu modifications (MM+LR+HSU) (Right Column) for a flow velocity of 3 $m.s^{-1}$ and 40 % (v/v) particle concentration. **172**

Figure 6.1 – (a) *SOLARTRON 1250 Frequency Response Analyser*; (b) 16 electrode vertical test section. **179**

Figure 6.2 – Alumina cylinders employed as obstacles. **179**

Figure 6.3 – Preliminary tests involving obstacles. **180**

Figure 6.4 – Static testing: first column (Left) contains pictures of the object, the second column contains reconstructed images using mesh 1, the third column contains reconstructed images using mesh 2 and the last column contains reconstructed images using mesh 3. **182**

Figure 6.5 – Solid-liquid suspension tests carried out with an average particle concentration of 3,9 g/L for flow rates of 0, 12, 33 and 52 $m^3.h^{-1}$, respectively, from top to bottom (left column contains pictures of the section under study, middle column images obtained using mesh 2 and the right column images obtained using mesh 3). **184**

Figure 6.6 – Picture and schematics (adapted from (S. A. Miedema 2014)) of the observed flow regimes for the 0.1-0.2 mm sized particles at 0.5(Top) and 1.0 and 2.0 $l.s^{-1}$ (Bottom). **187**

Figure 6.7 – Picture and schematics of the observed flow regimes at 0.5 $l.s^{-1}$ with the 0.4-0.6 mm particles in the 34 mm ID pipe tests. **188**

Figure 6.8 – Pictures of the lateral (Left Column) and bottom views (Right Column) of the observed flow regimes at 2.0 (Top Line) and 4.0 $l.s^{-1}$ (Bottom Line) with the 0.4-0.6 mm particles in the 50 mm ID pipe tests. **188**

Figure 6.9 – Finite Element Mesh used in the numerical studies for the KTH data. **193**

Figure 6.10 – Experimental MRI and Numerical *k*-*ε* normalized horizontal (Top) and vertical (Bottom) velocity profiles for flowrates of 2.0 (Left), 1.0 (Middle) and 0.5 l.s^{-1} (Right) in a 34 mm ID pipe. **196**

Figure 6.11 – Experimental MRI and Numerical *k*-*ε* normalized horizontal (Top) and vertical (Bottom) velocity profiles for flowrates of 2.0 (Left), 1.0 (Middle) and 0.5 l.s^{-1} (Right) in a 50 mm ID pipe. **197**

Figure 6.12 – Experimental, Numerical and Darcy-Weisbach pressure gradients profiles for water flow in 34 (Left) and 50 mm ID (Right) pipes. **199**

Figure 6.13 – MRI and Numerical 2D velocity profiles for water at the flowrates of 2.0 (Bottom), 1.0 (Middle) and 0.5 l. s^{-1} (Top) in a 34 mm ID pipe. **200**

Figure 6.14 – Experimental MRI, UPV and Numerical normalized horizontal (Top) and vertical (Bottom) velocity profiles for flowrates of 2.0 (Left), 1.0 (Middle) and 0.5 l. s^{-1} (Right) in a 34 mm ID pipe for a solids volumetric concentration of 0.5 % (v/v). **202**

Figure 6.15 – Experimental MRI, UPV and Numerical normalized horizontal (Top) and vertical (Bottom) velocity profiles for flowrates of 2.0 (Left), 1.0 (Middle) and 0.5 l. s^{-1} (Right) in a 34 mm ID pipe for a solids volumetric concentration of 1.0 % (v/v). **203**

Figure 6.16 – Experimental MRI, UPV and Numerical normalized horizontal (Top) and vertical (Bottom) velocity profiles for flowrates of 2.0 (Left), 1.0 (Middle) and 0.5 l. s^{-1} (Right) in a 34 mm ID pipe for a solids volumetric concentration of 3.0 % (v/v). **204**

Figure 6.17 – Experimental, Numerical and Durand-Condolios pressure gradients profiles for solid-liquid suspensions of 0.1-0.2 mm particles for 0.5 (Top), 1.0 (Middle) and 3.0 % (v/v) (Bottom) solids volumetric concentration in a 34 mm ID pipe. **205**

Figure 6.18 – MRI and Numerical 2D velocity profiles for solid-liquid suspensions of 0.1-0.2 mm particles with flowrates of 2.0 (Bottom), 1.0 (Middle) and 0.5 l. s^{-1} (Top) in a 34 mm ID pipe for a solids volumetric concentration of 0.5 % (v/v). **207**

Figure 6.19 – MRI and Numerical 2D velocity profiles for solid-liquid suspensions of 0.1-0.2 mm particles with flowrates of 2.0 (Bottom), 1.0 (Middle) and 0.5 l. s^{-1} (Top) in a 34 mm ID pipe for a solids volumetric concentration of **208**

1.0 % (v/v).

Figure 6.20 – MRI and Numerical 2D velocity profiles for solid-liquid suspensions of 0.1-0.2 mm particles with flowrates of 2.0 (Bottom), 1.0 (Middle) and 0.5 $l.s^{-1}$ (Top) in a 34 mm ID pipe for a solids volumetric concentration of 3.0 % (v/v). **209**

Figure 6.21 – Experimental MRI, UPV and Numerical normalized horizontal (Top) and vertical (Bottom) velocity profiles for solid-liquid suspensions of 0.4-0.6 mm particles with flowrates of 2.0 (Left) and 1.0 $l.s^{-1}$ (Right) in a 34 mm ID pipe for a solids volumetric concentration of 0.5 % (v/v). **211**

Figure 6.22 – Experimental MRI, UPV and Numerical normalized horizontal (Top) and vertical (Bottom) velocity profiles for solid-liquid suspensions of 0.4-0.6 mm particles with flowrates of 2.0 (Left) and 1.0 $l.s^{-1}$ (Right) in a 34 mm ID pipe for a solids volumetric concentration of 1.0 % (v/v). **212**

Figure 6.23 – Experimental MRI, UPV and Numerical normalized horizontal (Top) and vertical (Bottom) velocity profiles for solid-liquid suspensions of 0.4-0.6 mm particles with flowrates of 2.0 (Left) and 1.0 $l.s^{-1}$ (Right) in a 34 mm ID pipe for a solids volumetric concentration of 3.0 % (v/v). **213**

Figure 6.24 – Experimental, Numerical and Durand-Condolios pressure gradients profiles for solid-liquid suspensions of 0.4-0.6 mm particles with 0.5 (Top), 1.0 (Middle) and 3.0 % (v/v) (Bottom) solids volumetric concentration in a 34mm ID pipe. **214**

Figure 6.25 – MRI and Numerical 2D velocity profiles for solid-liquid suspensions of 0.4-0.6 mm particles with flowrates of 2.0 (Bottom) and 1.0 $l.s^{-1}$ (Top) in a 34 mm ID pipe for a solids volumetric concentration of 0.5 % (v/v). **215**

Figure 6.26 – MRI and Numerical 2D velocity profiles for solid-liquid suspensions of 0.4-0.6 mm particles with flowrates of 2.0 (Bottom) and 1.0 $l.s^{-1}$ (Top) in a 34 mm ID pipe for a solids volumetric concentration of 1.0 % (v/v). **216**

Figure 6.27 – MRI and Numerical 2D velocity profiles for solid-liquid suspensions of 0.4-0.6 mm particles with flowrates of 2.0 (Bottom) and 1.0 $l.s^{-1}$ (Top) in a 34 mm ID pipe for a solids volumetric concentration of 3.0 % (v/v). **217**

Figure 6.28 – Reconstructed 2D images of the pipe cross-section using EIT normalized conductivity measurements for solid-liquid suspensions of 0.4-0.6 mm particles for 1.0 (Top), 3.0 (Middle) and 5.0 % (v/v) (Bottom) solids volumetric concentration in a 50 mm ID pipe. **219**

Figure 6.29 – 1D vertical slice schematics for both reconstructed EIT 2D images of the pipe cross-section and numerical data with the Mixture Model in a 50 mm ID pipe. **220**

Figure 6.30 – 1D vertical normalized electrical conductivity profiles (η) with EIT and particle concentrations profiles (ϕ_s) with the Mixture Model in a 50 mm ID pipe.. **221**

Figure 6.31 – Comparison between 1D calculated vertical particle distribution profiles with EIT, $\phi(z)$, and Maxwell Equation, ϕ_{ap}, with the particle concentrations profiles from the Mixture Model in a 50 mm ID pipe. **224**

Figure 6.32 – Experimental MRI, UPV and Numerical normalized horizontal (Top) and vertical (Bottom) velocity profiles for solid-liquid suspensions of 0.4-0.6 mm particles with flowrates of 4.0 (Left) and 2.0 $l.s^{-1}$ (Right) in a 50 mm ID pipe for a solids volumetric concentration of 1.0% (v/v). **226**

Figure 6.33 – Experimental MRI, UPV and Numerical normalized horizontal (Top) and vertical (Bottom) velocity profiles for solid-liquid suspensions of 0.4-0.6 mm particles with flowrates of 4.0 (Left) and 2.0 $l.s^{-1}$ (Right) in a 50 mm ID pipe for a solids volumetric concentration of 3.0% (v/v). **227**

Figure 6.34 – Experimental MRI, UPV and Numerical normalized horizontal (Top) and vertical (Bottom) velocity profiles for solid-liquid suspensions of 0.4-0.6 mm particles with flowrates of 4.0 (Left) and 2.0 $l.s^{-1}$ (Right) in a 50 mm ID pipe for a solids volumetric concentration of 5.0% (v/v). **228**

Figure 6.35 – Experimental, Numerical and Durand-Condolios pressure gradients profiles for solid-liquid suspensions of 0.4-0.6 mm particles for 1.0 (Top), 3.0 (Middle) and 5.0% (v/v) (Bottom) solids volumetric concentration in a 50 mm ID pipe. **229**

Figure 6.36 –Comparison of the numerical turbulent kinetic energy, k, (Top Row) and turbulent dissipation rate, ε, (Bottom Row) profiles for the studied flows at KTH for a flow velocity of $2\ m.s^{-1}$ between water and solid-liquid suspensions with 3.0 % (v/v) solids volumetric concentration for both 34 and 50 mm ID pipes. **233**

Figure 6.37 – Pictures of the observed flow regimes for the 0.1-0.2 mm sized particles with particle concentrations of 0.8 % (v/v) at $28\ m^3.h^{-1}$ (Left) and 5.0 % (v/v) at $84\ m^3.h^{-1}$ (Right). **236**

Figure 6.38 – Picture of the dune formation observed at a $28\ m^3.h^{-1}$ flowrate **237**

with the 0.4-0.6 mm particles at 5.0 % (v/v) particle concentration in the 100 mm ID pipe tests.

Figure 6.39 – Pictures of the moving bed regime (Top) and heterogeneous flow (Bottom) regimes with the 0.4-0.6 mm particles at 5.0 % (v/v) particle concentration in the 100 mm ID pipe tests. **237**

Figure 6.40 – Finite Element Swept Mesh used in the numerical studies for the DEQ data. **240**

Figure 6.41 – Experimental, Numerical and Darcy-Weisbach pressure gradients profiles for water flow in a 100 mm ID pipe. **242**

Figure 6.42 – Reconstructed 2D images of the pipe cross-section using EIT normalized conductivity measurements for solid-liquid suspensions of 0.1-0.2 mm particles in a 100 mm ID pipe. **243**

Figure 6.43 – Comparison between the experimental 1D vertical particle concentrations profiles from the (SP) with the calculated profiles using the EIT, Maxwell Equation, and the Mixture Model (using the Schiller-Naumann (SN) and Haider-Levenspiel (HL) drag correlations) in a 100 mm ID pipe for 0.1-0.2 mm particle concentrations of 11.0 (Left Column), 8.0 (Middle Column) and 5.0 % (v/v) (Right Column) and for 28 (Bottom Line), 56 (Middle Line) and 84 $m^3.h^{-1}$ (Top Line) flowrates **247**

Figure 6.44 – Comparison between the experimental 1D vertical particle concentrations profiles from the (SP) with the calculated profiles using the EIT, Maxwell Equation, and the Mixture Model (using the Schiller-Naumann (SN) and Haider-Levenspiel (HL) drag correlations) in a 100 mm ID pipe for 0.1-0.2 mm particle concentrations of 2.0 (Left Column) and 0.8 % (v/v) (Right Column) and for 28 (Bottom Line), 56 (Middle Line) and 84 m3/h (Top Line) flowrates. **248**

Figure 6.45 – Experimental, Numerical and Durand-Condolios pressure gradients profiles for solid-liquid suspensions of 0.1-0.2 mm particles for 11.0 to 0.8 % (v/v) solids volumetric concentration with 28, 56 and 84 $m^3.h^{-1}$flowrates in a 100 mm ID pipe. **252**

Figure 6.46 – Reconstructed 2D images of the pipe cross-section using EIT normalized conductivity measurements for solid-liquid suspensions of 0.4-0.6 mm particles in a 100 mm ID pipe. **254**

Figure 6.47 – Comparison between the experimental 1D vertical particle concentrations profiles from the Sampling Probe (SP) with the calculated profiles using the EIT, Maxwell Equation, and the Mixture Model (using the **258**

Schiller-Naumann (SN) and Haider-Levenspiel (HL) drag correlations) in a 100 mm ID pipe for 0.4-06 mm particle concentrations of 11.0 (Left Column), 8.0 (Middle Column) and 5.0 % (v/v) (Right Column) and for 28 (Bottom Line), 56 (Middle Line) and 84 $m^3.h^{-1}$ (Top Line) flowrates.

Figure 6.48 – Comparison between the experimental 1D vertical particle concentrations profiles from the Sampling Probe (SP) with the calculated profiles using the EIT, Maxwell Equation, and the Mixture Model (using the Schiller-Naumann (SN) and Haider-Levenspiel (HL) drag correlations) in a 100 mm ID pipe for 0.4-0.6 mm particle concentrations of 2.0 (Left Column) and 0.8 % (v/v) (Right Column) and for 28 (Bottom Line), 56 (Middle Line) and 84 $m^3.h^{-1}$ (Top Line) flowrates. **259**

Figure 6.49 – Experimental, Numerical and Durand-Condolios pressure gradients profiles for solid-liquid suspensions of 0.4-0.6 mm particles for 11.0 to 0.8 % (v/v) solids volumetric concentration with 28, 56 and 84 $m^3.h^{-1}$flowrates in a 100 mm ID pipe. **260**

Figure 6.50 –Comparison of the numerical turbulent kinetic energy, k, (Left Column) and turbulent dissipation rate, ε, (Right Column) profiles for the studied flows at DEQ for a flow velocity of 3 $m.s^{-1}$ between water and solid-liquid suspensions with 5.0 and 11.0 % (v/v) solids volumetric concentration for a 100 mm ID pipes. **263**

Figure A.1 – Neumann boundary condition derivation, where J_{s1} and J_{s2} are the electric current densities outsider and inside the volume τ, respectively. E_1 and E_2 are the corresponding electric fields (adapted from (M. Vauhkonen 1997). **274**

Figure A.2 – Forward Problem in EIT (A): the electrical conductivity and electric current are known and the electric potential distribution is calculated; Inverse Problem in EIT (B): the physical model is wanted based on the aforementioned electric potential distribution (Adapted from (Molinari 2003)). **277**

Figure A.3 – Meshes utilized in the 2D EIT image reconstruction. **283**

Figure A.4 – Regularization application to a mesh element. **288**

Figure B1 – Front Panel image. **299**

Figure B2 – Block Diagram code. **301**

Figure C.1 – Mastersizer 2000 profile for the 0.1-0.2 mm particles. **303**

Figure C.2 – Mastersizer 2000 profile for the 0.4-0.6 mm particles. **304**

Figure D1 – 3D mixture velocity for Case 1, 2 and 3 along the pipe radius for a flow velocity of 1 m. s^{-1} (Left) and 4 m. s^{-1} (Right). **308**

Figure D2 – 3D turbulent kinetic energy for Case 1, 2 and 3 along the pipe radius for a flow velocity of 1 m. s^{-1} (Left) and 4 m. s^{-1} (Right). **308**

Figure D3 – 3D turbulent dissipation rate for Case 1, 2 and 3 along the pipe radius for a flow velocity of 1 m. s^{-1} (Left) and 4 m. s^{-1} (Right). **308**

Figure D4 – Cross sectional images of the 3D turbulent kinetic energy (Left) and turbulent dissipation rate for Case 2 for a flow velocity of 4 m. s^{-1}. **309**

Figure D5 – Pipe cross section profile of the 3D Turbulent Kinetic Energy (Left) and Turbulent Dissipation Rate (Right) for an increase of 20% in the standard value of $C_{\varepsilon 1}$ (Top) and $C_{\varepsilon 2}$ (Bottom) for a flow velocity of 4 m. s^{-1}. **312**

Figure D6 – Pipe cross section profile of the 3D Turbulent Kinetic Energy (Left) and Turbulent Dissipation Rate (Right) for an increase of 20% in the standard value of σ_ε (Top) and σ_k (Bottom) for a flow velocity of 4 m. s^{-1}. **312**

Figure D7 – 3D Turbulent Kinetic Energy (Left) and Turbulent Dissipation Rate (Right) for an increase of 20% in the standard value of C_μ (Top) and σ_t (Bottom) for a flow velocity of 4 m. s^{-1}. **313**

Figure D8 – 3D Turbulent Kinetic Energy (Left) and Turbulent Dissipation Rate (Right) for all closure coefficients for a flow velocity of 1 m. s^{-1} (Top) and 4 m. s^{-1} (Bottom). **313**

LIST OF TABLES

Table 2.1 – Sensor characteristics for process tomography (adapted from (M. Beck and Williams 1996; M. Beck and Williams 1995)). **20**

Table 3.1 – Particle data for the performed tests at Coimbra. **57**

Table 3.2 – Solid-liquid suspensions data for the performed tests at KTH Mekanics. **77**

Table 4.1 – Low Reynolds k-ε damping functions and boundary conditions. **111**

Table 5.1 – Conditions for the numerical studies with Shook (1985) data for 0.3 mm buoyant particles with 34% (v/v) particle concentration. **127**

Table 5.2 – Deposition velocities for the buoyant particles from (C. Shook 1985) for 0.3 mm sized particles with a particle concentration of 34 % (v/v) in a 52.23 mm ID pipe. **129**

Table 5.3 – Particle data for Shook's experiments with the 34 % (v/v) particle concentration (C. Shook 1985). **130**

Table 5.4 – Mesh parameters for the buoyant particles numerical studies. **131**

Table 5.5 – Influence of the turbulence scales on the numerical turbulence variables and comparison between the experimental and numerical pressure drops for the 2D numerical studies. **134**

Table 5.6 – Standard Closure Coefficients and Modified Values for the numerical studies with the buoyant particles. **139**

Table 5.7 – Comparison between the 2D numerical results for Case 2 and for a 20% increase in the k-ε turbulence closure coefficients. **140**

Table 5.8 – Conditions for the numerical studies with Lahiri & Ghanta (2010) data. **146**

Table 5.9 – Deposition velocities for the settling particles numerical studies using Lahiri & Ghanta (2010) experimental data. **147**

Table 5.10 – Particle data for Lahiri & Ghanta (2010) experiments. **148**

Table 5.11 – Mesh parameters for the initial studies with the settling particles. **148**

Table 5.12 – Mesh parameters for the initial studies with the settling particles using a Low Reynolds Turbulence closure. **153**

Table 5.13 – Comparison between experimental and numerical pressure drops for settling particles. **157**

Table 5.14 – Comparison between the experimental and simulated pressure gradients with the Mixture Model coupled with a High Reynolds Turbulence closure (MM+HR) and the Mixture Model with the modified wall shear stress (MM+HR+τ_s) for a flow velocity of $3\ \mathrm{m.s^{-1}}$ and 40 % (v/v) particle **159**

concentration.

Table 5.15 – Low Reynolds numerical vs experimental pressure gradient for 2, 3 and 5 m. s^{-1} for a solid volumetric fractions of 30 and 40 % (v/v) – Influence of the Drag Correlations. **170**

Table 5.16 – Comparison between the experimental and simulated pressure gradient with the Mixture Model coupled with a Low Reynolds Turbulence closure (MM+LR) and the Mixture Model coupled with a Low Reynolds Turbulence closure and the HSU modification (MM+LR+HSU) for flow velocities of 3 and 5 m. $s^{-1}$and 40 % (v/v) particle concentration. **173**

Table 5.17 – Stokes Number (St) based Particle Moment Number (Pa_{St}) values for the buoyant particles in Shook (1985) study with a 34 % (v/v) particle concentration. **173**

Table 5.18 – Stokes Number (St) based Particle Moment Number (Pa_{St}) for the settling particles in Lahiri & Ghanta (2010)study with 30 and 40 % (v/v) particle concentrations. **174**

Table 6.1 – Tests conditions for the preliminary tests. **181**

Table 6.2 – Experimental Conditions for the KTH tests. **186**

Table 6.3 – Deposition velocities for the KTH tests. **190**

Table 6.4 – Particle data for the KTH experiments. **192**

Table 6.5 – Finite Element Mesh characteristics for the numerical studies with the KTH data. **193**

Table 6.6 – Comparison of Experimental, Numerical and Darcy-Weisbach pressure gradients profiles for water flow in 34 and 50 mm ID pipes (deviations from experimental are in bold). **197**

Table 6.7 – Stokes Number (St) based Particle Moment Number (Pa_{St}) values for the KTH tests. **230**

Table 6.8 – Conditions for the DEQ experiments. **235**

Table 6.9 – Deposition velocities for the DEQ tests. **238**

Table 6.10 – Particle data for the DEQ experiments. **239**

Table 6.11 – Finite Element Mesh characteristics for the numerical studies with the DEQ data. **240**

Table 6.12 – Comparison of Experimental, Numerical and Darcy-Weisbach pressure gradients profiles for water flow in the 100 mm ID pipes. **241**

Table 6.13 – Operating experimental temperatures and final electrical conductivity of the suspension measured during data acquisition for the 0.1-0.2 mm particles in the 100 mm ID pipes. **245**

Table 6.14 – Operating experimental temperatures and final electrical **253**

conductivity of the suspension measured during data acquisition for the 0.4-0.6 mm particles in the 100 mm ID pipes.

Table 6.15 – Stokes Number (St) based Particle Moment Number (Pa_{St}) values for the DEQ tests. **261**

Table C.1 – Volume fraction per particle sizes for the 0.1-0.2 mm particles. **304**

Table C.2 – Volume fraction per particle sizes for the 0.4-0.6 mm particles **305**

Table D1 – Influence of the different turbulence scales on the numerical turbulence variables and comparison between the experimental and numerical pressure drops for the 3D numerical studies **307**

Table D2 – Comparison between the simulated three dimensional results for Case 2 and for a 20% increase in the closure coefficients. **310**

NOMENCLATURE

EIT	Electrical Impedance Tomography
FEM	Finite Element Method
MRI	Magnetic Resonance Imaging
SP	Sampling Probe
UPV	Ultrasound Pulse Velocimetry
UVP	Ultrasound Doppler Velocimetry Profiling
∇	Mathematical gradient
$\nabla \cdot$	Mathematical divergence
α	Regularization parameter
β_j	Voltage at electrode j
γ	Gyromagnetic ratio
Γ_k	Mass conservation of phase k
δ	First gradient pulse duration
ΔP	Pressure drop
ϵ	Pipe equivalent roughness
ε	Turbulent dissipation rate
ε^*	Jones-Launder dissipation rate for the Low Reynolds k-ε turbulence model
η	Normalized conductivity measurements
θ	Phase shift between the current and the voltage brought upon by the domain impedance in Chapter III
θ	Parameter to be estimated in Galerkin Formulation
λ	Represents the average interparticular space
λ	Solids concentration by Bagnold
μ_m	Mixture dynamic viscosity
μ_c	Dynamic viscosity of the continuous phase
μ_d	Dynamic viscosity of the dispersed phase
ν	Mixture kinematic viscosity
ν_T	Turbulent kinematic viscosity
ρ_m	Mixture density
$\rho_c; \rho_L$	Continuous phase density
ρ_k	Density of phase k
$\rho_d; \rho_s$	Dispersed phase density
τ	Volume at the boundary $\partial\Omega$
τ_{Gm}	Turbulent and viscous stresses
τ_m	Viscous stress
τ_{Tm}	Turbulent stress
τ_{Dm}	Diffusion stress
$\tau_{xx}\,; \tau_{yy};\ \tau_{zz}$	Normal Reynolds stresses:
$\tau_{xy} = \tau_{yx}$	
$\tau_{xz} = \tau_{zx}$	Shear Reynolds stresses
$\tau_{yz} = \tau_{zy}$	

σ	Electrical conductivity
σ_m	Mixture electrical conductivity
σ_0	Reference electrical conductivity
σ_w	Water electrical conductivity
σ_{s0}	Electrical conductivity for a known initial concentration of solids
σ_T	Particle Schmidt Number
τ_w	Wall shear stress
τ_s	Solids shear stress
ϕ_{ap}	Apparent solids concentration
ϕ_c	Continuous phase volumetric fraction
$\phi; \phi_d$	Dispersed phase volumetric fraction
ϕ_k	Volumetric concentration of phase k
ϕ_{vf}	Average inlet volumetric fraction of particles
ϕ_0	Initial concentration of solids
$\phi(z)$	Calculated vertical particle distribution profile
ϕ_{max}	Maximum packing of solids
$\boldsymbol{\Phi}$	Scalar in the transport Equation 4.62
ϑ	Arbitrary function of the Galerkin formulation
o	Objective function
φ	Electrical potential
φ_h	Approximate solution or weak solution from FEM
Φ_i	Voltage in node i to be determined
Φ_ℓ	Voltage measured in electrode ℓ
ω	Electrical signal frequency
ω_L	Resonance or Larmor frequency
Ω	Isotropic domain
$\partial\Omega$	Boundary of isotropic domain
ψ	Instantaneous phase
A_σ	Area under the normalized electrical conductivity curve
AR	Arquimedes Number
B_0	Static magnetic field strength
$\boldsymbol{B}$	Magnetic flux density
c_d	Dispersed phase mass fraction
C_D	Drag coefficient
C_o	Volumetric concentration of solids
$C_{\varepsilon 1}$	Closure coefficients for the k-ε turbulence model
$C_{\varepsilon 2}$	Closure coefficients for the k-ε turbulence model
σ_ε	Closure coefficients for the k-ε turbulence model
σ_k	Closure coefficients for the k-ε turbulence model
C_μ	Closure coefficients for the k-ε turbulence model
d_p	Particle diameter
$D; D_i$	Pipe internal diameter
D_{md}	Turbulent eddy diffusion
D_t	Scalar diffusivity coefficient
D	Jones-Launder damping functions for the Low Reynolds k-ε
E	Turbulence model

$\boldsymbol{D}$	Electric flux density
$\boldsymbol{E}$	Electric field
e_ℓ	Area of Electrode ℓ
$\lvert e_j \rvert$	Size of electrode j
$f_\mu; f_1; f_2$	Jones-Launder damping functions for the Low Reynolds k-ε turbulence model
$f; f_D$	Friction factor
F	Volume forces
F_D	Drag Force
g	Gravitational acceleration
$\mathbf{G}$	Magnetic gradient vector
H	Magnetic field
$\mathcal{H}$	Moore-Penrose Inverse or pseudo-inverse
H^1	Space of functions where the basis or weight functions are integrable
i	Pressure drop of slurry
i_w	Pressure drop of water
I	Identity matrix
I_ℓ	Injected electric current on Electrode ℓ
I_m	Electrical current amplitude (Chapter III)
I_T	Turbulence intensity
J	Electric current density
J_{s1}	Electric current densities outside the volume τ
J_{s2}	Electric current densities inside the volume τ
$\mathcal{J}$	Jacobian
k	Constant for Equation 2.7
k	Turbulent kinetic energy
K	Number of elements of FEM mesh
K_2	Constant for Equation 2.8
K_i	Proportionality coefficient
l_P	Length scale of the acceleration
L	Characteristic length of the equipment
L_e	Maximum entrance length
L_H	Hydraulic diameter
L_i	Represents the length scale of the flow without particles
L_T	Turbulence length scale
L	Number of electrodes in Chapter III and Appendix A
L_1	Square root of the pondered matrix
L_2	Regularization matrix
$m(r)$	Local magnetic spin density
m_{dc}	Mass transfer ratio between phases
M_k	Momentum source term
M_k'	Fluctuating part of the momentum source term
M_m	Surface tension force
n	Empirical parameter of Equation 2.9
$\boldsymbol{n}$	Normal vector
N	Number of nodes in a FEM mesh

p_m	Pressure of the mixture
P_k	Turbulence production
$\mathbf{r}$	Position vector
$\mathbf{r_0}$	Initial position vector
r_p	Particle radius
Re_p	Particle Reynolds Number
S_{k1}	Correlation between the fluid and sediment velocity fluctuations
S_{k2}	Production of k due to the drag force
t_P	Relaxation time of a particle
T_i	Turbulence intensity
$u'v'w'$	Velocity fluctuations in the x, y and z directions, respectively
u	Concentrated suspensions settling velocity in Equation 2.9
u_o	Individual particle settling velocity
u_k	Velocity of phase k
u_m	Mixture velocity
u_{mk}	Velocity of phase k in function of the center of the mass of the mixture.
u^T	Transpose of the mixture velocity
u_c	Continuous phase velocity
u_{ck}	Diffusion velocity
u_d	Dispersed phase velocity
u_t	Terminal velocity
$\hat{u}$	Approximation function
u_*	Friction velocity at the wall
$\mathbf{U}$	Velocity vector
$U\ V\ W$	Velocity in the x, y and z directions, respectively.
$\mathbf{v}$	Constant average velocity
$v(x, y)$	Weight approximation function
V_D	Deposition Velocity
V_k	Volume of particle
V_ℓ	Vector of measured voltages on all the electrodes
V_m	Average flow velocity
V_m	Potential measured in one of the electrodes (Chapter III)
V_t	Terminal velocity of the particle
y^+	Wall lift-off in viscous units
y_p	Distance from the wall
$\mathcal{W}$	Pondered matrix
w_i	Shape function in FEM
z_ℓ	Impedance at Electrode ℓ
$\mathbb{Z}$	Observation

CHAPTER I

INTRODUCTION

1. CHAPTER I – INTRODUCTION

In this chapter the aims and objectives supporting this thesis are presented. Additionally, a general introduction with some relevant fundamental notions on solid-liquid suspensions flows and an historical overview on non-invading characterization techniques ensues to provide the reader with a better understanding of the frame of the present work and of the contribution of this manuscript to multiphase flows study. Lastly, this thesis is outlined.

1.1. GENERAL INTRODUCTION

The transport of solid-liquid suspensions in pipelines is of critical importance in industrial applications such as the production of chemicals, pharmaceuticals or foodstuffs, as also in the transportation of minerals and environmental remediation processes. Other examples include not only the aforementioned classical industrial applications but also emerging ones as those dealing with "intelligent" materials and biological systems. In these applications an array of different particle sizes and concentrations can be found, displaying unique behaviours and originating very different flow regimes.

In spite of the widespread application of solid-liquid suspensions, their inherent complexity has yet to be properly predicted by a unified numerical model or empirical correlation, and usually industries still possess custom charts or data for their particular suspension. This is rather inefficient and can lead to oversized dimensioning, low energy efficiency and even operation limitations/difficulties.

Particle concentration is one of the major process variables in solid-liquid suspensions flows. In the literature a considerable number of methods can be found that have been developed for online measurement of particle concentration and, in general, quantify a different property that later can be correlated to the particle concentration (Clayton Thomas Crowe 2005; Balachandar and Eaton 2010). Such examples are methods based on the

electrical conductivity of the solid-liquid suspension, where the electrical conductivity of the carrier fluid is a function of particle concentration.

With this study the intention is to focus on flowing solid-liquid suspensions. To this end, an Electrical Impedance Tomography (EIT) system was developed in order to characterize particle distribution in the pipeline. Additionally, another objective of this study was to compare the experimental results from the aforementioned EIT system with Computational Fluid Dynamics (CFD) numerical results.

For the CFD studies the Mixture Model, present in the software COMSOL Multiphysics®, was employed either in its standard formulation or incorporating adequate modifications to represent both experimental data and data published in the literature. These modifications depended on the turbulence behaviour since it is well established that particles influence the behaviour of the flows. This has been extensively documented for solid-gas suspensions flows, where the particles size influences directly the production of turbulence, i.e., bigger particles augment and small particles damp the turbulence production, respectively (C.T. Crowe 2000; Balachandar and Eaton 2010).

For liquid based flows the knowledge on turbulence modulation is scarcer; however, recent contributions can be found in the literature that contradict the aforesaid behaviour of solid-gas flows, stating that for solid-liquid suspensions, small particles can cause an augmentation of turbulence and medium size particles can attenuate turbulence. Moreover, highly concentrated solid-liquid suspensions of medium sized particles have shown pressure gradients in the same order of single-phase water flows under the same experimental conditions (Václav Matoušek 2005; D.R. Kaushal et al. 2012; S. Lahiri and Ghanta 2010). This posed an interesting research opportunity since understating the conditions conducing to this behaviour would prove valuable in the design of pipelines and pumping systems from an energy consumption standpoint.

1.2. AIMS AND OBJECTIVES

The main objective with this study was to get further knowledge on solid-liquid suspensions flows. In that regard, both experimental and numerical approaches were undertaken.

With the experimental approach the following intentions were:

i. To develop an low cost Electrical Impedance Tomography (EIT) apparatus, and thus feasible for industrial applications, and still capable of providing high resolution images allowing for accurate representation of particle distribution in the pipeline;
ii. To employ additional characterization techniques, namely Magnetic Resonance Imaging (MRI) and Ultrasonic Pulse Velocimetry (UPV) for fluid and particle characterization, respectively;
iii. Setup solid-liquid suspensions flow experiments where varied particle sizes and concentrations would be characterized using the aforementioned techniques in addition to pressure gradient, flow rate and temperature data acquisition using proper equipment;

Regarding the numerical simulation approach the motivation was:

iv. Establish a Computational Fluid Dynamics model for examining the solid-liquid suspensions flow, and to that effect the Mixture Model, present in the software package COMSOL Multiphysics®, was used to simulate the previous experiments under the same conditions;
v. Additionally, employ the Mixture Model to study the effect of particles in the turbulence production in the experimental data acquired in this study and on data available from the literature;
vi. Analyse modifications to the CFD model to accurately depict data from solid-liquid suspensions complex flows, where turbulence attenuation occurs under specific conditions;

1.3. THESIS OUTLINE

The thesis is divided into self-contained chapters, as follows:

The current chapter, **Chapter I**, introduces the subjects of research, the aims and objectives motivating the developed work, and finally the thesis outline.

Chapter II encompasses the literature review considering current issues in solid-liquid suspension flows, non-invading characterization techniques and their industrial dissemination. Furthermore, solid-liquid suspensions CFD modelling procedures and methodologies strategies are considered, and the advantages and drawbacks encountered are presented.

Chapter III details the experimental setups and test conditions. Moreover, the characteristics of the MRI and UPV apparatus are described as well as a thorough description of the development procedure behind the EIT apparatus.

Chapter IV presents an in depth description of the Mixture Model used in the solid-liquid suspensions flow simulations. This includes considerations on the choice of an adequate numerical model, COMSOL Multiphysics® Finite Element Model Formulation, drag formulations, turbulence models and turbulence modulation. The boundary conditions imposed on the CFD model are detailed.

Chapter V holds the key outcomes of this thesis where the CFD numerical results are discussed and evaluated.

In **Chapter VI** the experimental results attained at both KTH and DEQ laboratories are analysed.

Chapter VII unifies all the conclusions from the studies presented in the thesis. Future works to continue from the current results are also presented and discussed.

In **Appendix A,** a description of the mathematical theory behind the

Electrical Impedance Tomography is detailed.

Appendix B the MATLAB® and LabVIEW® codes employed in the reconstruction of the 2D EIT images and EIT operation, respectively, are imparted.

Appendix C contains the data on the particles size distribution analysis.

Appendix D includes the 3D results for the buoyant particles numerical studies depicted in Chapter V.

Lastly, in **Appendix E**, current and future conference and journal publications resulting from this study

CHAPTER II

STATE OF THE ART

2. CHAPTER II – STATE OF THE ART

In this chapter a literature review is imparted on the topics of process tomographic techniques, computational fluid dynamics numerical models and turbulence modification in solid-liquid suspensions.

The relevance of process tomographic techniques, which served as a conceptual basis for the development of the electrical impedance tomography system employed in this work, is demonstrated. Magnetic, acoustic and electrical based techniques are analysed and their advantages as well as drawbacks are differentiated. Also, an historical overview of process tomography is drawn and some considerations on the basis of a tomographic system are presented.

The importance of solid-liquid suspensions in industrial applications and their classification are briefly discussed in the next section.

The prevalence of Computational Fluid Dynamics in practically every field of engineering is undeniable and solid-liquid suspensions flows are no exception. Some of the most known turbulence models, empirical correlations and modelling strategies for solid-liquid suspensions are analysed, and their capability of predicting the modification of the turbulence structure by the presence of solid particles is evaluated. Finally, the factors that are involved in turbulence modulation are reviewed.

2.1. SOLID-LIQUID SUSPENSIONS FLOWS

A suspension is a mixture of solid particles in a fluid. Solid-liquid suspensions are a subclass of multiphase flows where solid particles are dispersed in a turbulent liquid flow. These are present in everyday life in our household with many assuming, under a naked eye, the appearance of a liquid. Some examples are liquid abrasive cleaners, fabric washer, mustard, paints, glues, cements, lotions and toothpaste, amongst countless others.

The flow of solid-liquid suspensions, sometimes referred as slurry flow for

higher particle concentrations, have been used by different civilizations through the time, most notably the Egyptian, Roman and Greek empires, but the earliest record from an engineering application of solid-liquid suspension flow was in 1860 in the Suez Canal, in Egypt (Abulnaga 2002)

The aim of this section is to provide a better understanding of solid-liquid suspensions flow classification and their importance in industrial applications.

2.1.1. CLASSIFICATION OF SOLID-LIQUID SUSPENSIONS FLOWS

Different sized particles, ranging from nanometres to millimetres, and having varied densities, can incorporate a solid-liquid suspension. If the densities of the liquid droplets or solid particles, small in size, are similar, then settling will not occur and these are called non-settling suspensions. A typical way to approach non-settling suspensions is to treat the flow as a single-phase pseudo-fluid with the rheological properties of the mixture (Peker and Helvaci 2011). These flows can be Newtonian or non-Newtonian; however, in this study we are only concerned with the Newtonian behaviour. Particles with size less than 1 μm (Liu 2003; Barnes 2000) and with similar density as the suspending fluid are called colloidal particles and they exhibit Brownian motion or, in other words, random motion in a zig-zag trajectory. Since the gravitational effect on the particles is small this results in small terminal velocities, these particles will remain suspended with little or no motion (Liu 2003). However, if the particle density is much higher than the density of the fluid, then settling may occur after a period of time, but the mixture can still be homogeneous if movement occurs even in a laminar regime (Liu 2003).

Suspensions or slurries containing medium or coarser particles with density higher than the density of the liquid tend to settle and accumulate at the bottom of the vessel or pipe, resulting in different flow regimes depending on particle concentration and flow velocity (Peker and Helvaci 2011). Settling slurries or suspensions exhibit different flow regimes or flow patterns which are defined by visual inspection of the solid or dispersed phase.

The flow regime is intrinsically linked to the particle size and density. It affects the pressure drop magnitude, pipe erosion or wear and other performance characteristics. The complex nature of slurry flows and transitions between flow regimes hinders a perfect classification of the regimes or patterns.

The first classification of solid-liquid suspensions in horizontal pipelines based on the Reynolds Number (*Re*) and average particle size came from Durand and Condolios (Clayton Thomas Crowe 2005; Liu 2003) in 1952 for particles with a specific gravity of 2.65, and it was as follows:

i. Homogeneous suspensions for particles smaller than 40 μm;
ii. Suspensions maintained by turbulence for particle sizes from 40 μm to 0.15 mm;
iii. Suspension with saltation for particle sizes between 0.15 mm and 1.5 mm;
iv. Saltation for particles greater than 1.5 mm;

This classification was refined throughout the years by several researchers, amongst them Govier & Aziz (Abulnaga 2002; Clayton Thomas Crowe 2005), who brought forward the following classification for fine and coarse particles, which is also the classification adopted in this manuscript:

i. Ultrafine particles: particle size smaller than 10 μm where gravitational forces are negligible;
ii. Fine particles: particle sizes between 10 μm and 100 μm, carried fully suspended although subject to concentration gradients and gravitational forces;
iii. Medium sized particles: from 100 μm until 1000 μm particles move with a deposit at the bottom of the pipe and with a vertical concentration gradient;
iv. Coarse particles: particles sizes ranging from 1000 μm until 10,000 μm. These are seldom fully suspended and form deposits on the bottom of the pipe;

v. Ultra-coarse particles are larger than 10 mm. These particles are transported as a moving bed on the bottom of the pipe;

Since Govier & Aziz did not account for particle density in their work, the above specified ranges serve only as guidelines and will shift according to density variations.

From Figure 2.1 four main flow regimes can be identified:

A. Fully Suspended or Homogeneous Flow;
B. Heterogeneous flow;
C. Flow with Moving Bed;
D. Flow with Stationary Bed;

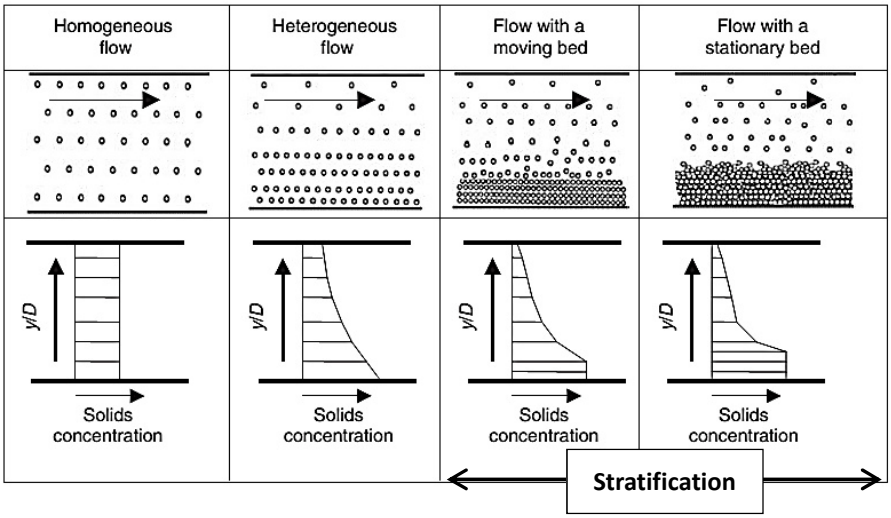

Figure 2.1 – Illustration of particle distributions and solids concentration profiles in a pipe for solid-liquid suspensions flow regimes (adapted from (Clayton Thomas Crowe 2005)).

For high flow rates, if the particles are uniformly distributed across the pipe section then it's called a pseudo-homogeneous suspension flow; however, if there is a gradient of particles in the cross sectional area then it's a heterogeneous suspension flow. With low flow rates the particles tend to gather at the bottom of the pipe forming a layer, and this layer moves along the pipe wall, while in the upper part of the cross section an heterogeneous suspension is flowing, thus resulting in a moving bed flow or two layer flow. Lastly, when the flow rate is too low to suspend all the particles there is a moving layer on top of the stationary bed. Phenomena designated as saltation

often occurs, where dune shaped agglomerations of particles on the bottom of the pipe are observed. In the remaining cross sectional area a heterogeneous suspension is flowing but with a much steeper gradient of particle distribution than in the previous flow regimens. The combination of this heterogeneous suspension, moving top layer and the stationary layer at the bottom form the three layer flow or flow with stationary bed. Usually two and three layer flows are referred to as stratified flows.

2.1.2. INDUSTRIAL APPLICATIONS

Solid-liquid suspensions are of great practical interest because of their widespread occurrence in everyday life, either as a natural or formulated product (Abulnaga 2002; Schramm 2005).

The first systematic investigation of a solid–water mixture flow was performed in 1906 by Nora Blatch using a 25 mm (1 in) diameter horizontal pipe. In her studies pressure drops were accounted as a function of flow, density, and solid concentration.

The mining industry has used solid-liquid suspensions flows since the mid-nineteenth century to obtain gold from placer deposits in California (USA), and today the hydraulic transport of mineral concentrates over various distances is preferred on economic grounds (Abulnaga 2002; Schramm 2005).

In the 1950s slurry pipelines for long distance transportation have been implemented in all the continents. Industry wise solid-liquid suspensions are not only fundamental in established technologies such as paints, oil, cement and coal slurries, drugs and foodstuffs, but also in emerging fields as nanotechnologies and “intelligent” materials, as in biological systems. Solid-liquid suspensions with bimodal particle sizes distributions are widely employed in inks, ceramics and low-calorie high solid content food products. In many industrial processes the concentrated solid–liquid mixtures, called pastes, are either subjected to moulding as in the case of casting metals, or to

extrusion, as in the case of ceramics, polymers, and foods such as pasta (Schramm 2005; Peker and Helvaci 2011) .

Increasingly, solid-liquid suspensions flows are being used for transporting solids as in the case of minerals (such as coal, iron ore, phosphate, etc.), construction materials (sand, crushed rock, cement, and even wet concrete), municipal and industrial wastes; radioactive materials, grain, hospital supplies, and hundreds of other products (Liu 2003; Schramm 2005).

Beyond industrial applications, everyday life applications of solid-liquid suspensions, such as water from treatment plants to individual homes and sewage from homes, are omnipresent in all modern societies (Liu 2003).

2.2. CONTROL AND MONITORING: IMPORTANCE OF NON-INVASIVE TECHNIQUES

2.2.1. HISTORICAL OVERVIEW

The ability to control and monitor operations in process plants is a crucial issue in chemical industries. On-line data acquisition is pivotal for high quality products, smooth plant operation, economical management of wastes and resources as well as for design improvement of the flow and pumping equipment. Although it may seem of straightforward application in theory, the practical implementation is quite complex. A number of discrete sensors distributed throughout critical locations of the plant sums up the traditional course of action when monitoring and/or controlling the plant operation. As a consequence from this oversimplified solution, an invariable loss of key information of both physical and chemical processes occurs in the manufacturing process.

To address this limitation of traditional methods, over the past two decades, process tomography techniques have been developed (M. Beck and Williams 1996; Clayton Thomas Crowe 2005). Initially designed for non-invasive monitoring of multiphase phenomena present in petroleum pipelines, it promptly proliferated in other applications such as batch reactors, mixing vessels, hydraulic and pneumatic conveying (T. Dyakowski and Jaworski

2003). Process tomography offers several advantages when compared with the traditional methods, such as providing information on the boundaries between mixture components, flow regimes and velocity fields, concentration distribution in the cross section and mixing zones distribution in stirred tanks, amongst others, resulting in a better understanding of the monitored process and as a means of validating physical models. Through the manipulation of data obtained from sensors placed around the section of interest, tomographic images are reconstructed using a computational algorithm. These images are then analysed and the data obtained is incorporated in the improvement of both design strategies and numerical models (M. Beck and Williams 1996; Clayton Thomas Crowe 2005). The acceptance of process tomography as a research tool in the measurement and instrumentation areas is corroborated by the increasing number of publications in the literature. Using Scopus search engine and two different sets of keywords, the results in Figure 2.2 clearly reveal that the importance and interest in process tomography has been continuously growing over the years. The real amount of results is probably higher than those displayed in Figure 2.2; however, due to refinement in the search process some papers might have been omitted.

The word tomography derives from the Greek *tomé* which means “to cut” and *graphein* meaning “to write”. A Norwegian physicist, named Niels Henrik Abel (Landau 2014) was the first to publish the concept of tomography for an axisymmetric object, which was later extended to irregular geometries by Johann Radon, an Austrian mathematician, nearly 100 years later.

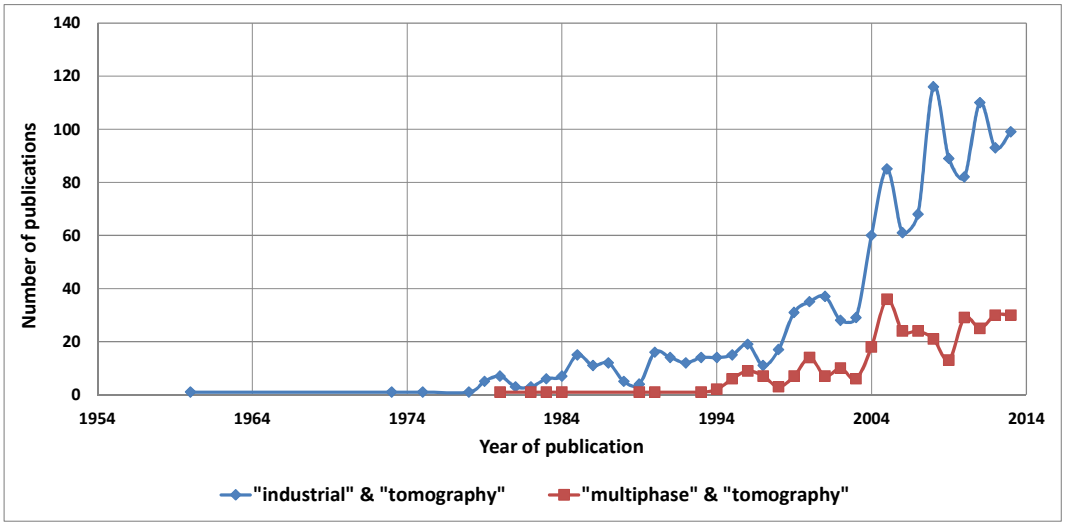

Figure 2.2 – Scopus' results for publications per year according to keywords "industrial & tomography" and "multiphase & tomography".

The first application of tomographic imaging occurred for lung diseases diagnosis in the 1930s but only during the 1970s the tomographic techniques were developed for medical purposes, culminating with the Nobel Prize for Physiology or Medicine being granted to Godfrey Hounsfield and Allan McLeod Cormack in 1979 for the development of the diagnostic technique of X-Ray computed tomography (CT) (Nobelprize.org 2014; M. Beck and Williams 1996). The implementation of industrial applications occurred in the late 1980s and early 1990s. Initially most of the apparatus developed were based on ionizing radiation from X-Ray, but these are potentially hazardous to health and require high cost equipment; also, since these systems are based on photon quantification in a detector, they become ill-suited for fast flow monitoring unless a higher intensity radiation source is employed, thus aggravating its' economical and hazardous aspects (Dickin, Waterfall, and Williams 1992; Clayton Thomas Crowe 2005). The departure from ionizing and isotope sourced tomography came from England in the middle 1980s, at the University of Manchester Institute of Science and Technology (UMIST), with the advent of electrical capacitance tomographic systems for imaging of oil wells and pneumatic conveyors (M. Beck and Williams 1995). Also, in the mid-1980s, the Sheffield University Royal Hallamshire Hospital in the UK was developing an electrical impedance

tomographic system for medical purposes. This imaging technique showed promise due to its' low cost and safety to human health. Impelled by the groundwork in the medical field, in 1988, the UMIST initiated the development of an electrical impedance tomography system for application in electrically conducting fluids. And in 1990 a 4 year European Concerted Action on Process Tomography program was established, acknowledging process tomography as a mature technique with potential in the industrial processes and design. From this Action the first workshop followed and took place in Manchester, in 1992, where several sensor systems such as acoustic, optical, NMR and radiation were introduced as ready for industrial applications. Today the tomographic classification can be sorted in two groups, soft and hard field tomography (University of Leeds 2014). In hard field tomography the direction of the energy waves from the power source is constant and the sensor field sensitivity is independent of the type of material or medium. X-Ray computed tomography (CT), Nuclear Magnetic Resonance Tomography (NMRT) and Positron Emission Tomography (PET) fall in this group. In soft field tomography the physical electrical properties of the material heavily influence the sensing field. This requires considerably more computational analysis and algorithms to reconstruct the image while limiting the resolution when compared to hard field tomography. Electrical Capacitance Tomography, Electrical Impedance Tomography, Ultrasonic Computed Tomography and Optical Coherence Tomography, amongst others, fall in this soft field tomography (Dickin, Waterfall, and Williams 1992).

A major contribution to the increasing popularity of process tomography, especially in soft field tomography, has been the continuous evolution of faster processors and computer architectures at lower costs. This cost effectiveness and computer sophistication also enabled the proliferation of computational fluid dynamics (CFD) models for more accurate design strategies. Under these circumstances process tomography presents itself as a validation technique for CFD models. Aside from model validation, it is expected, with continuous computer modernization, that process

tomography will develop in a 3D imaging technique that allows for plant control, full mass balance and process monitoring.

2.3. BASICS OF A TOMOGRAPHIC SYSTEM

The purpose of tomographic imaging is to acquire information from sensors to form a cross-sectional image. To interrogate about the full cross section it is necessary to measure several projections through the rotation of either the sensors or section in the normal direction to the field of interest (M. Beck and Williams 1996; M. Beck and Williams 1995; Clayton Thomas Crowe 2005).

The basic components of a tomographic system can be separated into two major branches: hardware and software (see Figure 2.3). The sensors and data acquisition system compose the hardware branch, and the signal reconstruction and hardware signal control represent the software branch (M. Beck and Williams 1996; M. Beck and Williams 1995).

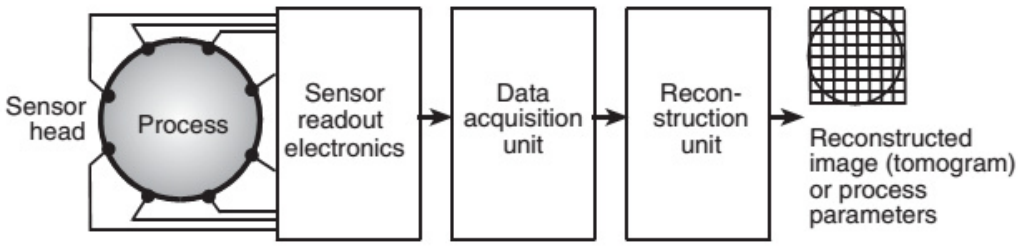

Figure 2.3 – Typical arrangement of an industrial process tomography system. The main components are the sensor head, sensor (detector) readout electronics, data acquisition, and a reconstruction unit which usually incorporates image processing (adapted from (Clayton Thomas Crowe 2005)).

Ultimately, beyond obtaining high resolution reconstructed images, the objective of a process tomography system is to provide quantitative information, rather than just relative changes in the process characteristics (Clayton Thomas Crowe 2005). This could be in the form, as an example, of absolute values for particle concentration in a pipe cross-section in solid-liquid pipe flow. Visual inspection of the images will serve only as a form of verification for system malfunctions. This constitutes the first fundamental discrepancy between medical and process tomography. The second is that

medical tomography tracks relative changes to a reference and process tomography concerns itself with absolutes values.

Ideally, process tomography systems should be non-invasive, where the walls of the object or vessel to be studied should not be breached by probes or sensors, and non-intrusive, where the nature of the process should not be modified by the data acquisition system.

2.4. CHOOSING A TOMOGRAPHIC SYSTEM

The choice of tomographic system is determinant for an accurate depiction of the physical phenomena being studied. The sensor is the key factor to be considered. Many sensing methods can be found in the literature (M. Beck and Williams 1996; M. Beck and Williams 1995; Clayton Thomas Crowe 2005) that are based on transmission, diffraction and electrical phenomena and their choice is determined, mainly, by the following criteria:

a. nature of the material present in the vessel (pipeline, reactor, etc.) and its' proportions, in case of a multiphase mixture;

b. nature of the process (steady state or dynamic), the information sought (resolution and sensitivity necessary) and the objective of the system (academic research, process optimization or plant control);

c. surrounding environment (operating conditions, safety concerns, maintenance, etc.);

d. the necessary size of the system and the scale of the process involved;

Taking the above criteria and considering the resolution as the first requirement in a tomographic system, it is understood that higher resolution involves a more expensive apparatus, longer exposure times and commonly imposes special safety requirements. In opposition, lower resolutions systems are relatively inexpensive, need lower exposure times and there are no special safety requirements. In Table 2.1 the characteristics of each sensor in process tomography based on spatial resolution are summed up. As an

example for imaging dispersed particles where high resolution is necessary, an ionizing radiation technique is used, either X-Ray or γ-Ray tomography. However, these techniques are not suited for on-line measurements as they are not fast enough and the apparatus is too large.

In some cases, where the only pertinent information are the void fraction in a gas/liquid mixture or the volume fraction of particles, electrical tomography is a consistent alternative when the resolution requirements are not inferior to 10 %, as can be seen in Table 2.1. It is necessary to define the nature of the object to be studied. If ferrous materials are present, or for some reason the electrodes cannot be in contact with the fluid due to pressure damage or fouling, then electromagnetic inductance tomography is a possibility. Objects with electrically insulating boundaries (gas/liquid systems, insulating liquids, etc.) can be identified with electrical capacitance tomography techniques. If the process does not have an electrically insulating boundary and the electrodes can be in contact with the fluid, then electrical resistance tomography is a proven technique with a considerable amount of medical and process applications (M. Beck and Williams 1996; M. Beck and Williams 1995).

The electrical field equipotential lines may be distorted by the electrical properties of the object that is being studied, thus resulting in distorted tomographic images. This is not uncommon in electrical tomographic studies, but it can be of less importance as long as the precise location of the objects is not relevant information when compared to the overall distribution of objects or flow regimen.

Considering the sensors characteristics, as mentioned above and in Table 2.1, the resolution expectations need to be careful studied when choosing a tomographic system so that the process is accurately characterized.

Table 2.1 – Sensor characteristics for process tomography (adapted from (M. Beck and Williams 1996; M. Beck and Williams 1995)).

SOURCE	SPATIAL RESOLUTION (% OF CROSS SECTION DIAMETER)	IMPLEMENTATION	CHARACTERISTICS
Electromagnetic Radiation	1 %	Optical	- Fast - Optical access required
		X-Ray and γ-Ray	- Slow - Radiation containment
		Positron Emission	- Tracer particles - Off-line measurements
		Magnetic Resonance	- Fast - Expensive for large vessels
Acoustic	3 %	Ultrasonic	- Sonic speed limitation - Complex to use
Measurement of electrical properties	10 %	Capacitive Conductive Inductive	- Fast - Low Cost - Suitable for small or large vessels

2.5. ELECTRICAL IMPEDANCE TOMOGRAPHY (EIT)

Electrical impedance tomography, henceforth referred as EIT, was first applied as a visualization technique in the geological field over 70 years ago. Nowadays this technique is used in industrial environments to detect air bubbles in process pipes to monitor mixing processes, amongst other applications. In the clinical field, EIT has been employed in breast cancer detection, monitoring brain function and strokes (Bayford 2006). EIT major drawback is the low spatial resolution when compared with other methods as Magnetic Resonance Imaging (MRI) or Computer Tomography (CT), but offers the advantage of increased temporal resolution in the order of the milliseconds.

The invention of EIT is attributed to John G. Webster as published in 1978 (Henderson and Webster 1978); however, the first practical application, named *Applied Potential Tomography*, only occurred in 1984 by Barber &

Brown (Barber and Brown 1984) for the imaging of a human forearm. A considerable number of publications on the use of EIT in the clinical field and an analysis of existing EIT systems can be found in the literature (Goharian et al. 2008; York 2001). The use of EIT in industrial environments is fairly new with a wide array of potential applications.

2.5.1. ELECTRICAL IMPEDANCE TOMOGRAPHY HARDWARE HISTORY

Electrical tomographic systems can be subdivided in three main branches: Electrical Resistance Tomography (ERT); Electrical Capacitance Tomography (ECT); and Electrical Impedance Tomography (EIT). Among them the most commonly implemented is ERT, ideal for purely resistive media (Wilkinson et al. 2006); ECT requires a more intricate sensor array and issues may arise when dealing with media containing conductive materials (Donthi and Subramanyan 2004; Tom Dyakowski et al. 2006; Yang 2007); in a dissimilar manner than ERT (Jia et al. 2010; Pakzad, Ein-Mozaffari, and Chan 2008; Razzak, Barghi, and Zhu 2009), EIT systems (Grootveld 1996; Holliday, Williams, and Lucas 2005; S. Zhang et al. 2006) measure both the magnitude and phase parts of the impedance, so no data is lost. A more comprehensive study on the variations of electrical tomographic systems, which is beyond the scope of this review, can be found in the literature (Rasteiro et al. 2011).

A search in the literature for EIT systems will provide an extended list of existing hardware apparatus, and this list is continuously growing. One of the first systems was developed in Sheffield (Bayford 2006), the MK1 system, that initially consisted of a 16 electrode ring with a single current source and that has been improved throughout the years.

As pointed out earlier, this is not the only existing EIT system. Each research group in this field has developed its own version. The reason behind the several iterations of hardware present in the literature is due to the reconstructing method and the medium to be studied, which require different degrees of complexity from the hardware (Bayford 2006).

In the clinical field the following systems are examples of the advancement of the EIT hardware since the MK1 system: the Rensselar's Adaptive Current Tomograph (ACT4) system, which is a high precision EIT multi-frequency system with a modular design, comprising 72 electrodes and an excitation frequency selection range from 300 Hz to 1 MHz, whose primary application is for characterizing pulmonary function. In Dartmouth, a digital signal processing EIT system with a frequency range from 10 kHz to 10 MHz that acquires 30 frames per second was used for breast imaging. The UCLH Mk 1b system, that is portable, possesses 64 electrodes and operates at very low frequencies, specifically for brain activity resolution, between 225 Hz to 77 kHz. While most groups opted for a complete design of their apparatus, some prefer to adapt the existing systems like the Sheffield group, and modify it to their specific needs (Bayford 2006).

2.5.2. ELECTRICAL IMPEDANCE TOMOGRAPHY MATHEMATICAL FORMULATION

Based on the principle that each material possesses unique electrical properties, EIT uses the electrical field distribution to infer on the material distribution in a certain domain. An electrical current or potential is applied to an electrode pair on the domain boundary and hence an electrical field ensues.

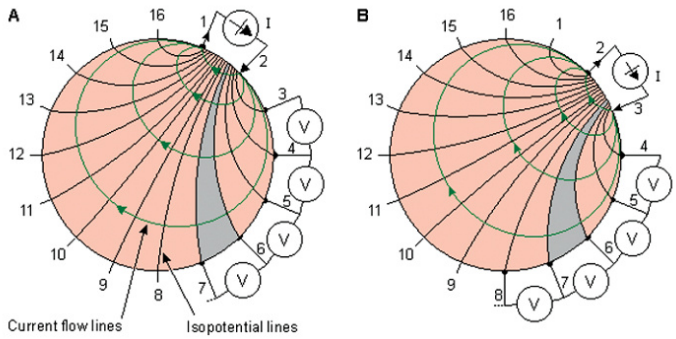

Figure 2.4 – EIT injection and measurement adjacent protocols for the first (A) and second (B) projections (adapted from (Malmivuo and Plonsey 1995)).

This electrical field is conditioned by the materials distributed inside the domain and the disturbance on the equipotential lines can be measured using the remaining electrodes (see Figure 2.4); this data is then introduced in a

reconstruction algorithm to attain the conductivity/resistivity distribution inside the domain. The procedure is complete only when all electrodes are used for injection or projection (see Section 3.2.6), so the cycle has as many projections as the number of electrodes, if, for instance, an adjacent injection protocol is implemented (as exemplified in Figure 2.4).

From a mathematical standpoint, the EIT problem can be divided in 1) the forward problem, which calculates the electrical potentials on the boundary using an initial estimation of the conductivity/resistivity distribution, and 2) the inverse problem that reconstructs the conductivity/resistivity distribution based on the electrical potentials measured in the boundary, through the use of a reconstruction algorithm.

The mathematical formulation for the EIT physical model is based on Maxwell's equations for electromagnetism for the distribution of the electrical filed in the domain. A summary of the equations is presented below and the complete derivation of the physical model can be found in the literature (Noor 2007; M. Vauhkonen 1997).

FORWARD PROBLEM

Of the several models developed to solve the forward problem of EIT, the most common is the complete electrode model (CEM), based on a Finite Element Method (FEM) formulation, which is the most utilized mathematical technique for solving the forward problem, since its early implementation by Murai & Kagawa (Cheng et al. 1989; Murai and Kagawa 1985). This model incorporates the shunt effect and the contact impedance in the electrode/domain interface (Noor 2007; N. Polydorides 2002; M. Vauhkonen 1997). A detailed description of the different electrode models has been given by Cheng et al (1989). The fundamental equation for this model, derived from the Maxwell equations, is the Laplace equation, in which σ represents the electrical conductivity and φ is the electrical potential (see Equation 2.1).

$$\nabla \cdot (\sigma \nabla \varphi) = 0 \qquad \textbf{(2.1)}$$

$$\int_{e_\ell} \sigma \frac{\partial \varphi}{\partial \nu} dS = I_\ell \ if \ \ x \epsilon \ e_\ell \ , \ \ \ell = 1, \dots, L \tag{2.2}$$

$$\sigma \frac{\partial \varphi}{\partial \nu} = 0 \ if \ x \epsilon \ \partial\Omega / \Phi(e_\ell)_{\ell=1}^{L} \tag{2.3}$$

$$\varphi + z_\ell \sigma \frac{\partial \varphi}{\partial \nu} = \Phi_\ell \ if \ \ x \epsilon \ e_\ell \ , \ \ \ell = 1, \dots, L \tag{2.4}$$

For each projection the boundary conditions of the model characterize the injection of the electrical current (Neumann boundary condition), the space between electrodes, and the electrical potential measurement (Dirichlet boundary condition), as seen in Equations 2.2, 2.3 and 2.4, respectively (Cheng et al. 1989).

In order to insure the existence of a unique solution the equations for charge conservation and of the choice of an electrical potential as reference (usually the choice is the earth electrical potential), Equations 2.5 and 2.6 respectively, are incorporated in the model:

$$\int_{\partial\Omega} j = 0 \quad \Leftrightarrow \quad \sum_{\ell=1}^{L} I_\ell = 0 \tag{2.5}$$

$$\int_{\partial\Omega} \varphi = 0 \quad \Leftrightarrow \quad \sum_{\ell=1}^{L} \Phi_\ell = 0 \tag{2.6}$$

INVERSE PROBLEM

The mathematical inverse problem, that is, the reconstruction algorithm is ill-posed, ill-conditioned and non-linear, which makes very challenging to obtain a proper image in terms of computational effort. To circumvent the reconstruction issues a regularization technique is often required.

As stated before, the forward problem calculates the electrical potentials at the boundary using an initial estimation of the conductivity/resistivity distribution in the considered domain and the inverse problem uses the measured electrical potentials at the electrodes placed in the boundary to estimate the actual conductivity distribution inside the domain through a

mathematical algorithm.

From the literature three main types of mathematical methods, which can be used for solving the inverse problem, can be highlighted: linear, non-linear and heuristic methods.

Linear Methods

From all the reconstruction methodologies linear methods are the fastest because images are generated by a simple multiplication operation between the measured data and a pre-calculated matrix. Amongst the linear methods the most widely employed is Linear Back Projection (LBP). This method is a single step calculation that tends to produce poor quality images, due to a poor estimate of the solution for the forward problem, resulting from an incorrect assumption that the electrical field is not altered by changes in the conductivity/resistivity (similarly to hard tomographic techniques as X-Ray tomography). In spite of this drawback single step LBP methods provide a fast qualitative view of the process and have successfully been applied to gas-solid and gas-oil systems.

An iterative version of LBP has been presented in a publication by Yang (2007) which showed increased accuracy and a higher resolution for the images.

Non-Linear Methods

Non-linear iterative methods as Newton-Raphson (NR) or adaptive mesh regeneration methods (Chan Kim et al. 2005) use numerical forward solvers and sensitivity maps to estimate an image based on calculated measurement residuals. This estimated image is updated through a non-linear method. NR methods introduce significant errors and are prone to convergence issues if a regularization technique is not employed Notwithstanding, improved convergence regularization methods such as Marcquard and Tikhonov, can introduce further numerical noise in the obtained image. Alternatives to the NR method are direct inverse solution algorithms such as the Sensitivity

Conjugate Gradients algorithm (SGC) that searches for the minimized residual vector and provides images with improved accuracy. Although non-linear iterative methods provide additional flexibility from a measurement protocol standpoint, they do require additional computational cost and are quite slower than the previously mentioned linear methods. At this time these methods are better suited for offline imaging; with increasing algorithm efficiency and continuous lowering of computational power costs, it can become an online imaging method in the near future.

Heuristic Methods

These methods can be either linear or non-linear. For these methods a relationship between calibration (or training) sets and measurements is empirically modelled, and the calibrations sets can be obtained either numerically, analytically or experimentally. Multiple Linear Regression (Tapp and Wilson 1997) is an example of a linear heuristic model with self-organized maps; artificial neural networks are examples of non-linear heuristic methods. These models use image reconstruction as a step towards relating the variable of interest to the measurements.

Other Methods

Kim et al. (2005) have solved the inverse problem of EIT using a stochastic nonlinear state estimation algorithm based on an unscented Kalman Filter for non-stationary phase boundary estimation in the flow of a two fluid mixture.

2.5.3. INDUSTRIAL APPLICATIONS OF ELECTRICAL TOMOGRAPHY

Although most of the publications in the literature of electrical tomography are in an academic environment, slowly they are transferring to industrial plants.

Electrical capacitance tomography (ECT) has been implemented in several industrial fields, ranging from hydrodynamics of gas-liquid packed beds (Hamidipour and Larachi 2010), measuring solids concentration in a cyclone

separator (M. Sun et al. 2008), monitor flow regimes during hydraulic and pneumatic conveying (Arko et al. 1999; M. S. Beck et al. 1993; K. Zhu et al. 2003), study low water fraction foams (Bennett et al. 2002), to combustion phenomena in an internal combustion engine (Vilar et al. 2008), just to name a few.

ERT has had some applications in the visualization of swirling flows (M. Wang, Jones, and Williams 2003), in the improvement of a differential pressure flow meter (Venturi type) in two-phase measurements (Meng et al. 2010), 3D imaging of concrete (Karhunen et al. 2010), controlling the emulsion process of a sunflower oil/water mixture (Boonkhao et al. 2011), investigation of the influence of the reactor geometry on multiphase processes typical of pharmaceutical industries (Ricard et al. 2005) amongst others. In a more indirect way, this technique was also used to provide valuable data for the refinement of CFD models in slurry mixing (Williams, Jia, and McKee 1996),

EIT has been employed, for instance, in the study of paste extrusion (West et al. 2002), in the mixing of two miscible liquids in a turbulent flow in a papermaking trump-jet system (Kourunen et al. 2008), in the monitoring of 3D drug release as a function of time (Rimpiläinen et al. 2010) and for the visualization of conductivity in a cell culture (T. Sun et al. 2010).

A more detailed depiction of electrical tomography applications in the scope of industrial chemical engineering can be found in a publication by Tapp et al. (2003).

2.6. NUCLEAR MAGNETIC RESONANCE IMAGING

1995 was the fiftieth anniversary of the invention of magnetic resonance. A few years later one of its major sub-fields, Nuclear Magnetic Resonance (NMR), originated and became a driving technique in such fields as physics and biology. In the chemistry field, particularly in organic chemistry, NMR is a fundamental workhorse (Bonn et al. 2008; Fukushima 1999). Although NMR

was originally developed for the field of physics, most of its applications occur in the medical field where it has a widespread presence, in the form of Magnetic Resonance Imaging (MRI), and many believe that only 3D spatial information is attainable from this technique. It is well known that most hospitals around the world possess MRI scanners with dedicated and user-friendly interface that are used for medical diagnosis, but they can be perfectly used for the measurement of 3D flow fields (Bonn et al. 2008). Although a search for "MRI and flow" in the literature will result in a considerable number of hits, only a very small fraction of these are for engineering applications.

NMR has the capability of distinguishing between atoms and molecules having different amounts of translational or rotational diffusion (Relaxation), as well as being able to distinguish between nuclei of atoms in chemically unequal sites (Spectroscopy). Apart from Relaxation and Spectroscopy, there is Spatial Imaging that has added a third dimension to NMR. Today, NMR is effectively used for flow studies by overlapping the aforementioned three dimensions (Fukushima 1999).

Amongst the advantages of NMR the following can be highlighted: lack of directional preference, where micron scale resolution images can be obtained without the need of sensor or probe to be placed in a specific position or angle; non-invasiveness, contrarily to other tomographic techniques where sensor must be in contact with the medium; being able to measure several parameters; immune to opaque media; and being able to provide accurate measurements while acquiring a small number of points in several spatial dimensions in a short amount of time (Bonn et al. 2008). Also, it presents itself as an optimum choice for flow studies since it measures statistical averages of spatial and temporal scales comparable to transport theories (Fukushima 1999; Gladden 1994). When compared with a proven high resolution technique as X-Ray tomography a question arises about the spatial resolution. X-Ray devices have proven to provide 1 μm resolution images while MRI can provide a 10 μm resolution, by comparison. However, MRI has

superior behaviour due to its high motion sensitivity, where an apparatus with resolution in the millimetre order can still measure spatial and velocities displacements in the micrometre order. This coupled with the aforementioned insensitivity to opaque media supports MRI's application in flow studies in detriment of X-Ray tomography (Bonn et al. 2008).

The amount of NMR sensitive atomic nuclei is scarce but protons are quite sensitive, so it is more adequate to employ NMR studies on systems that have protons in abundance. Nuclei that are fixed in a lattice give poor NMR signals when compared with nuclei that are on molecules that possess translational and rotational degrees of freedom, which means that liquids or gases are the easiest media to study using NMR. For solid-liquid suspension flows it is straightforward to get liquid velocity profiles or study the concentration of solids/liquids but it becomes cumbersome to measure the solids velocity profile (Fukushima 1999; Gladden 1994).

The main issue with NMR, when compared with other techniques, is its inability to study ferromagnetic materials. Apart from the typical drawbacks from hard tomography (like for example non portability), another significant NMR drawback is its specificity, in other words, data obtained from NMR in solid-liquid suspensions is unintelligible for a biology scientist and vice-versa. It also means that the instrumentation and software have to be different for each experiment. And this explains why the NMR apparatus has not become widespread in engineering and other fields (Bonn et al. 2008; Fukushima 1999).

However, due to the spatial and time scales that NMR can measure, in the near future this technique will become extremely important for engineers and scientists that work on parameters such as velocity fluctuation, dispersion and diffusion, which are fundamental for the flow community.

Broader and more detail oriented reviews for flow studies and NMR theory by Gladden (1994), Fukushima (1999), Bonn et al. (2008) and Powell (2008) can be found in the literature.

2.6.1. NMR APPLICATION IN MULTIPHASE FLOWS

The predominance of multiphase flows and its importance in industrial environments has already been stated. The phase distribution is a fundamental piece of information for the engineers and techniques that provide this information for online control are still unsatisfactory. NMR imaging can be a powerful tool for velocity and solids concentration profiles by inference over the measured liquid concentration profile; however, few applications of this technique on multiphase flows exist (Bonn et al. 2008; Gladden 1994). Several reviews are present in the literature on NMR/MRI theory and its applications on different fields. The more pertinent review studies are used here as the main references (Bonn et al. 2008; Gladden 1994; Powell 2008; Fukushima 1999).

Gladden (1994) has done quite an exhaustive and thorough review of NMR application in the chemical engineering field. In this publication, the author divides NMR applications in its dimensions:

a) NMR Spectroscopy, where the topics of study are the structure of materials, interface characterisation and adsorbed species. In this regard, Gladden (1994) highlighted: the work done by Amundson et al. (1991) in the microstructure of crystalline polymers; the characterisation of materials for electronic applications by Levy et al. (1993); the study of catalysis, through the characterisation of materials and intermediates formed during the reaction, done by Mehring (1983); that Hansent (1988) has used NMR data in the construction of phases diagrams of non-ideal liquid mixtures with results showing great promise; and that Robertson et al. (1992) and Nicolay (1992) have all contributed significantly in the application of NMR spectroscopy in the quality control in food processing.

b) Spatially Non-Resolved Measurement of Transport, which is divided in two sub-sections: the first, Pulsed Gradient Spin-Echo NMR (PGSE

NMR) that detects molecular self-displacement in the Angstroms length scale allowing structural analysis of macromolecular solution, liquid crystals, porosity in rocks, adsorbents and catalysis. Gladden (1994), acknowledges the review done by Stilbs (1987) which has thorough descriptions of various authors contributions. The main contributions referenced by Gladden (1994) are: the diffusion coefficients study using PGSE NMR by Stilbs & Lindman (1984), the study of the structure of microemulsions and solvent diffusion in gels by Nystrom et al. (1981) and the diffusion of moisture in foods by Watanabe & Fukuoka (1992), just to name a few applications of PSGE NMR. In the second part of his publication, Gladden (1994) acknowledges the contributions of Banavar & Schwartz (1989) in the field of NMR relaxometry or spin-lattice relaxation time experiments, which is a technique used to obtain the surface area of pore-volume ration in porous solids. Additionally, the theoretical basis to apply NMR in diffusion studies in porous media was laid out by Zimmerman & Brittin (1957).

c) NMR Imaging, apart from living applications in the medical field, is employed in non-living systems in two areas: solid-state imaging of polymers and composites, and liquids imaging in porous media. The development of NMR imaging in recent years has led to the possibility of non-invasive measurement of non-equilibrium distribution of heat to the characterization of transport phenomena and of the progress extent of chemical reactions. Gladden (1994) mentions the works of Shimokawa & Yamada (1985) in phase equilibria NMR imaging. NMR imaging becomes of paramount importance in the study of microstructured products as in ceramics processing. Typical examples are the works carried by Garrido et al. (2008). In the polymer structural and swelling characterisation as well as in the time-evolution of the polymerisation process, NMR imaging has been reviewed by Blümich & Blümber (1992), as pointed out by Gladden

(1994). In the food industry NMR imaging is mainly applied to internal composition and quality control. Chen et al. (1989), Wang et al. (1988) have investigated NMR imaging as a method of non-destructively determining product quality by searching for bruised areas, dry regions, ripeness, etc.

Suryan (1951) performed the first flow measurement with NMR. Kose et al. (1985) and Caprihan and Fukushima (1990) were some of the firsts to published NMR applications resulting in hydrodynamic parameters of interest such as velocity, diffusion coefficient, acceleration and even parameters related to fluctuations such as turbulence. Over the years, flow imaging has advanced from the early experiments of Abouelwafa and Kendall (1979), who measured the average value of velocity and fraction of oil-water mixtures but without spatial resolution, to the work of Kose et al. (1985), who reported 2D NMR flow velocity and concentration profiles under laminar conditions. Majors et al. (1991) used a 3D version of the frequency encoded technique which allowed to obtain velocity and concentration profiles data. Amongst the practical applications of NMR imaging, Gladden (1994) reports in its review, the drainage of aqueous foams under the influence of gravity by German and McCarthy (1989) and by McCarthy (1990). Xia et al. (1992) studied Poiseuille flow and diffusion in a non-Newtonian polymer solution. Xia et al. (1992) also documented NMR studies to obtain velocity profiles of water flow in an expansion/contraction in a cylindrical tube.

Gladden (1994) and Fukushima (1999) both reported on two-phase flow measurements using NMR imaging, which are quite cumbersome with traditional non-invasive methods; the focus was on understanding the rheology and microstructural behaviour of solid-liquid suspensions (Altobelli, Givler, and Fukushima 1991). Altobelli measured velocity and concentration profiles of a horizontal flow containing negatively buoyant particles (between 4 and 40% by volume) suspended in a lubricant oil: the evolution of the solids distribution as a function of strain, shear rate, particle diameter and liquid viscosity demonstrated that particles migrate

irreversibly from a high shear to low shear regions. The images obtained revealed the spatial distribution of both liquid and solid phases and this data was used to develop constitutive equations and CFD models describing the behaviour of concentrated suspensions. Nakagawa et al. (1993) also used NMR imaging of velocity and concentration profiles to improve existing models for granular flows. Graham (1991) has demonstrated evidence of shear-induced particle migration in a Couette suspension flow. Abbott et al. (1991) extended this to show shear-induced particle migration in a similar flow using NMR images. These studies served to demonstrate that Stokes equations did not adequately describe the observed hydrodynamic diffusion effects.

Dyverfeldt et al.(2006) have performed turbulence studies using NMR data from velocity in a voxel to calculate the standard deviation and to exploit its relationship with turbulence intensity, allowing for quantitative studies of turbulence.

Sitckel & Powell (2005) reviewed several techniques used in multiphase studies and focused on MRI application for suspension flows, including advantages and pitfalls. The efforts of several authors using MRI for characterising velocity and solid concentrations profiles in solid-liquid suspensions and emulsions were also reviewed: Powell, in particular, studied sedimentation and concentration of solid particles, shear-induced migration and also turbulence intensity using velocity fluctuations.

In summation, MRI has evolved considerably in the last two decades and has proven to provide a considerable amount of data essential for either industrial or academic field. Its versatility has been demonstrated by the vast number of publications in very different fields of study. The potential of this technique is great and the transition from research lab to industrial environment has only been slowed due to the cost and complexity of operating the equipment.

2.7. ULTRASONIC PULSE VELOCIMETRY

The first application of ultrasonics for velocity measurements occurred in 1970s for blood flow (Y. Takeda 1999). The goal was to attain an average value of the blood velocity flowing in small diameter pipes. Takeda credits Fox (1978) as the first to implement UPV theoretically and experimentally to form a velocity profile.

In his review manuscript, Powell (2008) also cites the work of Takeda as one of the firsts to use ultrasonic techniques on flow measurement.

The implementation of this technique, called Ultrasonic Pulse Velocimetry (UPV) or Ultrasonic Pulse Doppler Velocimetry (UPDV), is based on the Doppler shift in the frequency of an ultrasonic wave by interacting with a moving particle (Powell 2008). The Doppler shift of scattered transmitted ultrasonic pulse through the suspensions is converted to the relative velocity of the dispersion particles (Hunter, Peakall, and Biggs 2011).

UPV has the following advantages, when compared with classical approaches (Yasushi Takeda 1995):

a) Provides spatial-temporal information about the flow field, i.e., quantitative information about the velocity field as a function of time which can be acquired without prior knowledge of the flow. The instantaneous velocity profile is a fundamental quantity in fluid flow studies and also one of the most changelings to attain;

b) Applicable in opaque media which is impossible with optical methods. This is extremely important in flows of liquid metals, ferrofluids and liquids foodstuffs;

c) Allows for flow mapping, due to its inline measurement, which is important as a basis of comparison with numerical simulation data in CFD code validation;

Also, UPV is non-invasive, inexpensive when compared with other existing techniques, portable and easy to implement, contrarily to other velocity profile measuring techniques.

2.7.1. UPV IN MULTIPHASE FLOWS

The use of UPV has been ubiquitous in a variety of fields of study and to review all pertinent publications in every field is beyond the scope of this thesis. For a more in depth analysis of UPV applications, Powell (2008) dedicated a section in his review where an assortment of examples are presented.

In this section focus will be kept on recent UPV applications in solid-liquid suspension flows.

Wang et al. (2003) modified a commercial UPV (DOP2000) to correct the ultrasound refraction accounting for the presence of solids in a homogeneous solid-liquid suspension. An increase in the attenuation coefficient of the received echo energy was observed with increasing solid concentration and a calibration curve can be inferred by this relationship, resulting in a proposed model that relates solid holdup and the received echo energy.

Shukla et al. (2007) used ultrasonic studies to recognize attenuations peaks and to distinguish between flow regime transitions: they observed that the viscous absorption losses caused dissipation of the acoustic signal when the flow regime changed from suspended to settled bed. With these results, the potential of UPV was demonstrated as an online monitoring technique for suspensions flow regimes and particle distribution.

Wiklund & Stading (2008) provide a very thorough study of industrial suspensions using real-time UPV-PD measurements (ultrasound velocity profile coupled with pressure drop measurements). For a pressure driven flow several suspensions were characterized for different volumetric flow rates, particles sizes, distributions, shapes and rheological characteristics. The results demonstrated good agreement with both on- and off-line

rheometers data and UPV-PD demonstrated the capability of on-line process monitoring.

Hunter et al. (2011) employed a commercial UPV system to measure the particle velocity in the dispersion and time evolution of sediment bed interface. Colloidal suspensions of bi-modal distributed non-coagulated and coagulated glass particles were characterized, using the acoustic technique and it was demonstrated that, in spite of the error observed for the velocity profile of the non-coagulated particles, the bed interface was clear and particle tracking was still possible. For the coagulated particles the measured velocities were accurate and bed formation was demonstrated, while settling velocities and bed height with hindered settling were quantified. An important result from this work was the particle hindered settling within the dispersion, which would not be possible with the classical approaches. This study also demonstrated that, in spite of its limitations for the colloidal regime, UPV is suitable for free-settling multiphase environments. Harbottle et al. (2011) also worked with colloidal silica-water suspensions and used UPV for the determination of the minimum transport velocity. Their study demonstrated that the critical transport velocity can be lowered, for a colloidal suspension, by inducing particle aggregation.

Guer et al. (2003) experimental tests using UPV on pipe flows of solid-liquid suspensions buoyant particles allowed detection of different flow patterns: moving bed, sliding and saltation regimes. Mass fraction effects on velocity profiles were also quantified. Additional information on velocity profiles, space-time diagrams, probability density functions (PDF) and cumulative probability distribution functions (CPDF) of the velocities was also achieved for solids concentrations up to 20% by mass for polypropylene particles having a density of 0.889 $g.cm^{-3}$. Chemloul et al. (2009) measured particle diameter and volumetric concentration effects on the local velocity and concentration in a solid-liquid suspension flow in a horizontal pipe. The volumetric concentration of glass beads was limited to 2%; above that concentration, attenuation of the ultrasonic integral occurred. For finer

particles, the suspension behaved as a homogeneous fluid. For larger particles different flow regimes, such as saltation and heterogeneous flows, were observed. These regimes were dependent on flow velocity, particle diameter and concentration. The slip velocity, which is related to the particle-fluid interaction, was also dependent on the flow regime. An important observation for larger particles was the turbulence attenuation that occurred for increased particle concentrations. Chemloul et al. (2009), by using two identical transducers for simultaneous measurements of velocity and local concentration, were able to ascertain that the particles modified the turbulent length scale of the continuous phase.

2.8. SOLID-LIQUID SUSPENSIONS FLOW MODELLING

In this section a review of empirical and semi-empirical correlations, mechanistic models and deterministic numerical models that have been employed to predict the behaviour of settling suspensions is delineated, providing information on the advantages and drawbacks of each method. Their evolution throughout the years is outlined: from Durand and Condolios correlations, to empirical models by Wasp or from single phase simplifications with mixture properties by Shook and Roco, to other Euler-Euler or Euler-Lagrangian numerical models. Some considerations on recent particle migration and turbulence modulation publications will be added. In addition, information about some current CFD application of Lattice-Boltzmann (LB) and Discrete Element Method (DEM) will also be depicted.

2.8.1. EMPIRICAL CORRELATIONS

One of the first recorded empirical correlations for pressure drop estimation, considering fully suspended heterogeneous flows of solid-liquid settling suspensions in horizontal pipes, was developed by Durand and Condolios in 1952. This correlation was constructed based on a collection of pressure drop data associated with the flow of sand-water and gravel-water mixtures with particles of sizes ranging from 0.2 to 25 mm, for pipe diameters between 3.8 and 58 cm and with solids concentrations up to 60% by volume (Aziz and

Mohamed 2013). These studies culminated with the establishment of a relation between the pressure drops of water and slurry, given by Equation 2.7, where i and i_w are the pressure drop of slurry and of water respectively, k is a constant, C_D is the drag coefficient for the free falling particle at its terminal velocity, g is the gravity constant, D_i is the pipe internal diameter, C_o is the volumetric concentration of solids and V_m is the average flow velocity.

$$\frac{i - i_w}{i_w C_o} = k \left[\frac{V_m^2}{g.D_i} \sqrt{C_D} \right]^{-1.5} \quad \textbf{(2.7)}$$

In 1967 Zandi & Govatos, using an extensive number of data points, improved Durand's correlation to different solids and mixtures (Abulnaga 2002) and defined an index number, *Ne*, that defined the limit between saltation and heterogeneous flows. While Durand and Condolios based their studies on the drag coefficient, Newitt (Clayton Thomas Crowe 2005; Abulnaga 2002), who published in 1955 a thorough study on solid-liquid flows that resulted in several flow regime specific correlations, based his work on the terminal velocity as a means to determine the pressure drop (see Equation 2.8). These correlations, which were not more than a set of criteria, allowed to define the flow regime and their-specific set of equations (Abulnaga 2002).

$$\frac{i - i_w}{i_w C_o} = K_2 \left[\frac{\rho_s - \rho_L}{\rho_L} \right] \frac{g D_i V_t}{V_m^3} \quad \textbf{(2.8)}$$

where K_2 is a constant, ρ_s represents the density of the solids, ρ_L is the density of the liquid and V_t is the terminal velocity of the particle.

Other authors obtained the pressure drop using the dispersion coefficient as a function of local distribution of solids, also describing the settling phenomena making use of the Richardson-Zaki equation (Rasteiro, Figueiredo, and Franco 1993; Rasteiro, Rebola, and Scarlet 1988). Although the coupling of these concepts provided somewhat accurate good comparisons with experimental data, they were only possible to implement

through significant simplifications.

An engineer or researcher examining the literature will be overwhelmed by the sheer amount of publications on empirical correlations based on dimension analysis for the critical velocity and pressure loss in settling and non-settling suspension pipe flows and listing all of them is beyond the scope of this literature summary. Each one of these correlations assumes an enhancement on the quality of the results when compared to the ones in previous existing publications. Traditionally, empirical correlations have been used to effectively design pipelines; nevertheless, these successful predictions are limited to specific ranges of variables and lack universality, since outside the specified range these correlations produce disappointing results. Moreover, for empirical correlations to be effective predictive tools, their coefficients need to be fine-tuned using experimental data from tests in the specific pipeline system. This is in itself a logical fallacy since accurate predictions from empirical correlations to properly design a pipeline need data from that same pipeline.

Some thorough reviews and books on earlier iterations on empirical and semi-empirical correlations for both pressure drop and critical deposition velocity can be found in the literature (Abulnaga 2002; Clayton Thomas Crowe 2005; Peker and Helvaci 2011; C. A. Shook 1976).

2.8.2. SEMI-EMPIRICAL CORRELATIONS

Acknowledging the limitations of purely empirical methods, researchers devoted their attention to other methods that incorporated both theoretical and semi-empirical knowledge as found in the work carried by Bagnold (R. A. Bagnold 1966; C. A. Shook and Daniel 1965). These works had diverse outcomes being one of the most relevant an equation for energy loss, based on the dispersive stress defined by Bagnold, in an attempt to describe solid-liquid settling suspensions flow. Some studies (C. A. Shook et al. 1968) added on the work done by Bagnold, proposing mechanisms describing particle suspension by dispersive stress, incorporating the influence of turbulence

suspension of particles using the eddy diffusivity concept together with Richardson-Zaki equation for settling velocity (C. A. Shook et al. 1968), which allowed deriving an equation for concentration distribution in steady state. The Richardson-Zaki equation (Equation 2.9) was introduced in 1954 (Richardson and Zaki 1954) and it is the most widely employed semi-empirical correlation used to depict concentrated suspensions settling velocity, u, of non-Brownian hard spheres in liquids ($0.05 < \phi < 0.5$) where ϕ is the volumetric fraction of solids (Peker & Helvaci, 2011).

$$u = u_o(1-\phi)^n \tag{2.9}$$

This correlation is a modification of the individual particle settling velocity, u_o, based on an empirical parameter, n, dependent on the flow regime, represented by the terminal Reynolds number (Clayton Thomas Crowe 2005; Felice and Kehlenbeck 2000; Peker and Helvaci 2011), and also on the ratio between particle and vessel diameter, dp/D. The empirical parameter, n, also known as the Richardson-Zaki exponent, has been the subject of several publications. Traditionally this parameter was determined using a set of equations, each defined for a different range of terminal Reynolds number. However, these equations can be cumbersome to use, since there are regions where overlapping occurs, and a continuous function was presented as an alternative, by Rowe (1987), for the determination of the Richardson-Zaki exponent. Batchelor (Batchelor and Wen 1982; Batchelor 1982) extended the work of Richardson and Zaki to dilute suspensions (Equation 2.10).

$$u = u_o(1-n\phi) \tag{2.10}$$

Equation 2.10 provides the settling velocity of randomly dispersed spheres in suspensions in Stokesian regime (Batchelor and Wen 1982; Peker and Helvaci 2011). This expression is valid when the volumetric fraction of solids is not high enough to be considered as concentrated and yet sufficiently high for flocculation to occur. In the studies conducted by Batchelor, the empirical parameter, n, was suggested, for suspensions with negligible interparticular

forces, to be 5.5 when the Péclet Number (Pe) is large and 6.5 for suspensions with very small Pe (Batchelor and Wen 1982).

Similarly to empirical correlations, semi-empirical correlations suffer from similar drawbacks as their coefficients need to be fine-tuned using experimental data from tests in pipeline systems (Abulnaga, 2002; Crowe, 2006; Peker & Helvaci, 2011; Shook, 1976).

2.9. MECHANISTIC MODELS

The study of solid-liquid settling suspension flows where a non-homogeneous distribution of particles exists has provided us with one certainty: any model or correlation accuracy in predicting flow characteristics is intrinsically related to its capability of incorporating the flow regime mechanisms (Clayton Thomas Crowe 2005).

2.9.1. TWO LAYER MODEL

In 1970, Wilson (S. Miedema, Riet, and Matoušek 1995; Wilson 1970) developed a mechanistic model in which the flow is divided in two layers. In the first layer of the Two-Layer model, the upper part of the flow, the suspended particles linger while in the bottom layer, the second layer, the particles have settled. This model development started with experimental results obtained for narrow particle size distributions of solid-liquid settling suspensions; however, it is not suited for cases where there is a low contact of the particles with the bottom layer. In such cases a homogenous model is preferred. One of the issues with the Two-Layer model is that the existence of two layers and an interface inside the pipe is purely conceptual and used only for the sake of numerical representation purposes.

The fundamental bases of this model are as follows (Clayton Thomas Crowe 2005):

a) The flow is divided in two hypothetical layers: an upper layer of particles less than 74 μm and a lower layer containing all particle sizes

in the slurry;

b) Each layer has its own uniform velocity and volumetric solids concentration and there is no slip between the solids and the liquid within the layers;
c) Since the suspension in the upper layer behaves essentially as a liquid, as far as the wall shear stress is concerned, then the wall shear stress in the upper layer is kinematic, i.e., velocity-dependent;
d) In the lower layer the particles experience a Coulombic friction force;

Several iterations of the Two-Layer model have been proposed in the literature that are either simplifications or modifications of the original model in which a stationary or moving bed is in the bottom layer, while in the upper layer a heterogeneous suspension with a particle concentration gradient is present (Clayton Thomas Crowe 2005). Additional developments were later introduced by other authors (Clayton Thomas Crowe 2005; R. G. Gillies, Shook, and Wilson 1991; C. A. Shook et al. 1981; C. A. Shook et al. 1982). A more detailed description of the Two-Layer model can be found in the literature (Clayton Thomas Crowe 2005; Peker and Helvaci 2011).

2.9.2. THREE LAYER MODEL

The Three-Layer model was introduced in 1995 (Doron and Barnea 1995) and was developed by joining experimental information with the Two-Layer model. Since the Two-Layer model fails to accurately predict the suspension behaviour for low flow rates, where a stationary bed is present, this model states that in suspension pipe flow three different flow regimes occur at the same time. In the top layer a heterogeneous flow, in the middle layer a moving bed and in the bottom layer a stationary bed. The additional complexity of the Three-Layer model equips it with the capability of predicting flow pattern transitions; however, due to the aforementioned complexity, supplementary expressions and constitutive relations are required for closure of the equations set (Clayton Thomas Crowe 2005; Ramadan, Skalle, and Saasen 2005; Doron and Barnea 1995).

Mechanistic methodologies are a considerable improvement to empirical correlations in the depiction of settling and non-settling suspensions flows. Still, layered models present difficulties in predicting the flow of particles between layers (Roco and Shook 1984) and, additionally, these models' predictions are still obtained with the help of parameters that require accurate experimental data. Again, this defeats the purpose of the "predictive" aspect intended for a model. In addition, some of the assumptions required for the successful application of mechanistic models may not hold in this case, as is the case for the assumption that velocity in each layer is uniform in both Two and Three-layer models (Clayton Thomas Crowe 2005).

2.10. DETERMINISTIC MODELS

Traditional approaches for predicting the behaviour of multiphase flows were based on empirical correlations and mechanistic approaches, as seen in previous sections, which resulted from extensive experimental data compiled by equipment designers. These methods had the drawback of being case specific, i.e., they failed to produce accurate predictions if any of the conditions, such as particle data, inlet conditions or geometry, were altered. With the advent of computational modelling techniques and ever evolving computer hardware, the traditional approaches have been refined or replaced, providing scientists, engineers and equipment designers with an enhanced predictive capability and lack of restrictions to adjust process conditions to better suit their demands (Massoudi 2010).

The number of CFD codes and software, either proprietary or open source, has grown considerably through recent years. Although single phase CFD codes are well established in the literature, for multiphase flows they are still an open problem (Balachandar and Eaton 2010; Borhani 2010; Sommerfeld, Wachem, and Oliemans 2008) in spite of extensive research. When categorizing CFD codes for multiphase flow, more precisely for solid-liquid settling suspension flows, the following approaches have been considered:

2.10.1. SINGLE-PHASE NUMERICAL MODELS

This approach is only suitable for solid-liquid settling suspension flows where the solids concentration is quite low and there is one-way coupling, i.e., where the presence of the particles has little or no impact on the overall properties of the liquid phase (C.T. Crowe, Troutt, and Chung 1996). Earlier works derived a turbulent model that used the properties of the mixture for the calculations of settling suspensions flow behaviour (Roco and Shook 1984). Two equations turbulence models (Wilcox 2006) became increasingly popular in two-phase applications, and some recent works have employed this approach to highly concentrated solid-liquid settling suspension flows with turbulence modulation (Bartosik 2010; Bartosik 2011) for Low Reynolds turbulence models.

In other approaches and using two-equation single phase turbulence models for solid-liquid settling suspension, Hsu, Jha and Elghobashi added additional parameters into the equations allowing to account for the particle influence on the carrier phase (Hsu 2003; Jha and Bombardelli 2009; Rizk and Elghobashi 1989).

Single-phase numerical models offer a computational inexpensive tool for predicting pressure drop, velocity and turbulence profiles, while providing some insight into particle-boundary layer information, although in a limited fashion. Presently, there are available more complex numerical models in software packages, either commercial or open-source, that perform better.

2.10.2. EULER-EULER NUMERICAL MODELS

In the “Dense Phase approach”, Eulerian or even “two-fluid” approach, the two components are interacting with each other in a way that the behaviour of each phase influences the other and are considered to be at the same location at the same time. The volumetric fraction is of paramount importance as this variable will dictate the amount of each phase at a given time and place. The Eulerian models provide an averaged depiction of a

multiphase system, and in the literature a wide range of averaging processes can be found, namely time, volume or ensemble based averaging (Ishii and Hibiki 2011). With this averaging methodology two advantages arise, one being that with the averaging process all the forces are inherently present in the model, being the other advantage that the computational cost is not dependent on the number of particles, making the Eulerian approach more suited for large systems with a great number of particles. A drawback of the Eulerian modelling approach, also a consequence of the averaging process, is the loss of detail, which creates the need for closure equations for the turbulence and interaction forces. This approach is widely employed in fluidization, gas-solid flows, pneumatic and hydraulic conveying, and suspension flows (Balachandar and Eaton 2010; Sommerfeld, Wachem, and Oliemans 2008). The Eulerian approach has become increasingly popular for concentrated or dense suspension flows, either using a single fluid approximation (Mixture Model, Volume of Fluid, cavitation models, etc.) or two-fluid approximation (Euler-Euler Model or Euler-Granular Models) (Brennen 2005).

The Mixture Model (Manninen, Taivassalo, and Kallio 1996) was used to perform a series of numerical studies on pipe flows of both zirconia-water and silica-water mixtures to a maximum of 20% solid volumetric fraction: all of them showed good agreement with the experimental data (Ling et al. 2003); this same model was also used together with the High Reynolds k-ε Turbulence Model for highly concentrated solid-liquid flow in pipes (D.R. Kaushal et al. 2012) with results far from satisfactory due to an over-prediction of the pressure drop in the pipe section, which increased with solids concentration. Another approach, using the Mixture Model and a Low Reynolds Turbulence closure, was employed to describe highly concentrated flows of solid-liquid suspensions (Silva et al. 2014; Silva et al. 2013). Also a new photocatalytic reactor (XiaoWei and LieJin 2010) with solar concentrator for hydrogen production was simulated using an Algebraic Slip Mixture model (ASM) with a catalyst volumetric fraction up to 15% .

An increasing number of publications, where the Two-Fluid approach incorporating the Kinetic Theory of Granular Flow is employed to characterize particle-particle interaction, can also be found in the literature, to study highly concentrated solid-liquid settling suspensions pipe flow (D.R. Kaushal et al. 2012; S. Lahiri and Ghanta 2010; S. K. Lahiri and Ghanta 2008) slush nitrogen (Jiang and Zhang 2012) and ice slurry (Jihong Wang et al. 2013), with good results in reproducing experimental data. The Kinetic Theory of Granular Flow is an adaptation from the Kinetic Theory of Gases, and in this way the particle-particle interactions are quantified in the flow. However, although it provides some good results for concentrated solid-liquid flows for different size and density of the particles, it is a very complex numerical model, with a high computational requirement and often with boundary conditions issues that require some simplifying assumptions.

The predominant applications of the existing two-fluid models exhibit problems hindering their use for more complex flows of engineering interest. Amongst the main issues, one can point out numerical instabilities, very time-consuming, difficulty in dealing with complex geometries, since the calculation time becomes prohibitively expensive and none of the existing models has shown to be able to determine the minimum in the pressure gradient versus slurry velocity, which characterizes the transition to bed flows (Messa, Malin, and Malavasi 2014).

2.10.3. EULER-LAGRANGE NUMERICAL MODELS

The Lagrangian approach, also known as “Dilute Phase approach”, is employed when the amount of the dispersed phase is small and does not disturb the motion of the continuous phase. This approach is predominant in case studies of sprays, atomization and flows with bubbles, where droplets and particles are treated as the dispersed phase. Amongst the Lagrangian approach three major modelling techniques can be outlined: “Point-Particle Direct Numerical Simulation (DNS)”, “Point-Particle Large Eddy Simulations (LES)” and “Point-Particle Reynolds Averaged Navier-Stokes (RANS)”. The

DNS modelling approach requires that the particles must be smaller than the Kolmogorov scales, i.e., the time scales of the particle have to be smaller than the time scales of the smaller scales of the fluid. This requirement limits the DNS application to very low Reynolds numbers or to very small particles. To overcome this limitation LES modelling can be used. Both DNS and LES application are limited to dilute systems where collisions and hydrodynamic interactions can be neglected and a one-way coupling between the dispersed and carrier phases is assumed (Balachandar and Eaton 2010; R. O. Fox 2012; Hiltunen et al. 2009; Mashayek and Pandya 2003).

In recent works (Adams, Fairweather, and Yao 2011; Soldati and Marchioli 2012), one-way coupled Eulerian-Lagrangian models were employed in the study of dilute solid-liquid flows suspension and re-suspension of particles. In another work a solid-liquid settling suspension flow in horizontal pipes was investigated (Capecelatro and Desjardins 2013) for operating conditions above and below the critical deposition velocity. A high-fidelity large eddy simulation framework is combined with a Lagrangian particle tracking solver to account for polydispersed settling particles in a fully developed turbulent flow. Two cases were simulated, the first having a Reynolds number of 85 000 and the second one considered a lower Reynolds number of 42 660. Since most studies of the Lagrangian properties of turbulence consider point-like particles (Toschi & Bodenschatz 2009), they still cannot be generally applied to all types of particles, and also to systems with a large number of particles, due to the high computational demand. They will, nevertheless, most likely become standard tools in the future.

Some excellent reviews on Lagrangian-Eulerian Methods on multiphase flows were given by Subramanian (2013) and Zhou (2010).

2.10.4. LATTICE-BOLTZMANN NUMERICAL MODELS

In the last two decades the Lattice Boltzmann Method (LBM) has been developed into an established CFD approach for solving fluid flow problems. Important developments have been done in LBM's capability for several flow

problems, containing multiphase flows, turbulence, and microfluidics. Amongst numerous areas, the solid-liquid systems have received special emphasis considering the unique advantage of LBM in its computational efficiency and parallel scalability. Traditionally, conventional CFD numerical schemes are based on the discretisation of macroscopic continuum equations, like finite-difference, finite-element or finite-volume methods, which have been used to solve the velocity and pressure fields from Navier–Stokes equations: on the other hand, LBM is based on microscopic models and mesoscopic kinetic equations in which the fluid is described by a group of discrete particles that propagate along a regular lattice and collide with each other. This scheme is particularly successful in fluid flow applications involving interfacial dynamics and complex boundaries (Aidun and Clausen 2010; Liangyong Chen et al. 2010; Yu and Fan 2010).

The LBM can serve as an alternative flow solver for different types of incompressible flows. The incompressible Navier-Stokes (NS) equations can be obtained in the nearly incompressible limit of the LBM. Pressure, in the LBM, is calculated using an equation of state. In contrast, in the direct numerical simulation of the incompressible NS equations, pressure satisfies a Poisson equation with velocity strains acting as sources, and solving this equation often produces numerical difficulties requiring special treatment, such as iteration or relaxation ((Aidun and Clausen 2010; Liangyong Chen et al. 2010; Yu and Fan 2010). For the modelling of solid-liquid systems, the LBM, due to its simple implementation, becomes particularly appropriate for simulations involving large numbers of particles. Furthermore, it can be coupled, if it is regarded only as a solver for the fluid flow, with various methods for particles such as Discrete Element Method (DEM) or Lagrangian tracking (Aidun and Clausen 2010; Balachandar and Eaton 2010; Borhani 2010).

Among recent publications on LBM application to solid-liquid settling suspensions flows, it is important to refer the following contributions: a) Shardt & Derksen (2012) simulated up to 45% solids volume fraction of rigid

non-spherical particles with low density ratios at moderate particle Reynolds numbers (< 1) using the LBM coupled with DNS studies; b) two-dimensional (2D) and three-dimensional (3D) CFD studies of solid-liquid settling suspensions flows, by Kromkamp et al. (2006) where Couette flows of single, two and multi-particle systems were described; c) Gao et al. (2013) presented a particle-resolved simulation method for turbulent flow laden with finite size particles, based on the multiple-relaxation-time Lattice-Boltzmann equation. In the later, a maximum of 51200 particles in 3D have been considered for the simulations and the authors noted that particle-laden turbulent flow is a multi-scale problem that requires state of the art computers to include all relevant scales into the simulations with realistic physical parameters.

The Lattice-Boltzmann approach, due to its relatively simple implementation for parallel computing and hybrid combinations of the Eulerian lattice with a Lagrangian grid system (Aidun and Clausen 2010; Subramaniam 2013), shows great promise relatively to traditional approaches; still it is only possible to employ it in simulations of suspension flows with dilute concentrations.

Detailed reviews on LBM theory and multiphase applications can be found in the literature (Aidun and Clausen 2010; Li Chen et al. 2014; S. Chen and Doolen 1998; Yu and Fan 2010).

2.10.5. DISCRETE ELEMENT METHOD (DEM) NUMERICAL MODELS

One of the main challenges in simulating settling suspensions flows derives from their intricate behaviour brought about by the complex interactions between individual particles and their interactions with surrounding liquid and wall. Understanding the underlying mechanisms has been the aim of particle scale research which in recent years has grown worldwide, as a result from the intense development of both discrete particle simulation techniques and computational capabilities. An important discrete model is the discrete element method (DEM) originally developed in 1979 by Cundall

and Strack (1979). This method uses the Newton's equation of motion to contemplate a finite number of discrete particles interacting through contact and non-contact forces moving translationally and rotationally. Both trajectories and transient forces acting on individual particles are extremely difficult to obtain by experimental techniques, which is the type of information provided by DEM simulations (H. P. Zhu, Zhou, and Yang 2008).

In recent publications DEM has been combined with CFD techniques to describe solid-liquid settling suspensions. For instance: modelling of solid-liquid suspension flows in the density-driven segregation of a binary particulate suspension incorporating 10 000 particles in a closed container, using a hybrid combination of the discrete element method (DEM) with computational fluid dynamics (CFD) (Qiu and Wu 2014); use of a new Lagrangian–Lagrangian algorithm, also referred to as the DEM–SPH method, for solid–liquid flows in both a dam break problem and a quasi-steady solid–liquid flow in a cylindrical tank (X. Sun, Sakai, and Yamada 2013); simulation of dense medium cyclone separation (DMC), combining DEM with CFD in coal preparation, which is a process with a simple design but where the flow pattern in the cyclone is complex, due to the size and density distributions of the feed as well as the turbulent vortex formed (Chu et al. 2009). In its case study, Chu employs DEM to model the motion of discrete particles by applying Newton's laws of motion, and CFD is used to model the motion of the slurry medium by numerically solving the local-averaged Navier–Stokes equations, using the Volume of Fluid (VOF) and Mixture multiphase flow models; in Zhang et al. (2012) studies on transport of particles in a fluid, for predicting the particles puncture point location in an elbow, DEM was used to describe the kinematics and trajectory of the discrete particles as well as the particle–particle interaction. The hydrodynamic modelling of the fluid phase was based on the volume-averaged Navier–Stokes equations, and a fluid density-based buoyancy model was adopted to calculate the solid–fluid interaction force.

Regarding numerical studies involving DEM for solid-liquid settling

suspensions in horizontal pipes there seems to exist a lack or a complete absence of publications on the subject, which can be attributed to the limitation on the number of particles that it is possible to simulate, even with this method, that offers an alternative to DNS due to its parallel computing capability (H. Zhang et al. 2012; H. P. Zhu, Zhou, and Yang 2008). A review on DEM application in particulate systems was presented by Zhu et al. (2008) .

2.11. TURBULENCE MODULATION

As pointed out in section 2.10.1, with low solids volumetric fraction the usual assumption is that the turbulence of the fluid phase is equal or very similar to the single-phase flow. Yet, as the solids volumetric fraction increases additional phenomena appear where turbulence augmentation, dissipation and distortion become significant. For solid-liquid settling suspensions flows the phenomena of turbulence attenuation is a rather interesting one for design engineers, since this would allow solids conveying of concentrated suspensions at energy expenditures similar to those of single-phase flows (Balachandar and Eaton 2010; C.T. Crowe, Troutt, and Chung 1996).

Crowe and Elghobashi have done extensive work on turbulence modification, but mainly for gas-liquid and gas-solid flows (C.T. Crowe 2000; Elghobashi and Truesdell 1993; Truesdell and Elghobashi 1994; Kenning and Crowe 1997). In their research, the following conclusion was attained “small particles will attenuate the turbulence while large particles will generate turbulence” (Crowe et al., 1996). And while this seems to hold true for gas-solid and gas-liquid suspensions flows, recent studies (D.R. Kaushal et al. 2012; S. Lahiri and Ghanta 2010; Václav Matoušek 2005) seem to contradict this statement for solid-liquid settling suspensions flows. In fact, quite the opposite seems to be the case for solid-liquid settling suspensions but only for highly concentrated solids volumetric fractions.

In a recent publication Tanaka and Eaton (2008) presents a dimensionless parameter, the particle moment number, Pa, that was derived using dimensional analysis of the particle-laden Navier-Stokes equations. This

parameter can be calculated using either the particle Reynolds Number (see Equation 2.11) or the Stokes Number (see Equation 2.12).

$$Pa_{Re} = \frac{1}{18}\frac{Re_L^2}{Re_p}\frac{\rho_p}{\rho_f}\left(\frac{d_p}{L}\right)^3 \quad \textbf{(2.11)}$$

$$Pa_{St} = St\ Re_L^2\left(\frac{\eta}{L}\right)^3 = \frac{1}{54\sqrt{2}}\frac{Re_L^2}{St^{1/2}}\frac{{\rho_p}^{3/2}}{{\rho_f}^{3/2}}\left(\frac{d_p}{L}\right)^3 \quad \textbf{(2.12)}$$

This analysis was based on a set of 80 experimental measurements where the turbulent kinetic energy was modified by particles. Data for the turbulent kinetic energy augmentation in air and water were included as well as data for the turbulent kinetic energy attenuation in air, but there is a void of data for the turbulent kinetic energy attenuation for water. This is a very thorough study that, in spite of the absence of information on turbulence attenuation when the medium is water, represents a significant step towards predicting turbulence modification in particle laden flows.

Searching the literature for current numerical studies trying to characterize turbulence attenuation for solid-liquid settling suspensions, some manuscripts are found where: drag correlations are modified in an attempt to reproduce experimental data where turbulence modulation occurs (Hadinoto and Chew 2010; Hadinoto 2010); single-phase Low Reynolds turbulence models are modified to incorporate turbulence modulation (Bartosik 2010; Bartosik 2011); Mixture Models with a Low Reynolds Turbulence closure for turbulence modulation in highly concentrated solid-liquid flows is used (Silva et al. 2013); Euler-Euler model is used for pipe flow of concentrated slurries (D.R. Kaushal et al. 2012; S. Lahiri and Ghanta 2010).

Some thorough reviews and studies on turbulence modulation in particle laden flows are present in the literature (Balachandar and Eaton 2010; C.T. Crowe, Troutt, and Chung 1996; Hosokawa and Tomiyama 2004; Kiger and Pan 2002).

CHAPTER III

EXPERIMENTAL SETUPS

3. CHAPTER III – EXPERIMENTAL SETUPS

In this Chapter a detailed description of the experimental setups and techniques employed in attaining the experimental data will be advanced.

In this study experimental data, using an Electrical Impedance Tomography (EIT) apparatus and an Sampling Probe (ISP), was gathered at an existing pilot rig in the Chemical Engineering Department at the University of Coimbra, Portugal, for solid-liquid suspensions flows. Furthermore, experimental data on solid-liquid suspensions, including MRI and UPV profiles, was gathered at the Mekanics Department at KTH Royal Institute of Technology in Stockholm, Sweden.

Additionally, a thorough description of the development of the aforementioned EIT system, employed at the solid-liquid suspensions experimental studies in Coimbra, will be presented.

3.1. FLOW LOOP I – DEQ COIMBRA

3.1.1. INTRODUCTION

The flow loop existing in the Chemical Engineering Department at the University of Coimbra, with a useful capacity up to 800 litres, was previously designed by a previous Ph.D. student and a detailed depiction of the structure is present in the literature (Ventura et al. 2008) (see Figures 3.1 and 3.2).

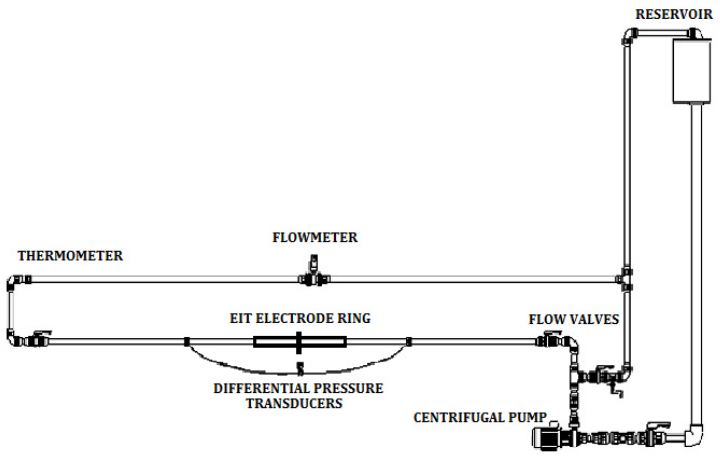

Figure 3.1 – Schematics of the flow loop at DEQ – Coimbra.

Figure 3.2 – Pilot rig at DEQ – Coimbra.

Some modifications were implemented on the aforementioned flow loop in order to mount a transparent Poly(methyl methacrylate) (Perspex®) section containing the EIT electrodes rings. In this setup, pressure drop and flow rate experimental data were acquired on solid-liquid suspension flows consisting on spherical glass particles suspended in an aqueous solution of NaCl. Additionally, EIT imaging and Sampling Probing were utilized in order to obtain vertical particle distribution in the pipe cross section. Testing was repeated for solid-liquid suspensions with increasing particle concentration and size. This experimental data would be matched with numerical simulations results in order to ascertain the accuracy of a CFD model.

3.1.2. FLOW LOOP I DESCRIPTION

The conveying system test section consisted of a horizontal PVC tube, 7.5 m in length and 0.1 m in internal diameter. The pumping system consisted of a GRUNDFOS Model MMG160MA 11.0 kW centrifugal pump. The flow rate could be regulated by simultaneous manipulation of two butterfly valves located after the "Tee" for diverging the flow (see Figure 3.1) and measured using an electromagnetic flowmeter consisted of a Fuji Electric MAGFLO 3100 sensor coupled with a MAGFLO 5000 signal converter. The pressure drop was measured by a Fuji Electric FCX-C series T-type differential pressure transducer (model number FKK-33) whose pressure taps were 4 m distant. Appropriate lengths were inserted before and after the test section to account

for entrance and exit effects (see Figure 3.1).

The distribution of particles was measured using EIT electrode rings and an sampling probe. The EIT electrodes were circumferentially and equally spaced mounted in a Perspex® tube 0.90 m in length and 0.1 m in internal diameter, which was inserted in the test section between the pressure taps. The sampling probe was inserted downstream of the pressure taps and had an internal diameter of 4 mm (see Figure 3.3).

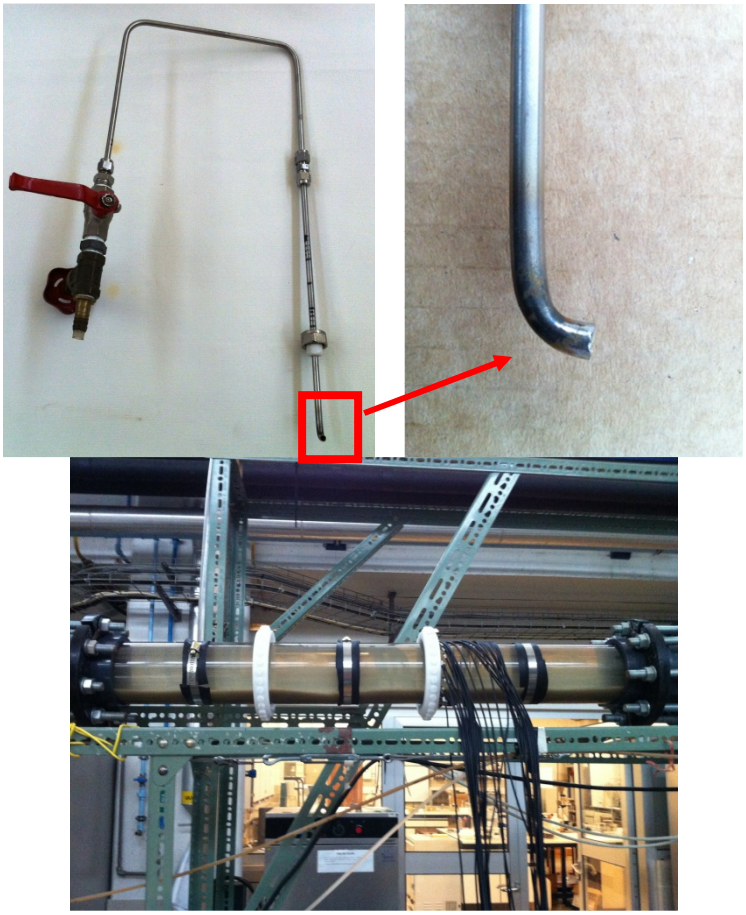

Figure 3.3 – Sampling probe (SP) (Top) and Perspex® section with EIT electrode rings (Bottom) at DEQ – Coimbra.

3.1.3. EXPERIMENTAL CONDITIONS & PARTICLE DATA

The flow was always allowed to stabilize before performing the tests and the data collected. The solid-liquid suspensions were composed of spherical glass beads (Silibeads Type S) supplied by Sigmund Lindner GmbH provided by Silibeads®, in diluted aqueous solutions of NaCl with an average electrical

conductivity of 696 μS.cm^{-1}. An electrical conductivity meter CRISON® MICROCM 2202 equipped with a conductivity probe model 545 and a temperature sensor was used to for electrical conductivity assessments.

The spherical glass beads sizes and concentrations as well as the flow rates, employed in the studies performed in Coimbra, depicted in this manuscript are summarized in Table 3.1. In Appendix C additional data for the size distribution of the particles can be found.

Table 3.1 – Particle data for the performed tests at Coimbra.

	SILIBEADS GLASS BEADS TYPE S	
PARTICLE DENSITY [kg.m^{-3}]	2500	2500
AVERAGE PARTICLE SIZE [mm]	0.15	0.5
PARTICLE VOLUMETRIC FRACTION [v/v]	0.0 to 0.11	0.0 to 0.11
FLOW RATE [m^3.h^{-1}]	0.0 to 84	0.0 to 84

3.2. ELECTRICAL IMPEDANCE TOMOGRAPHY (EIT)

In the following sections EIT equipment design will be addressed. Detailed information on the theory supporting the hardware development can be found in Appendix A.

3.2.1. EIT HARDWARE DESIGN

Electrical Impedance Tomography is a non-invasive technique based on the assumption that each material possesses unique electrical properties and therefore a characterization of the distribution of the electrical field is used to infer on the materials distribution within a domain.

A set of electrodes placed in the boundary of the domain under study where an electrical current/voltage is injected/applied resulting an electrical field that is conditioned by the materials distribution inside the domain (M. Wang,

Jones, and Williams 2003). The resulting electrical potentials in the domain perimeter can be measured using the remaining electrodes, and those values are introduced to a non-linear inverse algorithm to attain the previously unknown conductivity/resistivity distribution. This procedure is only complete when all electrodes are used for injection or projection, so the cycle can have as many projections as the number of electrodes. For a dynamic system such as suspension flow, it is required that the system performs the reconstruction of the conductivity/resistivity distribution in the smallest amount of time possible.

The EIT system design depicted in this manuscript (see Figure 3.4) can be used with 16 electrodes or 32 electrodes rings to provide 2D cross section tomographic slices. The system is composed of function specific modules: signal generation and phase shifting occur on the same module, signal multiplication, demodulation and conditioning are done in another module and multiplexing is done in a third module. The electrode rings are mounted on the surface of the pipe and communication with the computer where the signals are reconstructed into an image is attained using digital/analogical acquisition boards.

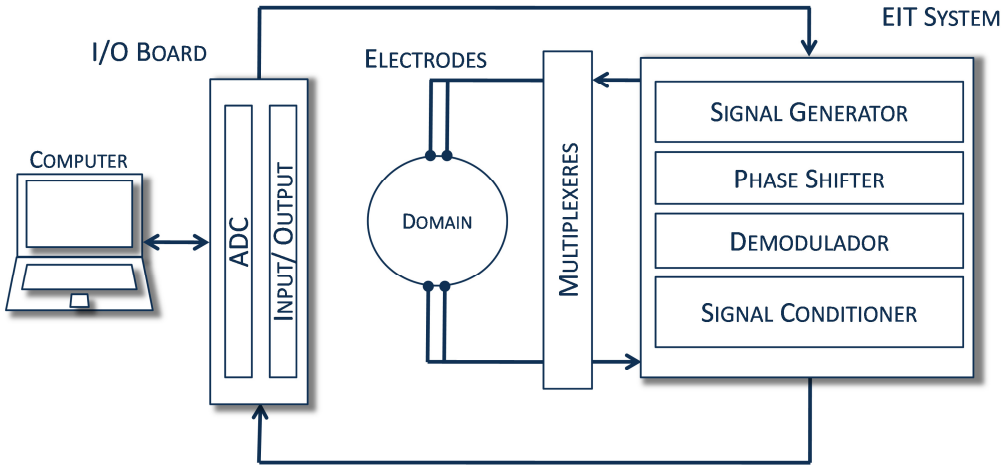

Figure 3.4 – Block diagram of the EIT design implemented in this study.

A conscious effort was placed in the design of a low-cost hardware with the purpose of establishing it as a motivating investment in industrial applications over the next years. Additionally, difficulties and costs associated

with the design of a current source that suited the goals of the EIT system, led to the choice of moving from traditional EIT systems and instead a voltage source was projected. The benefits of using this kind of signal generation have been reported by other authors (Jia et al. 2010).

In Figure 3.5 several stages of the development of the EIT apparatus are shown.

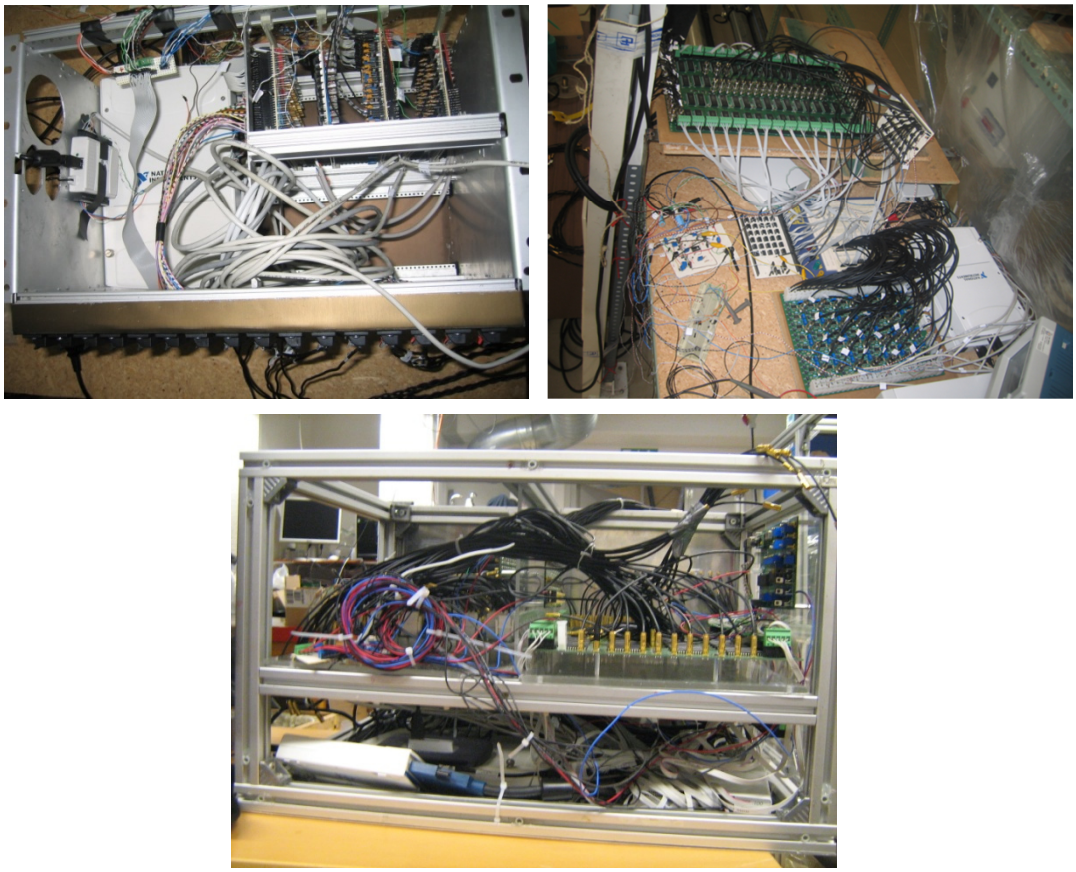

Figure 3.5 – Several stages of development the EIT system: earliest stage with wire-wrap modules (Top Left); intermediate stage with several modules already in PCB layout (Top Right); last stage with the EIT system already is transport case (Bottom).

3.2.2. FREQUENCY GENERATOR AND PHASE SHIFTER MODULE

The frequency generation and phase shifting module was designed to have an output frequency up to 100 kHz. This generator can produce triangular, sinusoidal and square waves (see Figure 3.6).

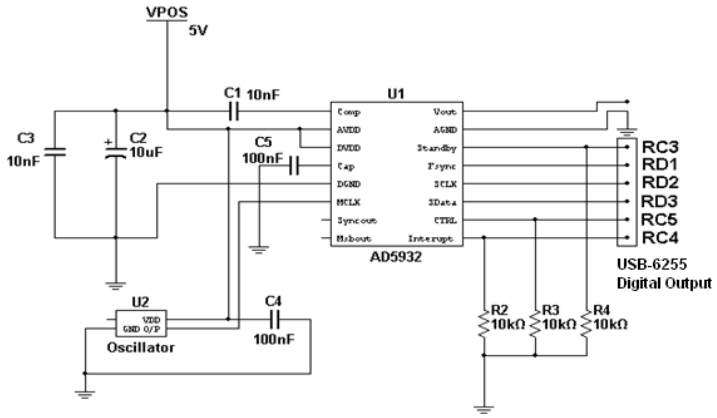

Figure 3.6 – Sinusoidal voltage signal generator schematics.

This is one of the highest frequency ranges amongst the existing electrical tomographic systems for medical applications and any other field (Goharian et al. 2008; Donthi and Subramanyan 2004). As stated previously, the EIT system designed in this study, contrarily to existing EIT systems, resorts to a voltage source that can be configured to produce, for instance, a sinusoidal waveform of 2 kHz frequency and 1.5 V of amplitude (see Figure 3.7).

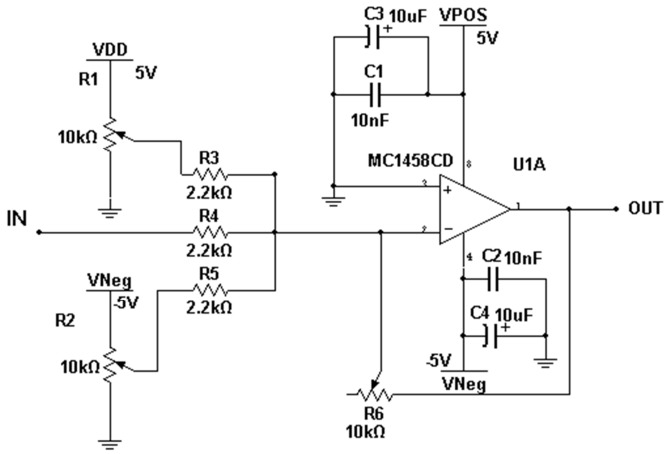

Figure 3.7 – Amplitude and DC component adjustment schematics.

In the studies depicted in this manuscript and using the previously described excitation procedure, a current amplitude of 90 μA was applied to the domain Ω. This low current amplitude prevents the development of polarization phenomena's inside the domain. Opting for this method of signal generation has proved to allow to surpass the limitations of a traditional current source when applied to more conductive media, as others have observed recently

(Jia et al. 2010). In most industrial processes, operating in a close-circuit, media with higher conductivity are predominant and, thus, this method of signal generation will be more adequate than the usual approach.

In the Frequency Generator & Phase Shifter modules, the three signals needed for the system's operation are generated (see Figure 3.8). The first, as described above, will be applied to the domain of study. As for the remaining two signals, both with unitary magnitude, one is 90 degrees out of phase with the applied signal and the other one is in phase with the applied signal. These last two signals will be later utilized by the demodulation module.

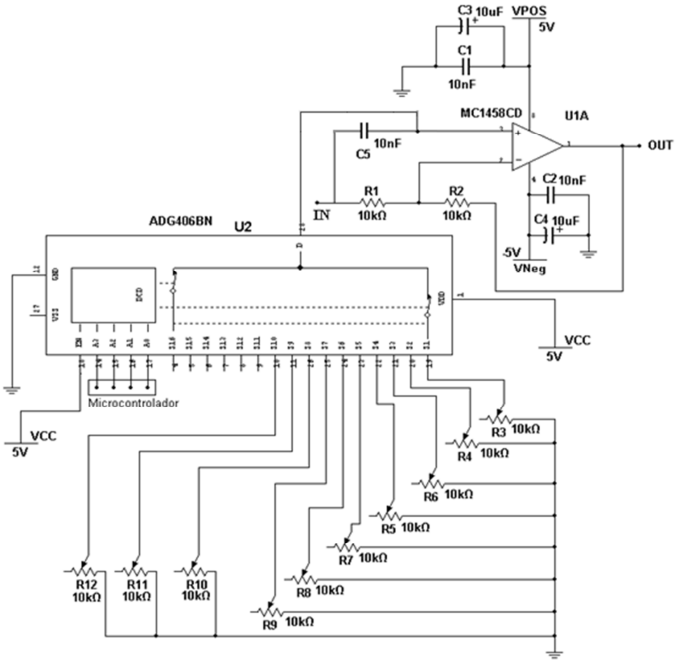

Figure 3.8 – Phase shifter schematics.

Pictures of earlier and final versions of the module are presented in Figure 3.9.

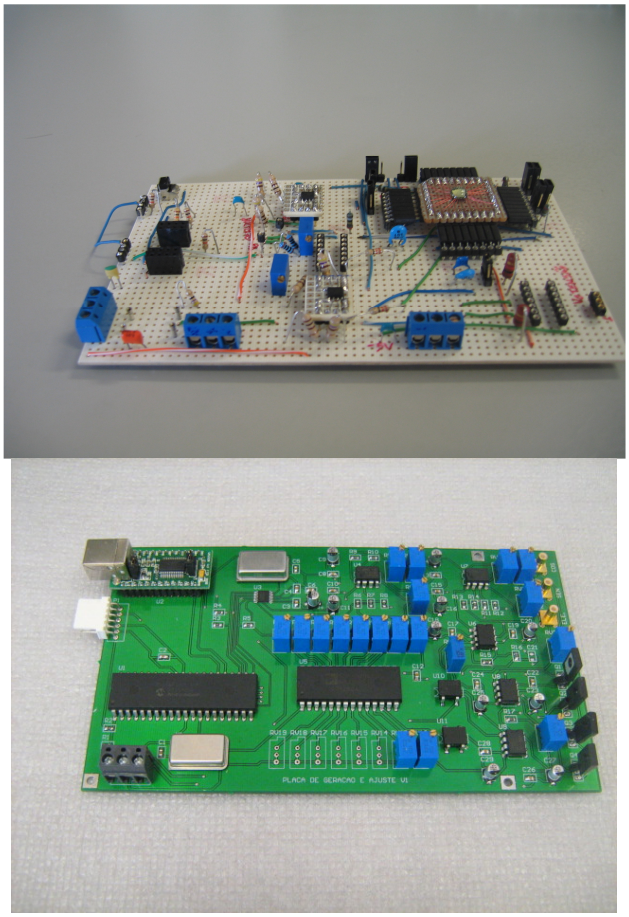

Figure 3.9 – Earlier wire wrap iteration (Top) and final version (Bottom) of frequency generation and phase shifting module.

3.2.3. DEMODULATOR AND SIGNAL CONDITIONER MODULE

In the Demodulator module the two signals, in and out of phase, generated in the previous module are multiplied by the measured electrical potentials in the electrodes, according to Equations 3.1 and 3.2.

$$V_m \cos(\omega t + \theta) \times \sin(\omega t) = \frac{V_m}{2}\sin(2\omega t + \theta) + \frac{V_m}{2}\sin(-\theta) \quad \textbf{(3.1)}$$

$$V_m \cos(\omega t + \theta) \times \cos(\omega t) = \frac{V_m}{2}\cos(2\omega t + \theta) + \frac{V_m}{2}\cos(-\theta) \quad \textbf{(3.2)}$$

The demodulation units are 28 or 60 depending if the 16 or 32 electrodes rings are employed for the measurements, two for each measured potential (see Figure 3.10).

Assuming that an excitation current given by $I_m \cos(\omega t)$ is injected in the

domain and that the potential measured in one of the electrodes is $V_m \cos(\omega t + \theta)$, where I_m represents the current amplitude, ω the frequency, V_m the potential amplitude and θ the phase shift between the current and the voltage brought upon by the domain impedance. Since it's the impedance that is wanted to be determined, we can retain from Equations 3.1 and 3.2 that, in both cases, the resulting signals are composed by an oscillating term with twice the frequency of the initial excitation current and a constant term.

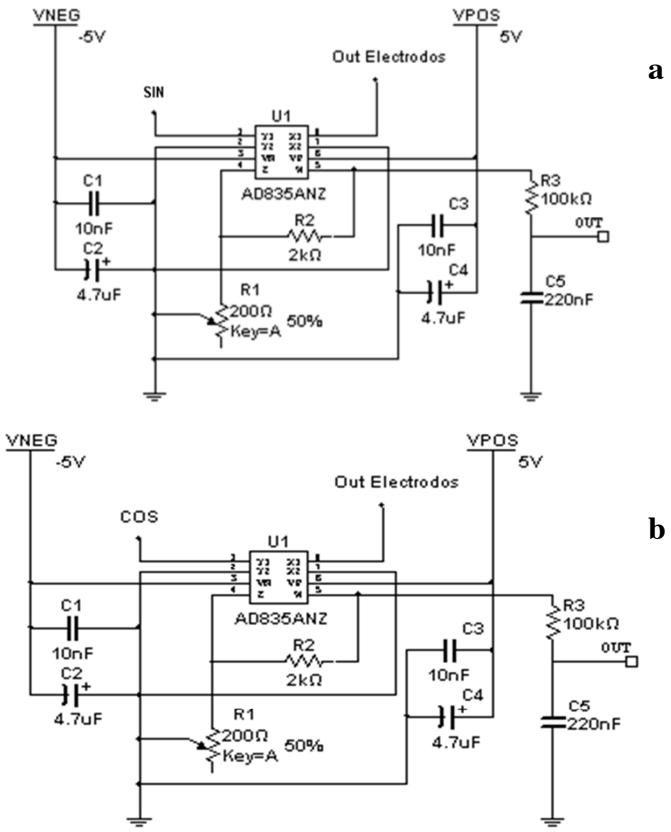

Figure 3.10 – Schematics of the two units in synchronous demodulation modules: in (a) the measured voltage and the in phase reference signal, from the previous Frequency and Phase Shifting module, are multiplied; in (b) the measured voltage at the electrode is multiplied by the 90 degrees out of phase reference signal.

For one electrode two demodulation circuits are wanted so as to obtain both components, real and imaginary, between the applied electrical current and the measured electrical potentials. Demodulation is performed using two demodulation units: in one of the units (see Figure 3.10 (a)) the measured

voltage and the in phase reference signal, from the previous Frequency and Phase Shifting module, are multiplied; in the other demodulation unit the measured voltage at the electrode is multiplied by the 90 degrees out of phase reference signal (see Figure 3.10 (b)).

Then, to determine the Impedance of the domain, it is necessary to isolate the two constant terms of Equation 3.1 and 3.2: that is done using two low pass filters, one for each pair of demodulation unit (see Figure 3.11).

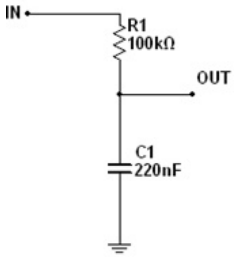

Figure 3.11 – Low-pass filter module schematics.

In Figure 3.12 pictures of earlier and final versions of the demodulation and signal conditioner module are presented.

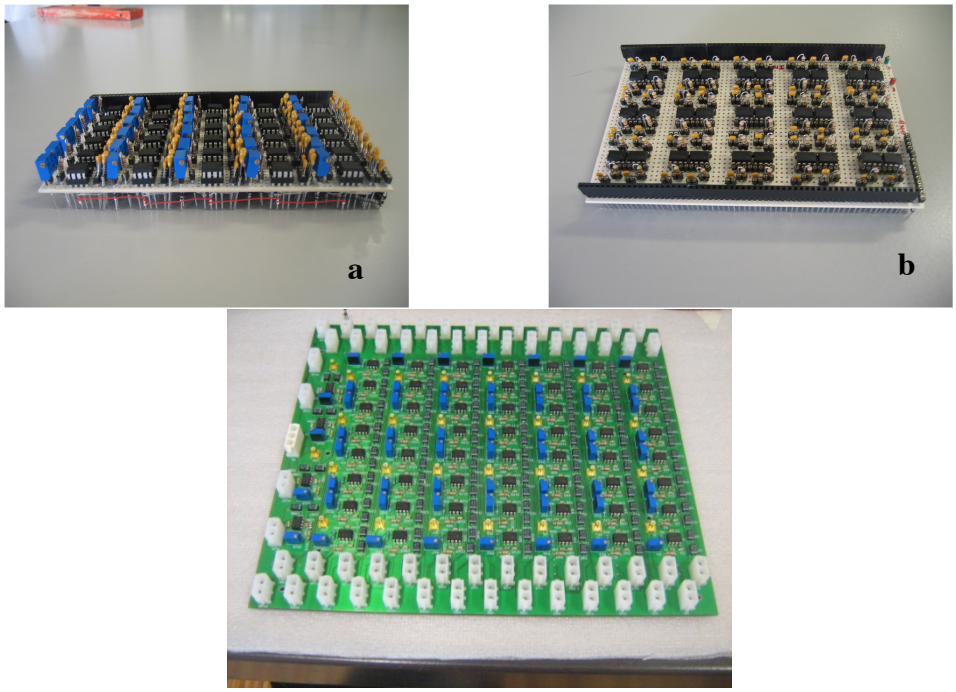

Figure 3.12 – Earlier wire wrap iteration (Top) of the shift control demodulation unit and synchronous demodulation unit (a) with the low-pass filter (b) and the demodulation and signal conditioning module final version (Bottom).

Additionally, two buffer circuit modules were inserted before the demodulation and signal conditioner module: the first between the frequency generation and phase shifting module and the demodulation module; the second between the electrode connectors and the demodulation module. These buffer circuits served for isolation and noise reduction in the electrical signals of the different channels (see Figure 3.13).

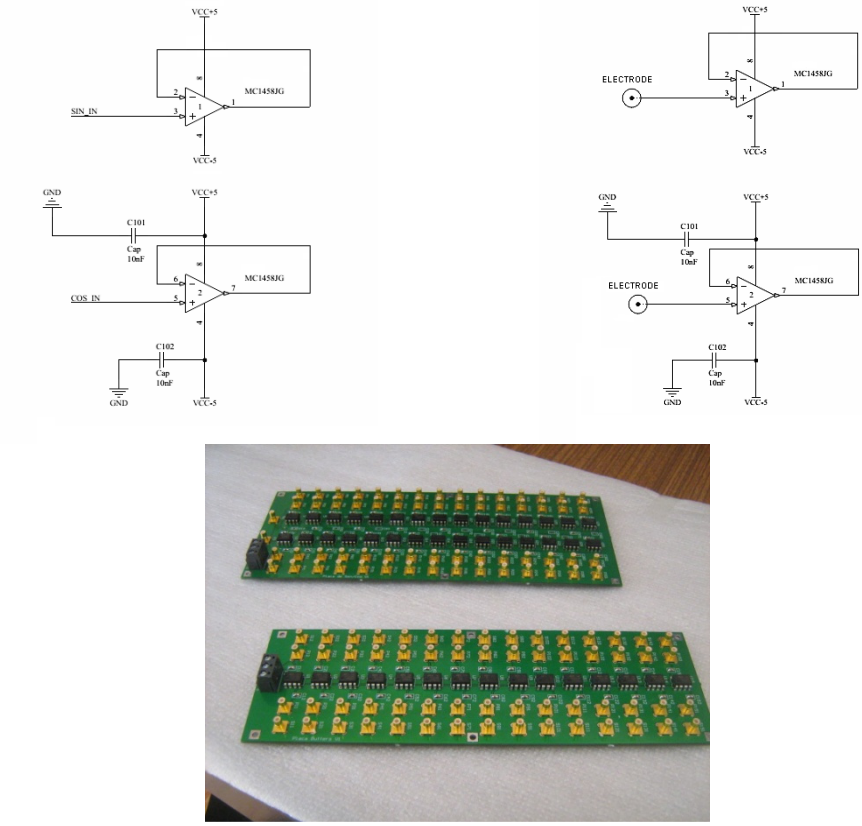

Figure 3.13 – Schematics for the buffer circuits modules between the frequency generation and the demodulation modules (Top Left) and between the electrodes and demodulation module (Top Right) and the final version (Bottom) of both modules.

3.2.4. MULTIPLEXING AND DEMULTIPLEXING MODULE

In this module the routing of the signal injection and potential measurements to and from the domain Ω, respectively, are executed. The multiplexing or demultiplexing is accomplished using either a set of 16 or 32 analogical multiplexers (depending if the 16 or 32 electrodes rings are employed for the measurements). The addressing of the multiplexers (see Figures 3.14 and 3.15) is accomplished through the digital outputs of the DAQ Boards in the

Data acquisition module (see Section 3.2.5). By changing the addressing of the multiplexers, various injection and measurement protocols can be implemented (see Section 3.2.6).

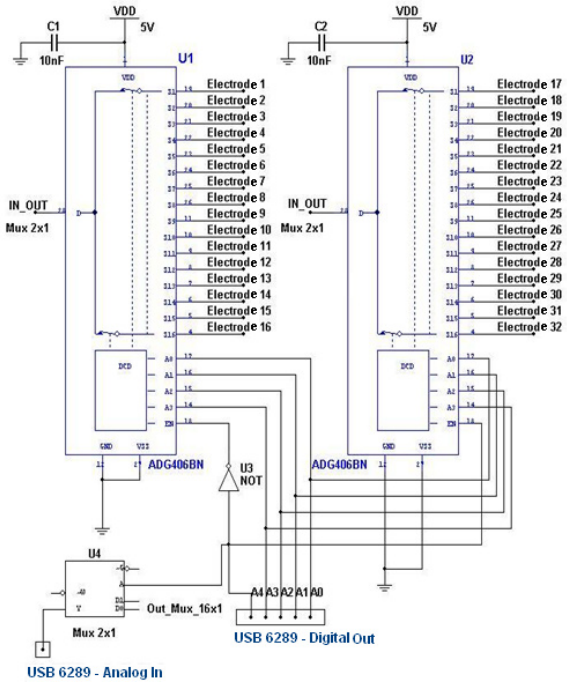

Figure 3.14 – Overall schematics of the multiplexing and demultiplexing module.

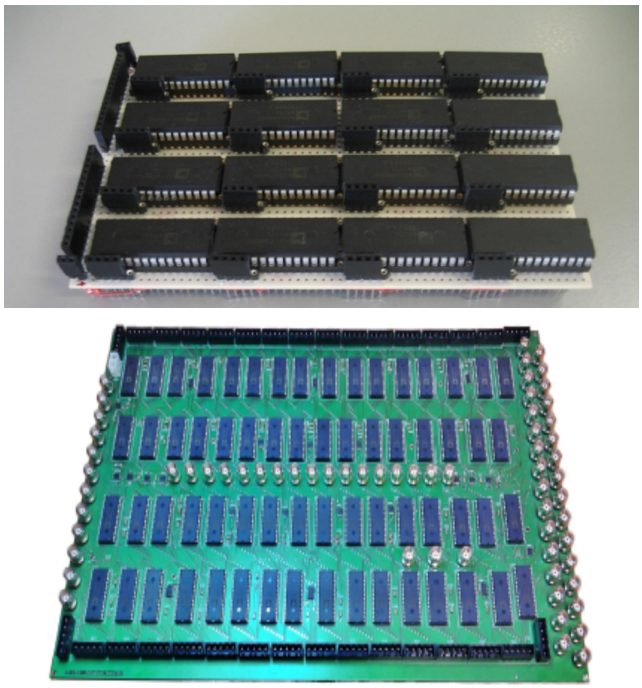

Figure 3.15 – Earlier wire wrap iteration (Top) and final version (Bottom) of the multiplexing and demultiplexing module.

3.2.5. DATA ACQUISITION MODULES

The Electrical Impedance Tomography system depicted in this study is capable of acquiring 4000 and 1000 frames per second for the 16 and 32 electrodes measurement rings, respectively. These frame rates are for single ring acquisition using the adjacent injection protocol (see Section 3.2.6). The frame rate for multiple rings will be similar, since back ring acquisition system is autonomous and will work concurrently.

In the 16 electrodes EIT system, a total of 14 single-ended raw voltage measurements per projection are obtained and using the DAQ board differential setup, are then converted to 13 differential voltage measurements, when adjacent injection and measuring protocols is used. For the 32 electrodes EIT system the differential measurements are obtained in similar fashion.

The frame rates of the EIT system presented in this study are higher when compared with other EIT systems used in medical applications (Goharian et al. 2008), and even when comparing with recent DSP based electrical tomographic systems (Wilkinson et al. 2006; Holliday, Williams, and Lucas 2005; S. Zhang et al. 2006).

For the data acquisition and digital addressing of the multiplexing module (see Section 3.2.4) National Instruments® NI USB-6255 Multifunction Data Acquisition and NI USB-6509 High-Density Industrial Digital I/O boards were employed (see Figure 3.16).

Figure 3.16 – National Instruments® NI USB-6255 Multifunction Data Acquisition (Left) and NI USB-6509 High-Density Industrial Digital I/O (Right).

3.2.6. INJECTION AND MEASUREMENT PROTOCOLS

The way electrodes are combined for introducing the electrical signal into the domain Ω is designated by Injection Protocol. In the literature thorough studies on injection and measurement protocols or patterns can be found. There are two main strategies in the data collection with the first being the so called two electrode method in which the voltages are measured from the same electrodes through which the signal is injected. The other strategy is called the four electrode method where the signal is injected through some electrodes and the voltages are measured from the remaining electrodes. This strategy has the advantage of minimizing error in voltage measurement resulting from the contact impedances that are present in the two electrode method (Molinari 2003; M. Vauhkonen 1997).

For the four electrode strategy the most widely used methodologies are summarized below (Molinari 2003; M. Vauhkonen 1997; Harikumar, Prabu, and Raghavan 2013):

a) Adjacent or Neighbouring Pattern: where the signal is injected through neighbouring or adjacent electrodes and the resulting electrical potential differences are measured in the remaining pairs of electrodes, in a similar adjacent combination. The neighbouring pattern results in a non-uniform electrical current density since most of the injected signal moves near the domains' boundary. As a result, the sensitivity will be reduced in at the centre of the domain. Figure 3.17 shows the adjacent strategy for a 16-electrode EIT system with a circular domain surrounded by 16 surface electrodes named as the electrode 1 to electrode 16. In adjacent method, the first projection is P1, the signal is injected through electrode 1 and 2 and the electrical potentials or voltages differences (V1,V2,V3, . . ., V13) are measured sequentially with 13 electrode pairs 3–4, 4–5, . . . and 15–16. Voltages are not measured between pairs (16-1), (1-2), or (2-3) (see Figure 3.17 (a)). Therefore the first current projection (P1) gives 13

differential voltage data. In second current projection (P2) a similar procedure takes place but with an increment of one electrode (see Figure 3.17 (b)) and so forth for the remaining projections. The adjacent method provides N^2 measurements, where N is the number of electrodes.

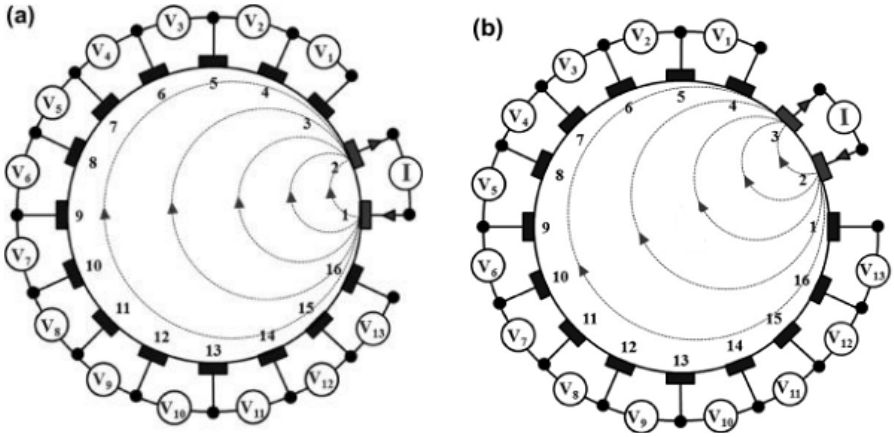

Figure 3.17 – Adjacent Current driven patterns (a) first current projection (P1) (b) second current projection (P2) (adapted from (Harikumar, Prabu, and Raghavan 2013)).

However, in order to circumvent the issue of unknown contact impedance, the voltage is not measured at the current injecting electrode so the number of measurements is reduced to N (N −3). In this study this was the pattern chosen.

b) Opposite or Polar Pattern: in this pattern the signal is injected through opposite electrodes and the electrical potential is measured with respect to one reference electrode adjacent to the injecting electrode. This method gives the same amount of independent measurements as neighbouring method with the advantage of a more uniform electrical current density and hence good sensitivity at the centre of the domain. In the first current projection (P1) of the opposite method (see Figure 3.18 (a)) the signal is injected through electrodes 1 and 9 and the differential voltages (V1, V2, V3, . . ., V13) are measured sequentially from 13 electrode pairs 2–3, 2–4, . . . and 2–16 considering the electrode 2 as the reference. Hence the P1 gives 13 differential voltage

data. Those measured 13 differential voltages are ten used to obtain the 12 differential potential voltages which will be feed to the reconstruction algorithm (pairs 2-3, 3-4, 4-5, 5-6, 6-7, 7-8, 10-11, 11,-12, 12-13, 13-14, 14-15, and 15-16). The second current projection (P2), the current is injected through electrodes 2 and 10 as shown in Figure 3.17 (b) and the differential voltages (V1,V2, V3,..., V13) are measured sequentially from the 13 electrode pairs 3–4, 3–5, . . . and 3–1 (see Figure 3.18 (b)) considering electrode 3 as the voltage reference electrode. Hence the second current projection gives 13 differential voltage data. Once again the measured 13 differential voltages are then fed to the reconstruction algorithm (pairs 3-4, 4-5, 5-6, 6-7, 7-8, 9-10, 11,-12, 12-13, 13-14, 14-15, 15-16, 16-1). This process is repeated until current has been injected between all 16 pairs of electrodes. Therefore in the opposite method, a complete scan of a 16 electrode EIT system yields 16 × 13 = 208 voltage measurements of which half (104) are independent. Thus the opposite method suffers from the disadvantage that for the same number of electrodes, the number of available current injections that can be applied is less than for the adjacent method (Harikumar, Prabu, and Raghavan 2013);

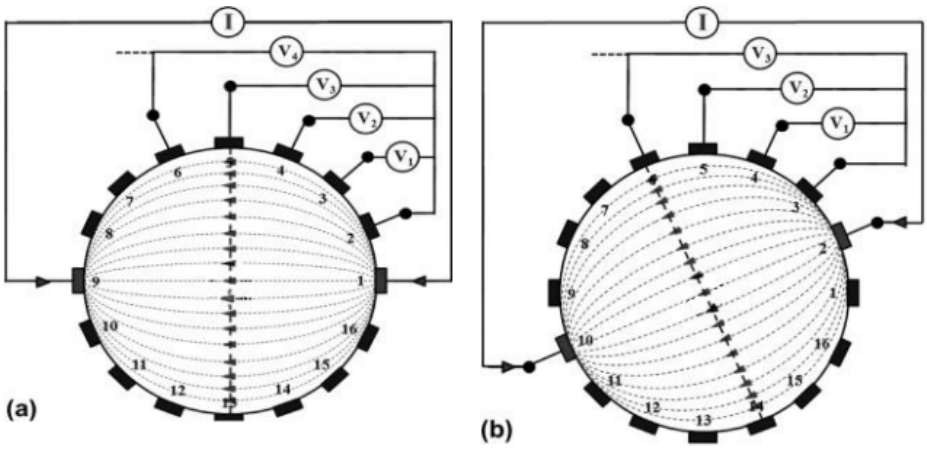

Figure 3.18 – Opposite current Driven pattern (a) first current projection (P1) (b) second current projection (P2) (adapted from (Harikumar, Prabu, and Raghavan 2013)).

c) Cross or Diagonal Pattern: The cross or diagonal pattern is rarely used. It is a combination of the previous two patterns in which one electrode, for instance electrode 1, serves as a reference and the signal is injected successively in the remaining electrodes. With each electrode pair the electrical potential is measured with respect to electrode 1 from all the electrodes except the electrode where the signal is being injected. Hence, in the (P1) projection the signal is injected through electrodes 16 and 2 and the differential voltages (V1, V2, V3,. . ., V13) are measured sequentially with 13 electrode pairs 1–3, 1–4,. . . and 1–15 (see Figure 3.19 (a)) considering electrode 1 as the voltage reference. Therefore the cross method gives 13 differential voltage data. In the (P2) projection (see Figure 3.19 (b)) the signal is applied to electrodes 16 and 4 while 13 voltage measurements are taken using electrode 1 as the reference. This is repeated for currents injected between electrodes (16-4), (16-8), (16-10), (16-12), (16-14). The entire procedure yields 7 X 13 = 91 measurements. The entire procedure is repeated once more, with the reference electrodes changed to electrodes 3 and 2. Therefore current is applied between electrode 3 and electrodes 5, 7, 9, 11... 1, with voltage measured at the other 13 electrodes with electrode 2 as a reference. This procedure gives a further 91 differential voltage measurements. From these 91 + 91 = 182 measurements, only 104 data are independent. The cross method does not have as good a sensitivity in the periphery as does the adjacent method, but has better sensitivity over the entire region;

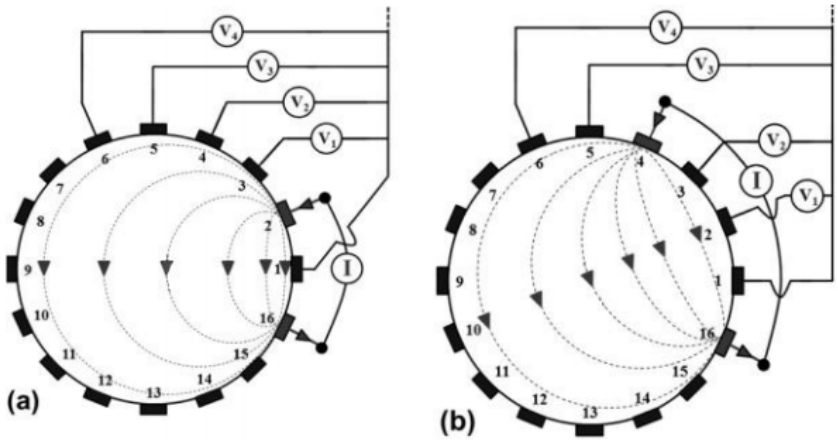

Figure 3.19 – Cross current driven pattern (a) first current projection (P1) (b) second current projection (P2) (adapted from (Harikumar, Prabu, and Raghavan 2013)).

Beyond the three electrode aforementioned strategies, with the signal being injected with a pair of electrodes and the differential electrical potentials being measured between different pairs of electrodes, some authors employed the Trigonometric or Adaptive Pattern (Harikumar, Prabu, and Raghavan 2013; Gisser, Isaacson, and Newell 1987) where the signal is injected on all electrodes and voltages are measured on all electrodes. For instance, since the signal flows through all electrodes simultaneously for a 16-electrode EIT system thus 16 independent signal injectors would be needed. The electrodes can be fed a current from $-I$ to $+I$, allowing different current distributions. In this strategy the boundary electrical potentials are measured with respect to a single grounded electrode, i.e., this strategy produces 15 independent electrical potential or voltage measurements. The trigonometric pattern allows eight different projections yielding $8 \times 15 = 120$ independent voltage data. The obvious disadvantage of this method is that current drivers are needed for each electrode and the unknown contact impedance will have an effect on the reconstruction.

3.2.7. RECONSTRUCTION ALGORITHM & HARDWARE CONTROL

The images reconstructed in this study using the gathered data with the boundary electrodes were attained by means of the open source software EIDORS (Electrical Impedance and Diffuse Optical reconstruction Software)

Versions 3.3 to 3.5 (Borsic, Lionheart, and Polydorides 2004; Nick Polydorides and Lionheart 2002). EIDORS employs MATLAB® based coding for image reconstruction. EIDORS is used to reconstruct the images from electrical or diffuse optical data which is developed with Gauss-Newton method. Forward problem and inverse problems are solved with a Finite Element Method (FEM). The subroutines written for the image reconstruction algorithm can be found in Appendix B.

Moreover, the hardware was controlled by means of an application developed using National Instruments® LabVIEW Software Version 8.6, which allowed for signal generation and acquisition as well as injection protocol handling. This code is given in Appendix B.

3.3. FLOW LOOP II – KTH MEKANICS

3.3.1. INTRODUCTION

A previously existing flow loop in the Mekanics Department at KTH Royal Institute of Technology in Stockholm, Sweden, was used with some modifications. This flow loop possesses both NMRI and UPV apparatus that allow for flow characterization and visualization. The flow data attained with these experimental techniques were the vertical and horizontal velocity profile for both liquid and solids using the MRI and UPV, respectively. Additionally, data for the pressure drop and flow rate variables were also acquired. The tests were conducted for a series of increasing flow rates and spherical glass particles concentrations and sizes. Beyond the data acquired with these experimental techniques it was possible, for a brief period of time at the KTH, to employ the EIT apparatus described in Section 3.2 to obtain data regarding the distribution of particles in the pipe section. The goal is to compare this experimental data to numerical simulations results for CFD modelling validation (see Chapter IV).

3.3.2. FLOW LOOP II DESCRIPTION

The tests were performed in the joint recirculatory pipe flow facility of KTH

Royal Institute of Technology and Innventia AB in Stockholm Sweden (see Figure 3.20). Two different configurations were assembled to perform tests for two different internal pipe diameters, 34 mm and 50 mm. The test sections of the flow loop for both configurations were built from cylindrical Perspex® piping possessing a total length of 7.0 m which allows the flow to be fully developed at the measuring sections. This test section can be switched allowing for testing to be done on different pipe diameters.

Additionally, for both configurations, an open tank with an internal diameter of 0.37 m capable of holding approximately 100 litres in volume served as a re-circularization reservoir. The pumping system consisted of an ITT 2.0 kW variable frequency drive (ABB ACS 550) centrifugal pump (Flygt pump 3102 - 135 mm impeller). The pressure drop was acquired using a Fuji Electric FCX-AII T-type differential pressure transducer with model number FKC-22.

Figure 3.20 – Images of the flow loop at KTH Mekanics.

Flow rate was measured with an ABB (or former Fischer & Porter) magnetic flowmeter model number 10DS3111. The flow was diverged and then re-converged with a flow splitter positioned at the upstream end of the test section. This served to minimize any effects such as swirl resulting from the approaching flow to the test section.

In the 34 mm internal diameter test configuration, which was employed initially, the MRI measurement section was located 4.7 m downstream from the flow splitter or an equivalent 147 pipe diameters (see Figure 3.20). The UPV measurement section was located 1.0 m further downstream the MRI equipment. The pressure transducers were placed 2.14 meters apart from each other with the second transducer placed before the UPV probes (see Figure 3.21).

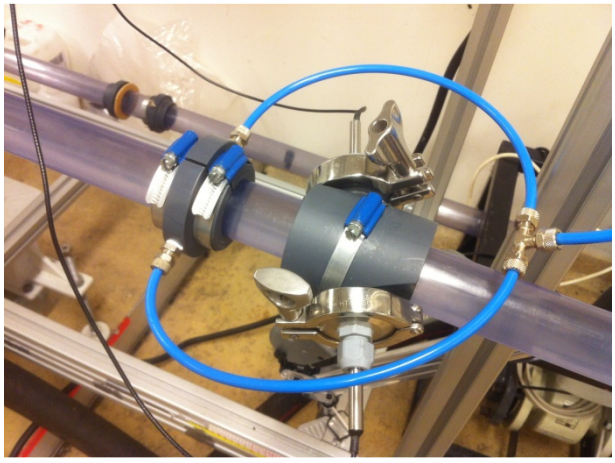

Figure 3.21 – UPV probes for the 34 mm pipe utilized for the data acquisition at KTH.

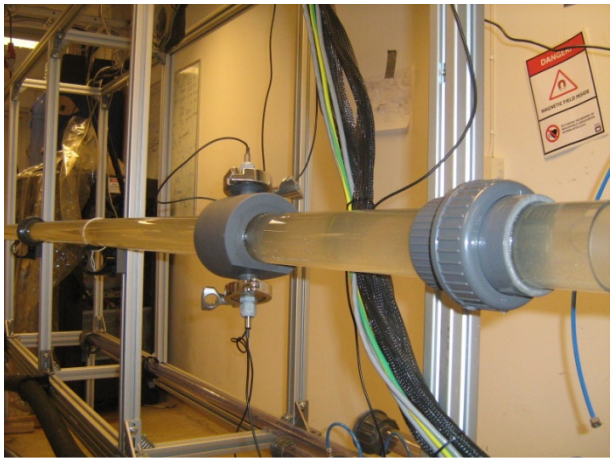

Figure 3.22 – UPV probes for the 50 mm pipe utilized for the data acquisition at KTH.

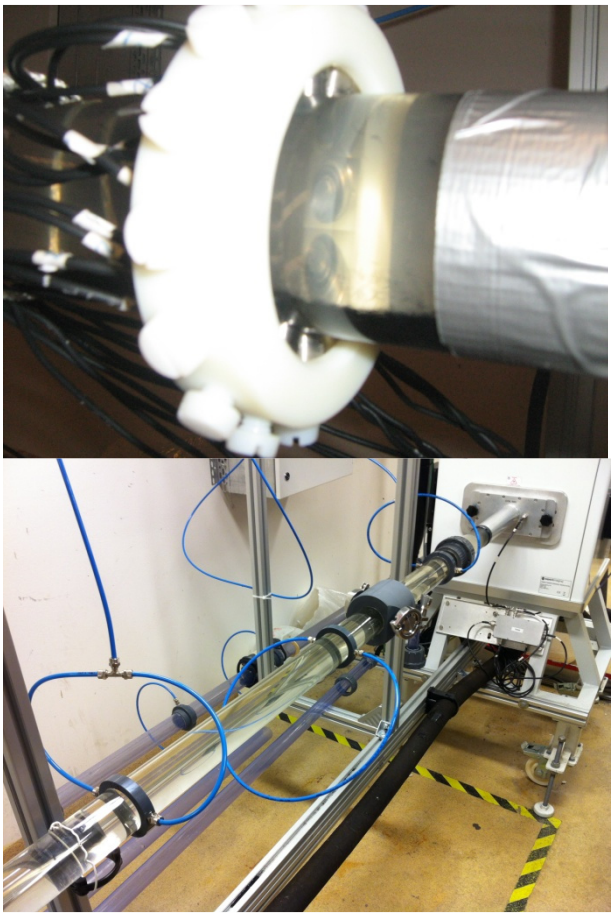

Figure 3.23 – EIT electrode ring (Top) and pressure transducer (Bottom) for the 50 mm pipe utilized for the data acquisition at KTH.

In the 50 mm internal diameter test configuration the UPV measurement section was located 3.5 m downstream from the flow-splitter (see Figure 3.22), the MRI measurement section is located 4.7 m downstream from the flow splitter or an equivalent 147 pipe diameters and the EIT was mounted at an additional 1.0m downstream of the MRI (see Figure III.31). The pressure transducers were upstream the MRI apparatus and were apart from each other by 1 m (see Figure 3.23). MRI measurements were made in both the vertical and horizontal planes while UPV measurements were collected along the horizontal plane. The EIT provided 2D images of the distribution of particles in the pipe cross section.

The schematics of the two flow loop configurations, 34 and 50 mm internal diameters pipes, can be seen in Figure 3.24.

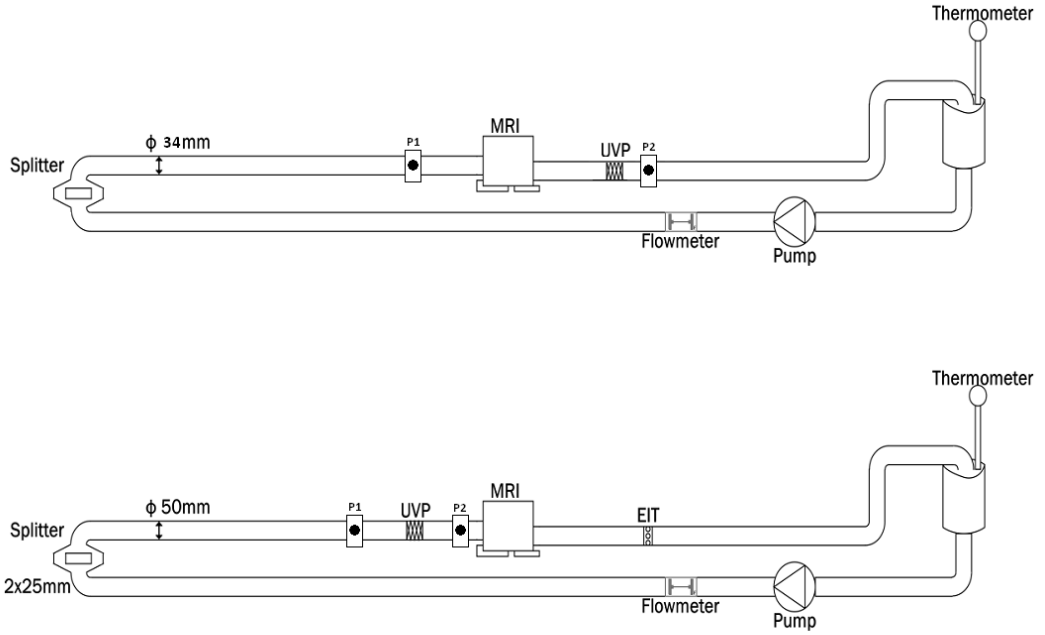

Figure 3.24 – Flow loop schematics for 34 (Top) and 50 (Bottom) mm.

3.3.3. EXPERIMENTAL CONDITIONS & PARTICLE DATA

Similarly to the initial tests performed in Coimbra, a few minutes were allowed to pass for the flow to be stabilized. The solid-liquid suspensions were composed of Type S Silibeads® spherical glass beads, provided by Sigmund Lindner GmbH, and tap water.

Table 3.2 – Solid-liquid suspensions data for the performed tests at KTH Mekanics.

	Silibeads Glass beads – Type S		
	(34mm pipe)	**(34mm pipe)**	**(50mm pipe)**
Particle Density [kg.m^{-3}]	2500	2500	2500
Average Particle Size [mm]	0.15	0.5	0.5
Particle Volumetric Fraction [v/v]	0.0 to 0.03	0.0 to 0.03	0.0 to 0.05
Flow rate [dm^3.s^{-1}]	0.0 to 2.0	0.0 to 4.0	0.0 to 2.0

The spherical glass beads sizes, concentrations and flow rates ranges employed are summarized in Table 3.2. In Appendix C additional data for the

size distribution of the particles can be found.

3.3.4. NUCLEAR MAGNETIC RESONANCE IMAGING EQUIPMENT

Nuclear Magnetic Resonance (NMR) imaging employs a magnetic field to non-invasively obtain a response from nuclei. This phenomenon is described by the Larmor equation

$$\omega_L = \gamma B_0 \tag{3.3}$$

In Equation 3.3 ω_L is the resonance or Larmor frequency, B_0 is the uniform static magnetic field strength and γ the gyromagnetic ratio.

In fact, the number of nuclei sufficiently sensitive to be characterized by NMRI is rather small. Protons are, however, quite sensitive to NMR, so for systems containing ^{1}H nuclei, i.e., large quantities of water, it becomes possible to attain a quantifiable signal-to-noise ratio. Thus, this imbues NMRI with the following advantages as a flow measurement technique:

i. the ability to measure the behaviour of water independently from the behaviour of solids (assuming no or relatively little H^1 is carried within the solids);
ii. independent of optical opaqueness and/or concentration of solids in the system;
iii. non-invasiveness;

Obtaining spatial resolution is done by applying a linear magnetic gradient, G, to the spatial domain so that the Larmor frequency becomes

$$\omega_L = \gamma(B_0 + \mathbf{G} \cdot \mathbf{r}) \tag{3.4}$$

where $\mathbf{r}$ is the position vector and $\mathbf{G}$ the magnetic gradient vector.

In a small volume of magnetic spins flowing at a constant average velocity, U, the time dependent Larmor frequency can be written as

$$\omega_L(t) = \gamma(B_0 + \mathbf{G} \cdot [\mathbf{v}t - \mathbf{r_0}]) \tag{3.5}$$

in which $\mathbf{r_0}$ stands for the initial position vector. In the surveyed volume the signal intensity is defined as the volume integral of the product of the local magnetic spin density, $m(r)$ and the instantaneous phase, $\psi = \omega_L \cdot t$.

$$s(t) = \int_V m(r) e^{2\pi i \omega_L(r) t} \, d\vec{r} \tag{3.6}$$

Using the previous relationships the phase for flowing spins is proportional to the velocity, U, which is encoded as an additional 'dimension', the local spectrum of which is obtained by a Fourier-Transform along this dimension. The objective is to find the axial velocity profile, and thus, the frequency-position gradient is applied only in the direction normal to the flow and phase-flow encoding is applied in the streamwise direction only.

For the NMRI flow characterization in this study, a gradient-echo pulse sequence was used (see Figure 3.25). A detailed description of this technique is found in the literature (Gladden 1994). The technique can be summarized as selective excitation of a streamwise slice of fluid and a 90° radiofrequency (RF) pulse rotating the magnetization orthogonally. The first gradient pulse is then applied for a duration, δ, giving each spin a spatially dependent phase offset. A 180° RF pulse is then applied rotating each spin isochromat (a microscopic group of spins, which resonate at the same frequency) through 180 degrees. A second gradient pulse is applied at a time Δ after the first one to obtain a phase offset relative to the fluid displacement. A frequency position encode gradient is applied at the end during readout step.

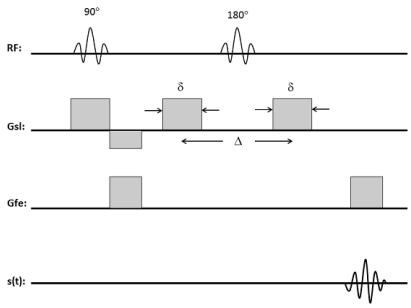

Figure 3.25 – Radiofrequency and magnetic pulse sequence used to obtain NMR velocity profile images for the flow of water within the pipe. Gsl is the slice selection gradient and Gfe is the frequency select gradient.

Throughout the experiments, the phase dispersion is sensitive to the mean and fluctuating velocities; therefore the duration and separation times for the phase flow encoding gradients need to be adjusted manually. For the higher speed flow, i.e., for $U = 2.2\ \mathrm{m.\,s^{-1}}$ profiles were averaged over 128 individual measurements and 64 measurements were averaged for slower flows. In all cases the slice was 10 mm long and the gain was on the order of 1000 dB. The MRI system consists of a 1 Tesla permanent magnet connected to a Bruker NMR spectrometer (see Figure 3.26). A 60 mm RF coil, calibrated to 43.5 MHz is used for transmission/reception. The entire system has been provided by Aspect Imaging® and is controlled using NTNMR® software. Devoted measurement and data processing software was developed at the University of California Davis and further adapted in-house for post-processing.

Figure 3.26 – Images of the NMR apparatus provide by Aspect Imaging present at KTH Mekanics.

3.3.5. ULTRASOUND DOPPLER VELOCIMETRY PROFILING IMAGING EQUIPMENT

Ultrasound Doppler Velocimetry Profiling (UVP), also designated Ultrasonic Pulse Velocimetry (UPV), was utilized to measure the velocity of the particles. UPV fundamentals have been well documented in the literature (Yasushi Takeda 1995; Y. Takeda 1999).

In this technique the basis are ultrasonic pulses that are emitted from a transducer and reflected by particles moving with the fluid, back to the transducer. The echo scattered by the particles in the measuring beam is Doppler shifted due to the motion of the particles. The echo is detected by the

transducer as a function of time after each pulse emission. A number of consecutive pulse trains are emitted and received, and the echo frequency is reconstructed and the velocity profile calculated by means of this frequency shift.

For multiphase flows UPV presents the following advantages:

i. provides position and velocity of reflecting particles in the fluid;
ii. insensitive to optical opaqueness;
iii. non-invasive;

In the studies presented in this manuscript a 4 MHz transducer with a 5 mm active diameter element (maximum resolution of 0.37 mm) and a minimum measuring distance (near field) of 16.9 mm was used. After this minimum, the beam diverges with a half-angle of 2.2°. The pulse repetition frequency was 10.762 kHz with 128 spatial measurement channels. Data was acquired over 768 measurement cycles to obtain a velocity distribution profile and mean data was obtained by averaging over 64 profiles, providing a spatial and velocity resolutions of 0.37 mm and 3.8 mm/s, respectively.

The transducer was flush mounted to the inside pipe wall at a 70 degree angle to the flow and was in direct contact with the suspension (see Figure 3.27).

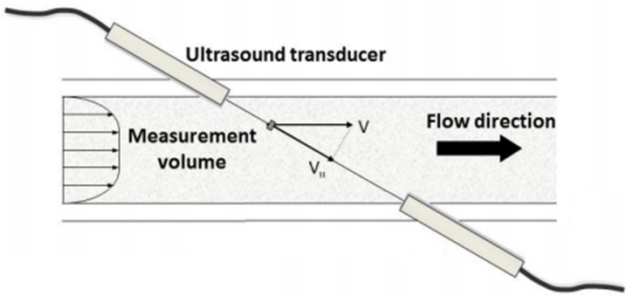

Figure 3.27 – General set-up for the UPV probe system.

With this approach, the effects of attenuation and wall reflections were reduced. The UPV hardware was provided by MetFlow® and the software, FlowViz®, was developed by SIK in Gothenburg, Sweden.

CHAPTER IV

CFD MODELLING

4. CHAPTER IV – CFD MODELLING

In this Chapter the Computational Fluid Dynamics (CFD), numerical modelling of multiphase flows is approached. The distinction between an Eulerian or Lagrangian numerical model is discussed as well as the choice of an adequate numerical model. A brief description of the Finite Element Method (FEM) implementation in COMSOL Multiphysics® numerical models is presented and the Mixture Model formulation is derived. The drag correlations employed in this study for assessing the relative velocity between phases are also presented. Furthermore, the High and Low Reynolds k-ε Turbulence models equations are introduced and modifications implemented in the Mixture Model are also discussed.

4.1. CHOOSING A NUMERICAL MODEL

In Section 2.4 a review of the existing numerical approaches has been presented as well as their respective advantages and drawbacks.

In the work presented in this manuscript an Euler-Euler methodology, also known as “Dense Phase approach” (see Figure 4.1), has been favoured. This methodology was the natural choice for the work developed throughout this thesis, with concentrated solid-liquid suspension flows. When dealing with millions of particles in a system solving the equations for each particle individually becomes computationally prohibitive while dealing with the flow variables with an average approach cuts the computational demands in both cost and time.

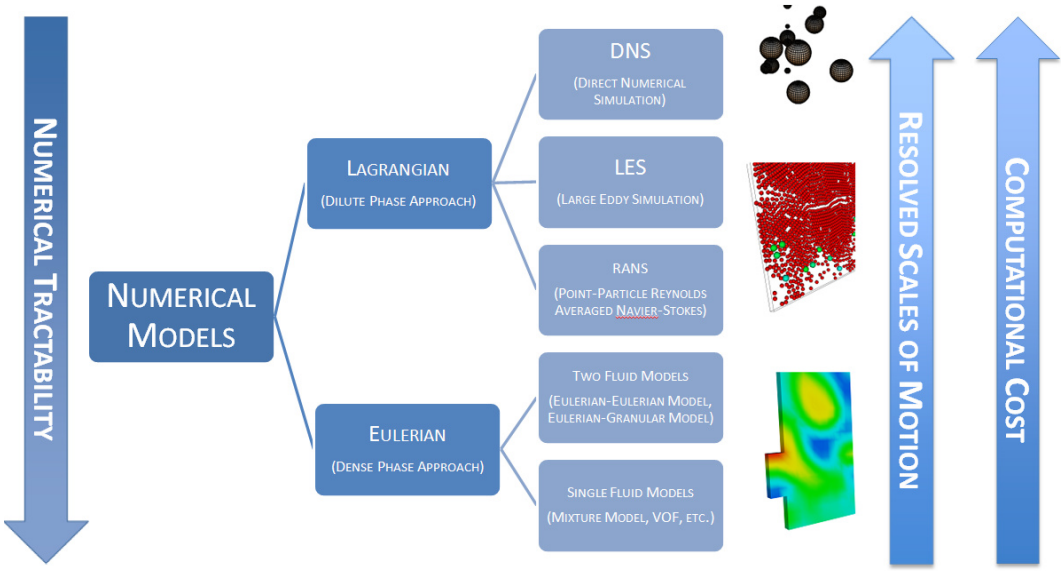

Figure 4.1 – Numerical models comparison for modelling particle flow (adapted from (Oevermann, Gerber, and Behrendt 2008)).

In the Eulerian approach, the two components are interacting with each other in a way that the behaviour of each phase influences the other and are considered to be at the same location at the same time (Massoudi 2010; Balachandar and Eaton 2010; Sommerfeld, Wachem, and Oliemans 2008). The volumetric fraction is of paramount importance as this variable will dictate the amount of each phase at a given time and place. The Eulerian models provide an averaged depiction of a multiphase system, and in the literature a wide number of averaging processes can be found, namely time, volume or ensemble based averaging. With this averaging methodology two advantages arise, one being that with the averaging process all the forces are inherently present in the model, while the other is that the computational cost is not dependent on the number of particles, making the Eulerian approach more suited for large systems with a great number of particles.

4.2. FINITE ELEMENT METHOD IN COMSOL

HISTORICAL BACKGROUND

Since the 1950s, with the inception of the digital computer, computational fluid dynamics (CFD) analysis slowly arose to become a ubiquitous and indispensable tool for engineers and scientists alike. Finite Difference Method

(FDM), Finite Element Method (FEM) and Finite Volume Method (FVM), have, historically (Bakker 2006), been the most used in CFD analysis: however, there are other approaches like Spectral Methods, Boundary Element, Vorticity based methods, Lattice -Boltzmann, etc.

The first numerical method utilized in CFD studies was the finite difference method (FDM) in 1910 by L. F. Richardson, at the Royal Society of London (Chung 2002; Bakker 2006), for the stress analysis of a masonry dam. It is believed that this method was introduced by Euler (Ferziger and Perić 2002) in the 18th century. At one point in time this was the most widely employed method for fluid dynamical studies due to its simplicity and ease of application for simple geometries. The drawback of this method is the lack of conservation of momentum, mass and energy in coarse grids as well as the restriction to simple geometries that limits it when dealing in modern applications with increasingly complex geometries (Ferziger and Perić 2002).

Zienkiewicz & Cheung, in 1965 (Chung 2002; Zienkiewicz and Cheung 1965) delivered the first application of Finite Element Method (FEM) to CFD studies. When compared to FDM, the FEM is more complex and more time consuming in its calculations; however, with the ever increasing computational capabilities, this limitation decreases and becomes lesser every day. In FEM analysis the domain is divided in elements, often unstructured, with triangular and quadrilateral shapes for 2D problems and in tetrahedral and hexahedral shapes for 3D studies. The feature that defines the FEM is a weight function that multiplies the equations before integration throughout the domain (Ferziger and Perić 2002; Arnesen 2010). To assure solution continuity across the elements, 2D or 3D, a shape function is utilized in each element to approximate the solution. One of the most important assets of the FEM is its ability to deal with arbitrary geometries as seen in the literature by the comprehensive number of documents regarding the construction of meshes for FEM (Ferziger and Perić 2002), in which it is demonstrated that the meshes can be easily refined and each element subdivided with simplicity. The main drawback, typical of methods that

employ unstructured meshes, is that the matrices of the linearized equations are not so well structured as those for regular meshes, proving difficult to reach convergence and an efficient solution (Ferziger and Perić 2002; Arnesen 2010).

In recent years, FVM has witnessed an increase of its application in CFD studies (Loth 2010), which it is a reflect of its simpler data structure. Its formulation borrows from both FDM and FEM. This method uses the integral form of the conservation equations as a starting point. The domain is split into control volumes and the equations are applied to each control volume; then at the centroid of each volume the variables are calculated and an interpolation is used to express the variables at the control volume surface as a function of the centroid values previously determined. The FVM handles any type of mesh, regular/structured or unstructured, and it behaves quite accurately in complex geometries. The mesh only defines the boundary of the control volumes and can be unrelated to the coordinate system (Ferziger and Perić 2002); due to its conservative construction, resulting from the surface integrals representing the convective and diffusive fluxes shared by the control volumes at the boundary, it has become quite popular in engineering applications. The main disadvantage of the FVM, resulting from the three kinds of approximations employed (interpolation, differentiation and integration), is the difficulty to code three dimensional methods of higher order other than second (Ferziger and Perić 2002).

In the above text the similarities and differences between the three methods have been explored. A simple summary is presented in the list below (F. White 1991; Rannacher 2000; Segal 2012; Arnesen 2010):

A. FDM

i. ease to formulate;

ii. meshes need to be structured for all dimensions, with curved boundaries transformed in orthogonal coordinates so FDM analysis can be applied;

iii. Neumann boundary conditions can only be approximated and not enforced;

B. FEM

i. principles and formulation involve complicated algebra;

ii. complex geometries and unstructured meshes are easily approached without the need of coordinate system transformation;

iii. Neumann boundary conditions are exactly enforced;

C. FVM

i. FEM or FDM based formulations;

ii. surface integrals of normal fluxes guarantee the conservation of properties in the domain;

iii. complex geometries and unstructured meshes are easily approached without the need of coordinate system transformation;

FINITE ELEMENT METHOD IN COMSOL MULTIPHYSICS

As stated above, the Finite Element Method (FEM) is a numerical approach to solve partial differential equations (PDE) and, to attain this objective, the PDE is rewritten in its Weak Formulation (Singh 2009; COMSOL Multiphysics 2012; Arnesen 2010; Segal 2012)]. This approach is the basis of FEM formulation in the software package COMSOL Multiphysics®.

To better illustrate the Weak Formulation in COMSOL Multiphysics® a known elliptical PDE, the Poisson Equation, will be used:

$$\Delta u = \nabla^2 u = \frac{d^2u}{dx^2} + \frac{d^2u}{dy^2} = f \text{ , defined on } \Omega \in \mathbb{R}^2 \quad \textbf{(4.1)}$$

Assuming $\Omega = (0,1)^2$, and using Homogeneous Dirichlet boundary conditions, represented by Equations 4.2 and 4.3.

$$\Delta u = \nabla^2 u = \frac{d^2u}{dx^2} + \frac{d^2u}{dy^2} = f \text{ , defined on } \Omega = (0,1)^2 \quad \textbf{(4.2)}$$

$$u(\partial\Omega) = 0 \quad \textbf{(4.3)}$$

$$\partial\Omega = \{(x, y)|x = 0{,}1 \; or \; y = 0{,}1\} \quad \textbf{(4.4)}$$

Equations 4.2 through 4.4 are known as the Strong or Classic Formulation in Finite Elements and it shows no more information than the original PDE. It's a boundary-value problem (Zielínski 2013) composed by the differential equation of the problem, by Neumann boundary conditions (natural conditions imposed on the secondary dependent variable) and by Dirichlet (essential) boundary conditions, that must be satisfied a priori (Zielínski 2013). In most cases solving the PDE directly is quite cumbersome because smooth solutions may not arise to the problem, and incorporating the boundary conditions directly in the Strong Formulation can be an intimidating task. Also, the requirement on the continuity of field variables is higher (Zielínski 2013).

Due to the aforementioned drawbacks of working with the Strong Formulation, the Weak Formulation becomes preferable. The last one reduces the continuity constrictions on the approximation (or basis) functions, thereby allowing the use of easy-to-construct polynomials (for example, widely used Lagrange polynomials): additionally, in the Weak Formulation, Neumann boundary conditions are easily implemented. These are the reasons that explain the popularity of weak formulations in spite of the many drawbacks, as seen in advection dominated fluid flow that require stabilization techniques to get accurate solutions (Singh 2009; Rannacher 2000; Segal 2012; Zielínski 2013).

The Weak Formulation is a re-write of the original PDE, also known as a

variational statement (Singh 2009; Rannacher 2000; Segal 2012; Zielínski 2013), which is achieved by multiplying the PDE by an arbitrary approximation function, called basis or weight, $v(x, y)$, such that

$$v\nabla^2 u = f\, v \tag{4.5}$$

Integrating Equation 4.5 over the domain Ω the following expression is obtained.

$$\int_\Omega v\nabla^2 u = \int_\Omega f\, v \tag{4.6}$$

The first term of Equation 4.6 can be further developed:

$$\int_\Omega v\nabla^2 u = \int_\Omega \nabla(v\nabla u) - \int_\Omega \nabla v \cdot \nabla u \tag{4.7}$$

and applying Gauss Theorem on the first term in the right side of Equation 4.7, a surface integral is transformed into a line integral where dS refers to an infinitesimal line segment.

$$\int_\Omega \nabla(v\nabla u) = \int_{\partial\Omega} \upsilon|_{\partial\Omega=0}\, \nabla u \cdot \hat{n} dS = 0 \tag{4.8}$$

So, Equation 4.7 is reduced to

$$\int_\Omega v\nabla^2 u = -\int_\Omega \nabla v \cdot \nabla u \tag{4.9}$$

and consequently

$$-\int_\Omega \nabla v \cdot \nabla u\, dA = \int_\Omega f\, v\, dA \tag{4.10}$$

Equation 4.10 is the final weak formulation. It is an equivalent to the aforementioned strong form.

Now, there is a need to define a space of functions where the basis or weight functions are integrable. The space defined will be designated has H^1.

$$H^1(\Omega) = \{v: \Omega \to \mathbb{R}: \int_\Omega v^2, \int_\Omega v_x^2, \int_\Omega v_y^2, < +\infty\} \quad \textbf{(4.11)}$$

The space H^1 is explained if the Strong Form requirements are taken into account, where it can be observed that there are two partial derivatives of u, which means that u must be continuously differentiable until at least the second partial derivative. With the new formulations this condition was lowered to only first partial derivatives by transforming one of the partial derivatives into a weight function $v(x, y)$. By doing so one of the biggest advantages of the Weak Formulation is demonstrated.

To attain a solution it's necessary to define a subspace of H^1, designated as X.

$$X = \{v \in H^1(\Omega): v|_{\partial\Omega} = 0\} \quad \textbf{(4.12)}$$

This subspace is straightforward to understand since the Strong Formulation demands that u must be zero at the boundary (Dirichlet boundary condition), so X is a subspace where all functions are zero at the boundary.

The next step regards the approximation of u, where the domain Ω to be studied is divided into several smaller parts (see Figure 4.2) and the approximation is done piecewise over each of these elements and, finally, u is approximated over the whole domain.

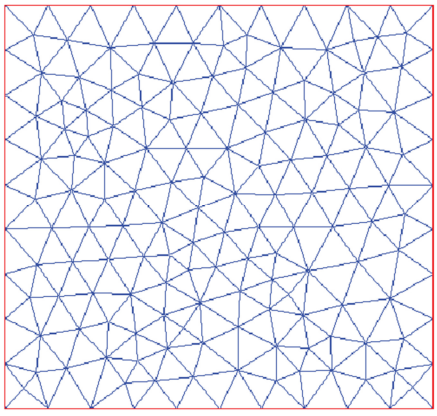

Figure 4.2 – Example of finite element mesh with triangular discretization (adapted from (Singh 2009)).

In Figure 4.2, the 2D domain Ω has been discretized using as elements

triangles with three nodes each and where each of these nodes can be shared by several triangles. The final formulation of the Finite Element Method will provide a system of linear equations with dimension $N \times N$, N corresponding to the number of nodes.

At this point the basis functions need to be defined in the 2D domain. The number of basis functions will be the same as the number of nodes, N. For node, i, the basis function is defined as $\phi_i(x, y) = \delta_{ij}$ and it will be set to zero in all elements that do not share the node i.

Returning to Equation 4.10, the Weak Formulation, the following definitions are implemented simply for convenience.

$$a(u, v) \equiv \int_{\Omega} \nabla v \cdot \nabla u \, dA \tag{4.13}$$

$$l(v) \equiv \int_{\Omega} f \, v \, dA \tag{4.14}$$

And now the Weak Formulation can be rewritten in the form:

$$a(u, v) \equiv l(v), \qquad with \;\; u, v \;\in X \tag{4.15}$$

Defining the approximation function, $\hat{u}$, and the weight function, v, as

$$\hat{u} = \sum_{i=1}^{N} \hat{u}_i \, \phi_i \tag{4.16}$$

$$v = \sum_{j=1}^{N} v_j \, \phi_j \tag{4.17}$$

This is designated as the Galerkin Formulation.

Weak forms seldom provide perfectly accurate solutions because of the reduction in the requirements of smoothness and also due to the weak imposition of Neumann boundary conditions. However, this comparison is valid only in the context, weak vs classical solutions. Weak forms still provide

relatively very accurate results with the mesh refinement, which are extremely good for engineering simulations. Moreover, a solution will be attained even if there is no 'classical' solution, as is usual for problems with complex domains and different materials. The accuracy of a solution in weak formulations depends upon the type of problem being solved. As an example, for elliptic problems the use of only mesh refinement would be sufficient, but when weak formulations are applied to advection-diffusion, as in Stokes or Navier-Stokes flows, the use of efficient stabilization techniques is mandatory, along with mesh refinement, to get accurate results. The accuracy can also be improved by using higher-order shape functions (Li and Wang 2013; Junping Wang and Ye 2013; Zienkiewicz, Taylor, and Nithiarasu 2014).

4.3. MIXTURE MODEL FORMULATION

The Mixture Model is a single fluid Euler-Euler model (Manninen, Taivassalo, and Kallio 1996; Ishii and Hibiki 2011), in which the phases consist of a dispersed phase (solid particles, liquid droplets, etc.) and a continuous phase (liquid). It is translated by a continuity equation for each phase and a momentum equation for the mixture, where an additional term is included to describe the effect of the velocity difference between the phases. The necessity of a strong coupling between phases makes the Mixture Model more suitable for liquid-particle mixtures than for gas-particle mixtures. Its application is conditioned by the following assumptions: each phase density is constant, both phases share the same pressure field, and the velocity difference between phases is determined assuming that pressure, gravity and viscous drag are all balanced.

4.3.1. CONTINUITY EQUATION

The Mixture Model's continuity equation for phase k is given by

$$\frac{\partial}{\partial t}\sum_{k=1}^{n}(\phi_k\rho_k) + \nabla\cdot\sum_{k=1}^{n}(\phi_k\rho_k u_k) = \sum_{k=1}^{n}\Gamma_k \qquad \textbf{(4.18)}$$

Since for rigid particles the total mass is conserved, then

$$\sum_{k=1}^{n} \Gamma_k = 0 \tag{4.19}$$

consequently, the continuity equation for the mixture becomes

$$\frac{\partial \rho_m}{\partial t} + \nabla \cdot \rho_m u_m = 0 \tag{4.20}$$

The mixture density is written as

$$\rho_m = \phi_c \, \rho_c + \phi_d \, \rho_d \tag{4.21}$$

and the mixture velocity is defined as

$$u_m = \frac{\phi_c \, \rho_c \, u_c + \phi_d \, \rho_d \, u_d}{\rho_m} \tag{4.22}$$

4.3.2. MOMENTUM EQUATION

The momentum equation for the Mixture Model for phase k is

$$\begin{aligned} \frac{\partial}{\partial t} \sum_{k=1}^{n} (\phi_k \rho_k u_k) + \nabla \cdot \sum_{k=1}^{n} (\phi_k \rho_k u_k u_k) \\ = -\sum_{k=1}^{n} \phi_k \nabla p_k + \nabla \cdot \sum_{k=1}^{n} \phi_k (\tau_k + \tau_{Tk}) + \sum_{k=1}^{n} (\phi_k \rho_k \mathfrak{g}) \\ + \sum_{k=1}^{n} M_k \end{aligned} \tag{4.23}$$

Combining the notions of mixture density and velocity from Equations 4.21 and 4.22, the second term in Equation 4.23 can be rewritten in the following form

$$\nabla \cdot \sum_{k=1}^{n} (\phi_k \rho_k u_k u_k) = \nabla \cdot (\rho_m u_m u_m) + \nabla \cdot \sum_{k=1}^{n} \phi_k \rho_k u_{mk} u_{mk} \tag{4.24}$$

A new term, u_{mk}, arises: it represents the velocity of phase k, which is a function of the center of the mass of the mixture, i.e., the diffusion velocity

$$u_{mk} = u_k - u_m \tag{4.25}$$

Writing the momentum equation in terms of the mixture variables

$$\frac{\partial}{\partial t}\rho_m u_m + \nabla \cdot (\rho_m u_m u_m) = -\nabla p_m + \nabla \cdot (\tau_m + \tau_{Tm}) + \nabla \cdot \tau_{Dm} + \rho_m \mathfrak{g} + M_m \tag{4.26}$$

where the stress tensors are defined as follows

$$\tau_m = \sum_{k=1}^{n} \phi_k \tau_k \tag{4.27}$$

$$\tau_{Tm} = -\sum_{k=1}^{n} \phi_k \overline{\rho_{Ik} u_{Fk} u_{Fk}} \tag{4.28}$$

$$\tau_{Dm} = -\sum_{k=1}^{n} \phi_k \rho_k u_{Mk} u_{Mk} \tag{4.29}$$

Equations 4.27 to 4.29 represent the viscous stress, turbulent stress and diffusion stress resulting from the velocity between phases, respectively.

Although the pressure for the mixture is defined as

$$\nabla p_m = \sum_{k=1}^{n} \phi_k \nabla p_k \tag{4.30}$$

it is often taken to be equal to the phases pressure, so $p_k = p_m$.

The remaining terms, $M_m = \sum_{k=1}^{n} M_k$ and $\nabla \cdot \tau_{Dm}$ stand for the surface tension force and the momentum diffusion stress, respectively, which are a consequence of the relative motion between phases. For rigid particles the surface tension force will be negligible.

4.3.3. CONTINUITY EQUATION FOR A PHASE

Considering an individual phase k and using the diffusion velocity equation (Equation 4.25), in order to obtain the phase velocity from the continuity

equation (see Equation 4.18), ensues the following expression.

$$\frac{\partial}{\partial t}(\phi_k \rho_k) + \nabla \cdot (\phi_k \rho_k u_m) = \Gamma_k - \nabla \cdot (\phi_k \rho_k u_{mk}) \tag{4.31}$$

Considering constant densities and that phases changes are not occurring, Equation 4.31 can be simplified in the following manner

$$\frac{\partial}{\partial t}\phi_k + \nabla \cdot (\phi_k u_m) = -\nabla \cdot (\phi_k u_{mk}) \tag{4.32}$$

The right side term represents the diffusion of the particles due to the phase slip. Equation 4.32 is sometimes referred as the diffusion equation (Manninen, Taivassalo, and Kallio 1996; Ishii and Hibiki 2011) and the Mixture Model as the Diffusion Model.

However, in reality, the diffusion velocity has to be obtained from the relative (slip) velocity which is defined as the velocity difference between the velocities of the dispersed and continuous phases.

$$u_{ck} = u_k - u_c \tag{4.33}$$

And the diffusion velocity of another dispersed phase, l, can be defined in terms of the relative velocities

$$u_{ml} = u_l - u_m = u_{cl} - \sum_{k=1}^{n} c_k u_{ck} \tag{4.34}$$

The diffusion velocity can be simplified and defined by the following expression if only one dispersed phase, p, is present

$$u_{mp} = \left(1 - c_p\right) u_{cp} \tag{4.35}$$

4.3.4. DIFFUSION VELOCITY

The momentum equations for the dispersed phase in the Mixture Model need a closure for the diffusion velocity. Resulting from the density differences between phases, that impose forces on particles that differ from the forces on

the fluid, the diffusion velocity needs to be determined before solving the momentum and continuity equations.

The balance equation for calculating the relative (slip) velocity can be rigorously derived by combining the momentum equations for the dispersed phase and the mixture. Combining the continuity equation (see Equation 4.18), the momentum equation (see Equation 4.23) of the dispersed phase, k, can be rewritten as follows using gravity as the external force

$$\phi_k \rho_k \frac{\partial u_k}{\partial t} + \phi_k \rho_k (u_k \cdot \nabla) u_k = -\phi_k \nabla p_k + \nabla \cdot [\phi_k (\tau_k + \tau_{Tk})] + \phi_k \rho_k \mathfrak{g} + M_k \quad \textbf{(4.36)}$$

with the equation for mixture assuming the form

$$\rho_m \frac{\partial u_m}{\partial t} + \rho_m (u_m \cdot \nabla) u_m = -\nabla p_m + \nabla \cdot (\tau_m + \tau_{Tm} + \tau_{Dm}) + \rho_m \mathfrak{g} \quad \textbf{(4.37)}$$

In Equation 4.37 the following assumptions were made: firstly, the phase pressures are equal assuring that the pressure gradient in Equations 4.36 and 4.37 is near to zero; secondly, the surface tension forces are negligible and, thus, $M_m = 0$.

The resulting equation for M_k is

$$\begin{aligned} M_k = \phi_k \left[\rho_k \frac{\partial u_{mk}}{\partial t} + (\rho_k - \rho_m) \frac{\partial u_m}{\partial t} \right] \\ + \phi_k [\rho_k (u_k \cdot \nabla) u_k - \rho_m (u_m \cdot \nabla) u_m] - \nabla \\ \cdot [\, \phi_k (\tau_k + \tau_{Tk})] + \phi_k \nabla \cdot (\tau_m + \tau_{Tm} + \tau_{Dm}) \\ - \phi_k (\rho_k - \rho_m) \mathfrak{g} \end{aligned} \quad \textbf{(4.38)}$$

In the previous Equation the definition of diffusion velocity (see Equation 4.25) was employed and now, several simplifications can be done to Equation 4.36:

i. Let's start by assuming that if local equilibrium is obtained then the first order derivative of u_{Mk} will be discarded in the first term.

$$(u_k \cdot \nabla)u_k \approx (u_m \cdot \nabla)u_m \quad \textbf{(4.39)}$$

ii. Next, considering that the viscous and diffusion stresses are very small, and so negligible, then the turbulent stress can be maintained: it represents the turbulent diffusion of the dispersed phase, which is paramount to the model.

Also, for the time being, the turbulent effects will be omitted, and the simplified form of M_k becomes

$$M_k = \phi_k(\rho_k - \rho_m)\left[\mathfrak{g} - (u_m \cdot \nabla)u_m - \frac{\partial u_m}{\partial t}\right] \quad \textbf{(4.40)}$$

As seen above, M_k is a function of the relative (slip) velocity (see Equation 4.33), leading Equation 4.30 to be an algebraic expression for the diffusion velocity, defined in Equation 4.25.

The Mixture Model general formulation consists of Equations 4.20, 4.32, 4.36 and 4.40 in tandem with the constitutive equations for the diffusion velocity and viscous and turbulent stresses.

4.4. CONSTITUTIVE EQUATIONS

In the previous sections the general formulation of the Mixture Model was derived. Next, some formulations of the constitutive equations, needed for the practical application of this model, are presented.

4.4.1. DIFFUSION VELOCITY

Considering a liquid-solid spherical particles suspension, the momentum source term, M_k, can assume the following form

$$M_k = \frac{\phi_k F_D}{V_k} \quad \textbf{(4.41)}$$

with V_k being the particle volume and F_D representing the Drag Force

$$F_D = -\frac{1}{2}A_k\rho_c C_D|u_{ck}|u_{ck} - \frac{1}{2}V_k\rho_c\frac{du_{ck}}{dt} - 6r_k^2\sqrt{\pi\rho_c\mu_c}\int_0^t \frac{\frac{du_{ck}}{ds}}{\sqrt{t-s}}ds \qquad \textbf{(4.42)}$$

On the right side of Equation 4.42 the three terms are the viscous drag, the virtual mass and the Basset history term, respectively. Other forces, that were excluded, are due to the rotation of the particle, to the concentration gradient and to the pressure gradient. Also, within this Mixture Model formulation, the virtual mass and Basset terms are also neglected: these issues will be addressed in the next section.

So, the Drag Force simplifies into viscous drag for a spherical particle

$$F_D = -\frac{1}{2}A_k\rho_c C_D|u_{ck}|u_{ck} \qquad \textbf{(4.43)}$$

and combining Equation 4.43 with Equation 4.40 and 4.41 the expression for the relative (slip) velocity becomes

$$\frac{1}{2}A_k\rho_c C_D|u_{ck}|u_{ck} = V_k(\rho_k - \rho_m)\left[\mathfrak{g} - (u_m\cdot\nabla)u_m - \frac{\partial u_m}{\partial t}\right] \qquad \textbf{(4.44)}$$

4.4.2. VISCOUS STRESS

Deriving the viscous shear stress in the Mixture Model using an incompressible single phase flow formulation as an analogy we obtain

$$\tau_m = \mu_m[\nabla u_m + (\nabla u_m)^t] \qquad \textbf{(4.45)}$$

Although the mixture viscosity is a property that depends on many factors, a good approximation was given by Ishii & Zuber (Ishii and Hibiki 2011).

$$\mu_m = \mu_c\left(1 - \frac{\phi_k}{\phi_{km}}\right)^{-2.5\phi_{km}\mu^*} \qquad \textbf{(4.46)}$$

The particle concentration for maximum packing, ϕ_{km}, has typically the value of 0.62 (Ishii and Hibiki 2011; Manninen, Taivassalo, and Kallio 1996). For solid particles μ^* is 1 and for bubbles or drops assumes the form

$$\mu^* = \frac{\mu_k + 0.4\mu_c}{\mu_k + \mu_c} \quad \textbf{(4.47)}$$

4.4.3. TURBULENCE

The contribution of the turbulence, in the Mixture Model, is found in the momentum equation as part of the general stress term. Through the general stress term, the contribution of fluid-particle interaction term and of the velocity fluctuations of the particle, in other words, the turbulent stresses, are found in the particle momentum equation.

In turbulent conditions, the contribution of fluid particle interaction force is written as

$$M_k = -\beta u_{ck} + M_k' \quad \textbf{(4.48)}$$

M_k' is the fluctatuing part that causes the particle to disperse. Under turbulent conditions, the term M_k' should be added in the right side of Equation 4.48.

In the Mixture Model, the turbulence influence is restricted to the diffusion velocity. This would imply the addition of extra terms in Equation 4.48, due to turbulent stresses and to the fluctuating term of M_k (see Equation 4.40). Rather than developing cumbersome models for these terms, a simpler approach makes use of the inclusion of a diffusion term that denotes the effect of the relative (slip) velocity in the continuity equation of the dispersed phase (see Equation 4.32). The studies by Csanady (1963) and Picart (1986) (Ishii and Hibiki 2011; Manninen, Taivassalo, and Kallio 1996), which were based on the *k-ε* turbulence model, suggested a simple model for the turbulent diffusion of particles in pipe flow.

$$D_{mk} = \frac{\mu_T}{\rho_k \sigma_T} \quad \textbf{(4.49)}$$

where σ_T is the turbulent particle Schmidt number (dimensionless). The particle Schmidt number is usually assumes a value ranging from 0.35 to 0.7 (COMSOL Multiphysics 2012).

4.5. VALIDITY OF THE MIXTURE MODEL

In the general formulation of the Mixture Model several assumptions were made, which will now be analysed in this section.

Equation 4.38 was the result of combining Equations 4.36 and 4.37 whilst using the definition of the diffusion velocity (see Equation 4.25). Some of the terms resulting from this combination were omitted and now are rewritten as follows

$$\phi_k \rho_k \left[\frac{\partial u_{mk}}{\partial t} + (u_{mk} \cdot \nabla) u_{mk}\right] + \phi_k \rho_k [(u_m \cdot \nabla) u_{mk} + (u_{mk} \cdot \nabla) u_m] + \phi_k \nabla \cdot (\tau_m + \tau_{Dm}) - \nabla \cdot (\phi_k \tau_k) \quad \textbf{(4.50)}$$

The used approximation for the local equilibrium requires that the particles rapidly accelerate to the terminal velocity, i.e., the first term in Equation 4.50 must be zero. If a constant body force, acting as gravity on a particle p is considered, then a criterion for neglecting the acceleration is directly connected to the relaxation time of a particle, t_P. In the Stokes regime, t_P is defined by

$$t_P = \frac{\rho_p d_p^2}{18 \mu_m}, Re_p < 1 \quad \textbf{(4.51)}$$

and in the Newton regime (constant C_D) by

$$t_P = \frac{4 \rho_p d_p}{3 \rho_c C_D u_t}, Re_p > 1000 \quad \textbf{(4.52)}$$

where u_t is the terminal velocity. During t_P the particle travels a distance equal to $l_P = t_P u_t / e$, which characterizes the length scale of the acceleration.

If the density ratio ρ_p / ρ_c is small, then the virtual mass and Basset terms in the equation of motion cannot be neglected, especially the Basset term that increases the relaxation time. The length scale $l_P{}'$ is defined as the distance the particle travels until it reaches $u_t(1 - e^{-1}) \approx 0.63 u_t$. An appropriate requirement for the local equilibrium is thus $l_P{}' << L$, where L is a typical

dimension of the system.

The second term in Equation 4.50, in rotational motion, is the Coriolis force, i.e., the radial particle velocity is caused by the centrifugal acceleration which causes in turn a tangential acceleration (Andersson 1996).

In the last two terms of Equation 4.50, the viscous stresses can be considered small when compared with the major contributing terms, what cannot be done inside the boundary layer. The diffusion stress can be neglected within the assumption of local equilibrium.

The application of the Mixture Model is valid if the suspension can be assumed as homogeneous in small spatial scales, i.e., as long as clustering of particles does not occur. Clustering in a scale of the order of the length scale of turbulent fluctuations is a phenomenon typical in gases containing particles with $d_p << 200$ μm. The clustering can result in decrease in the effective drag coefficient, thus increasing the particle relaxation time and the local equilibrium assumption is not valid.

4.6. DRAG CORRELATIONS

The drag coefficient, C_D, is a dimensionless quantity that quantifies the resistance of an object in a fluid environment. It is dependent on the flow regime of the fluid. In the laminar ($Re_p < 1$) and turbulent regimes ($Re_p > 1000$) C_D can be calculated using Stokes Law (see Equation 4.53) and Newton Law (see Equation 4.55), respectively. A closed form solution for the intermediate region ($1 > Re_p > 1000$) is still unavailable and several sphere drag correlations have been proposed in the literature linking C_D to the particle Reynolds number (Re_p), (Schlichting and Gersten 1979; Clift, Grace, and Weber 2005; Peker and Helvaci 2011; Rhodes 2008) having some of them been utilized in this study.

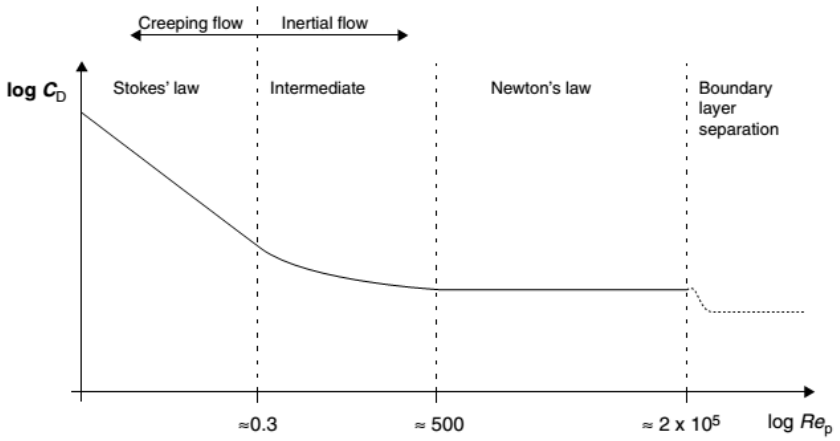

Figure 4.3 – Standard drag curve for motion of a sphere in a fluid (adapted from (Rhodes 2008)).

A survey in the literature reveals several studies on the influence of drag correlations in the accurate numerical representation of particle distribution in vessels. Visuri et al. (2012) employed several models commonly found in the literature to study solid-liquid fluidized systems in spite that those models were specifically developed for other systems: however, they felt that the models extended use to other systems would be of greater value for their study. From the drag models considered, either purely theoretical, experimental or a combination of both, Visuri concluded that in CFD there is no universal drag model since they are case specific. Lareo et al. (1997) has conducted a very thorough review on drag models for both single and multiparticle systems in Newtonian and Non-Newtonian fluids for solid-liquid food flows. Hadinoto & Chew (2010) and Hadinoto (2010) conducted studies on turbulence modulation for dilute solid-liquid systems and showed that the use of different combinations of drag correlations and turbulent closures is needed to correctly identify the dependence of fluid-particle interactions with the Reynolds number. Pang & Wei (2011) analysed key factors in both drag and lift correlations for bubbly flow systems, highlighting the difficulty in choosing adequate drag and lift correlations, and stressing the pivotal importance in properly modelling interphase forces in complex two-phase flows. A similar study for blood flow was undertook by Yilmaz & Gundogdu (2009) where the authors state the importance of powerful drag-

lift models for flows with complex phenomena like deformation, geometry, concentration and aggregation.

As seen in the previous sections, from the force balance equation and momentum source term M_k, the Drag Force plays a pivotal role in the assessment of relative (slip) velocity. The Drag Force depends on the drag coefficient, which in turn, rests on several factors. For small particle Reynolds numbers the drag coefficient obeys the Stokes Law (Toorman 2003; Pang and Wei 2011).

$$C_{D,ST} = \frac{24}{Re_p} \tag{4.53}$$

With the particle Reynolds number defined as

$$Re_p = \frac{\rho_p d_p |u_{cp}|}{\mu_c} \tag{4.54}$$

As the particle Reynolds number increases, Stokes Law underestimates the drag, and additional correlations are needed for an accurate portrayal of the Drag Force.

4.6.1. SCHILLER-NAUMANN CORRELATION

The *Schiller-Naumann* (SN) correlation (Pang and Wei 2011; Clift, Grace, and Weber 2005) employs the following relationship for the calculation of the drag coefficient, C_D.

$$C_D = \begin{cases} \frac{24}{Re_p}\left(1 + 0.15 {Re_p}^{0.687}\right) & if \;\; Re_p < 1000 \\ 0.44 & if \;\; Re_p > 1000 \end{cases} \tag{4.55}$$

Since the particle Reynolds Number depends on the relative (slip) velocity, an implicit relationship arises and must be solved to obtain the slip velocity.

4.6.2. GIDASPOW-SCHILLER-NAUMANN CORRELATION

The *Gidaspow-Schiller-Naumann* (GSN) correlation (Visuri, Wierink, and

Alopaeus 2012; Pang and Wei 2011) is an extension of the aforementioned (SN) correlation; however, contrarily to the (SN) correlation, it was developed to account for the presence of several particles.

$$C_D = \begin{cases} \frac{24}{(1-\phi_s)Re_p}\left(1+0.15\left((1-\phi_s)Re_p\right)^{0.687}\right) & if\ (1-\phi_s)Re_p > 1000 \\ 0.44 & if\ (1-\phi_s)Re_p < 1000 \end{cases} \quad \textbf{(4.56)}$$

4.6.3. HAIDER-LEVENSPIEL CORRELATION

In the literature the *Haider & Levenspiel* (HL) correlation (S. Lahiri and Ghanta 2010) has been employed to a wide range of data from different sources and this correlation showed better results than the remaining.

$$C_D = \frac{24}{Re_p}\left(1+0.1806\,Re_p^{0.6459}\right)+\frac{0.4251}{1+\left(\frac{6880.95}{Re_p}\right)} \qquad if\ \ Re_p < 2.6\times 10^5 \quad \textbf{(4.57)}$$

4.7. TURBULENCE MODELLING

The Reynolds number (see Equation 4.58) of a flow gives a measure of the relative importance of inertia forces (associated with convective effects) and viscous forces (Versteeg and Malalasekera 2007). In fluid systems, under certain experimental conditions, it is perceived that for values below the supposed critical Reynolds number, Re_{crit}, the flow is smooth and neighbouring layers of fluid slide past each other in an organized manner. The flow will be steady as long as the imposed boundary conditions are not altered with time. This regime is termed laminar flow.

$$Re = \frac{\rho DV}{\mu} = \frac{DV}{\nu} \quad \textbf{(4.58)}$$

Above Re_{crit} a complex series of events occurs which ultimately results in a radical change of the flow behaviour. The flow will become fundamentally unsteady, even when constant boundary conditions are imposed. The velocity and all other flow properties vary in a random and chaotic way. This is the turbulent flow regime, and it is characterized by fluctuations in velocity and

pressure in both space and time (Wilcox 2006; Versteeg and Malalasekera 2007). Turbulence causes the appearance of eddies with a wide range of length and time scales that interact in a dynamically complex way. The importance of the reduction or expansion of turbulence in engineering applications is demonstrated by the considerable amount of research effort devoted to the development of numerical methods that capture the important effects due to turbulence (Wilcox 2006; Versteeg and Malalasekera 2007).

In most engineering and industrial applications, CFD users are seldom concerned in resolving all the details of the turbulent fluctuations and stay satisfied with information about the time-averaged properties of the flow, i.e., mean velocities, mean pressures, mean stresses, etc. Thus, the vast majority of turbulent flow computations has been, and for the foreseeable future will continue to be, carried out with procedures based on the Reynolds-averaged Navier–Stokes (RANS) equations, as explained in Section 4.2 (Wilcox 2006; Versteeg and Malalasekera 2007).

Nevertheless, a description of the effects of turbulence on the mean flow is warranted because the time-averaging operation on the momentum equations discards all the details concerning the state of the flow contained in the instantaneous fluctuations. In the development of turbulent flows with the RANS equations the attention is focused on the mean flow and in the effects of turbulence on mean flow properties. Prior to the application of numerical methods, the Navier–Stokes equations are time averaged (or ensemble averaged in flows with time-dependent boundary conditions):

CONTINUITY EQUATION

$$\nabla \cdot \mathbf{U} = 0 \tag{4.59}$$

REYNOLDS EQUATIONS

$$\frac{\partial(U)}{\partial t} + (U\mathbf{U}) = -\frac{1}{\rho}\frac{\partial P}{\partial x} + \nu\,\nabla\cdot(\nabla U) + \left[-\frac{\partial\left(\overline{u'^2}\right)}{\partial x} - \frac{\partial(\overline{u'v'})}{\partial y} - \frac{\partial(\overline{u'w'})}{\partial z}\right] \quad \textbf{(4.60)}$$

$$\frac{\partial(V)}{\partial t} + (V\mathbf{U}) = -\frac{1}{\rho}\frac{\partial P}{\partial y} + \nu\,\nabla\cdot(\nabla V) + \left[-\frac{\partial(\overline{u'v'})}{\partial x} - \frac{\partial\left(\overline{v'^2}\right)}{\partial y} - \frac{\partial(\overline{v'w'})}{\partial z}\right] \quad \textbf{(4.61)}$$

$$\frac{\partial(W)}{\partial t} + (W\mathbf{U}) = -\frac{1}{\rho}\frac{\partial P}{\partial z} + \nu\,\nabla\cdot(\nabla W) + \left[-\frac{\partial(\overline{u'w'})}{\partial x} - \frac{\partial(\overline{v'w'})}{\partial y} - \frac{\partial\left(\overline{w'^2}\right)}{\partial z}\right] \quad \textbf{(4.62)}$$

SCALAR TRANSPORT EQUATION

$$\frac{\partial(\mathbf{\Phi})}{\partial t} + (\mathbf{\Phi}\mathbf{U}) = \nabla\cdot(\Gamma_\Phi\,\nabla\mathbf{\Phi}) + \left[-\frac{\partial(\overline{u'\varphi'})}{\partial x} - \frac{\partial(\overline{v'\varphi'})}{\partial y} - \frac{\partial(\overline{w'\varphi'})}{\partial z}\right] + S_\Phi \quad \textbf{(4.63)}$$

Equations 4.59 to 4.63 represent the Reynolds-averaged Navier-Stokes equations for incompressible flow, where the overbar indicates a time-averaged variable. Similarly, extra turbulent transport terms arise when we derive a transport equation for an arbitrary scalar quantity, e.g. temperature. The time-average transport equation for scalar **Φ** is given by Equation 4.63. So far it has been assumed that the fluid density is constant (Versteeg and Malalasekera 2007).

Some additional terms appear in the time-averaged (or Reynolds averaged) flow equations due to the interactions between various turbulent fluctuations. These six extra turbulent stresses terms, are called the Reynolds stresses: three normal stresses (see Equation 4.64) and three shear stresses

(see Equation 4.65).

$$\tau_{xx} = -\overline{\bar{\rho}u'^2}\ ; \tau_{yy} = -\overline{\bar{\rho}v'^2}\ ;\ \tau_{zz} = -\overline{\bar{\rho}w'^2} \tag{4.64}$$

$$\tau_{xy} = \tau_{yx} = -\overline{\bar{\rho}u'v'}\ ; \tau_{xz} = \tau_{zx} = -\overline{\bar{\rho}u'w'}\ \ ; \tau_{yz} = \tau_{zy} = -\overline{\bar{\rho}v'w} \tag{4.65}$$

These extra terms are modelled with classical turbulence models: among the best known, it can be found the *k*–*ε* model. The computing resources required for obtaining reasonably accurate flow computations are modest, so this approach has been the mainstream of engineering flow calculations over the last decades.

4.7.1. HIGH REYNOLDS *k-ε* TURBULENCE MODEL

The *k-ε* turbulence model is the most widely employed two-equation turbulence model (Wilcox 2006). The formulation of this model was done by Jones and Launder and published in 1972 (Wilcox 2006; Jones and Launder 1972).

The following expressions define the High Reynolds *k-ε* Turbulence Model, which is incorporated in the Mixture Model.

The Turbulent Eddy Viscosity is defined as

$$\mu_T = \rho\, C_\mu\, \frac{k^2}{\varepsilon} \tag{4.66}$$

and the Turbulent Kinetic Energy, k, is given by

$$\begin{aligned} \rho\, \frac{\partial k}{\partial t} + \rho u \cdot \nabla k \\ = \nabla \cdot \left(\left(\mu + \frac{\mu_T}{\sigma_k} \right) \nabla k \right) \\ + \mu_T \left(\nabla u : (\nabla u + (\nabla u)^T) - \frac{2}{3} (\nabla \cdot u)^2 \right) - \frac{2}{3} \rho\, k\, \nabla \cdot u \\ - \rho\, \varepsilon \end{aligned} \tag{4.67}$$

with the dissipation rate of energy, ε, given by

$$\begin{aligned}\rho\,\frac{\partial\varepsilon}{\partial t}+\ \rho u\cdot\ \nabla\varepsilon\\ &=\ \nabla\cdot\left(\left(\mu+\frac{\mu_T}{\sigma_\varepsilon}\right)\nabla\varepsilon\right)\\ &+\ C_{\varepsilon1}\frac{\varepsilon}{k}\,\mu_T\left(\nabla u:(\nabla u+\ (\nabla u)^T)-\frac{2}{3}\,(\nabla\cdot u)^2\right)\\ &-\frac{2}{3}\,\rho\,k\,\nabla\cdot u-C_{\varepsilon2}\frac{\varepsilon^2}{k}\end{aligned} \quad \textbf{(4.68)}$$

The closure coefficients ($C_{\varepsilon1}$=1.44; $C_{\varepsilon2}$=1.92; C_μ=0.09; σ_k=1.0; σ_ε=1.3) were obtained empirically (Wilcox 2006).

Turbulence information should be incorporated into the velocity of the dispersed phase calculation, and this is accomplished through the determination of the turbulent eddy diffusion coefficient D_{md} resulting from Equation 4.49.

4.7.2. JONES-LAUNDER LOW REYNOLDS *k-ε* TURBULENCE MODEL

The High Reynolds *k-ε* Turbulence Model suffers from limitations near the wall for wall-bounded flows since this model does not incorporate the effect of viscosity in this area. To overcome this shortcoming, empirical wall functions are used to connect the turbulent core and the boundary. Although these wall functions perform well for simple flows, they do not support all types of flow conditions independently of its characteristics, such as particle size and concentration, density, viscosity, etc. (Troshko and Hassan 2001).

The Low Reynolds *k-ε* Turbulence Models are an attempt to model directly the influence of viscosity in the flow, through the integration of the turbulence equations all the way to the wall (Costa, Oliveira, and Blay 1999; Lai and Yang 1997; Hrenya et al. 1995). Turbulent flows are modelled, again, using, transport equations for the Turbulent Kinetic Energy k (see Equation 4.70) and the Dissipation rate ε (see Equation 4.71) (with $\tilde{\varepsilon}=\varepsilon-D$ being the pseudo dissipation rate, defined this way for computational convenience, simultaneously allowing setting it equal to zero at the pipe wall), together

with the Prandtl-Kolmogorov turbulent viscosity expression (see Equation 4.69): the three mentioned equations compose the general formulation of the Jones-Launder Low Reynolds *k-ε* Turbulence Model, which was incorporated in the Mixture Model.

The Low Reynolds model strays from the High Reynolds model through the inclusion of viscous diffusion in all the transport equations. The damping functions (Table 4.1) and boundary conditions introduce the local level of turbulence, and, lastly the terms D and E are employed to represent the near-wall behaviour of turbulence (Costa, Oliveira, and Blay 1999; Lai and Yang 1997; Hrenya et al. 1995).

$$\mu_T = \rho\, C_\mu f_\mu\, \frac{k^2}{\varepsilon} \tag{4.69}$$

$$\begin{aligned} \rho\, \frac{\partial k}{\partial t} + \rho u \cdot \nabla k \\ = \nabla \cdot \left(\left(\mu + \frac{\mu_T}{\sigma_k} \right) \nabla k \right) \\ + \mu_T \left(\nabla u : (\nabla u + (\nabla u)^T) - \frac{2}{3} (\nabla \cdot u)^2 \right) - \frac{2}{3} \rho\, k\, \nabla \cdot u \\ - \rho\, \varepsilon - \rho\, D \end{aligned} \tag{4.70}$$

$$\begin{aligned} \rho\, \frac{\partial \varepsilon}{\partial t} + \rho u \cdot \nabla \varepsilon \\ = \nabla \cdot \left(\left(\mu + \frac{\mu_T}{\sigma_\varepsilon} \right) \nabla \varepsilon \right) \\ + f_1 C_{\varepsilon 1} \frac{\varepsilon}{k}\, \mu_T \left(\nabla u : (\nabla u + (\nabla u)^T) - \frac{2}{3} (\nabla \cdot u)^2 \right) \\ - \frac{2}{3} \rho\, k\, \nabla \cdot u - f_2 C_{\varepsilon 2} \frac{\varepsilon^2}{k} + \rho E \end{aligned} \tag{4.71}$$

The Low Reynolds *k-ε* Turbulence Model, incorporated in the Mixture Model, was the Jones-Launder model (JL) (Jones and Launder 1972). It was the first published Low Reynolds model and this was the reason for its choice.

Table 4.1 – Low Reynolds k-ε damping functions and boundary conditions.

f_μ	f_1	f_2	D	E	Re_T	k_{wall}	$\tilde{\varepsilon}_{wall}$
$e^{\left(-\frac{2.5}{1+\frac{Re_t}{50}}\right)}$	1	$1 - 0.3\, e^{(-Re_t{}^2)}$	$2\upsilon\left(\frac{\partial^2\sqrt{k}}{\partial x_j}\right)^2$	$2\upsilon\upsilon_t\left(\frac{\partial^2 u_i}{\partial x_j \partial x_k}\right)^2$	$\frac{k^2}{\nu\,\varepsilon}$	0	0

The closure coefficients used, are the same which were adopted in the High Reynolds k-ε Turbulence Model described previously.

4.7.3. BOUNDARY CONDITIONS

The gradient diffusion term present in the k and ε equations makes them elliptic. In order to attain a unique solution for elliptic equations, certain conditions must be specified for the dependent variable on all the boundaries of the solution domain. Problems requiring data over the entire boundary are called boundary-value problems (Versteeg and Malalasekera 2007).

Inlet

When conceiving a CFD simulation a user seldom has knowledge on the distributions for k and ε at the inlet. To circumvent this lack of information k and ε inlet values for internal flows can be estimated taking the turbulence intensity, T_i, and the characteristic length of the equipment, L, as a starting point, using the following expressions (Versteeg and Malalasekera 2007; Kuzmin, Mierka, and Turek 2007).

$$k = \frac{3}{2}\left(U_{ref} T_i\right)^2 \tag{4.72}$$

$$\varepsilon = \frac{3}{2} {C_\mu}^{3/4} \frac{k^{3/2}}{\ell} \tag{4.73}$$

$$\ell = 0.07\, L \tag{4.74}$$

Outlet & Symmetry Axis

At the outlet, the normal gradients of k and ε are fixed equal to zero, which corresponds to the Neumann ('do-nothing') boundary condition. In the finite

element framework, these homogeneous boundary conditions imply that the surface integrals resulting from integrating by parts the variational formulation, vanish (Kuzmin, Mierka, and Turek 2007; Rannacher 2000).

$$\frac{\partial k}{\partial n} = 0 \; and \; \frac{\partial \varepsilon}{\partial n} = 0 \qquad \textbf{(4.75)}$$

4.7.4. NEAR-WALL TREATMENT FOR TURBULENT FLOWS

One of the most common engineering problems is computing turbulent flows that are influenced by an adjacent wall. The two main effects of a wall are (Bredberg 2000):

i. Damping the wall normal components, making the turbulent flow anisotropic;
ii. Increasing the production of turbulence through the shearing mechanism in the flow;

A boundary layer arises, induced by the presence of the wall, where the velocity changes from the no-slip condition (zero velocity), at the wall, to its free stream value. The variation is usually largest in the near-wall region, where larger gradients in the solution variables, momentum and other scalar transports, occur most vigorously, thus requiring an increased number of grid points near the wall to encapsulate the anisotropy. From Figure 4.4 it can be observed that the viscosity-affected region (the inner layer in this case) can be divided up to three zones (Ariyaratne 2005; Salim and Cheah 2009; Chmielewski and Gieras 2013):

I. Viscous sub-layer ($y^+ < 5$): This is the closest layer to the wall where the flow is practically laminar due to the damping, by the wall itself, of the turbulence effects. Viscosity plays the governing part in momentum and heat or mass transfer;

II. Buffer layer or blending region ($5 < y^+ < 30$): The interim region where effects of molecular viscosity and turbulence are equally important;

III. Fully turbulent layer or log-law region ($30 < y^+ < 200$): This is the outer layer where the boundary layer and the external flow merge. Turbulence plays a major role;

Regarding near-wall treatment for turbulent flows, two types of turbulence models can be highlighted. The first type employs the so-called integration method, which requires an LRN (Low Reynolds Number) turbulence model. In this first category, the models call for a large number of nodes to accurately capture the near-wall anisotropies. From an engineering standpoint, this becomes computationally quite expensive and, as an alternative, a function (Jones and Launder 1972) was instead introduced that bridges the near-wall region, thus significantly reducing the computational requirements. The second type, is designated as Wall Function, and uses an HRN (High Reynolds Number) turbulence model (Bredberg 2000). The Wall Function Method, also known as "Law of the Wall", is strictly valid only in the inertial sub-layer (log-layer), 1D fully developed flow, where the pressure gradient can be neglected. The situations in which all these simplifications are fulfilled are relatively few, and the predictions made, using wall function or HRN turbulence models are thus generally less accurate than those that apply the integrated method of LRN turbulence models (Bredberg 2000).

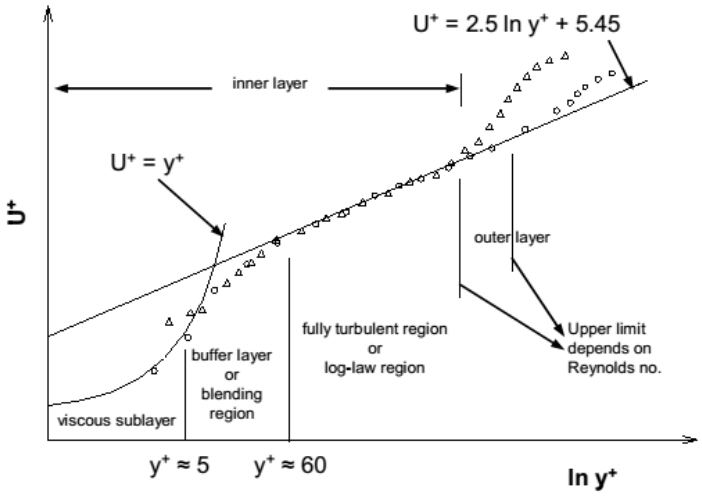

Figure 4.4 – Near-Wall Region in Turbulent Flows (adapted from (Ariyaratne 2005)).

HRN-Models: Standard Wall Function

At high Reynolds number the High Reynolds k-ε turbulence model (Wilcox 2006; Bredberg 2000; Jones and Launder 1972) circumvents the need to integrate the model equations right through to the wall: it uses the Law of the Wall, whereby the mean velocity is taken as a logarithmic function of the distance from the wall in the fully turbulent region. Therefore if the mesh is built so that the first point, where the velocity is calculated, is in the log-law region, then the anisotropy near the wall needs not be modelled.

As mentioned in the previous section, the wide spread use of wall functions stems from the reduced computational requirement, increased numerical stability and convergence speed. To complete the problem statement, we still need to describe the tangential stress as well as the boundary conditions for k and ε at the wall. The wall functions in COMSOL Multiphysics® (COMSOL Multiphysics 2012) are such that the computational domain is assumed to be located a distance y_p from the wall (see Figure 4.5) (Kuzmin, Mierka, and Turek 2007; Versteeg and Malalasekera 2007; Bredberg 2000; Ariyaratne 2005):

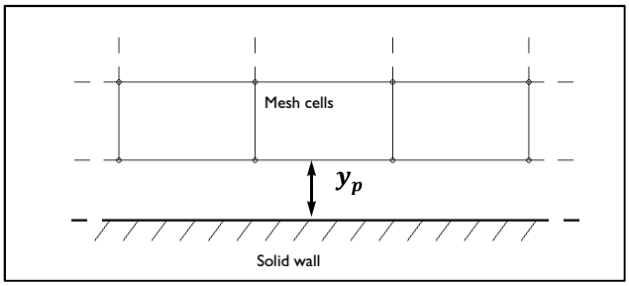

Figure 4.5 – The computational domain is located a distance y_p from the wall for wall functions (adapted from (COMSOL Multiphysics 2012)).

The distance y_p is automatically calculated so that y^+ (see Equation 4.76) equals 11.06 as defined in COMSOL Multiphysics® (COMSOL Multiphysics 2013). This corresponds to the distance from the wall where the logarithmic layer meets the viscous sub-layer (or, to some extent, would meet it if there were no buffer layer in between).

$$y^+ = \frac{\rho\, u_\tau y_p}{\mu} \tag{4.76}$$

In COMSOL Multiphysics® the boundary conditions for the velocity are a no-penetration condition (see Equation 4.77) and a shear stress condition (see Equation 4.78):

$$\boldsymbol{u} \cdot \boldsymbol{n} = 0 \tag{4.77}$$

$$\boldsymbol{n} \cdot \boldsymbol{\sigma} - (\boldsymbol{n} \cdot \boldsymbol{\sigma} \cdot \boldsymbol{n})\boldsymbol{n} = -\rho u_\tau \frac{\boldsymbol{u}}{\mathbf{U}} max(C_\mu{}^{1/4}\sqrt{k}, u_\tau) \tag{4.78}$$

$$\boldsymbol{\sigma} = \mu(\nabla \boldsymbol{u} + (\nabla \boldsymbol{u})^T) \tag{4.79}$$

where Equation 4.79 represents the viscous stress tensor and Equations 4.77 to 4.79 describe the wall functions defined for smooth walls: however, in common engineering applications the wall is seldom smooth (Cebeci 2004) and an additional term is introduced (see Equation 4.80):

$$u^+ = \frac{\mathbf{U}}{u_\tau} = \frac{1}{\kappa}\ln y^+ + B = \frac{1}{\kappa}\ln(Ey^+) \tag{4.80}$$

$$k = \frac{u_\tau^2}{\sqrt{C_\mu}} \tag{4.81}$$

$$\varepsilon = \frac{u_\tau^3}{\kappa y} \tag{4.82}$$

Reworking Equation 4.80 and introducing an additional term for the wall roughness (COMSOL Multiphysics 2012; Cebeci 2004)

$$u_\tau = \frac{\mathbf{U}}{\frac{1}{\kappa}\ln y^+ + B - AB} \tag{4.83}$$

$$AB = \begin{cases} 0 & k_s^+ \le 2.25 \\ \frac{1}{\kappa}\ln\left[\frac{k_s^+ - 2.25}{87.75} + C_s k_s^+\right]\sin[0.4258(\ln k_s^+ - 0.811)] & 2.25 \le k_s^+ \le 90 \\ \frac{1}{\kappa}\ln(1 + C_s k_s^+) & k_s^+ \ge 90 \end{cases} \tag{4.84}$$

With k_s^+ as the roughness height in viscous units when the roughness height, k_s, is the peak-to-peak value of the surface variations. C_s is a parameter that depends on the shape and distribution of the roughness elements. The turbulence parameters κ and B values are usually 0.41 and 5.2, respectively (COMSOL Multiphysics 2013).

When y^+ near the wall adjacent cells is low ($y^+ < 11.06$) the laminar stress-strain relationship is applied (see Equation 4.85)(Ariyaratne 2005; Kuzmin, Mierka, and Turek 2007).

$$u^+ = y^+ \tag{4.85}$$

LRN-Models: Integration Method

It is generally implied that a turbulence model that can be integrated toward the wall is denoted a LRN (Low Reynolds Number) turbulence model. To predict the sharp peak in turbulence kinetic energy and the viscous effects near a wall of a pipe, damping functions are introduced. Successfully devised damping functions (Table 4.1) should reproduce the correct asymptotic behaviour in the limit of a wall (Versteeg and Malalasekera 2007; Jones and

Launder 1972; Cebeci 2004).

In order to avoid the numerical stiffness that can be associated with these boundary conditions, some of the earlier models (Jones-Launder, Launder-Sharma, and Chien) formulate the governing equations in terms of ε^*, which is equal to the true dissipation rate minus its value at the wall D, rather than ε itself.

$$\varepsilon^* = \varepsilon - D \tag{4.86}$$

In these models ε^* is set equal to zero at the wall, a numerically convenient boundary condition. Hence, when this approach is taken, the additional term D is needed to balance the molecular diffusion of k in order to satisfy the k transport equation in the near-wall region. In several of the existing Low Reynolds Turbulence models found in the literature the E term has no physical justification (Costa, Oliveira, and Blay 1999; Hrenya et al. 1995). It was included to increase the predicted dissipation rate in order to obtain a realistic k profile in the near-wall region. Thus,

$$k = \varepsilon^* = 0 \;\; at\ the\ wall \tag{4.87}$$

Additionally to the inclusion of damping functions, LRN-model require very fine meshes close to the wall; therefore, the first computational element must have its centroid in $y^+ \approx 1$ (see Figure 4.6) (Kalitzin et al. 2005; Bredberg 2000).

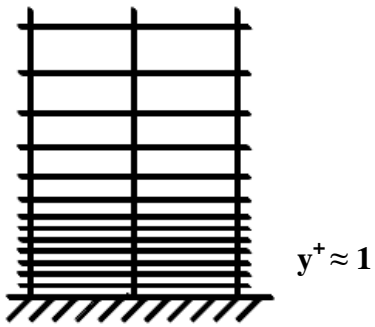

Figure 4.6 – Near Wall Treatment for Low Reynolds Number approach (adapted from (Kalitzin et al. 2005)).

Using the $y^+ \approx 1$ and the flow conditions, it is possible to estimate the height of the first mesh cell off the wall (F. M. White 1998; Schlichting and Gersten 1979) using flat-plate boundary layer theory:

I. Compute the Re number;

$$Re = \frac{\rho L_{boundarylayer} U_{freestream}}{\mu} \quad \textbf{(4.88)}$$

II. Estimate the skin friction using, for example, the Schlichting skin-friction correlation (Schlichting and Gersten 1979; F. M. White 1998);

$$C_f = [2\log_{10}(Re) - 0.65]^{-2.3} \qquad Re < 10^9 \quad \textbf{(4.89)}$$

III. Compute the Wall shear stress;

$$\tau_w = C_f \frac{1}{2} \rho U_{reestream}^2 \quad \textbf{(4.90)}$$

IV. Compute the Friction velocity;

$$u_* = \sqrt{\frac{\tau_w}{\rho}} \quad \textbf{(4.91)}$$

V. Compute the wall distance

$$y = \frac{\mu\, y^+}{\rho\, u_*} \quad \textbf{(4.92)}$$

4.8. PARTICLE-WALL STRESSES

One of most influential publications on the flow dynamics of a concentrated suspension of solids particles in a Newtonian fluid was given by Bagnold (R. Bagnold 1954; Hunt et al. 2002). In his manuscript Bagnold stated that the wall stresses were strongly dependent on the particle concentration.

It is known that the friction losses in pipeline flow of settling suspensions

depend on the flow pattern developed in the pipeline. A moving bed is formed at the bottom of the pipe when the flow velocity is low and the bed is stationary at velocities below the deposition-limit threshold (V. Matoušek 2002). The moving bed is in contact with the pipe wall and becomes a key contributor to solids friction in suspension flow. Suspended particles do not contribute to the friction as they are not in contact with the wall.

When the particles settle so rapidly that turbulence does not contribute significantly to particle suspension, the immersed weight of the particles is transmitted by particle-particle interaction to the pipe wall. These slurries are highly stratified and the frictional resistance to flow at the pipe wall depends upon the normal force that arises from the immersed weight of the particles. This Coulombic friction is quite different from the velocity dependent friction which arises in both laminar and turbulent fluid flow.

In the literature several authors studied vertical (C. A. Shook and Bartosik 1994; V. Matoušek 2002) or horizontal pipeline flows (Václav Matoušek 2005; Randall G Gillies, Shook, and Xu 2004; Schaan et al. 1997) of solid-liquid suspensions and have made attempts to quantify the additional stresses at the wall. Horizontal flows have shown increased particle-wall stresses, compared to vertical flows, due to a higher degree of flow stratification that results in a higher friction than for flows with a lower degree of stratification.

In the numerical studies referred in this thesis, the Mixture Model (Section 4.4) formulation was modified in order to account for the increasing contribution of the solids concentration on the particle-wall stresses. The expression added to the viscous shear stress expression in the Mixture Model numerical implementation, was a Bagnold type expression (see Equation 4.93) that accounts for the additional solids shear stress (Václav Matoušek 2005; Schaan et al. 1997).

$$\tau_s = K_i \, \rho_s \, \lambda^2 \, V_m^2 \qquad \textbf{(4.93)}$$

with K_i being a proportionality coefficient equal to 0.003 (Randall G Gillies,

Shook, and Xu 2004), while ρ_s is the solids density, V_m is the mean flow velocity and λ is the solids concentration (R. Bagnold 1954; Schaan et al. 1997) given by Equation 4.94

$$\lambda = \frac{1}{\left[\left(\frac{\phi_{max}}{\phi}\right)^{\frac{1}{3}} - 1\right]} \tag{4.94}$$

4.9. TURBULENCE MODULATION

The influence of particles on the fluid, in the Mixture Model, is imposed by the interphase forces (drag, lift, etc.), and, consequently, the turbulence modification by the particles is restricted to the diffusion velocity (see Section 4.4.1). Introducing a diffusion term, that denotes the effect of the relative (slip) velocity in the continuity equation of the dispersed phase (see Equation 4.32) is a simple way to avoid cumbersome terms in Equation 4.38 due to both the turbulent stresses and the fluctuating term of M_k.

Turbulence modification or modulation is important because it can be so large that can qualitatively change the natural behaviour of the engineering system. The mechanisms of turbulence modulation are poorly understood due to the difficulty in acquiring accurate experimental turbulence data for the carrier phase in particle-laden flows (Bohnet and Triesch 2003), and also because of the wide range of relevant length scales from the particle diameter to the size of the largest eddies, causes problems for detailed simulations. Lastly, different mechanisms can cause turbulence modulation and often act simultaneously. Due to all these competing factors, the present state of turbulence modulation knowledge is incomplete, and many contradictory results have been published (Balachandar and Eaton 2010). The literature is ample with studies on turbulence modulation where particle-laden flows have shown that a dilute dispersion of fine particles can either augment or attenuate the carrier-phase turbulent kinetic energy (Druzhinin and Elghobashi 1999; Truesdell and Elghobashi 1994; Elghobashi and Truesdell 1993). To date, no method has emerged capable of accurately predicting

turbulence modification by particles over a broad range of parameters.

There have been numerous experiments and numerical simulations that show turbulence modification in gas flows with solid particles (C.T. Crowe 2000; Kenning and Crowe 1997) that have successfully categorized the turbulence modification into augmentation and attenuation by proposing an intuitive parameter, d_p/l_e, taking into consideration the particle diameter, d_p, and the characteristic size of large eddies, l_e. However, the classification does not describe the effects of changing particle material density, nor does predict the magnitude of the turbulence modification (Tanaka and Eaton 2008).

Work on solid-liquid turbulence modulation has been scarce (R. Chen 1994), particularly for concentrated solid-liquid suspensions flows (as seen in Chapter II). In an attempt to characterize turbulence modulation in numerical studies of concentrated solid-liquid suspensions flows, several modifications to the *k-ε* turbulence model applied to gas-solid flows have been selected from the literature and incorporated into the turbulence equations in the Mixture Model numerical implementation, for the work reported in this thesis.

4.9.1. *k-ε* TURBULENCE MODEL MODIFICATIONS

The considered modification was by Hsu (Hsu 2003; Jha and Bombardelli 2009) who presented a model describing dilute sediment transport that incorporates the dissipation of the flow turbulent energy due to the presence of sediment. An extended version of the *k-ε* model was used, considering the following expressions for S_k and S_ε, the terms they added to the *k*–*ε* model to account for the presence of a second phase.

$$\rho \frac{\partial k}{\partial t} + \rho u \cdot \nabla k = \nabla \cdot \left(\left(\mu + \frac{\mu_T}{\sigma_k} \right) \nabla k \right) + P_k - \rho \varepsilon + S_K \qquad \textbf{(4.95)}$$

$$\rho \frac{\partial \varepsilon}{\partial t} + \rho u \cdot \nabla \varepsilon = \nabla \cdot \left(\left(\mu + \frac{\mu_T}{\sigma_\varepsilon} \right) \nabla \varepsilon \right) + C_{\varepsilon 1} \frac{\varepsilon}{k} P_k - C_{\varepsilon 2} \frac{\varepsilon^2}{k} + S_\varepsilon \qquad \textbf{(4.96)}$$

$$S_k = S_{k1} + S_{k2} \quad \textbf{(4.97)}$$

$$S_\varepsilon = C_{\varepsilon 3} S_k \frac{\varepsilon}{k} \quad \textbf{(4.98)}$$

$$S_{k1} = -\frac{2\rho_d \alpha_d k}{T_p + T_L} \quad \textbf{(4.99)}$$

$$S_{k2} = \frac{3}{4\, d_p} \rho_c C_D |\overline{U_r}| \nu_T \frac{\partial \alpha_d}{\partial x_i} \left(U_{i,c} - U_{i,d}\right) \quad \textbf{(4.100)}$$

$$T_p = \frac{\rho_d}{\frac{3}{4\, d_p} \rho_c C_D |\overline{U_r}|} \quad \textbf{(4.101)}$$

$$T_L = 0.165 \frac{k}{\varepsilon} \quad \textbf{(4.102)}$$

In Equations 4.95 to 4.102, S_{k1} represents the correlation between the fluid and sediment velocity fluctuations and S_{k2} represents the production of k due to the drag force (Jha and Bombardelli 2009; Hsu 2003), T_p is the particle time scale or particle response time, T_L is the flow time scale, U_r is the relative velocity between phases and $C_{\varepsilon 3}$ is a closure coefficient with a value of 1.2.

4.9.2. TURBULENCE MODULATION CLASSIFICATION

Conflicting information is found in the literature where, in many experiments, little changes in the mean fluid phase velocity profile with the addition of particles were found, and thus, there should be little change in the production of turbulence due to mean velocity gradients. On the other hand, other studies with heavy particles falling through the flow are releasing gravitational potential energy and introducing random velocity fluctuations to the fluid phase. This suggests that the addition of particles would increase the turbulence level, a phenomenon observed in many flows. Challenging the previous studies, in other particle-laden flows, extra dissipation caused by local distortion of the turbulence around inertial particles, leads to an overall reduction in the turbulent kinetic energy. And so, no method has emerged that is capable of accurately predicting turbulence modification by particles over a broad range of parameters (Tanaka and Eaton 2008).

The aforementioned parameter d_p/l_e (Kenning and Crowe 1997) does not describe the effects of changing particle material density, nor does it predict the magnitude of the turbulence modification, and the Stokes number and particle Reynolds number are even less effective.

In their study, Tanaka & Eaton (2008), gathered a comprehensive number of experimental measurements where the turbulent kinetic energy was modified by particles and divided the results into three groups of $Re - Pa$ mappings. Pa is the particle moment number, derived using dimensional analysis of the particle-laden Navier-Stokes equations. They proposed a mapping method to classify turbulence augmentation and attenuation with this non-dimensional parameter, Pa, which can be calculated using either the particle Reynolds number (see Equation 4.103) or the Stokes number (see Equation 4.104).

$$Pa_{Re} = \frac{1}{18}\frac{Re_L^2}{Re_p}\frac{\rho_p}{\rho_f}\left(\frac{d_p}{L}\right)^3 \tag{4.103}$$

$$Pa_{St} = St\, Re_L^2\left(\frac{\eta}{L}\right)^3 = \frac{1}{54\sqrt{2}}\frac{Re_L^2}{St^{1/2}}\frac{{\rho_p}^{3/2}}{{\rho_f}^{3/2}}\left(\frac{d_p}{L}\right)^3 \tag{4.104}$$

Using Equation 4.104 becomes more intuitive since it depends on the particle Reynolds number, which in turn depends on the relative velocity between phases. Estimating this latter parameter can be cumbersome and one possibility is to use the terminal velocity of a particle (see Equation 4.108) as an initial guess (Rasteiro 1988; Tanaka and Eaton 2008).

$$Re_{p=}\frac{U_{slip}d_p}{\nu} \tag{4.105}$$

$$Re_{L=}\frac{U_L D}{\nu} \tag{4.106}$$

$$St = \frac{2}{9}\left(\frac{r_p}{L_H}\right)^2\frac{Re_L}{R} \quad with \quad R = \frac{2\rho_f}{2\rho_p + \rho_f} \tag{4.107}$$

$$V_T = \frac{1}{18}.\frac{{d_p}^2 g\left(\rho_p - \rho_f\right)}{\mu_L} \tag{4.108}$$

For low Stokes number, particles tend to follow the flow and velocities fluctuations are almost non-existing, as confirmed by several authors (Druzhinin and Elghobashi 1999; Druzhinin 2001) for homogeneous flows of particles. For small *Pa* values the particles have no effect on the flow (Druzhinin 2001).

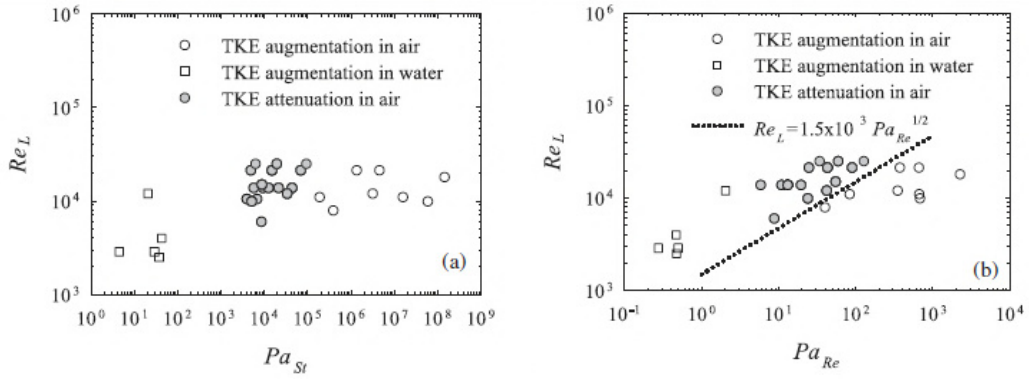

Figure 4.7 – Mapping of turbulence modification experiments based on (a) Pa_{St} and Re_L, and (b) Pa_{Re} and Re_L. The circle and square symbols represent air and water turbulence, respectively. The open symbols represent *k* augmentation and filled symbols show *k* attenuation (adapted from (Tanaka and Eaton 2008)).

The following interval, $10^3 < Pa_{St} < 10^5$ (see Figure 4.7), was defined by Tanaka & Eaton (2008) as the turbulence attenuation critical values with the Stokes number formulation, while $3 < Pa_{Re} < 200$ (see Figure 4.7) is the interval for attenuation for the particle Reynolds number formulation. A closer inspection of Figure 4.7(b) allows perceiving the existence of a dependence of turbulence modification with the flow Reynolds number, Re_L, denoted by the dotted line. This allowed the authors to specify that for air and for values of Re_L smaller than $1.5x10^3 Pa_{Re}^{1/2}$ there is turbulence augmentation and for values above to the dotted line there is attenuation of the turbulence.

Regretfully, data for turbulence attenuation in water is lacking from their analysis. This is one area of interest for the work presented in this thesis.

CHAPTER V

NUMERICAL STUDIES RESULTS

5. CHAPTER V – NUMERICAL STUDIES RESULTS

In this Chapter the numerical results from the Mixture Model described in Chapter IV are presented. Prior to using the Mixture Model to depict, numerically, the experimental data gathered at both KTH and DEQ, its adequacy in the study of solid-liquid suspensions flows had to be validated. To this end, works found in the literature were carefully chosen to match the following criteria: concentrated solid-liquid suspensions of both buoyant and settling particles; pressure drop as a function of flow regimes; and finally, turbulence modulation by the particles. Numerical simulations were carried out in an attempt to portray the aforementioned chosen data from the literature.

5.1. NUMERICAL STUDIES ON SOLID-LIQUID SUSPENSIONS FLOWS – BUOYANT PARTICLES

For the buoyant particles the Mixture Model coupled with a High Reynolds k-ε turbulence model was used to evaluate, through a sensitivity analysis procedure with Computational Fluid Dynamics (CFD), the influence of the closure coefficients and the turbulence scales on a fully developed homogenous horizontal flow of spherical particles in a circular pipe section. From the literature report that depicts a homogenous flow of concentrated buoyant spherical particles (C. Shook 1985) under the conditions described in Table 5.1, was chosen. For the undertaken studies, both 2D and 3D modelling approaches were implemented as to ascertain the premise that for homogeneous flows the particles were well distributed in the pipe section and thus, that a 3D model use would become unnecessary. The 2D results are presented in this Section and the 3D are collected in Appendix D, since it was, in fact, demonstrated that the 2D Mixture Model implementation with a homogeneous flow assumption provided a good representation of the experimental data demonstrating that 3D simulations of pipe flows with buoyant particles are unnecessary, due to longer computational times and effort.

Furthermore, the results displayed in this Section are divided into two main sub-Sections, one for the Closure Coefficients Study and the other for Turbulence Scales Study.

5.1.1. EXPERIMENTAL CONDITIONS

As from the literature (C. Shook 1985), the flow conditions as well as the particle data for a multiphase Newtonian flow of spherical polystyrene particles, with a density of 1050 kg. m^{-3} and 0.3 mm diameter with a volumetric fraction of 34 % (v/v) are shown in Table 5.1.

Table 5.1 – Conditions for the numerical studies with Shook (1985) data for 0.3 mm buoyant particles with 34% (v/v) particle concentration.

	Flow Data
PIPE ID [mm]	52.23
$U\ [m.s^{-1}]$	1.0 2.0 3.0 4.0
$\rho_F\ [kg.m^{-3}]$	998*
$\mu_F\ [Pa.s]$	1.02×10^{-3}*
Re	51103 102207 153310 204414
	PARTICLE DATA
$\rho_P\ [kg.m^{-3}]$	1050
$d_p\ [mm]$	0.3
$\phi\ [v/v]$	0.34

*** Values at 20ºC**

5.1.2. FLOW REGIME CONSIDERATIONS

A homogeneous flow regime was observed by Shook (1985) for the 34 % (v/v) particle concentration.

Deposition Velocities

The deposition velocity is the velocity below which the particles start to settle and form a bed. This is an important parameter since most industries use this value as a guideline for the minimum operating velocity.

In the literature several correlations can be found to estimate this parameter. Three different sources were used in this study:

Correlation I

Uses the first correlation (Randall G. Gillies et al. 2000) and the Arquimedes Number (AR) as the deciding factor to which correlation to use:

$$Ar = \frac{4}{3}\left[\frac{g\ d_p^3\ \rho_F(\rho_P - \rho_F)}{\mu_F^2}\right] \quad \textbf{(5.1)}$$

If AR < 80 and d_p < 0.5 mm, then

$$F_L = 2.0 + 0.3log_{10}\Delta$$
$$with\ \Delta = \left(\frac{d_p}{D}\ C_D\right) \quad \textbf{(5.2)}$$

$$V_D = F_L\sqrt{2gD(S_s - 1)} \quad \textbf{(5.3)}$$

Otherwise if AR > 80 and d_p > 0.5 mm, using Figure 4 from the original article, as supplied by Gillies et al. (2000) for an Arquimedes number of 2355 the F_L value is 1.2. Since the previous Equations are independent of the particle concentration and flow velocity this value will be constant.

Correlation II

A second correlation was given by Kaushal et al. (2002) as follows:

$$V_D = 1.87\left(\frac{d_p}{D}\right)^{\frac{1}{6}}\sqrt{2gD\left(\frac{\rho_p}{\rho_F} - 1\right)}\ for\ \phi \leq 1\% \quad \textbf{(5.4)}$$

$$V_D = 1.87\left(\frac{d_p}{D}\right)^{1/6}\phi^{1/5}\sqrt{2gD\left(\frac{\rho_p}{\rho_F}-1\right)}\,for\;\phi > 1\% \qquad \textbf{(5.5)}$$

Correlation III

The third correlation employed was by Abulnaga (2002):

$$F_L = 1.3\,\phi^{0.125}[1-e^{-6.9\,dp_{50}}]\;with\;d_{p50}\;expressed\;in\;\boldsymbol{mm} \qquad \textbf{(5.6)}$$

$$V_D = F_L\sqrt{2gD(S_s-1)} \qquad \textbf{(5.7)}$$

Using the deposition velocities Correlations I, II and III described above for the buoyant particles resulted in the values presented in Table 5.2.

Table 5.2 – Deposition velocities for the buoyant particles from (C. Shook 1985) for 0.3 mm sized particles with a particle concentration of 34 % (v/v) in a 52.23 mm ID pipe.

Correlation I				Correlation II	Correlation III	
AR	**Δ**	**F_L**	**V_D (m.s^{-1})**	**V_D (m.s^{-1})**	**F_L**	**V_D (m.s^{-1})**
17.6	0.27	2.13	0.49	0.32	1.14	0.26

The deposition velocities from Correlations II and III, in Table 5.2, appear to provide values that agree with the visual inspection of the flows by the author (C. Shook 1985). Values from Correlation I seem high considering the homogeneous flow depiction by the author for the 34 % (v/v) particle concentration even at low flow velocities.

5.1.3. NUMERICAL STUDIES CONDITIONS

Validity of the Mixture Model

The Reynolds Number (Re) displayed in Table 5.1 shows that the flows were all turbulent. With a homogeneous distribution of particles there was no need to model the interphase forces and no drag correlations were used. The Particle Stokes Numbers, attained with Equation 4.107, are presented in Table 5.3. All the values are smaller than one, thus validating the application

of the Mixture Model in these studies (Manninen, Taivassalo, and Kallio 1996; Hiltunen et al. 2009).

Table 5.3 – Particle Stokes Number for Shook's experiments with the 34 % (v/v) particle concentration (C. Shook 1985).

Particle Data	52.23 mm ID Pipe
$\rho_P\ [kg.m^{-3}]$	1050
$d_p\ [mm]$	0.3
$U\ [m.s^{-1}]$	1.0 2.0 3.0 4.0
$\phi\ [v/v]$	0.34
St_p	0.145 0.291 0.436 0.582

Geometry

In the 2D simulations an axisymmetric domain was implemented with two different pipe sections with an internal diameter of 52.23 m (C. Shook 1985) as shown in Table 5.1, were defined. The first section, 2 meters long, serves the purpose of facilitating the full development of the flow (entry length) while the second section, the region of study, is 2.9 meters long. A 3D simulation domain, for conditions equal to the ones used in the 2D simulations, was also implemented (see Appendix D).

Finite Element Meshes

The finite element meshes, both 2D and 3D (see Figure 5.1), were refined until grid independent results were obtained in the numerical studies. The final mesh characteristics are presented in Table 5.4.

Table 5.4 – Mesh parameters for the buoyant particles numerical studies.

	2D	3D
Number of Elements	24 488	1 083 662
Number of Boundary Layers	12	10
Wall Lift off in Viscous Units (y^+)	11.06	11.06

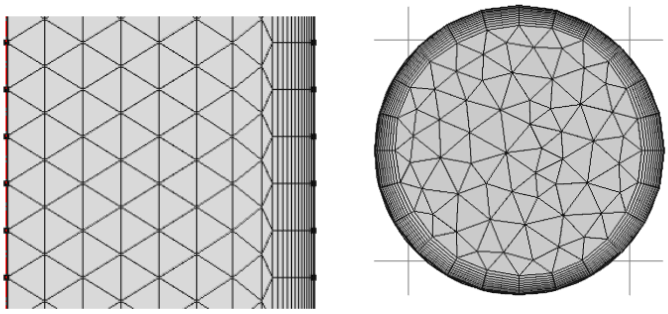

Figure 5.1 – 2D (Left) and 3D (Right) unstructured meshes.

The wall lift-off in viscous units is 11.06, throughout both the 2D and 3D meshes, as suggested in the CFD software manual for the k-ε turbulence model (Bardow et al. 2008; COMSOL Multiphysics 2013).

Boundary Conditions

For the numerical studies emulating the experimental data from the buoyant suspensions flows (C. Shook 1985), the applied boundary conditions are described below:

i. at the inlet the initial velocities (see Table 5.1) were imposed in the direction perpendicular to the pipe cross-section and the turbulence intensity and length scales employed are depicted in Section 5.1.4.
ii. The normal gradients of k and ε, at the outlet, were again fixed to zero, according to Equation 4.75, and pressure values were also assigned to zero.
iii. Wall Functions (see Equation 4.80) were once again employed to the numerical depiction of the near wall treatment of the flow. These simulations were developed early in the work., therefore, the versions available for COMSOL Multiphysics® were 4.1 and 4.2, that did not

possess the option to impose any roughness height (COMSOL Multiphysics 2013); thus the term AB was null.

5.1.4. TURBULENCE SCALES ANALYSIS – NUMERICAL RESULTS

In the turbulence scales study, several assumptions described in the literature were used in the numerical simulations to ascertain their influence in a fully developed flow, for both the 2D and 3D situations (Kenning and Crowe 1997; Ling et al. 2003; Mandø et al. 2009; Rizk and Elghobashi 1989):

Case 1

The turbulence scales usually used for single phase flows were the first set of scales that were studied. Equations 5.8 and 5.9 define the turbulence intensity scale and the turbulence length scale, respectively (Bardow et al. 2008; COMSOL Multiphysics 2012).

$$I_T = 0.16Re^{-0.125} \quad \textbf{(5.8)}$$

$$L_T = 0.07\,D \quad \textbf{(5.9)}$$

where Re is the Reynolds Number for the flow and D is the pipe diameter.

Case 2

The second set of turbulence scales employed were (Lin and Ebadian 2008):

$$\mathrm{I}_T = 0.04 \quad \textbf{(5.10)}$$

$$L_T = d_p \quad \textbf{(5.11)}$$

Lin & Ebadian (2008) assumed a value of 0.04 for the turbulence intensity scale for solid-liquid horizontal flows. The turbulence length scale was equal to the particle diameter, d_p, which is justified by the fact that the wakes generated by the particles would be of similar size to their diameter.

Case 3

In the third and final set of turbulence scales studied, the same value of 0.04 for the turbulence intensity scale is used. For the turbulence length scale Kenning & Crowe (1997) stated that, if the particle concentration is high enough, then it is safe to assume that the particles will interfere with the existing turbulence eddies and the new length scale will be proportional to the average interparticular space. Thus a new hybrid length scale is defined where both the particle and interparticular space interference are quantified (see Equations 5.12 to 5.14).

$$\mathrm{I}_T = 0.04 \tag{5.12}$$

$$L_T = L_H = \frac{2\lambda L_i}{L_i + \lambda} \tag{5.13}$$

$$\frac{\lambda}{dp} \approx \left(\frac{\Pi}{6\,\phi_d}\right)^{\frac{1}{3}} - 1 \tag{5.14}$$

where λ represents the average interparticular space and ϕ_d the volumetric fraction of the spheres. The inherent dissipation length scale, L_i , represents the length scale of the flow without particles, i.e., $L_i = L_T$ in Equation 5.9 (Kenning & Crowe, 1997).

2D Numerical Results

For the 2D numerical simulations, Table 5.5 summarizes the influence of the turbulence scales on the fully developed homogenous solid-liquid suspension flow. The numerical studies results show the pressure drop (deviations from experimental values are displayed in parenthesis, ΔExp), turbulent kinetic energy and turbulent dissipation rate at the pipe wall for flow velocities of 1 and 4 $\mathrm{m.\,s^{-1}}$ for the different turbulence scales depicted in Equations 5.8 to 5.14.

The sharpest variations in k and in ε occur at the pipe wall. These variations are displayed in Figures 5.2 and 5.3 (Left) for a flow velocity of 1 $\mathrm{m.\,s^{-1}}$ and in Figures 5.2 and 5.3 (Right) for a flow velocity of 4 $\mathrm{m.\,s^{-1}}$.

Table 5.5 – Influence of the turbulence scales on the numerical turbulence variables and comparison between the experimental and numerical pressure drops for the 2D numerical studies.

			$1\ m.s^{-1}$			$4\ m.s^{-1}$		
Case	I_T	L_T	**ΔP (Pa) ΔExp**	k **($m^2.s^{-2}$)**	ε **($m^2.s^{-3}$)**	**ΔP (Pa) ΔExp**	k **($m^2.s^{-2}$)**	ε **($m^2.s^{-3}$)**
1	0.04126	0.003656	787.68 (0.03%)	0.01000	0.5620	7589.2 (-3.92%)	0.1074	54.484
2	0.04000	0.000300	777.07 (1.32%)	0.009899	0.5476	7591.8 (-3.96%)	0.1077	54.464
3	0.04000	0.000046	776.89 (1.34%)	0.009897	0.5476	7591.3 (-3.95%)	0.1078	54.461

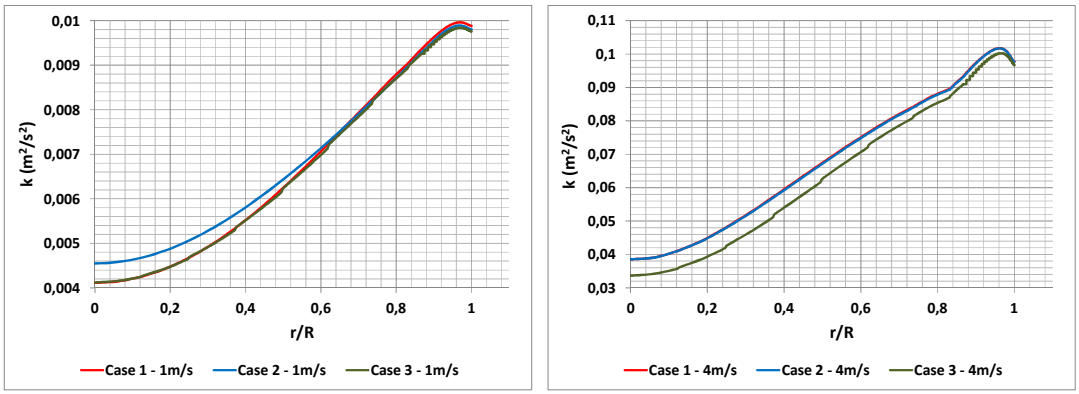

Figure 5.2 – 2D turbulent kinetic energy profiles for Case 1, 2 and 3 along the pipe radius for a flow velocity of 1 $m.s^{-1}$ (Left) and 4 $m.s^{-1}$ (Right).

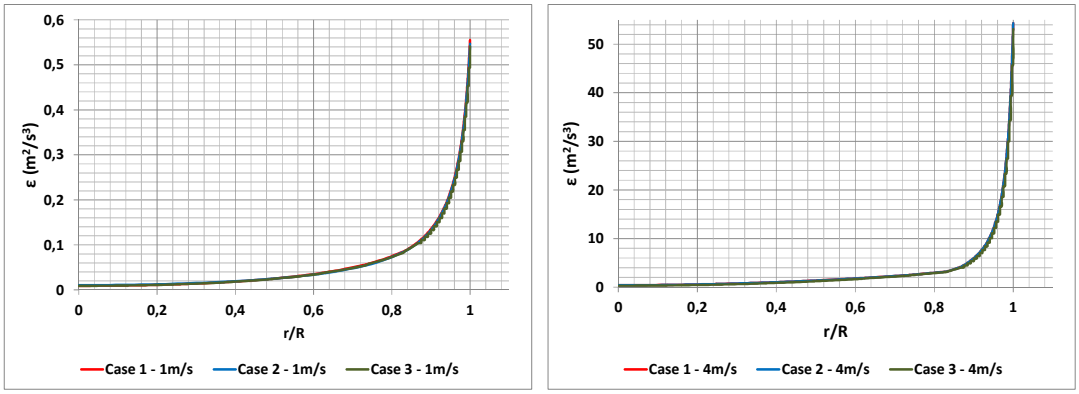

Figure 5.3 – 2D turbulent dissipation rate for Case 1, 2 and 3 along the pipe radius for a flow velocity of 1 $m.s^{-1}$ (Left) and 4 $m.s^{-1}$ (Right).

In Figure 5.4, representing the radial velocity profiles for the different

turbulence scales tested, it is obvious that they are always very similar, almost independent of the turbulence scales model that was used. The velocity at the wall of the pipe is slightly lower in Case 1, although, these differences are not significant. As expected, in the viscous sub-layer, near the pipe wall, there is a significant decrease in velocity, when compared with the centre of the pipe, which is more noticeable for 4 m. s^{-1}.

From Figures 5.2 to 5.4 and from Table 5.5 it becomes apparent that the simulated cases using the Mixture Model incorporating the High Reynolds k-ε turbulence model produce similar results, regardless of the selected turbulence scale model. The turbulence scales effect in the fully developed homogeneous flow is very small, even when the turbulence length scale is decrease by a factor of 100 from Case 1 to Case 3. Despite the slight changes in the profiles that are observed from Figure 5.2 to 5.4, their overall effect is negligible. Still, looking at Table 5.5, the lowest deviation between calculated and experimental pressure drop is obtained when using Case 1 turbulence scales.

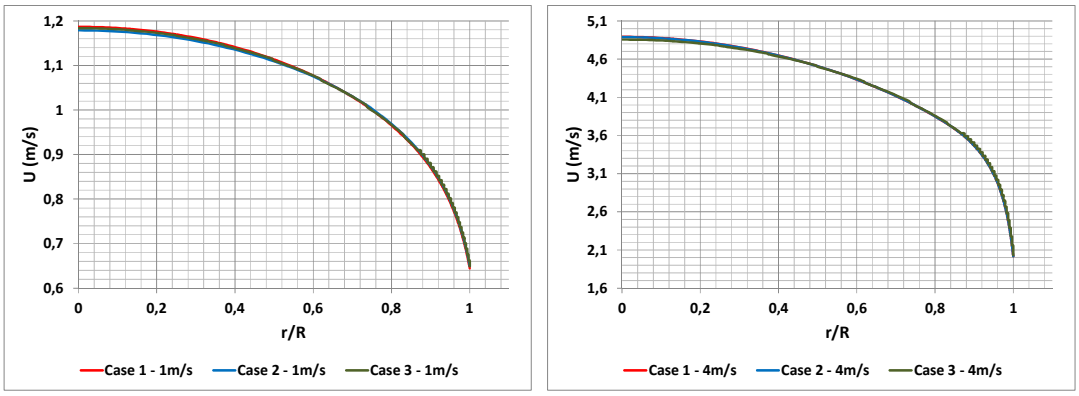

Figure 5.4 – 2D mixture velocity profiles for Case 1, 2 and 3 along the pipe radius, velocity of 1 m. s^{-1} (Left) and 4 m. s^{-1} (Right).

Moreover, when k at the wall decreases the calculated pressure drop decreases, as anticipated. Examples of two dimensional profiles for k and ε are presented in Figure 5.5.

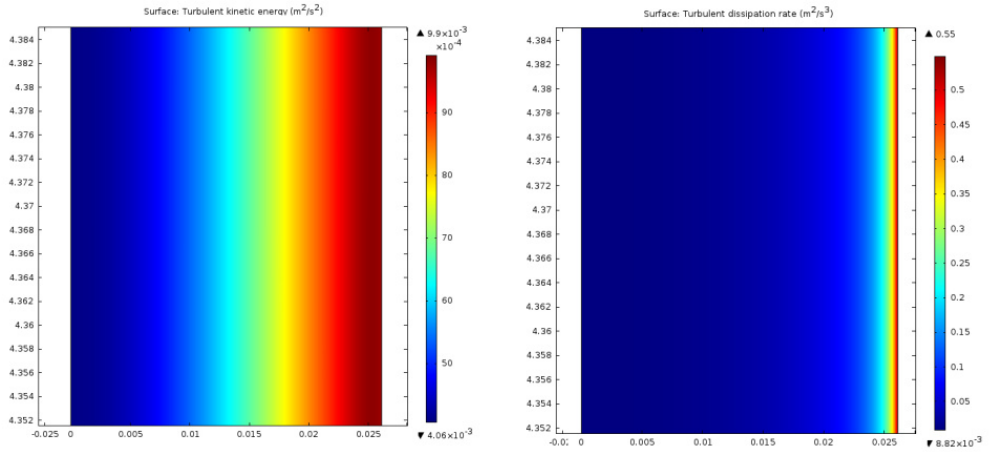

Figure 5.5 – 2D turbulent kinetic energy (Left) and turbulent dissipation rate (Right) for Case 2 along the pipe radius for a flow velocity of 1 m. s^{-1}.

Also, in Figure 5.6, the 2D simulation results, using the standard closure coefficients for the *k-ε* turbulence model, and the turbulence scales from Case 2, are compared with the experimental data and results using Durand-Condolios correlation (Peker and Helvaci 2011). The pressure drop values will serve as the control variable for the quality of the numerical studies.

The turbulence scales from Case 2 where used in the remaining numerical studies from both this Chapter and Chapter VI.

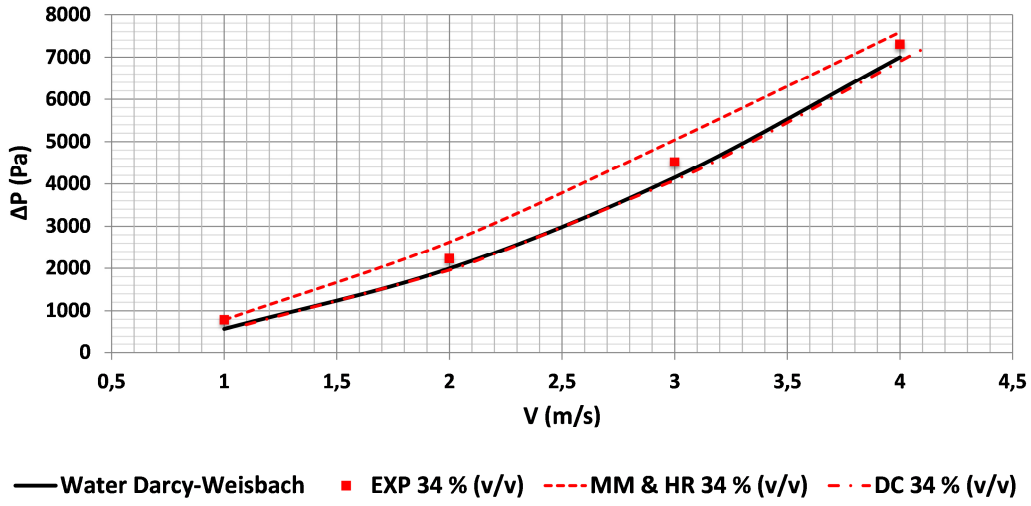

Figure 5.6 – Comparison between pressure drop values from experimental data by Shook (1985) (EXP) and numerical results with the Mixture Model coupled with a High Reynolds closure (MM & HR) and calculated values from Durand-Condolios correlation (DC) for the solid-liquid flows using buoyant particles with 0.3 mm diameter and 34 % (v/v).

In Figures 5.7 and 5.8 the numerical and experimental data regarding concentration and velocity profiles, respectively, are compared. Overall, there is a good agreement between numerical and experimental results. This shows that the Mixture Model with a High Reynolds *k-ε* Turbulence Model is adequate in predicting the behaviour of homogeneous flows with buoyant particles, in spite of some minor fluctuations in the numerical results. The experimental information for the concentration profiles is scarce. Shook (C. Shook 1985) used an Isokinetic Sampling method for a solid volumetric fraction of 35 % (v/v) (2 samples) and demonstrated the homogeneous distribution of the particles as can be seen in Figure 5.7. It was assumed that the difference between 34 and 35 % (v/v) data was negligible and the numerical and experimental normalized particle concentration profiles would be the same.

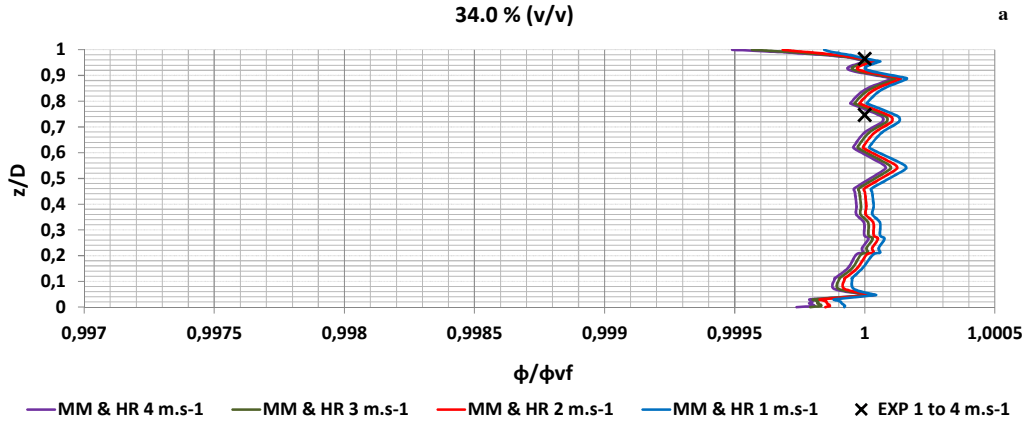

Figure 5.7 – Normalized numerical and experimental vertical solids concentration profiles for buoyant particles with solids volumetric fraction of 34.0 % (v/v).

In Figure 5.8 the velocity profiles are presented, and it can be seen that, in spite some numerical deviations, overall the numerical profiles follow the experimental data and are homogeneous for all flow velocities. As velocity increases the influence of the wall becomes more pronounced.

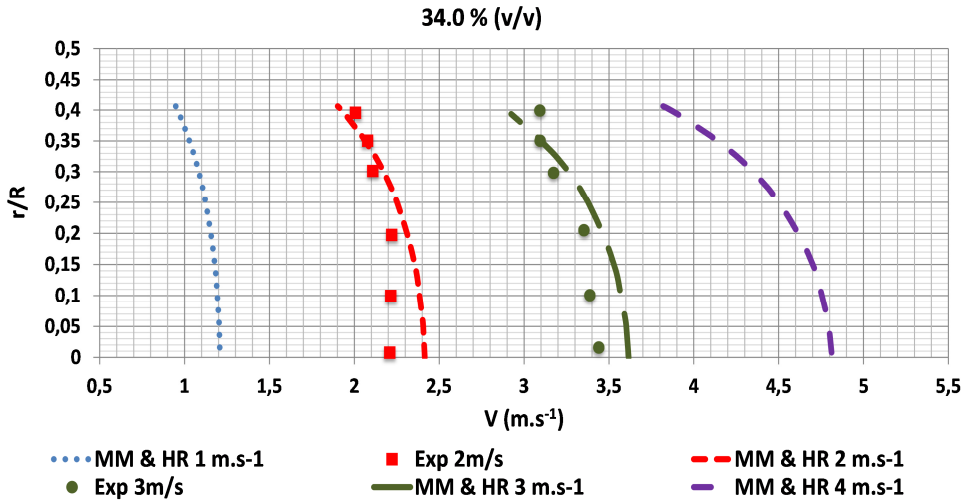

Figure 5.8 – Experimental and numerical horizontal velocity profiles for neutrally buoyant particles with solids volumetric fractions of 34 % (v/v).

5.1.5. CLOSURE COEFFICIENTS ANALYSIS – NUMERICAL RESULTS

The turbulence closure coefficients have been the subject of study by many authors (Bardow et al. 2008; Lai and Yang 1997; Rizk and Elghobashi 1989; Costa, Oliveira, and Blay 1999; Wilcox 2006); however, there is no consensus about which values to employ for suspension flows and their effect on the predicted flow results. Most authors who studied the k-ε turbulence model for multiphase flows, employ the same coefficients values utilized for single-phase flows (Bardow et al. 2008; Lai and Yang 1997; Rizk and Elghobashi 1989; Costa, Oliveira, and Blay 1999). Results on the optimization of these coefficients for multiphase flows are almost inexistent in the literature: even for single phase monophasic flows very few studies can be found; an example is given by Wilcox (2006) where a process to evaluate the k-ω turbulence model closure coefficients is depicted and is stated that the k-ε closure coefficients can be evaluated by an analogous procedure. This process is quite complex from an algebraic standpoint and some empirical simplifications are required. In a different approach (Rizk and Elghobashi 1989), each coefficient is modified and its impact on the flow parameters is quantified. This is also the methodology followed in the work presented in this thesis. A 20% increase in the standard numeric value was implemented (see Table 5.6) and

the influence on the solid-liquid horizontal flow parameters is analysed in this Section.

Table 5.6 – Standard Closure Coefficients and Modified Values for the numerical studies with the buoyant particles.

Closure Coefficients	Standard Value	Modified Value
$C_{\varepsilon 1}$	1.44	1.728
$C_{\varepsilon 2}$	1.92	2.304
σ_{ε}	1.3	1.56
σ_{k}	1.0	1.2
C_{μ}	0.09	0.0918
σ_{t}	0.35	0.42

2D Numerical Results

The influence of an increase of 20% on the standard value of the closure coefficients, using the same Turbulence Scales as in Case 2, for mixture velocities of 1 and 4 m. s^{-1}, is summarized in Table 5.7. The pressure drop values and their relative deviation from the experimental values (ΔExp) are presented in the second column, while the numerical pressure drop, turbulent kinetic energy and turbulent dissipation rate relative deviations from the reference case ($\Delta Case2$), Case 2, are presented in columns 3, 5 and 7 respectively.

In each simulation only one closure coefficient was varied, while the others were kept as in Table 5.6. As described in the literature by Bardow et al. (2008), the closure coefficients $C_{\varepsilon 1}$ and $C_{\varepsilon 2}$ influence the radial turbulence distribution. The production and production-dissipation terms of Equations 4.66 and 4.67 dominate over the remaining terms for the same pipe flow. These terms are modelled using $C_{\varepsilon 1}$ and $C_{\varepsilon 2}$. Looking at the results summarised in Table 5.7 it is obvious that the highest influence on the calculated pressure drop comes from the variation in these two coefficients. This influence is even more notorious in the case of the higher velocity.

Table 5.7 – Comparison between the 2D numerical results for Case 2 and for a 20% increase in the *k*-*ε* turbulence closure coefficients.

	1 m.s^{-1}					
	ΔP (Pa) ΔExp (%)	**ΔP (Pa) $\Delta Case2$(%)**	**k (m^2.s^{-2})**	**k (m^2.s^{-2}) $\Delta Case2$(%)**	**ε(m^2.s^{-3})**	**ε(m^2.s^{-3}) $\Delta Case2$(%)**
Case 2	757.07 (3.85)	--	0.00900	--	0.5721	--
$C_{\varepsilon1}$+ 20%	664.38 (15.63)	12.24	0.00760	15.56	0.3328	41.83
$C_{\varepsilon2}$+ 20%	915.19 (16.22)	20.88	0.01070	18.89	0.6883	20.31
σ_ε+ 20%	813.16 (3.27)	7.409	0.00920	2.22	0.5167	9.684
σ_k+ 20%	813.16 (3.27)	7.409	0.00930	3.33	0.5199	9.124
C_μ+ 20%	813.16 (3.27)	7.409	0.00920	2.22	0.5109	10.69
σ_t+ 20%	811.84 (3.10)	7.234	0.00930	3.33	0.5172	9.596
	4 m.s^{-1}					
	ΔP (Pa) ΔExp (%)	**ΔP (Pa) $\Delta Case2$(%)**	**k (m^2.s^{-2})**	**k (m^2.s^{-2}) $\Delta Case2$(%)**	**ε(m^2.s^{-3})**	**ε(m^2.s^{-3}) $\Delta Case2$(%)**
Case 2	7591.8 (3.96)	--	0.1077	--	54.464	--
$C_{\varepsilon1}$+ 20%	5551.1 (23.98)	26.88	0.0750	30.36	29.949	45.01
$C_{\varepsilon2}$+ 20%	9076.5 (24.29)	19.56	0.1262	17.18	83.344	53.03
σ_ε+ 20%	7835.5 (7.30)	3.210	0.1087	0.930	60.554	11.18
σ_k+ 20%	7660.3 (4.90)	0.900	0.1058	1.760	57.114	4.870
C_μ+ 20%	7672.8 (5.07)	1.070	0.1049	2.600	57.534	5.640
σ_t+ 20%	7591.8 (3.96)	0.000	0.1077	0.000	54.443	0.040

Moreover, for k and ε values, the highest variations occur at the pipe wall, as

confirmed by Figure 5.9. Also, from Figures 5.6 and 5.9, when comparing the turbulence production and dissipation at the wall, it is clear in Figure 5.9 that the boundary layer turbulence production has increased substantially when $C_{\varepsilon 1}$ or $C_{\varepsilon 2}$ increase.

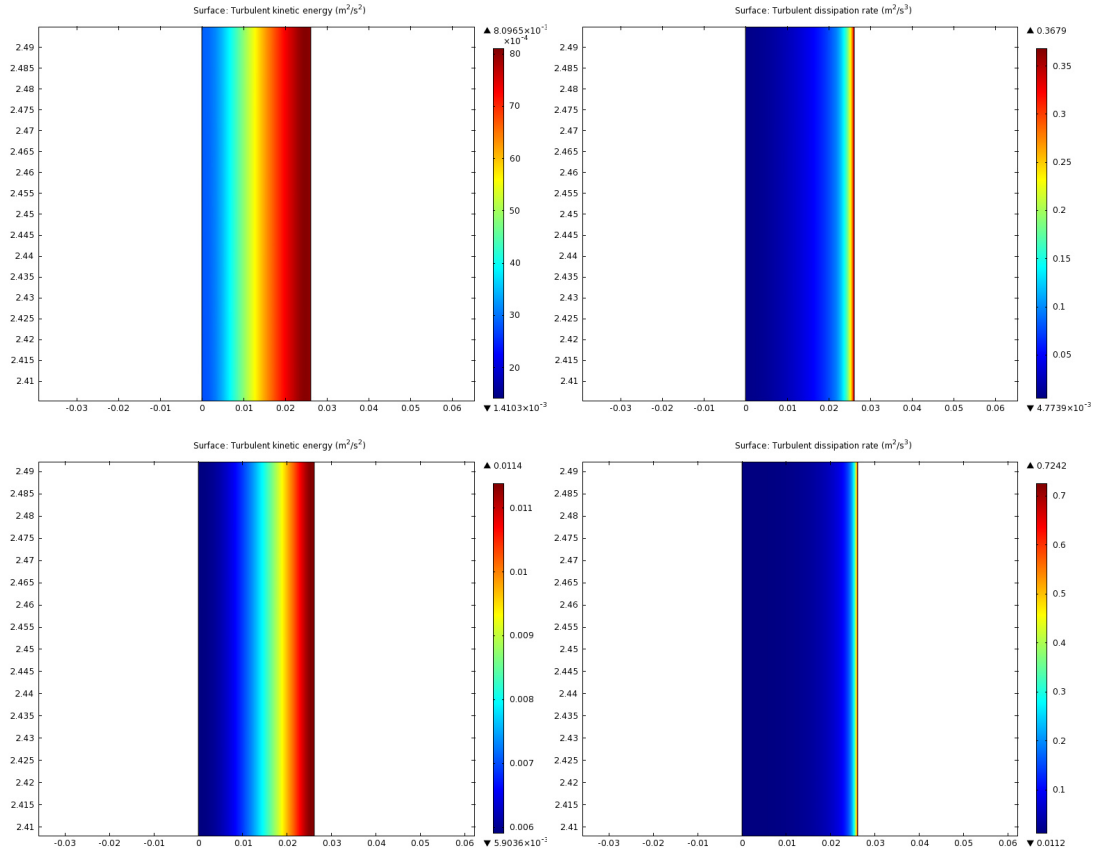

Figure 5.9 – 2D Turbulent Kinetic Energy (Left) and Turbulent Dissipation Rate (Right) for an increase of 20% in the standard value of $C_{\varepsilon 1}$ (Top) and $C_{\varepsilon 2}$ (Bottom) for a flow velocity of 1 m. s^{-1}.

In a similar way, a variation in the values of σ_{ε}also caused an increase in the turbulence production and dissipation intensity at the wall (see Figure 5.9); however, it is not as pronounced as when $C_{\varepsilon 1}$ or $C_{\varepsilon 2}$ are varied. In Equation 4.68, this coefficient is used to model the diffusive term along with the turbulent dynamic viscosity and, thus, its influence is still considerable. This was translated by a lower influence in the calculated pressure drop.

The σ_k parameter is related with the pressure diffusion term in Equation 4.67. The influence of this parameter is significantly lower when compared to

the previous ones (Bardow et al. 2008), which is confirmed by Figure 5.10 and by the values in Table 5.7. For the case tested and considering Equation 4.67, the weak contribution of this parameter shows that the dominant terms are the production and dissipation terms while the contribution of the pressure diffusion term can be neglected, for this particular case. Also, since this parameter is linked to pressure diffusion, its lower significance in this scenario could be related to the lack of vertical pressure gradient resultant from the homogeneous particle distribution. The influence of this parameter on the global pressure drop is almost negligible.

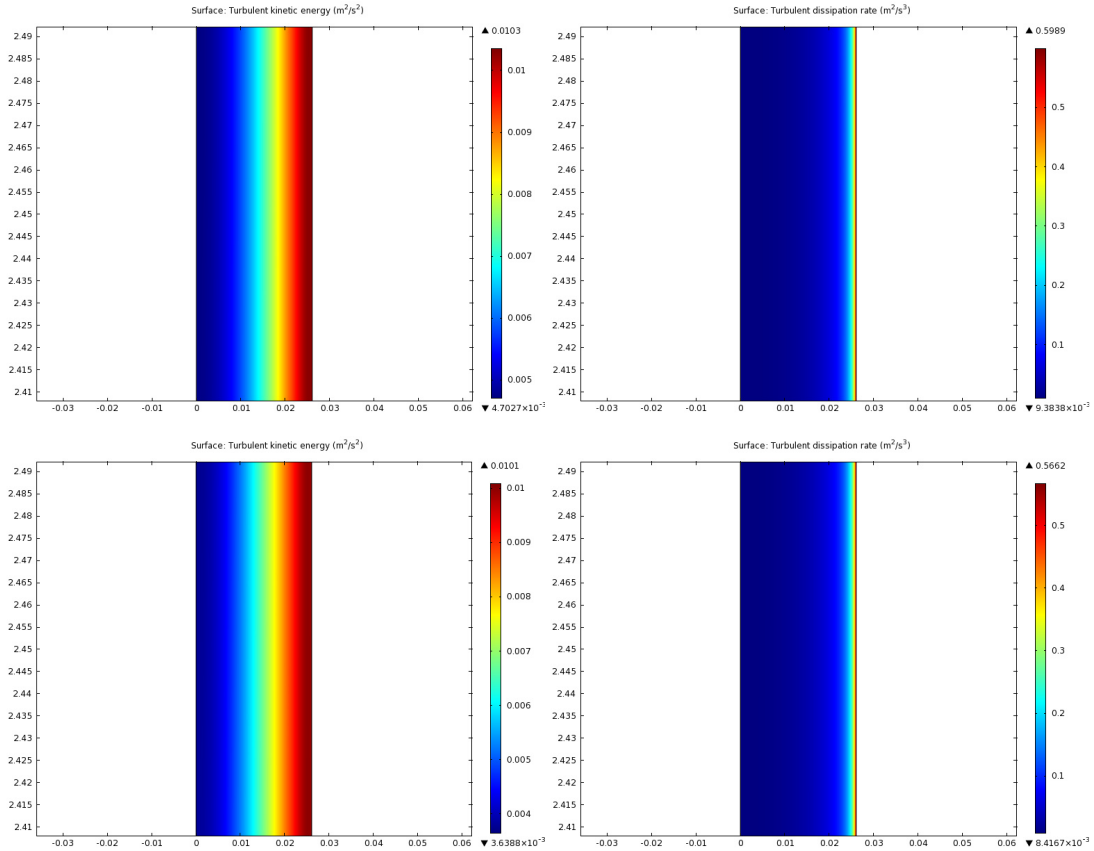

Figure 5.10 – 2D Turbulent Kinetic Energy (Right) and Turbulent Dissipation Rate (Left) for an increase of 20% in the standard value of σ_ε (Top) and σ_k (Bottom) for a flow velocity of $1\ \mathrm{m.s^{-1}}$

The contribution of the C_μ parameter is visible both in the turbulent dynamic viscosity, as well as in the production and dissipation terms, see Equations 4.66, 4.67 and 4.68. Thus, it is expected that its effect on the boundary layer should be high (Bardow et al. 2008); however, in this particular study that it

is not the case, because the significant majority of particles are fluidized and the viscosity at the wall will be mostly constant, and similar to the water viscosity, since particles will not settle and interaction between boundary layer and particles will be scarce. Also, as demonstrated in previous studies (V. Matoušek 2002), at high flow velocities the particles tend to migrate to low shear rate areas of the flow that is, in this case, away from the wall. This is even more pronounced for neutrally buoyant particles, and, thus, any variation in this parameter causes only very small variations of the flow turbulence when compared to standard Case 2, as demonstrated by the results in Table 5.7.

The Schmidt Turbulent Number, σ_T, is defined as the ratio between the turbulent kinematic viscosity and the scalar diffusivity coefficient (see Equation 5.15), and this parameter is related to the axial diffusion of particles (Ekambara et al. 2009).

$$\sigma_T = \frac{\nu_T}{D_t} \tag{5.15}$$

In Table 5.7 it is shown that the variation of this parameter causes little effect on the turbulent flow parameters, contrarily to what was expected. However, in the literature (Ekambara et al. 2009), it was observed through CFD studies that this particular parameter had no effect on the simulated results when the Reynolds Number of a flow was higher than 10 000; this is clearly the case in this study, where the Reynolds Number is of 51 100 for a flow velocity of $1\ \mathrm{m.\,s^{-1}}$. This agrees also with the observation that the influence of the σ_T variation on the turbulence parameters is even smaller for the higher velocities tested, as seen in Table 5.7. Another aspect of this particular study that could influence the Schmidt Number is the slip velocity which, in this case, is zero, or close to zero, since velocity is high enough for the flow to be homogeneous. A possible assumption, therefore, is that the influence of this parameter could be more pronounced for heterogeneous flow.

An overall influence of a 20% variation of the closure coefficients, on the

turbulence parameters k and ε, is summarized in Figure 5.11. It is obvious from Figure 5.11 that the turbulence kinetic energy is more influenced by the variations in the closure coefficients than the turbulent dissipation rate.

From the analysis of Table 5.7 and Figures 5.9 to 5.11 for the flow velocity of 1 m. s^{-1} the increase of 20% in the value of the closure coefficients $C_{\varepsilon 1}$ and $C_{\varepsilon 2}$ deviated the pressure drop values (our control variable) further from the experimental results. For this velocity the impact of the closure coefficients, σ_ε, σ_k, C_μ and σ_t was negligible. As the flow velocity increased, for 4 m. s^{-1},

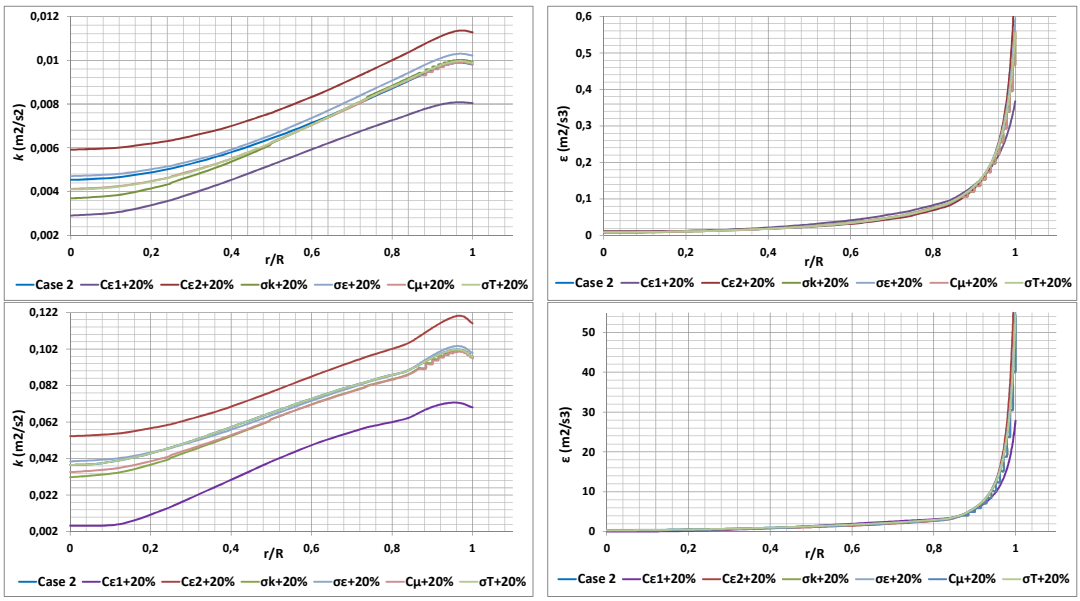

Figure 5.11 – 2D Turbulent Kinetic Energy (Right) and Turbulent Dissipation Rate (Left) for all closure coefficients values tested for a flow velocity of 1 m. s^{-1} (Top) and 4 m. s^{-1} (Bottom).

the deviation on calculated pressure drop for all closure coefficients increased, when the value of the closure coefficients was changed. This was expected, since at higher velocities the turbulence intensity will also be higher, and increasing $C_{\varepsilon 1}$ and $C_{\varepsilon 2}$ further contributes to that increase. Overall, it seems that the standard closure coefficients values, which were initially optimized for single phase-flows, are the adequate choice for homogeneous solid-liquid flows. As pointed out by Bardow et al. (2008) the optimization of the closure coefficients should be case specific and their study can lead to problem adapted turbulence models.

5.2. NUMERICAL STUDIES OF SOLID-LIQUID SUSPENSIONS FLOWS – SETTLING PARTICLES

After the numerical studies involving concentrated solid-liquid suspensions with the buoyant particles, the focus was shifted towards concentrated flows including settling particles. A publication by Lahiri & Ghanta (2010) was chosen, from the literature, that presented a study on horizontal flows of concentrated solid-liquid suspensions up to 40 % (v/v) of settling particles. Additionally, this study appeared to present a turbulence modulation by the particles at the highest particle concentration and highest flow velocity.

Based on this settling particles study, simulations were implemented, initially, with the Mixture Model coupled with a High Reynolds *k-ε* Turbulence Model and the Schiller-Naumann drag correlation, which demonstrated to overshoot the pressure gradient estimation considerably. Furthermore, for the settling particles data, modification of the particle-wall shear stress and implementations of different drag correlations were studied for the work depicted in this thesis. Numerical studies on highly concentrated flows of settling particles were conducted where the Schiller-Naumann (SN), the Haider-Levenspiel (SN) and the Gidaspow-Schiller-Naumann (GSN) drag correlations were implemented, as depicted in Section 4.5.

Finally, additional modifications by Hsu (Hsu 2003) were implemented to the Low Reynolds *k-ε* Turbulence Model, as seen in Section 4.8.1., to ascertain its influence on the dispersed phase in the turbulence modulation.

5.2.1. EXPERIMENTAL CONDITIONS

The flow conditions for the numerical studies involving settling particles are presented in Table 5.8. The flow was Newtonian and the particles were glass spheres with a density of 2470 $\mathrm{kg.m^{-3}}$ and 0.44 mm diameter with volumetric fractions ranging from 10 to 40 % (v/v) as shown in Table 5.8.

Table 5.8 – Conditions for the numerical studies with Lahiri & Ghanta (2010) data.

	FLOW DATA
PIPE ID [mm]	**54.9**
$U\ [m.s^{-1}]$	1.0 2.0 3.0 5.0
$\rho_F\ [kg.m^{-3}]$	998*
$\mu_F\ [Pa.s]$	1.02×10^{-3}*
Re	53430 107630 161109 268984
	PARTICLE DATA
$\rho_P\ [kg.m^{-3}]$	2470
$d_p\ [mm]$	0.44
$\phi\ [v/v]$	0.1 0.2 0.3 0.4

*** Values at 20ºC**

5.2.2. FLOW REGIME CONSIDERATIONS

Lahiri & Ghanta (2010) observed that the particles were asymmetrically distributed in the vertical plane with the degree of asymmetry, for the same concentration of particles, increasing with decreasing flow velocity. This was as expected since with the decrease in flow velocity there will be a decrease in turbulent energy that is responsible for keeping the solids in suspension. Also, it was further observed that for a given flow velocity, increasing particle concentration reduced the asymmetry due to enhanced interference effect between solid particles. The effect of this interference was so strong that the asymmetry, even at lower velocities, was attenuated at higher concentrations.

For the lower flow velocities and higher particle concentrations a moving or

sliding regime was observed and for the highest flow velocities a heterogeneous flow regime was acknowledged.

Deposition Velocities

From their experiments Lahiri & Ghanta (2010) observed that around 3 m. s^{-1} the vertical asymmetry in the solids distribution started to diminish. In their publication, data for the deposition velocities was not provided. The deposition velocities values attained from Correlations I to III (see Equations 5.1 to 5.7) were all similar (see Table 5.9) and they seem to contradict Lahiri & Ghanta (2010) considerations that the deposition velocity diminished as the particle concentration increased. This behaviour was attributed to increasing particle-particle interactions as result from increasing particle concentrations. Thus, for highly concentrated settling suspensions flows, further improvements are wanted on the deposition velocities calculation.

Table 5.9 – Deposition velocities for the settling particles numerical studies using Lahiri & Ghanta (2010) experimental data.

			Correlation I			Correlation II	Correlation III	
	d_p (mm)	ϕ	AR	F_L	V_D ($m.s^{-1}$)	V_D ($m.s^{-1}$)	F_L	V_D ($m.s^{-1}$)
54.9 mm pipe	0.44	0.1	1573	1.06	1.34	1.42	0.97	1.23
		0.2	1573	1.06	1.34	1.63	1.06	1.34
		0.3	1573	1.06	1.34	1.77	1.12	1.41
		0.4	1573	1.06	1.34	1.88	1.16	1.46

5.2.3. NUMERICAL STUDIES WITH THE MIXTURE MODEL & HIGH REYNOLDS k-ε TURBULENCE MODEL

Validity of the Mixture Model

The flows studied by Lahiri & Ghanta (2010) were all turbulent (see Table 5.8) which requires a turbulence closure and a model for the interphase forces, namely the drag force (see Section 4.6). To ascertain which drag correlation was needed, the Particle Reynolds Number (Re_p) was calculated

using Equation 4.60. The particle Terminal Velocity (V_T) was again used as an initial estimate for the slip velocity (see Equation 4.108). The calculated values for the Particle Stokes Number, Particle Reynolds Number and Terminal Velocity are displayed in Table 5.10.

Table 5.10 – Particle data for Lahiri & Ghanta (2010) experiments.

	$\rho_P\ [kg.m^{-3}]$	$d_p\ [mm]$	$V_T\ [m.s^{-1}]$	Re_p	$U\ [m.s^{-1}]$	$\phi\ [v/v]$	St_p
Particle Data	2470	0.44	0.152	65.6	1.0	0.1	0.57
					2.0	0.2	1.14
					3.0	0.3	1.71
					5.0	0.4	2.85

Geometry

The 3D simulations domain had a vertical symmetrical assumption, i.e., it was assumed that the flow was mirrored in regards to a vertical plane at the centre of the flow. Two different pipe sections with the internal diameter shown in Table 5.8 were implemented. An entry length of 3 meters long was imposed to allow the full development of the flow while the second section was 0.25 m long, where the flow was assumed as stabilized.

Finite Element Mesh

Grid independent results were obtained with the FEM mesh displayed in Figure 5.12 with the characteristics presented in Table 5.11.

Table 5.11 – Mesh parameters for the initial studies with the settling particles.

	3D
Number of Elements	413 950
Number of Boundary Layers	6
Wall Lift off in Viscous Units (y^+)	11.06

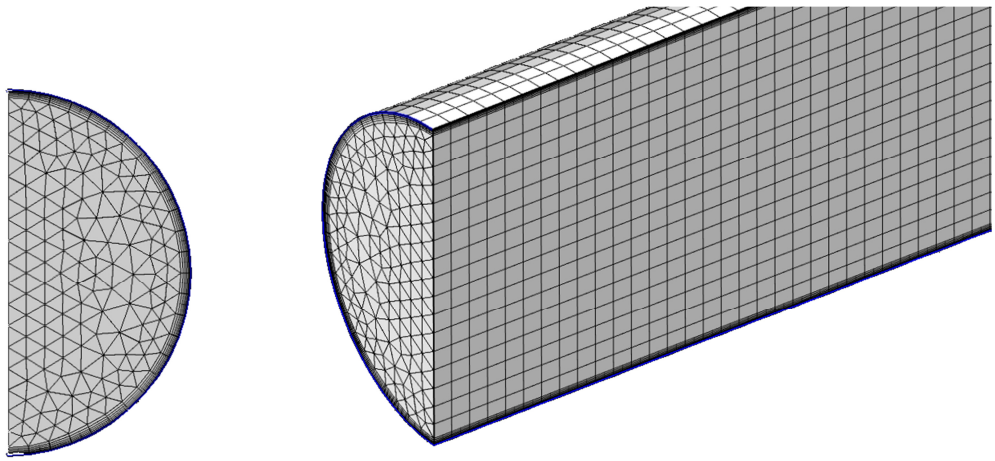

Figure 5.12 – 3D unstructured mesh employed with the Mixture Model and High Reynolds Turbulence closure for the settling particles numerical studies.

The wall lift-off in viscous units was the same as with the previous simulations for the buoyant particles, 11.06 (COMSOL Multiphysics 2013).

Boundary Conditions

The applied boundary conditions for these initial studies with the settling particles were as described below:

i. at the inlet, the initial velocities (see Table 5.8) were imposed in the direction perpendicular to the pipe cross-section and the turbulence intensity and length scales were equal to those depicted in Equations 5.10 and 5.11.
ii. the normal gradients of k and ε, at the outlet, were again fixed to zero as given by Equation 4.75, and the pressure value was also assigned to zero.
iii. the near wall treatment was done using Wall Functions (see Equation 4.80). As with the previous numerical studies for the buoyant particles, the simulations were developed early in the work: therefore, the versions available for COMSOL Multiphysics® were 4.1 and 4.2, which did not possess the option to impose any roughness height (COMSOL Multiphysics 2013), thus the term AB was null.

Numerical Results

As mentioned above, one of the characteristics that conditioned the choice of the published studies to validate the modelling results was the existence of experimental data where, seemingly, turbulence modulation by the particles occurred, more specifically, turbulence dampening or turbulence attenuation. Looking at Figure 5.13, and using the pressure gradient as a control variable, one of the indications of turbulence attenuation is a pressure gradient similar to single phase flows, particularly for the highest flow velocities and particle concentrations (see black highlight in Figure 5.13). In the highlighted zone, the 40 % (v/v) particle concentration flow has a similar pressure gradient, for the same flow velocity, as the water flow and this is considered turbulence attenuation.

The Mixture Model coupled with a High Reynolds k-ε Turbulence Model used to simulate the experimental conditions, using the data in Table 5.8, provided the numerical results shown in Figure 5.13. From Figure 5.13 it can be seen that the deviations between the experimental data (designated "EXP" in Figure 5.13) and the numerical results with the Mixture Model and the High Reynolds k-ε Turbulence Model (designated "MM & k-ε" in Figure 5.13), are, overall, quite high. The lowest deviation occurs for a solid volumetric fraction of 10 % (v/v) and for a flow velocity of 5 m. s^{-1}.

Generally, the Mixture Model coupled with the High Reynolds k-ε Turbulence closure behaves poorly for all flow velocities with the settling particles and the biggest deviations occur at the lowest flow velocities for the higher particle concentrations. These deviations are attributed to the mechanical friction between the particle moving bed and the pipe wall, a drawback of the Mixture Model (Ling et al. 2003). For higher concentrations at intermediate velocities, the mechanical friction between the particle moving bed is lower due to the increase of particle-particle interactions, causing particle dispersion and decreasing the frictional pressure drop (D.R. Kaushal and Tomita 2007; V. Matoušek 2002).

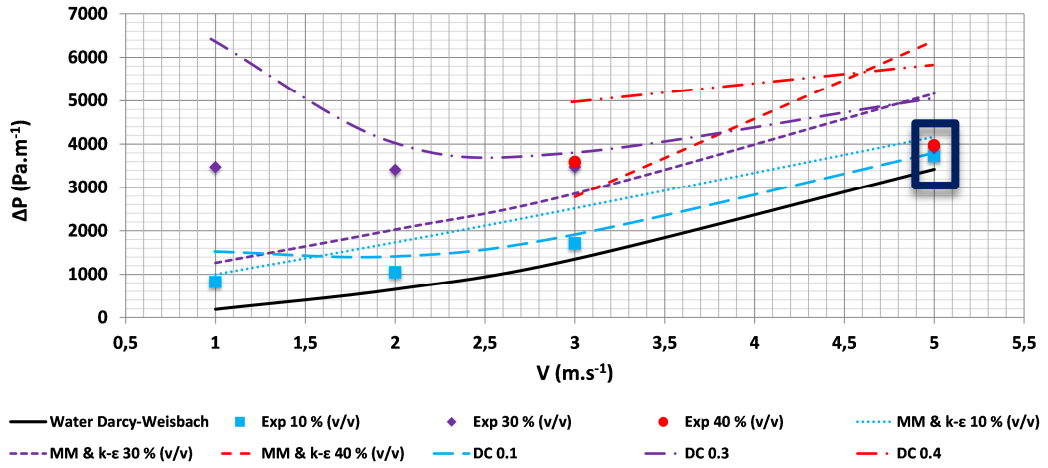

Figure 5.13 – Pressure gradients comparison between Lahiri & Ghanta (2010) experimental results (EXP) and the calculated pressure gradients for the settling particles using the Mixture Model with the High Reynolds k-ε Turbulence model (MM & k-ε) and the Durand-Condolios correlation (DC).

Results obtained using the Durand-Condolios correlation (designated "DC Correlation" in Figure 5.13), typically utilized for concentrated suspensions flow predictions, were included in Figure 5.13 to serve as comparison with the numerical simulations results. It is noticeable that these correlations only provide reasonable estimations for the lowest concentration of 10 % (v/v), especially for the highest velocities. The pressure drops for the remaining concentrations have a considerable offset and do not provide a good estimate of the reality.

Overall, the tendencies detected in the normalized numerical and experimental vertical particle concentrations profiles (see Figure 5.14) are in concordance. In Figure 5.14 ϕ is the particle volumetric fraction in the vertical axis and ϕ_{vf} is particle volumetric fraction at the inlet. The general tendency of the particle concentrations profiles is followed by the numerical ones, with the exception of the lower flow velocities, where the deviations are more pronounced, especially in the bottom region of the pipe cross-section. This can be again attributed to the aforementioned drawback of the Mixture Model when numerically depicting the presence of a moving bed regime. Additionally, the pressure gradients are not well described by the model, as seen in Figure 5.13, and so, it can be inferred that the Mixture Model with a

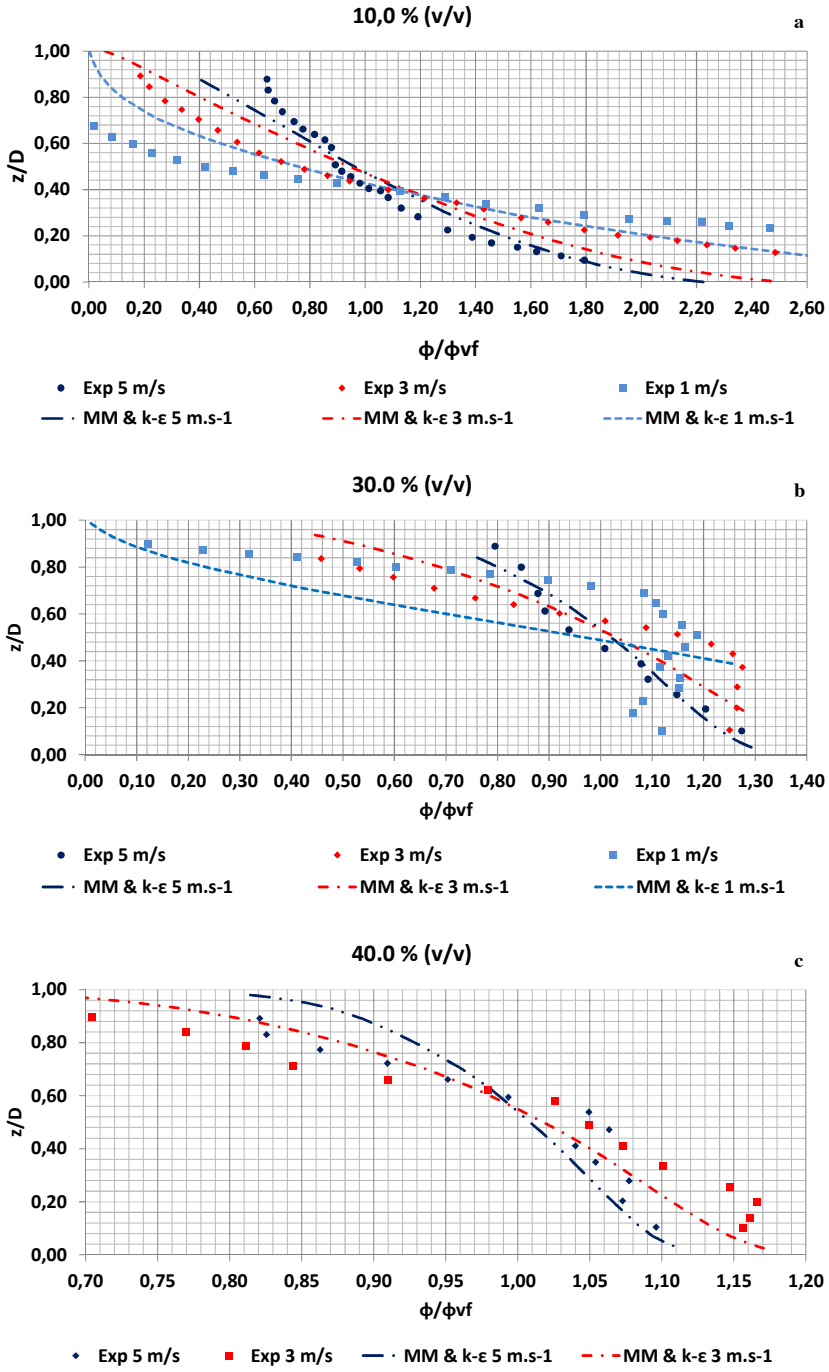

Figure 5.14 – Normalized vertical solid concentration profiles with (a) 10 % (v/v), (b) 30 % (v/v), (c) 40 % (v/v) of settling particles comparison between the experimental data (EXP) and numerical results for the Mixture Model with the High Reynolds *k-ε* Turbulence model (MM & k-ε).

High Reynolds *k-ε* Turbulence closure is an inadequate modelling choice for settling particles, becoming increasingly inaccurate with the increase in particle concentration and with the decrease in the flow velocity.

5.2.4. NUMERICAL STUDIES WITH THE MIXTURE MODEL & JONES-LAUNDER (JL) LOW REYNOLDS *k-ε* TURBULENCE MODEL

Following the numerical studies with the Mixture Model coupled with the High Reynolds *k-ε* Turbulence Model it became evident that this model, in its standard formulation, was not suited for the study of concentrated solid-liquid suspensions flows. The possible explanation assumption was that the Law of the Wall or Wall Functions, which are empirical approximations employed in single-phase models, are not adequate for the numerical study of concentrated solid-liquid suspensions flows (D.R. Kaushal and Tomita 2007; S. Lahiri and Ghanta 2010; V. Matoušek 2002; Ekambara et al. 2009): consequently, incorporation of a Jones-Launder Low Reynolds Turbulence closure in the Mixture Model, for the settling particles studied, can circumvent this issue, since the Low Reynolds Closures solves the model through the integration of the turbulence equations until the wall.

Finite Element Mesh

The Jones-Launder Low Reynold Turbulence Model, as most Low Reynolds Turbulence Models, requires very fine meshes close to the wall; therefore, the first computational element must have its centroid in $y^+ \approx 1$ (See Section 4.7.4, LRN-Models: Integration Method). For the numerical studies with the Mixture Model coupled with the Jones-Launder Low Reynolds *k-ε* turbulence model (MM+LR) a value of 1 wall lift-off in viscous units was employed (Table 5.12) and the mesh was refined until grid independent results were attained (see Figure 5.15).

Table 5.12 – Mesh parameters for the initial studies with the settling particles using a Low Reynolds Turbulence closure.

	3D
Number of Elements	472 905
Number of Boundary Layers	12
Wall Lift off in Viscous Units (y^+)	1

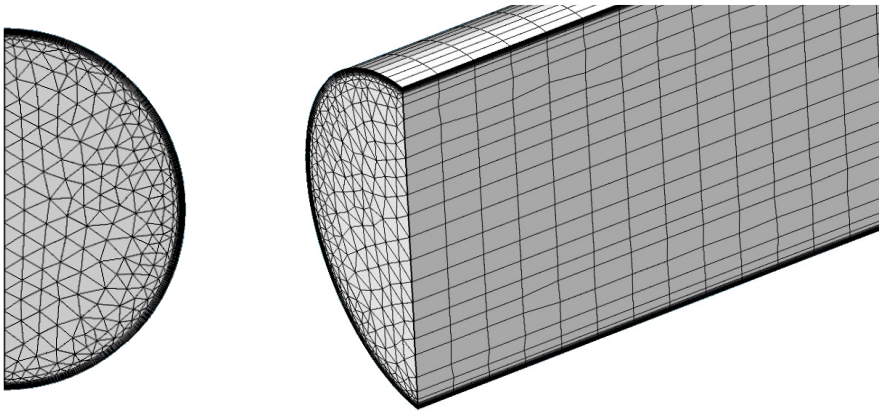

Figure 5.15 – 3D unstructured mesh employed with the Mixture Model and a Low Reynolds Turbulence closure for the settling particles numerical studies.

Boundary Conditions

The applied boundary conditions for the Mixture Model and Low Reynolds Turbulence closure are depicted in Table 4.1 in Section 4.6.3, in detail. These conditions are summed up below:

i. at the inlet, the initial velocities (see Table 5.8) were imposed in the direction perpendicular to the pipe cross-section and the turbulence intensity and length scales were equal to those depicted in Equations 5.10 and 5.11.
ii. the normal gradients of k and ε, at the outlet, were again fixed to zero as given by Equation 4.75, and the pressure value was also assigned to zero.
iii. the near wall treatment was done as shown in Table 4.1, with $k_{wall} = 0$ and $\tilde{\varepsilon}_{wall} = 0$. Additionally, the "no-slip" boundary condition is imposed at the pipe wall, i.e., the flow velocity is set to zero at the pipe wall (COMSOL Multiphysics 2012; Versteeg and Malalasekera 2007).

Numerical Results

The numerical results attained with this formulation (designated "MM & LR" in Figure 5.16) are compared to the experimental pressure gradients (designated "EXP" in Figure 5.16) for different concentrations and flow velocities in Figure 5.16.

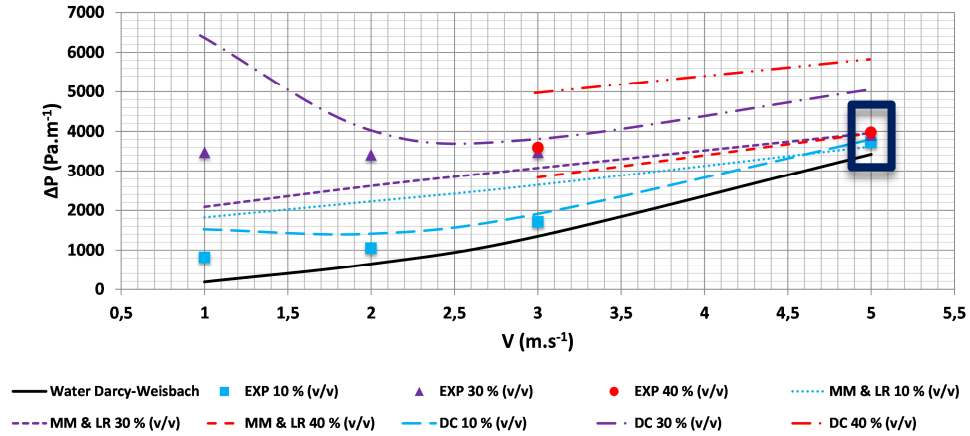

Figure 5.16 – Pressure gradients comparison between Lahiri & Ghanta (2010) experimental results (EXP) and the calculated pressure gradients for the settling particles using the Mixture Model with the Low Reynolds k-ε Turbulence model (MM & LR) and the Durand-Condolios correlation (DC).

There is an improvement in pressure drop predictions for flow velocities from 3 up to 5 $\mathrm{m.s^{-1}}$ for all particles concentrations. This improvement is more notorious for the highest particle concentrations of 30 and 40 % (v/v). For 5 $\mathrm{m.s^{-1}}$ there is a similarity between this pressure drop values and the monophasic pressure drops: the reason for this is explained in the literature (V. Matoušek 2002; D.R. Kaushal and Tomita 2007) and is caused by lift-forces resulting from the viscous-turbulent interface at the bottom layer of particles, closest to the pipe wall. By using a Low Reynolds turbulence closure the flow is resolved until the wall, and the correct behaviour of the turbulence in that region is depicted for high flow velocities. By comparison, the Durand and Condolios correlations perform worst for the highest concentration and velocities.

The biggest deviations occur for the lower flow velocities (see Table 5.13);

however, when working with solid-liquid suspension flows the highest velocity is desired to prevent settling of particles, thus making this value of less importance when compared with the deviations at the highest velocity. In summary, for the settling particles, the Mixture Model with the High Reynolds *k-ε* Turbulent closure responds quite well for low particle concentrations, but with increasing particles in the flow, the deviation rises significantly peaking at a 60 % deviation for a solid volumetric fraction of 40 % (v/v) and a flow velocity of 5 $\mathrm{m.\,s^{-1}}$.

With the inclusion of the Jones-Launder Low Reynolds Turbulence closure in the Mixture Model, the deviations for the solids volumetric fractions with the highest velocities decrease significantly and overall the deviations are smaller when compared with the High Reynolds Turbulence closure, for the highest concentrations. For the lowest solid volumetric concentration, however the High Reynolds Turbulence closure behaves superiorly for all the velocities, except for the highest velocity of 5 $\mathrm{m.\,s^{-1}}$. For these lower velocities and for the lowest particle concentrations, the Mixture Model with the inclusion of the Jones-Launder Low Reynolds Turbulence closure behaves poorly by comparison with the High Reynolds Turbulence closure, which can be attributed to the fact that the suspension viscosity is higher at the pipe bottom. Since the Low Reynolds Turbulence closure integrates the turbulence equations all the way to the wall, the pressure drop will rise accordingly due to an overshoot of the suspension and turbulent viscosity with this closure: in fact, for this concentration, the mentioned overshoot is not compensated by the presence of strong lift forces resulting from particle-particle interactions in that region, as happens for the higher concentrations.

Table 5.13 – Comparison between experimental and numerical pressure drops for settling particles.

	Settling Particles			
	V (m.s^{-1})	ΔP (Pa/m)		
		$\phi_d = 0.1$	$\phi_d = 0.3$	$\phi_d = 0.4$
MM+HR	**1**	1000.86 **(22.39%)**	1265.76 **(-63.56%)**	----
	2	1735.4 **(65.93%)**	2027.81 **(-40.57%)**	----
	3	2517.93 **(47.31%)**	2857.2 **(-17.87%)**	2782.2 **(-22.51%)**
	5	4168.03 **(11.92%)**	5166 **(32.14%)**	6385.4 **(60.71%)**
MM+LR	**1**	1824.72 **(123.13%)**	2089.9 **(-39.83 %)**	----
	2	2228.3 **(113.1%)**	2620.96 **(-23.18%)**	----
	3	2645.4 **(54.77%)**	3076.28 **(-11.57%)**	2838.52 **(-20.94%)**
	5	3620 **(-2.8%)**	3959.84 **(1.29%)**	3955.98 **(-0.44%)**
Durand Condolios	**1**	1525.9 **(86.60%)**	6425.7 **(170.81%)**	----
	2	1412.5 **(35.06%)**	4044.7 **(40.22%)**	----
	3	1904.6 **(11.43%)**	3802.9 **(16.59%)**	4967.7 **(38.36%)**
	5	3792.7 **(1.84%)**	5053.4 **(29.82%)**	5827.4 **(46.66%)**

Regarding the particle concentration profiles which are presented in Figure 5.17, there was also a slight improvement, as can be seen by comparing Figures 5.14 and 5.17, more notorious for the case of the highest particle concentration, 40 % (v/v). In Figure 5.17 ϕ is the particle volumetric fraction in the vertical axis and ϕ_{vf} is particle volumetric fraction at the inlet.

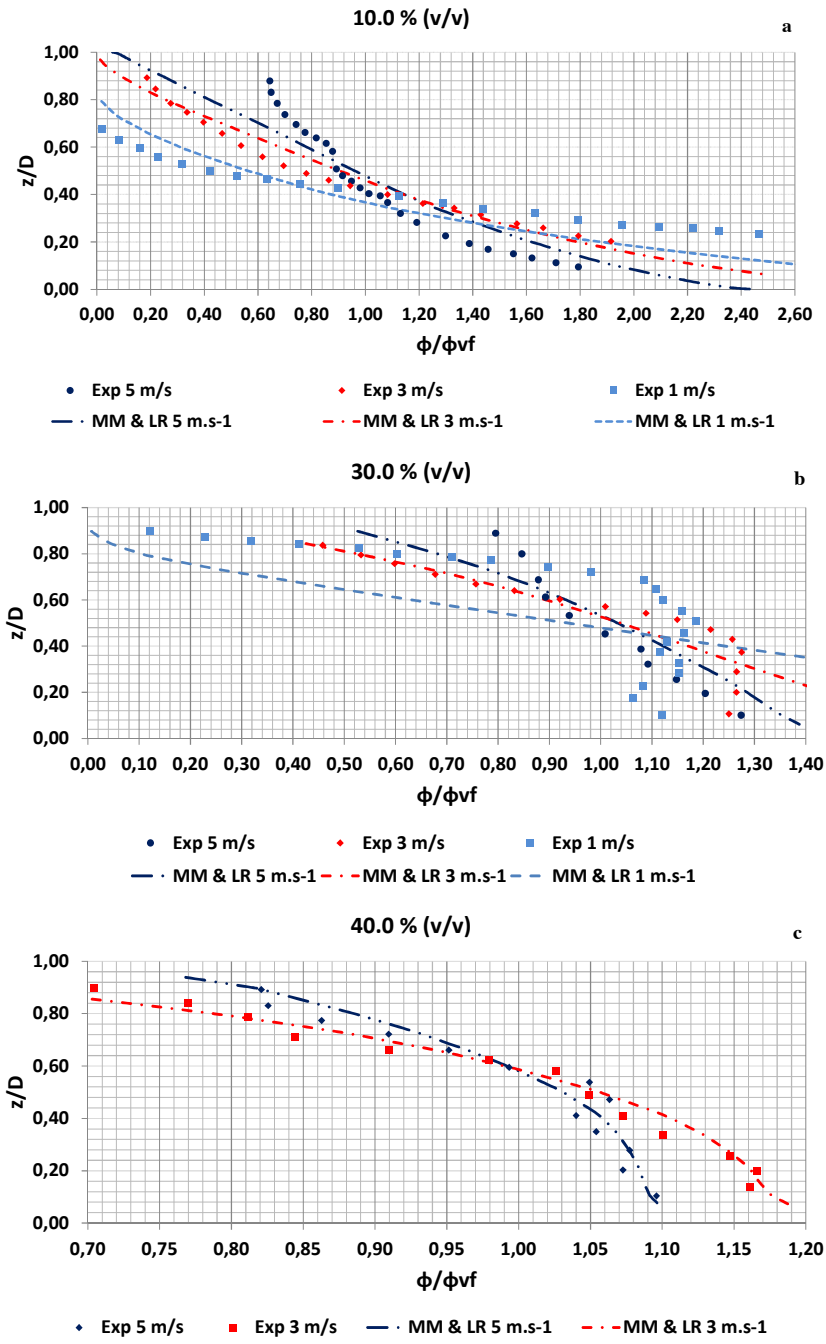

Figure 5.17 – Normalized vertical solid concentration profiles with (a) 10 % (v/v), (b) 30 % (v/v), (c) 40 % (v/v) of settling particles comparison between the experimental data (EXP) and numerical results of the Mixture Model with the Low Reynolds k-ε Turbulence model (MM & LR).

5.2.5. EFFECT OF PARTICLE–WALL SHEAR STRESS

As pointed out in Section 5.2.2, for flow velocities below 3 m. s^{-1} there was a presence of either a stationary or a moving bed. For these flow regimes the

Mixture Model does not provide accurate depictions of the flow (Ling et al. 2003), as was also demonstrated here. So, in the remaining numerical studies in this Chapter the focus will be on the higher flow velocities, 3 and 5 m. s^{-1}. Additionally, in industrial environments higher flow velocities, where the particles are more uniformly fluidized, are preferred.

An inspection of Figures 5.13 and 5.16 shows that the Mixture Model undershoots the pressure gradient for the 3 m. s^{-1} for the highest concentrations, of 30 and 40 % (v/v). Thus, for the case of this lower velocity and for these higher particle concentrations, the assumption made was that the Mixture Model did not properly depicted the contribution of particle-wall stresses at the bottom of the pipe; thus, introducing a Bagnold type expression (see Section 4.8), as seen in the literature (Václav Matoušek 2005; Schaan et al. 1997; Randall G Gillies, Shook, and Xu 2004), in the shear stress equation at the wall, should improve the Mixture Model performance.

Table 5.14 – Comparison between the experimental and simulated pressure gradient with the Mixture Model coupled with a Low Reynolds Turbulence closure (MM+LR) and the Mixture Model coupled with a Low Reynolds Turbulence closure and the modified wall shear stress (MM+LR+τ_s) for a flow velocity of 3 m. s^{-1} and 40 % (v/v) particle concentration.

V (m/s)	**ΔPexp (Pa/m)**	**ΔP MM**+LR **(Pa/m)**	**ΔP MM**+LR+$\boldsymbol{\tau_s}$ **(Pa/m)**
3.0	3587.2	2838.52 (-20.9%)	3065.58 (-14.5%)

The inclusion of the Bagnold Type expression (see Equation 4.93) into the Mixture Model coupled with a Low Reynolds Turbulence Closure there was a small improvement, as shown in Table 5.14, again considering a flow velocity of 3 m. s^{-1} and 40 % (v/v) particle concentration. These numerical studies employed the same flow and boundary conditions depicted in Section 5.3.4 and a comparison is shown in Figure 5.18 for the turbulence variables and the particle concentration profiles. From the Figure 5.18, with the inclusion of

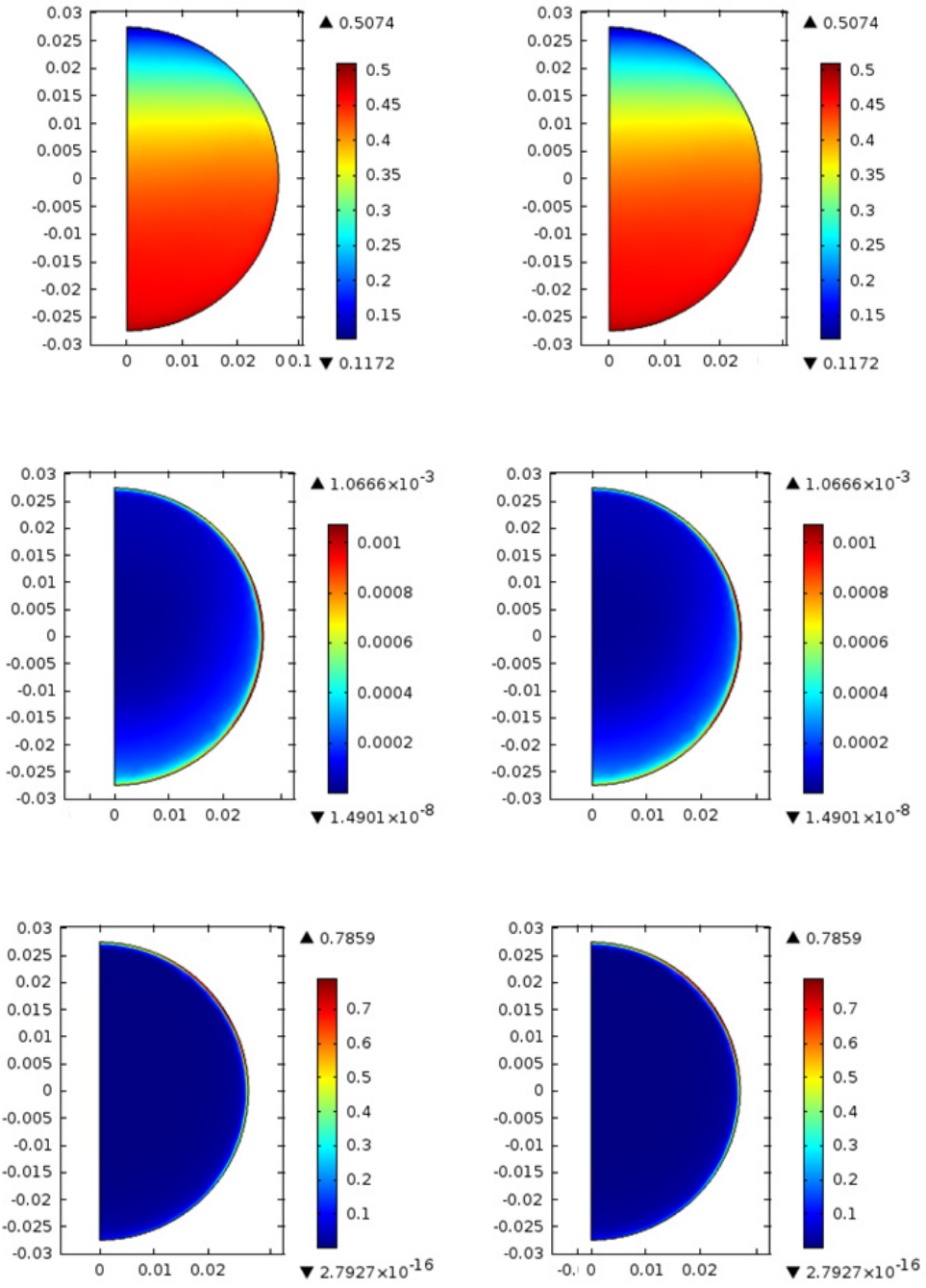

Figure 5.18 – Comparison between 2D cross-sectional profiles for the particle concentration (Top Row), Turbulent Kinetic Energy (Middle Row) and Turbulent Dissipation Rate (Bottom Row) for the MM+LR (Left Column) and MM+LR+τ_s (Right Column) for a flow velocity of 5 m. $s^{-1}$and 40 % (v/v) particle concentration.

Equation 4.93, the Turbulent Kinetic Energy, k, and the Turbulent Dissipation Rate, ε, have remained practically the same. This was expected as the pressure gradient variation was small with addition of the Equation 4.93 to

the wall shear stress.

In spite of this small improvement, the inclusion of the Bagnold type expression seems to provide a better depiction on the particle-wall interaction for these flow conditions. Additional numerical studies are warranted to fine tune the proportionality coefficient, K_i, for highly concentrated flows of solid-liquid suspensions.

5.2.6. DRAG CORRELATIONS STUDY

The numerical studies involving the drag correlations were based on the data for the vertical distribution of settling particles from the chosen literature (S. Lahiri and Ghanta 2010) and were focused on the highest particle concentrations, namely, 30 and 40 % (v/v) as well as the higher flow velocities, 3 and 5 m. s^{-1}.

For these numerical studies the flow and boundary conditions were equal to those depicted in Section 5.3.4 for the Mixture Model studies coupled with a Low Reynolds Turbulence closure.

Solids Volumetric Fraction of 40 % (v/v)

In the following Figures the numerical results for the vertical particle distribution, drag coefficient and slip velocity (velocity between phases) are presented for the highest particle volumetric concentration of 40 % (v/v) and for 3 and 5 m. s^{-1} flow velocities. In Figure 5.19, the numerical profiles for the vertical solids distribution profiles obtained with the different drag correlations are compared with experimental data of Lahiri & Ghanta (2010). From the comparison for the profiles for the two flow velocities in Figure 5.20 it is obvious that the GSN drag correlation is inadequate for both flow velocities at this particle concentration.

The other two drag correlations depict quite well the concentration profiles, still, for the high flow velocity the SN drag correlation seems to depict more accurately the experimental particle distribution profiles and the HL drag

correlation performs better for medium flow velocities ($3\ \mathrm{m.s^{-1}}$). The GSN drag correlation inability to represent the experimental profiles could be related to the fact that, according to the literature, it only performs accurately for solid volumetric fractions below 20% (Visuri, Wierink, and Alopaeus 2012) when a homogeneous distribution is more common. In spite of being developed to account for particle-particle interaction, through the introduction of the voidage function (Visuri, Wierink, and Alopaeus 2012), there is an overshoot in the estimation of the fluidization of the particles.

For the medium flow velocity ($3\ \mathrm{m.s^{-1}}$) with the SN drag correlation, established for a single sphere, the calculated results loose quality towards the bottom of the pipe, where the moving bed is present and is dominated by particle-particle and particle-wall interactions with a behaviour that is considerably different from a single sphere.

Observing Figure 5.19 for both velocities the SN correlation seems to better describe flows where most particles are fluidized and where the particle-particle interactions are significantly lower when compared with a moving bed. Similar observations have been found in the literature where the SN drag correlation behaves accurately for two-phase complex flows (Yilmaz and Gundogdu 2009). The HL drag correlation behaviour, on the contrary, performs well for regions with high particle-particle interaction, as is the case of ones with a moving bed in the pipe bottom for the low flow velocities.

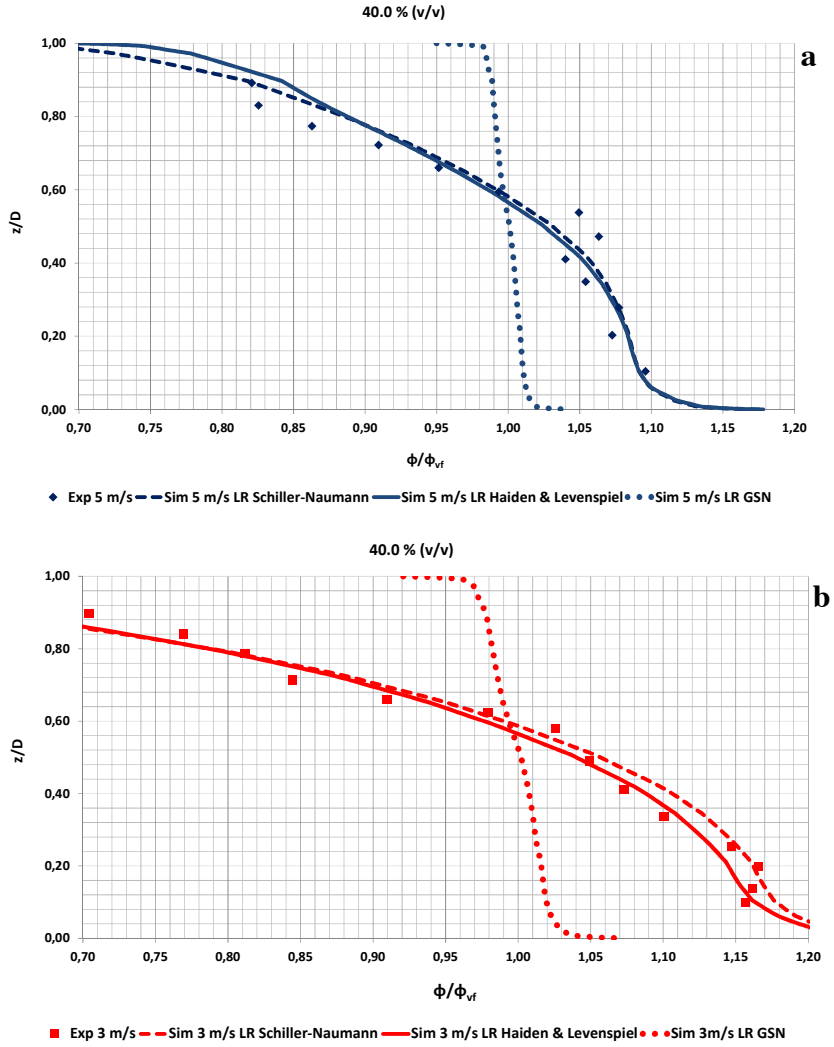

Figure 5.19 – Adimensional numerical vs experimental vertical particle distribution profiles (a) for a flow velocity of 5 m. s^{-1}; (b) for a flow velocity of 3 m. s^{-1} with a particle volumetric fraction of 40 % (v/v).

Although there is no experimental data, it is still worthy to analyse the numerical slip velocity profiles (see Figure 5.20) obtained with the different correlations. Again, as noted for the solids volumetric concentration profiles, the GSN correlation numerical data for the slip velocity for both horizontal and vertical axis, Figure 5.20, displays a behaviour that differs significantly from the other drag correlations. This, in conjunction with the experimental and numerical results for particles concentration in Figure 5.19, seems to further demonstrate that the GSN drag correlation is inadequate for these flows. This is even more noticeable for the medium flow velocity (3 m. s^{-1}) for which the numerical slip profiles obtained with the GSN correlation

display an almost homogeneous behaviour, with a near zero slip velocity and are practically uniform in the vertical direction. Both the SN and HL drag correlations provide similar results in both the horizontal and vertical axis, with the exception of the top of the pipe, for both flow velocities. The previous analysis for the vertical particle concentration profiles agrees with the slip velocity numerical data in the vertical direction, i.e., the slip velocity is lower near the bottom for a low flow velocity ($3\,\mathrm{m.s^{-1}}$), where the particles movement is hindered by the other particles, and higher at the top of the pipe where there are fewer particles and more space. This is a good indicator of the quality of the numerical slip profiles.

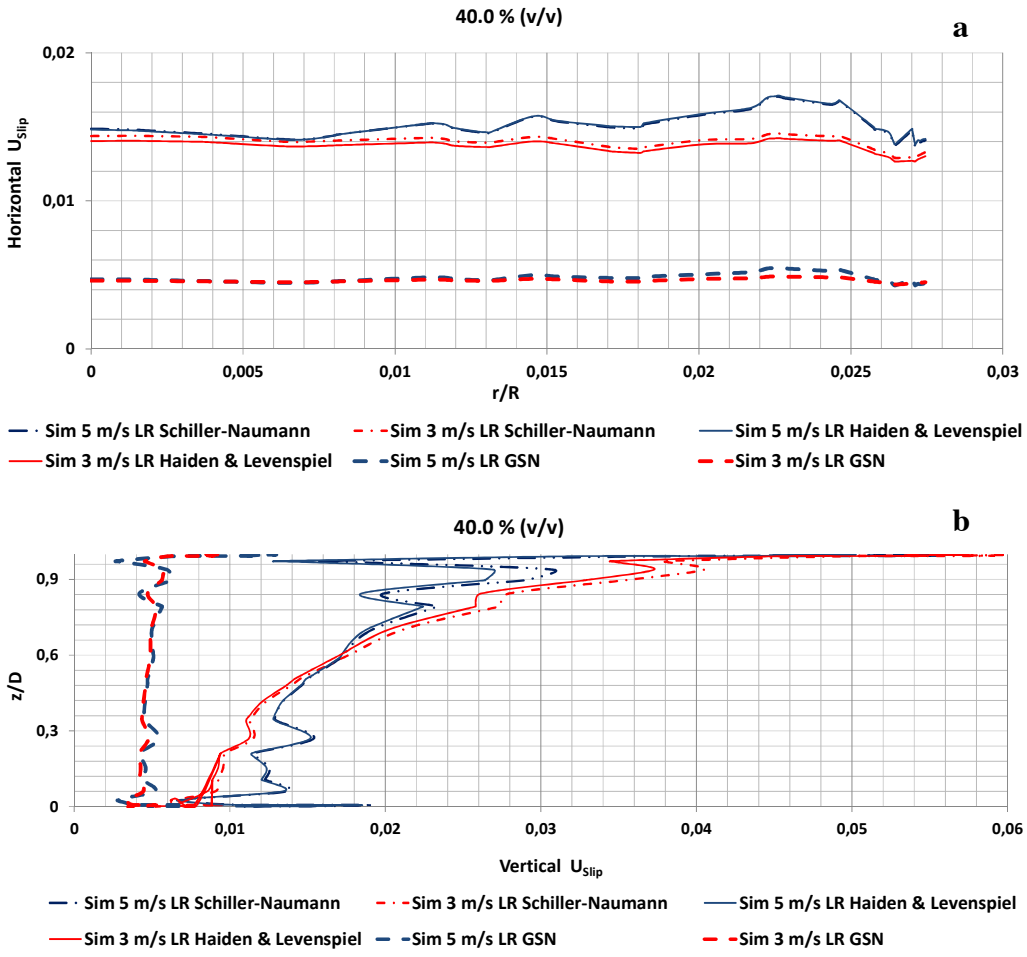

Figure 5.20– Numerical horizontal (a) and vertical (b) slip velocity profiles for flow velocities of 3 and 5 $\mathrm{m.s^{-1}}$ with a particle volumetric fraction of 40 % (v/v).

The tendencies for both the solid volumetric and slip velocity numerical

profiles are reflected in the numerical drag profiles (see Figure 5.21) with the GSN drag correlation. There is a considerable deviation from the remaining drag correlations, higher values being obtained with the GSN correlation, in line with the lack of accuracy of this correlation in depicting the experimental solid volumetric profiles. The HL and SN drag correlations provide similar values, again, for both flow velocities. It is also observable that the drag values are higher near the top of the pipe for the higher flow velocities (5 m. s^{-1}), as expected, since the amount of fluidized particles is higher in this flow regime.

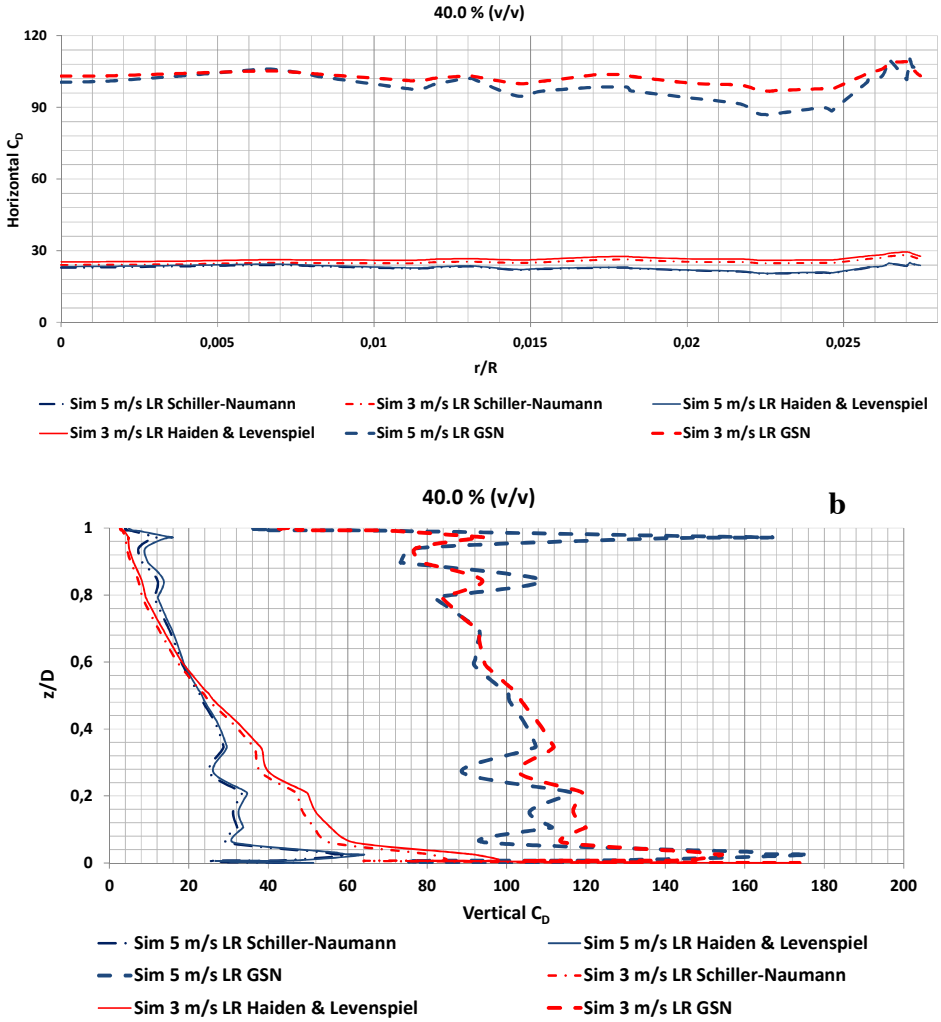

Figure 5.21 – Numerical horizontal (a) and vertical (b) drag profiles for flow velocities of 3 and 5 m. s^{-1} with a particle volumetric fraction of 40 % (v/v).

At 3 m. s^{-1} the drag is considerable higher in the bottom of the pipe, since

there is a moving bed flow regime where particle concentration is higher, in the bottom, and movement is hindered by other particles. The HL drag numerical values are slightly higher at the pipe bottom than the SN drag correlation, but the difference is not significant. An interesting observation, and contrarily to what happens at the lowest flow velocity ($3\ \mathrm{m.s^{-1}}$), is that the peak of the drag value for the highest flow velocity ($5\ \mathrm{m.s^{-1}}$) occurs slightly above the pipe bottom: it can indicate that at this flow velocity the particles migrate from the wall, i.e. they migrate from a region with high shear rate (pipe wall) towards a region with lower shear rate, when turbulence modulation occurs. This phenomenon has also been described in the literature (V. Matoušek 2002; D.R. Kaushal and Tomita 2007).

Solids Volumetric Fraction of 30 % (v/v)

A lower particle concentration, 30 % (v/v), was also studied for a lower velocity of $2\ \mathrm{m.s^{-1}}$, since there is no data by Lahiri & Ghanta (2010) below $3\ \mathrm{m.s^{-1}}$ flow velocity for 40 % (v/v) particle concentration. So, with a $2\ \mathrm{m.s^{-1}}$ flow velocity and 30 % (v/v) particle concentration, a different flow regime could be studied. Under these conditions they observed a stationary bed with moving particles at the bed interface. Although all drag correlations present deviations, particularly at the pipe centre, the GSN drag correlation contrarily to what was observed for 40 % (v/v) particle concentration, now seems to provide the more adequate numerical representation of the concentration profile, specifically for the lower half of the pipe (see Figure 5.22).

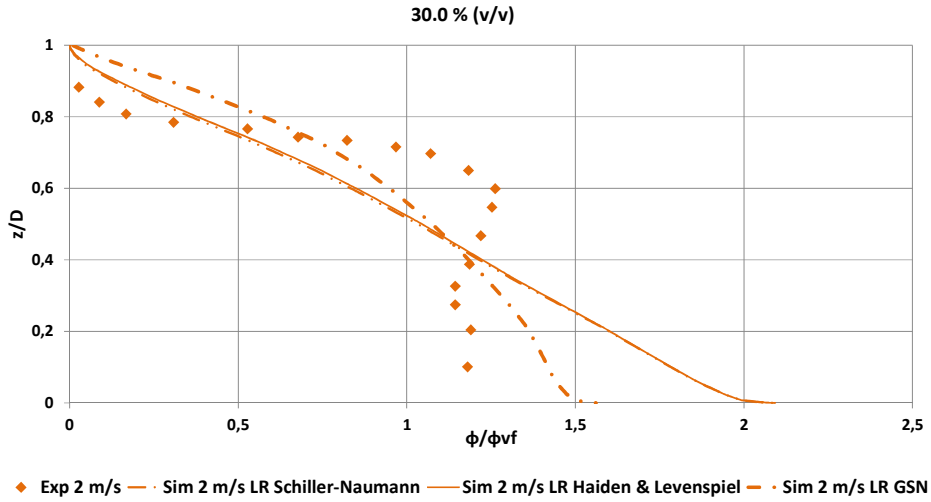

Figure 5.22 – Adimensional numerical vs experimental vertical particle distribution profiles for a flow velocity of 2 m. s^{-1} with a particle volumetric fraction of 30 % (v/v).

Following the same analysis as in the previous section, the GSN correlation provides lower values for both the horizontal and vertical numerical slip velocity values (see Figure 5.23). Moreover, looking at the vertical drag profiles, the GSN drag correlation (see Figure 5.24), it is perceptible that it presents the more reasonable profile for this particle concentration, with the drag being higher in the lower region, considering the presence of a stationary bed with moving particles at the bed interface, the bulk of the particles occupying the lower region of the pipe. The results for the drag and slip velocity obtained with the GSN correlation justify the better fit obtained for the concentration profiles when using this correlation. Another important aspect is the fact that the difference between numerical slip velocity values between drag correlations is less significant than for the 3 and 5 m. s^{-1} flow velocities for 40 % (v/v) particle concentration.

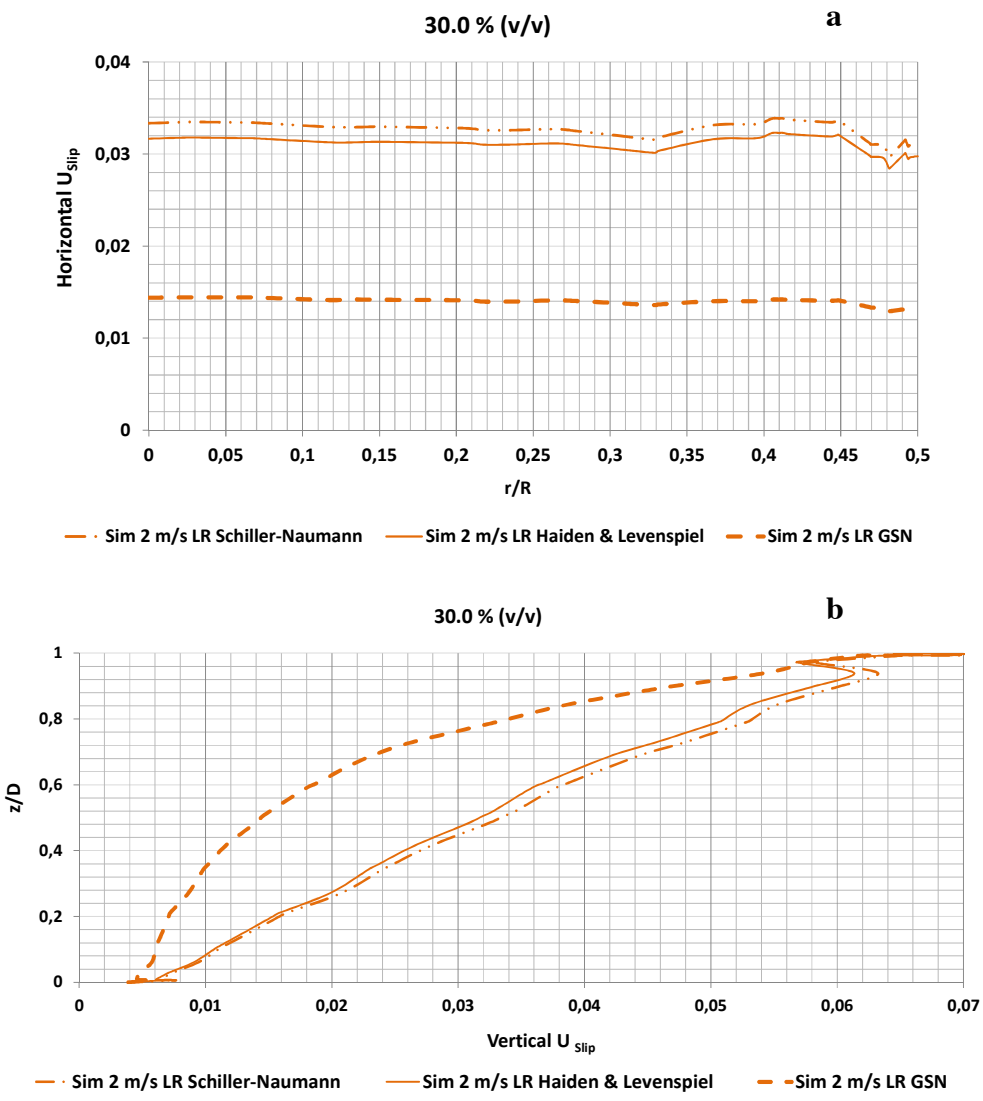

Figure 5.23– Numerical horizontal (a) and vertical (b) slip velocity for a flow velocity of 2 m. s^{-1} with a particle volumetric fraction of 30 % (v/v).

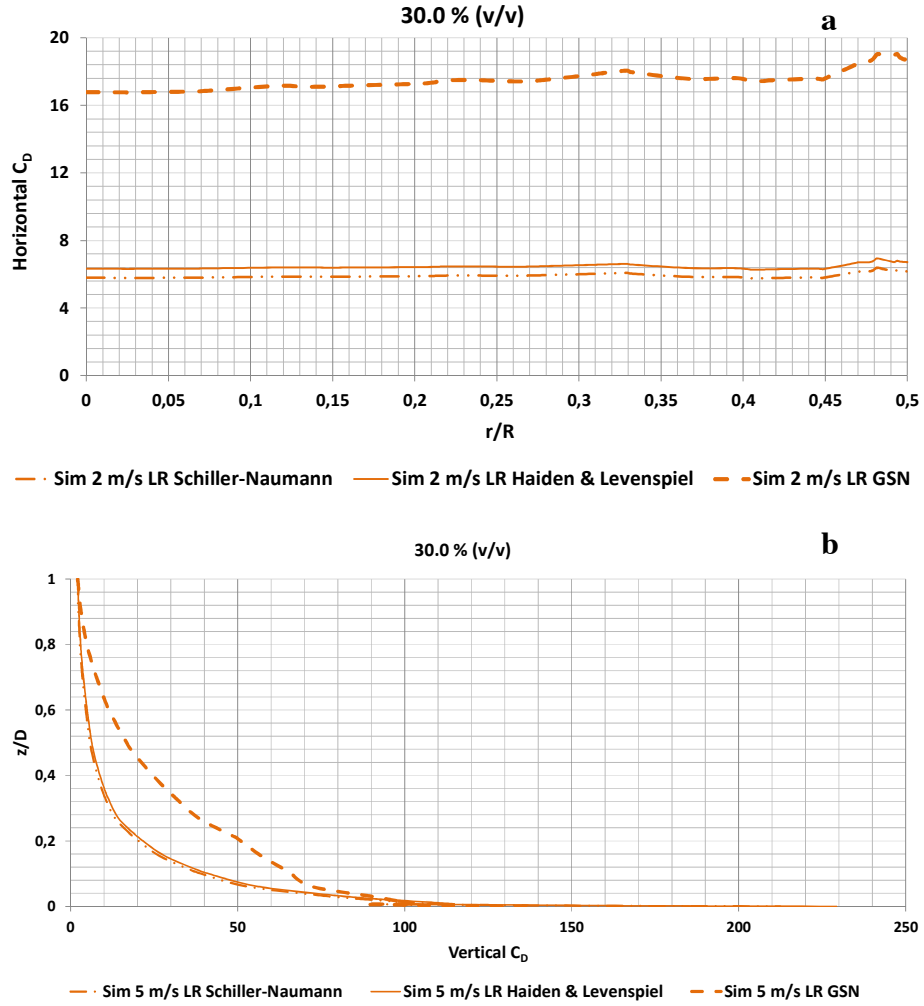

Figure 5.24 – Numerical horizontal (a) and vertical (b) drag profiles for a flow velocity of 2 m. s^{-1} with a particle volumetric fraction of 30 % (v/v).

Pressure Drop Profiles for the different Drag Correlations

Finally, for the pressure drop, which can be seen as a control variable in this study, at 40 % (v/v) particle concentration and for a flow velocity of 5 m. s^{-1}, where turbulence attenuation occurs, it can be observed in Table 5.15 that the pressure gradients values are quite similar for all drag correlations with a slight improvement being observed when compared with just the Low Reynolds turbulence model and the Schiller-Naumann results (see Table 5.13). For both velocities and particle concentrations the GSN is the drag correlation that presents the biggest deviations and, overall, the HL drag correlation depicts well the pressure gradients. For the lowest flow velocities there are still some considerable deviations which can be attributed to

particle-wall friction (as seen in Section 5.3.5), ensuing from the presence of stationary or moving bed regimes. This is even more notorious in the case of the 2 m. s^{-1} velocity for a particle concentration of 30 % (v/v).

All the studied drag correlations are dependent in the Particle Reynolds Number values, while the GSN drag correlation also depends on the local solids volumetric fraction. The GSN dependency on the particle concentration limits its performance since, according to the literature, it only performs accurately for solid volumetric fractions below 20% (Visuri, Wierink, and Alopaeus 2012), which seems to be accurate considering that GSN representation of particle distribution improved when the particle concentration was lowered from 40 to 30 %(v/v). For the 5 m. s^{-1} flow velocity and 40 % (v/v) particle concentration the amount of particles and turbulence dispersion are quite high which contributes to a higher particle-particle interaction. Both the HL and GSN where developed for account for the presence of particle-particle interactions which explain why they display a more accurate pressure drop, in spite the particle distribution being near homogeneous.

Table 5.15 – Low Reynolds numerical vs experimental pressure gradient for 2, 3 and 5 m. s^{-1} for a solid volumetric fractions of 30 and 40 % (v/v) – Influence of the Drag Correlations.

			Drag Correlations		
ΔPExp (Pa/m)	**ϕ (v/v)**	**V (m/s)**	**SN (Pa/m)**	**HL (Pa/m)**	**GSN (Pa/m)**
3411.0	0.3	2	2620.9 (-23.2%)	2583.8 (-24.3%)	2336.2 (-31.5%)
3587.2	0.4	3	2838.5 (-20.9%)	2804.9 (-21.8%)	2663.9 (-25.7%)
3971.5	0.4	5	3955.9 (0.44%)	3970.6 (0.20%)	3985.9 (0.36%)

5.2.7. ADDITIONAL *k-ε* TURBULENCE MODEL MODIFICATIONS

As mentioned in Section 4.9.1, additional modifications to the Turbulence closures were found in the literature. The influence of this modification was compared to the numerical results depicted in Section 5.2.4 using the Mixture Model coupled with a Low Reynolds Turbulence closure and the Schiller-

Naumann drag correlation. Similarly to Section 5.2.5 only the particle concentration profiles and the turbulence profiles will be analysed.

Hsu (2003)

These numerical studies were conducted for the 3 and 5 m. s^{-1} flow velocities and the highest particle concentration, 40 % (v/v) since this is where the

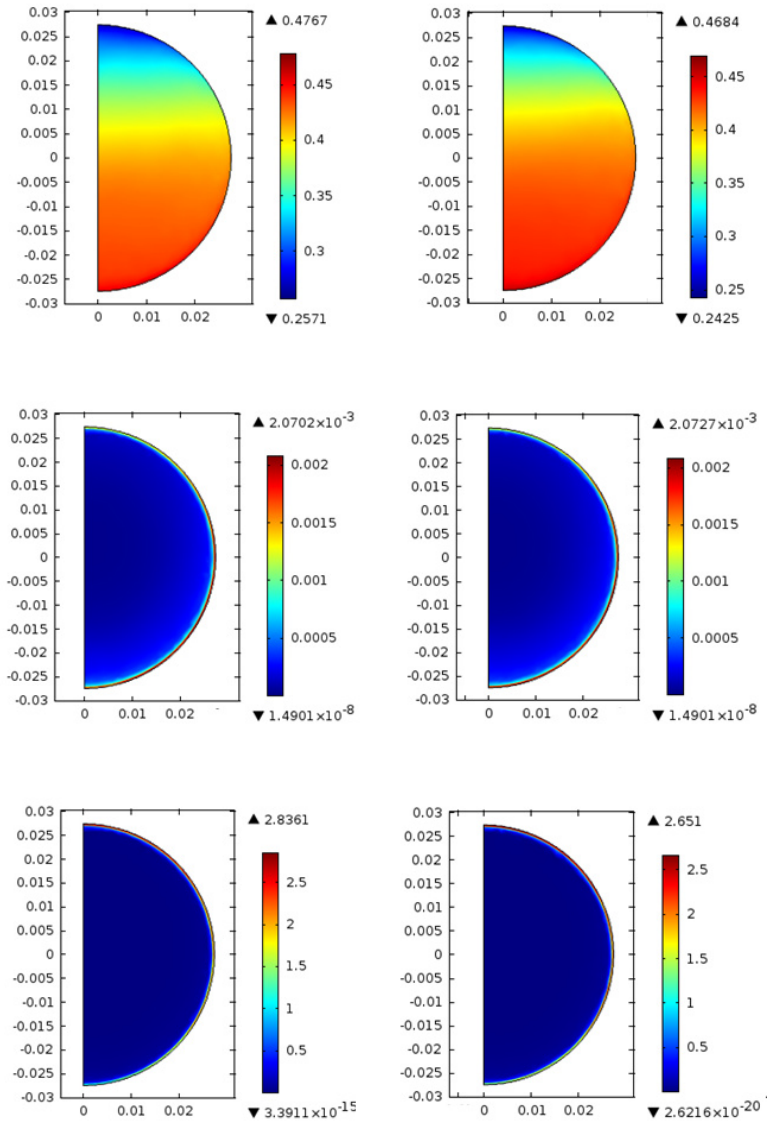

Figure 5.25 – Comparison between 2D cross-sectional profiles for the particle concentration (Top Row), Turbulent Kinetic Energy (Middle Row) and Turbulent Dissipation Rate (Bottom Row) for the Mixture Model with a Low Reynolds Turbulence closure (Left Column) and incorporating the Hsu modifications (MM+LR+HSU) (Right Column) for a flow velocity of 5 m. s^{-1} and 40 % (v/v) particle concentration.

turbulence attenuation is observed, and the results are depicted in Figures 5.25 and 5.26 as well as in Table 5.16. Including the terms in Equations 4.95 to 4.102 in the Low Reynolds *k*-*ε* Turbulence Equations showed a negligible effect on the overall numerical results (MM+LR+HSU) for the 3 and 5 $\mathrm{m.\,s^{-1}}$ as shown in Figures 5.25 and 5.26.

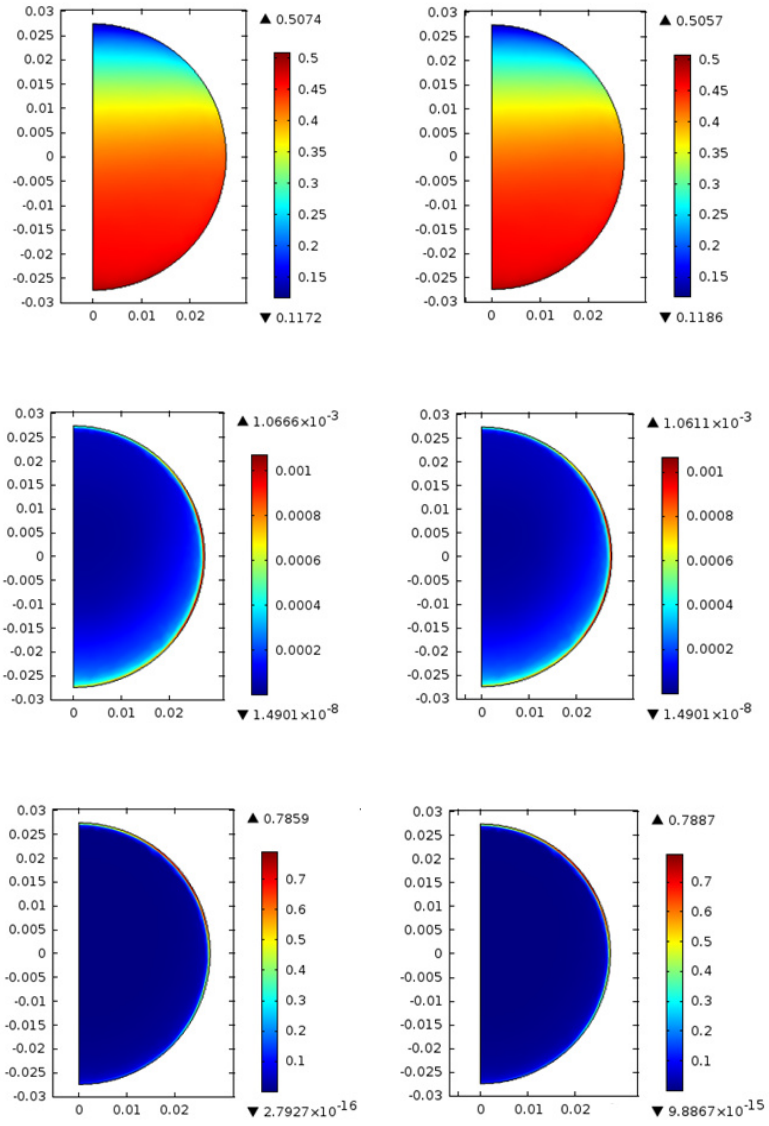

Figure 5.26 – Comparison between 2D cross-sectional profiles for the particle concentration (Top Row), Turbulent Kinetic Energy (Middle Row) and Turbulent Dissipation Rate (Bottom Row) for the Mixture Model with a Low Reynolds Turbulence closure (Left Column) and incorporating the Hsu modifications (MM+LR+HSU) (Right Column) for a flow velocity of 3 $\mathrm{m.\,s^{-1}}$ and 40 % (v/v) particle concentration.

A possible reason for the negligible effect of incorporating this modification is due to the fact that the extended *k-ε* Turbulence model by Hsu (2003) was based on the inclusion of the drag force and velocity between phases, both already incorporated in the Mixture Model. The pressure gradients were also very similar (see Table 5.16) with negligible differences, while the turbulence and particle concentrations profiles did not differ significantly.

Table 5.16 – Comparison between the experimental and simulated pressure gradient with the Mixture Model coupled with a Low Reynolds Turbulence closure (MM+LR) and the Mixture Model coupled with a Low Reynolds Turbulence closure and the HSU modification (MM+LR+HSU) for flow velocities of 3 and 5 m. $s^{-1}$and 40 % (v/v) particle concentration.

V (m/s)	**ΔPexp (Pa/m)**	**ΔP ML+HR (Pa/m)**	**ΔP MM+LR+HSU (Pa/m)**
3.0	3587.2	2838.52 (-20.4%)	2825.86 (-21.22%)
5.0	3971.5	3955.98 (0.44 %)	3952.34 (0.49%)

5.3. TURBULENCE MODULATION ANALYSIS

Based on the Tanaka & Eaton (2008) investigation, and Equation 4.104, the influence of the buoyant and settling particles on turbulence is depicted in Tables 5.17 and 5.18, respectively.

Table 5.17 – Stokes Number (St) based Particle Moment Number (Pa_{St}) for the buoyant particles in Shook (1985) study with a 34 % (v/v) particle concentration.

Buoyant Particles (C. Shook 1985)		
Pa_{St}	**V (m. s^{-1})**	**0.3 mm**
	1	21,1
	2	48,3
	3	60,7
	4	93,4

A comparison between the calculated values in Table 5.17 and the data from

Figure 4.7 appears to place these Pa_{St} values in the area of turbulence augmentation in water. The pressure gradients for the buoyant particles (see Figure 5.6) seem to validate the turbulence augmentation.

For the settling particles data from the study by Lahiri & Ghanta (2010), the calculated Pa_{St} values in Table 5.18, for flow velocities from 1 to 3 $m.s^{-1}$ also point to an augmentation of the turbulence, according to Figures 4.7 and 5.13.

Table 5.18 – Stokes Number (St) based Particle Moment Number (Pa_{St}) for the settling particles in Lahiri & Ghanta (2010)study with 30 and 40 % (v/v) particle concentrations.

Settling Particles (S. Lahiri and Ghanta 2010)			
	0.44 mm		
	V ($m.s^{-1}$)	**30 % (v/v)**	**40 % (v/v)**
Pa_{St}	1	96,4	-----
	2	280,7	-----
	3	516,8	516,7
	5	1118,2	1118,1

For the flow velocity of 5 $m.s^{-1}$, for both 30 and 40 % (v/v) particle concentrations, the Pa_{St} values are placed in the $10^3 < Pa_{St} < 10^5$ interval in Figure 4.7, defined by Tanaka & Eaton (2008) as the turbulence attenuation zone for air flows. Furthermore, in Figure 5.13 the pressure gradients values are very close to the pressure gradient in water which seems to further support the turbulence attenuation assumption

5.4. CONCLUDING REMARKS

Through the numerical studies depicted in this Chapter, using the Mixture Model and described modifications, the main concluding remarks can be drawn:

1. The Mixture Model, coupled with a High Reynolds *k-ε* Turbulence Model, allowed for an accurate depiction of solid-liquid suspensions flows of buoyant particles, even at high particle concentrations. Furthermore, for lower particle concentrations and high flow

velocities the aforementioned model also performed well for solid-liquid suspensions flows of settling particles;

2. Settling suspensions flows with higher particle concentrations were not well represented by the Mixture Model coupled with the High Reynolds k-ε Turbulence Model. Using the Mixture Model in tandem with a Low Reynolds Turbulence closure seemed to improve its numerical performance;
3. For higher particle concentrations and flow velocities just above the moving bed regime the introduction of the particle influence on the shear stress at the wall seemed to improve numerical representation by the Mixture Model.

.

CHAPTER VI

EXPERIMENTAL RESULTS

6. CHAPTER VI – EXPERIMENTAL RESULTS

In this Chapter the analysis of the experimental data is divided into three Sections.

In the first Section, preliminary tests with the Electrical Impedance Tomography apparatus (see Chapter III) are described where it was shown the viability of EIT to characterize multiphase flows.

The experimental data acquired in the flow loop in the KTH laboratory concerning dilute flows of solid-liquid suspensions, with particle concentration up until 5.0 % (v/v), is analyzed in the second Section. In these tests the dispersed phase consisted of spherical glass beads, with diameters in the ranges 0.1-0.2 and 0.4-0.6 mm. In these experiments three different experimental techniques were employed: (i) MRI and UPV were used to characterize the velocity profiles of the continuous and dispersed phases; and (ii) the aforementioned EIT was employed to attain normalized electrical conductivity profiles in the pipe cross-section in order to infer on the particles distribution. Additionally, pressure gradients and flow rates were also measured.

In the third and last section, similar experiments to those carried out in the KTH laboratory were also performed in DEQ/FCTUC, for both ranges of particles sizes, but with higher particle concentrations up until 11.0 % (v/v). Furthermore, vertical particle concentrations profiles were acquired using the sampling probe described in Chapter III.

The experimental data was then compared with numerical studies using the Mixture Model (see Chapter IV) with modifications that were based on the numerical studies described in Chapter V.

6.1. EIT PRELIMINARY TESTING

The development of the new EIT equipment requires a continuous testing to conclude the progresses that have been achieved. In the early stages of the

development, a SOLARTRON® 1250 Frequency Response Analyser available in LTMEU laboratory (Laboratório de Tecnologia dos Materiais Electrónicos e Ultrassons) in the Electrical and Computer Engineering Department was used for both electric current generation and electric potential acquisition, generating an electric current between 0.1 – 1.0 mA and measuring electric potentials for frequency ranges between 100 – 20000 Hz (Figure 6.1 (a)). A 16 electrode vertical test section was used in conjunction with the SOLARTRON Unit (see Figure 6.1 (b)).

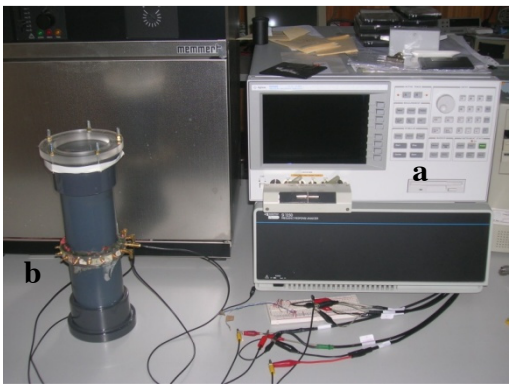

Figure 6.1 – (a) *SOLARTRON 1250 Frequency Response Analyser*; (b) 16 electrode vertical test section.

The test section had an internal diameter of 0.082 m and a height of 0.35 m. The electrode ring was placed at a height of 0.15 m; the electrodes were equally spaced in the ring, each with a diameter of 0.008 m. This will be called a static system used for "static imaging".

Figure 6.2 – Alumina cylinders employed as obstacles.

Several tests were conducted using distilled water with an electrical conductivity 7.2 $\mu S.\,cm^{-1}$. Two alumina (Aluminum Oxide (Al_2O_3)) cylinders

were placed inside the test section to act as obstacles. These alumina cylinders had an electrical resistivity of 1,0x10^{14} $\Omega.m$ and diameters of 0.035m for the wider cylinder and 0.009 m for the thinner cylinder (Figure 6.2).

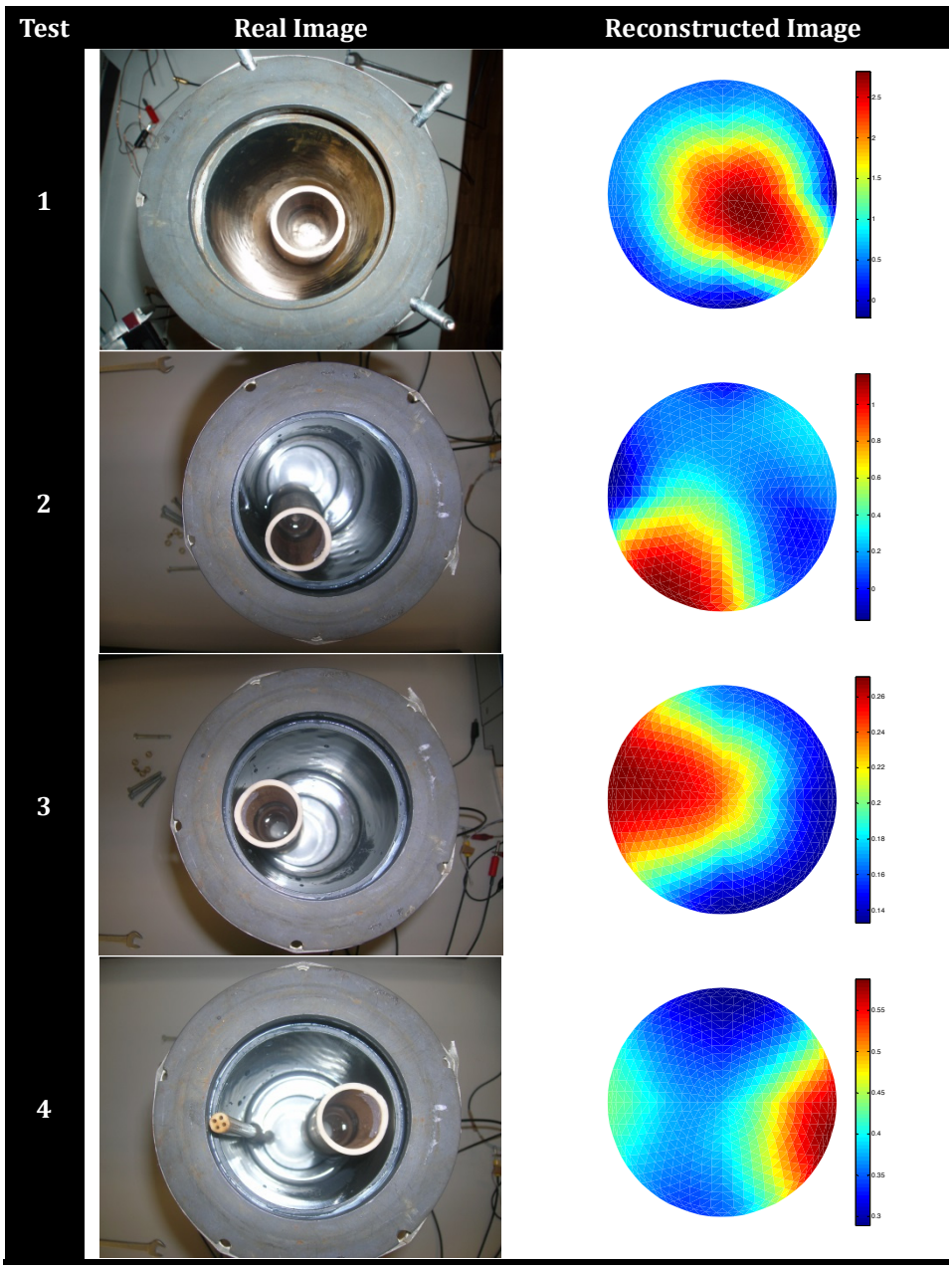

Figure 6.3 – Preliminary tests involving obstacles.

These tests served to prove that Impedance could be used to ascertain the position and size of the obstacles, as well as testing and fine-tuning the reconstruction algorithm.

The test conditions and reconstructed images are displayed in Table 6.1 and Figure 6.3, respectively.

Table 6.1 – Tests conditions for the preliminary tests.

Test	Injection and Measurement Protocol	Obstacles
1	Adjacent	1
2	Adjacent	1
3	Adjacent	1
4	Adjacent	2

These results showed that EIT is a promising technique to characterize the presence of solids in a liquid. They also served as the starting point for the EIT Equipment development described in Section 3.2.

6.2. STATIC IMAGING

After the completion of the EIT equipment, a battery of static tests were conducted in the vertical pipe section depicted in Figure 6.1 where an alumina tube (see Figure 6.2) was introduced in different positions inside the pipe section. The purpose of these tests was to verify if the object introduced in the domain, as well as the shift in its position, would be recognized.

The first results were not satisfactory when compared with existing EIT images acquired by other research groups (Goharian et al. 2008; Heikkinen et al. 2006) as well as ERT images (Jia et al. 2010) obtained for static tests. The expected object location was still diffuse, which commanded to more detailed inspection of the EIT system. Two problems were then found: the first one was an insufficient isolation of the cables that linked the electrodes on the pipe section to the multiplexer module and to the demodulator/signal condition modules; the second was the lack of power in the power lines feeding all of the hardware and ground loops, which introduced white and random noise along the EIT hardware system.

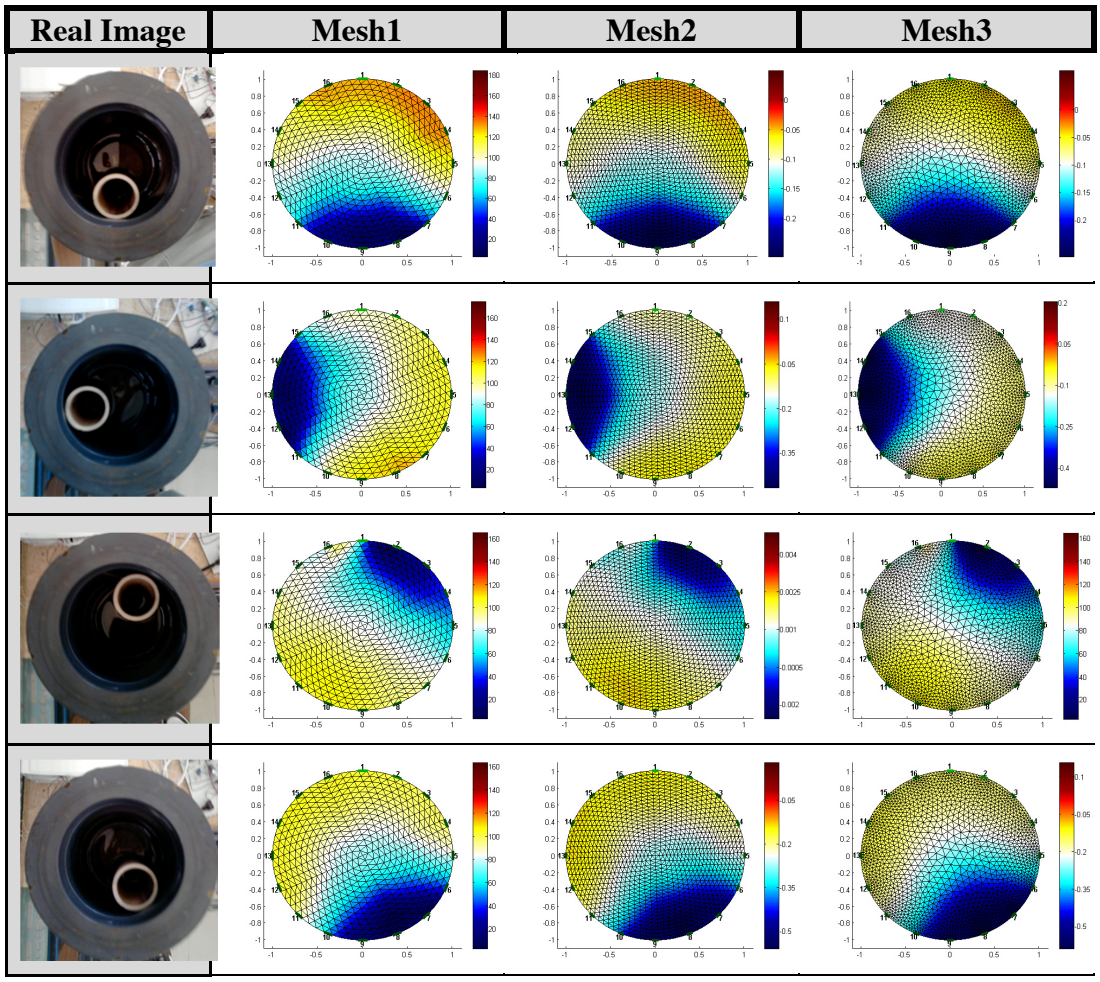

Figure 6.4 – Static testing: first column (Left) contains pictures of the object, the second column contains reconstructed images using mesh 1, the third column contains reconstructed images using mesh 2 and the last column contains reconstructed images using mesh 3.

Once these problems were solved, new tests were carried out and both the shift in position and the object location itself were now completely identified by the EIT system and visible in the images (see Figure 6.4). For the particular case presented in Figure 6.4 three new meshes were tested: Mesh 1 with 1024 linear elements and 545 nodes, Mesh 2 with 2304 linear elements and 1201 nodes, both structured meshes, and Mesh 3 which is non-structured with 415 linear elements and 241 nodes. For the image reconstruction the open source software EIDORS (Nick Polydorides and Lionheart 2002) was used. The colour mapping in Figure 6.4 represents gradients of conductivity where red stands for higher conductivity gradients and blue for lower conductivity gradients.

In all test cases presented here it is apparent that Mesh 2 reports a more accurate positioning of the object than Mesh 1. However, the non-structured mesh, Mesh 3, performed the best in all situations, but the image reconstruction time is in this case twice longer than for Mesh 2. So, in the following tested situations, images were obtained using only Meshes 2 and 3.

For static imaging the quality of the reconstructed images in Figure 6.4 is higher and sharper than with recent ERT (Wilkinson et al., 2006) and EIT systems (Heikkinen et al. 2006; S. Zhang et al. 2006).

6.3. IMAGING IN FLOW FIELDS

The next step was to employ the developed EIT apparatus in dynamic imaging of suspensions flows in the rig described in Section 3.1 and in the literature (Ventura et al. 2008). The rig was fitted with a Perspex® section possessing the EIT electrode rings (also described in Section 3.1) and testing was performed on flows of solid-liquid suspensions of spherical glass beads in a diluted aqueous solution of NaCl flowing in the system. The bead sizes were normally distributed in the range from 0.4 to 0.6 mm in diameter. Once the pumping system was initialized (see Section 3.1), several minutes were allowed to elapse until the flow regime was stabilized before tests could be performed.

Several flow rates were studied, ranging from 0 up to 52 $m^3.h^{-1}$, and it was observed that at very low flow rates the particles were not moving and persisted as a fixed bed sediment on the lower region of the horizontal pipe until the flow was increased enough to fluidize the bed; the particles were then moving, and, as the flow rate continued to increase, the amount of sedimented particles decreased and became continuously dispersed in the conveying solution. When the flow was 52 $m^3.h^{-1}$ the beads moved fully dispersed through the entire cross section of the tube, although slightly more concentrated near the lower region of the tube. This is evident in Figure 6.5 where each row respects to a value of the flow rate: respectively, 0, 13, 33 and 52 $m^3.h^{-1}$; the first column shows photographs of the conveying suspension

inside the tube, the second and the third columns show the reconstructed images using the aforementioned Mesh 2 and Mesh 3, respectively.

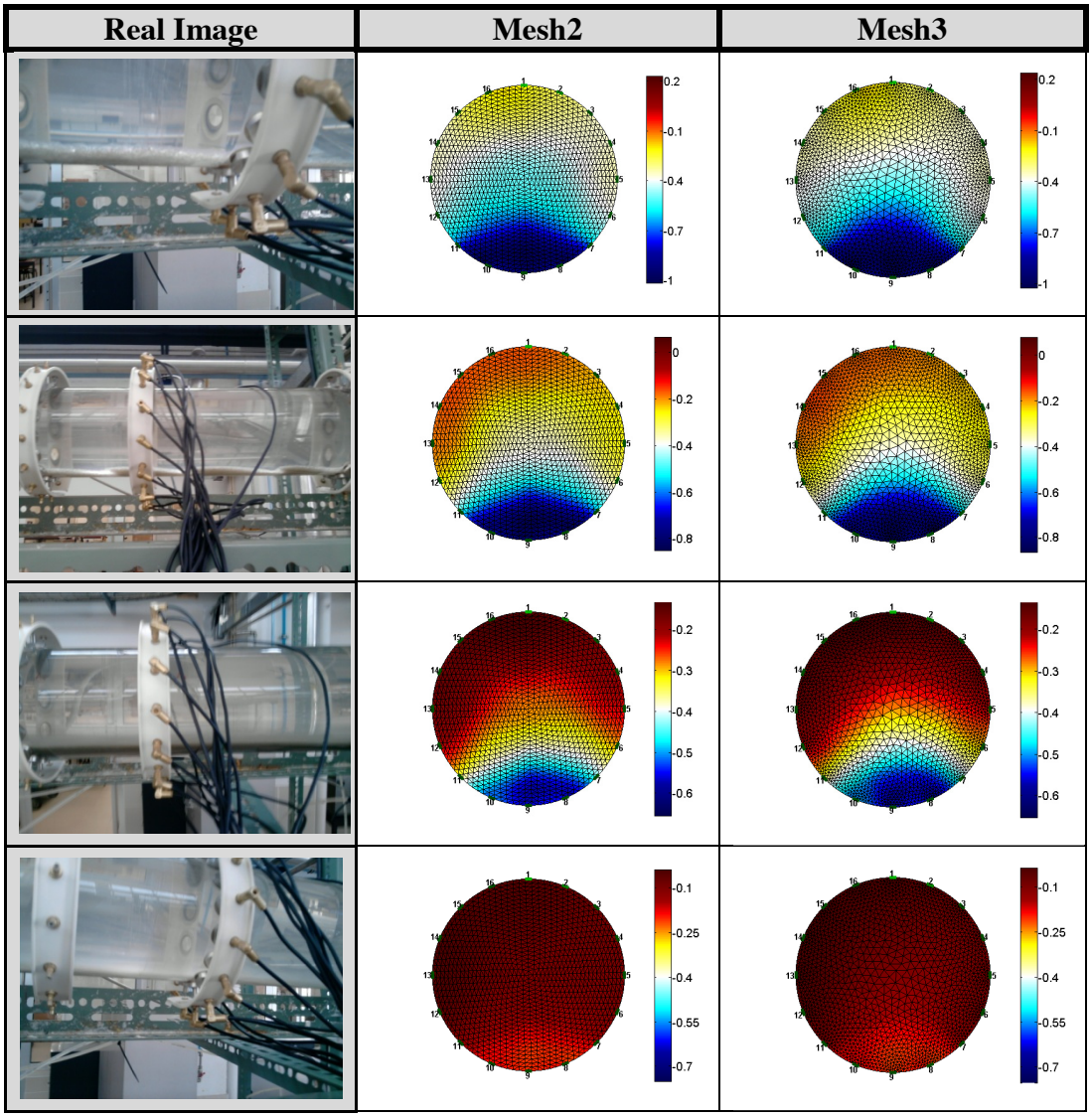

Figure 6.5 – Solid-liquid suspension tests carried out with an average particle concentration of 3,9 g/L for flow rates of 0, 12, 33 and 52 $m^3.h^{-1}$, respectively, from top to bottom (left column contains pictures of the section under study, middle column images obtained using mesh 2 and the right column images obtained using mesh 3).

When the pump was switched off the particles were sedimented in the lower region of the pipe and the gradient of conductivity was high (first row); when the flow rate was 12 $m^3.h^{-1}$ the particles were already moving but, generally dragged by the water in the lower region of the pipe, which obviously looks like a deposit in the bottom where the conductivity gradient is high (second row). For a higher flow rate of 33 $m^3.h^{-1}$ (third row), the particles were

already fluidized, and the smaller particles were distributed in the upper part of the cross section but with larger particles being dragged in the lower region as is translated by the conductivity distribution in the reconstructed images. Finally, when the flow was increased to 52 $m^3.h^{-1}$ the particles were almost completely distributed all over the entire cross section of the pipe, therefore a very small gradient of conductivity exists, corresponding to the red colour, with some slightly higher concentration near the bottom, as is evident in the fourth row of Figure 6.5.

The results showed that the developed EIT apparatus was capable of producing images with a resolution that is superior to EIT images found in literature (M. Wang 2005a; Holliday, Williams, and Lucas 2005) and also better than ERT published results (Razzak, Barghi, and Zhu 2009; Schlaberg et al. 2006), which opens good opportunities for industrial applications.

Additionally, in the approach adopted in this study, namely the injection strategy and the reconstruction method proved to be efficient for the study of solid-liquid systems, usually harder to characterize due to the lower contrast in conductivity. The developed EIT system was capable of identifying the particles concentration distribution in different test situations.

6.4. DILUTE SOLID-LIQUID SUSPENSIONS FLOWS – KTH MEKANICS

In this section are depicted the experimental results from the MRI, UPV and EIT tomographic techniques, obtained at KTH Mekanics laboratory. These results pertain to the study of dilute solid-liquid suspensions which will be analysed and compared to numerical results from the Mixture Model.

6.4.1. EXPERIMENTAL CONDITIONS

The flow and particle data for the experimental tests employed on both 34 and 50 mm internal diameter (ID) pipes configurations (see Section 3.4) are presented below in Table 6.2.

Table 6.2 – Experimental Conditions for the KTH tests.

	FLOW DATA		
PIPE ID [mm]	34		50
$Q\ [l.s^{-1}]$	0.5	0.5	1.0
	1.0	1.0	2.0
	2.0	2.0	4.0
$A\ [m^2]$	9.08×10^{-4}	9.08×10^{-4}	1.96×10^{-3}
$U\ [m.s^{-1}]$	0.55	0.55	0.51
	1.10	1.10	1.02
	2.20	2.20	2.04
$\rho_F\ [kg.m^{-3}]$	998**	998**	998**
$\mu_F\ [Pa.s]$	1.02×10^{-3}**	1.02×10^{-3}**	1.02×10^{-3}**
Re	18320.2	18320.3	24915.6
	36640.5	36640.5	49831.1
	73281.0	73281.0	99662.2
	PARTICLE DATA		
$\rho_P\ [kg.m^{-3}]$	2500	2500	2500
$d_p\ [mm]$	0.15*	0.5*	0.5*
$\phi\ [v/v]$	0.005	0.005	0.01
	0.01	0.01	0.03
	0.03	0.03	0.05

*** Averaged values, see Appendix C for additional details.**
**** Values at 20ºC.**

6.4.2. FLOW REGIME CONSIDERATIONS

In the tests, performed with the two size ranges of particles, several flow regimes were observed which varied with the flow velocities. Below, some pictures and considerations are introduced for each particle size.

0.1-0.2 mm Particles

In the 34 mm pipe configuration and for the 0.1-0.2 mm particles with a mean particle diameter of 0.15 mm (see Appendix C), a sliding or moving bed regime with very little particle fluidization was observed when the flow rate was $0.5\ \mathrm{l.s^{-1}}$ (see Figure 6.6). At the higher flow velocities the flow regime

always corresponded to a heterogeneous flow with increasing particle suspension at higher velocities (see Figure 6.6).

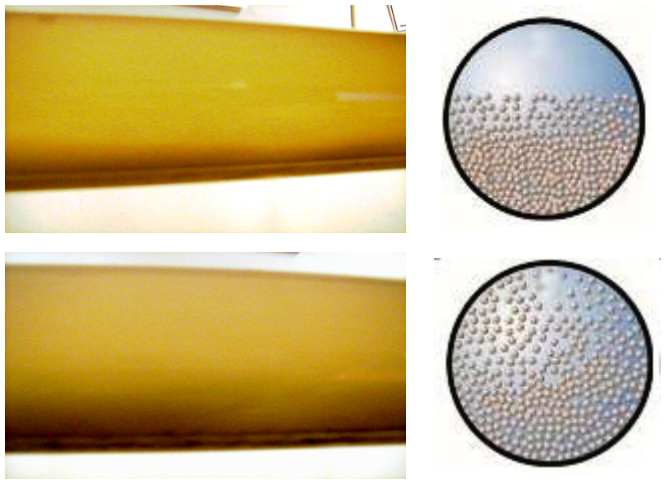

Figure 6.6 – Picture and schematics (adapted from (S. A. Miedema 2014)) of the observed flow regimes for the 0.1-0.2 mm sized particles at 0.5 l. s^{-1} (Top) and 1.0 and 2.0 l. s^{-1} (Bottom).

Comparing the top and bottom pictures in Figure 6.6 it is noticeable the increase of fluidized particles with the increase in flow velocity, as noted by the increased in the shaded area.

0.4-0.6 mm Particles

In both 34 and 50 mm ID pipe configurations the 0.4-0.6 mm particles with a mean particle diameter of 0.5 mm (see Appendix C) showed similar evolution of the flow regimes for the flow rates and particle concentrations studied. These flow regimes were, however, different from those observed with the previous smaller particles: at a flow rate of 0.5 l. s^{-1} the pump output was not sufficient to make the particles flow from the pump and up the splitter towards the measuring section (see Figure 3.24).

Figure 6.7 – Picture and schematics of the observed flow regimes at 0.5 l. s^{-1} with the 0.4-0.6 mm particles in the 34 mm ID pipe tests.

By increasing the flow rate and then reducing it again to 0.5 l. s^{-1} a dune formation was observed (see Figure 6.7) with no particle suspension. However, measurements for this regime took a long time to perform and towards the end of the measurements particles were not present in the measurement section, so the 0.5 l. s^{-1} measurements were disregarded;

In the 50 mm pipe and for a flow rate of 2.0 l. s^{-1} a moving bed with few particle suspended was observed (see Figure 6.8) and for the highest flow rate of 4.0 l. s^{-1} the flow regime was a heterogeneous flow (see Figure 6.8).

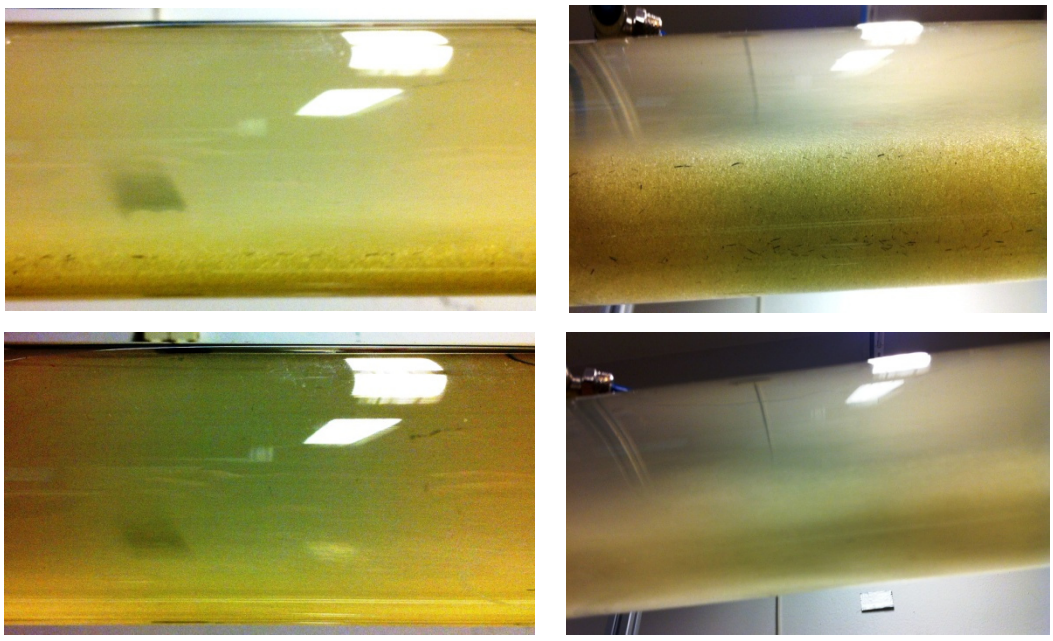

Figure 6.8 – Pictures of the lateral (Left Column) and bottom views (Right Column) of the observed flow regimes at 2.0 (Top Line) and 4.0 l. s^{-1} (Bottom Line) with the 0.4-0.6 mm particles in the 50 mm ID pipe tests.

Deposition Velocities

Similarly to Section 5.1.2 the deposition velocities were calculated using Equation 5.1 to 5.7:

Correlation I

Using the first correlation (Randall G. Gillies et al. 2000) and using the Arquimedes Number (AR) as the deciding factor to which correlation to use:

$$Ar = \frac{4}{3}\left[\frac{g\ d_p^3\ \rho_F(\rho_P - \rho_F)}{\mu_F^2}\right] \quad \textbf{(6.1)}$$

If AR < 80 and d_p < 0.5 mm, then

$$F_L = 2.0 + 0.3log_{10}\Delta$$
$$with\ \Delta = \left(\frac{d_p}{D}\ C_D\right) \quad \textbf{(6.2)}$$

$$V_D = F_L\sqrt{2gD(S_s - 1)} \quad \textbf{(6.3)}$$

Otherwise if AR > 80 and d_p > 0.5 mm then using Figure 4 from the original article, as supplied by the author (Randall G. Gillies et al. 2000) for an Arquimedes number of 2355 the F_L value is 1.2. And since the previous Equations are independent of particle concentration and flow velocity this value will be constant.

Correlation II

A second correlation was given by (D.R Kaushal, Tomita, and Dighade 2002) as follows:

$$V_D = 1.87\left(\frac{d_p}{D}\right)^{\frac{1}{6}}\sqrt{2gD\left(\frac{\rho_p}{\rho_F} - 1\right)}\ for\ \phi \leq 1\% \quad \textbf{(6.4)}$$

$$V_D = 1.87\left(\frac{d_p}{D}\right)^{1/6}\phi^{1/5}\sqrt{2gD\left(\frac{\rho_p}{\rho_F} - 1\right)}\ for\ \phi > 1\% \quad \textbf{(6.5)}$$

Correlation III

The third and final correlation employed (Abulnaga 2002):

$$F_L = 1.3\,\phi^{0.125}[1 - e^{-6.9\,dp_{50}}]\ with\ d_{p50}\ expressed\ in\ \boldsymbol{mm} \qquad \textbf{(6.6)}$$

$$V_D = F_L\sqrt{2gD(S_s - 1)} \qquad \textbf{(6.7)}$$

The results with the three correlations are presented below in Table 6.3.

Table 6.3 – Deposition velocities for the KTH tests.

			Correlation I				Correlation II	Correlation III	
	d_p (mm)	ϕ	AR	Δ	F_L	V_D (m.s^{-1})	V_D (m.s^{-1})	F_L	V_D (m.s^{-1})
34 mm pipe	0.15	0.005	63.6	2.07	2.1	2.1	0.76	0.43	0.43
		0.01	63.6	2.07	2.1	2.1	0.76	0.47	0.47
		0.03	63.6	2.07	2.1	2.1	0.81	0.54	0.54
	0.50	0.005	2355.69	--	1.2	1.2	0.93	0.65	0.65
		0.01	2355.69	--	1.2	1.2	0.93	0.71	0.71
		0.03	2355.69	--	1.2	1.2	0.98	0.81	0.81
50 mm pipe	0.50	0.01	2355.69	--	1.2	1.2	1.06	0.71	0.86
		0.03	2355.69	--	1.2	1.2	1.12	0.81	0.99
		0.05	2355.69	--	1.2	1.2	1.24	0.87	1.05

Considering the visual observation of the flows, Correlation III (Abulnaga 2002) seems to present a more accurate value for the deposition velocity. Correlation II provides similar values and Correlation I provides values that seem too high when compared to visual inspection of the flow.

6.4.3. NUMERICAL STUDIES CONDITIONS

The numerical results presented in the next sections were attained using the Mixture Model in the COMSOL Multiphysics® software, coupled with the High Reynolds *k-ε* Turbulence Model, as depicted in Sections 4.3 and 4.7.1. These studies were conducted by emulating the flow conditions depicted in Table 6.2.

Validity of the Mixture Model

The use of a turbulence model is justified by the values of the Reynolds Number (Re) in Table 6.2. Additionally to a turbulence closure, a model for the interphase forces, namely the drag force, is needed (see Section 4.6). Since drag models corresponding to different Particle Reynolds Number (Re_p) range of application it is necessary to have a good estimate of this value. Adding on the particle data in Table 6.2, the Particle Stokes Number (St_p) and Particle Reynolds Number where calculated using Equations 4.107 and 4.105, respectively. The Reynolds Number for the flow in Table 6.2 was calculated using Equation 4.106.

The Particle Reynolds Number calculation aids in determining the Slip Velocity Model to be utilized which is pivotal for accurate numerical studies as seen in Section 4.6; however, there is a circular dependency since the Re_p calculation also depends on the slip velocity as can be seen in Equation 4.105. To circumvent this, the Re_p calculation was accomplished using an approach found in the literature (Rasteiro 1988) where the particle Terminal Velocity (V_T) is used as an initial estimate for the slip velocity (see Equation 4.108).

The calculated values for the Particle Stokes Number, Particle Reynolds Number and Terminal Velocity can be seen below in Table 6.4. Since $Re_p > 1$ and the solid-liquid suspensions are dilute, in all experimental cases, the Schiller-Naumann correlation was chosen for the drag force modelling. The highest St_p is 2.20 for the bigger particles in the 34 mm ID pipe, while the remaining values are all close to one, thus validating the application of the Mixture Model in these studies (Manninen, Taivassalo, and Kallio 1996; Hiltunen et al. 2009). Additionally, considering the numerical results in Chapter V, using the Mixture Model coupled a High Reynolds Turbulence closure becomes feasible in view of the low particle concentrations tested at the KTH laboratory.

Table 6.4 – Particle data for the KTH experiments.

Particle Data	34 mm ID Pipe		50 mm ID Pipe
$\rho_P\ [kg.m^{-3}]$	2500	2500	2500
$d_p\ [mm]$	0.15*	0.5*	0.5*
$U\ [m.s^{-1}]$	0.55	0.55	0.51
	1.10	1.10	1.02
	2.20	2.20	2.04
$\phi\ [v/v]$	0.005	0.005	0.01
	0.01	0.01	0.03
	0.03	0.03	0.05
St_p	0.05	0.55	0.42
	0.10	1.10	0.83
	0.20	2.20	1.66
$V_T\ [m.s^{-1}]$	0.018	0.200	0.200
Re_p	2.65	98.2	98.2

*** Averaged values, see Appendix C for additional details**

Geometry

The flow geometry consisted of a horizontal pipe with a diameter of either 34 or 50 mm as shown in Table 6.2. The pipe length had to be longer than the minimum entrance length, L_e, i.e., the length required for the flow to be fully developed. For turbulent flows of solid-liquid suspensions the following relation has been used in the literature (Abulnaga 2002; Ling et al. 2003; Lin and Ebadian 2008):

$$\frac{L_e}{D} \geq 50 \qquad \textbf{(6.8)}$$

This implies a minimum entrance length of 1.7 m for the 34 mm ID pipe and 2.5 m for the 50 mm ID pipe. In these numerical studies an entrance length of 3 m was implemented, thus, assuring the flow as fully developed. After this section an additional 0.5 m of test section was introduced where the numerical data presented here will be collected.

Finite Element Mesh

After the validity of the Mixture Model applicability was established and a drag correlation chosen, the numerical studies were conducted until mesh independent results were attained, i.e., the meshes were refined until the numerical results remained constant. The finite element meshes images and characteristics employed in these numerical studies are shown in Figure 6.9 and Table 6.5, respectively. For the initial numerical studies with the 34 mm ID pipe no mesh symmetry was imposed, and later, for the 50 mm ID pipe mesh symmetry was assumed, as depicted in Figure 6.9, as to haste the numerical solver and to decrease the RAM requirements.

Table 6.5 – Finite Element Meshes characteristics for the numerical studies with the KTH data.

	Pipe ID [mm]	
	34	**50**
Number of Prism Elements	508 026	443 904
Number of Boundary Layers	6	6
Wall Lift off in Viscous Units (y^+)	11.06	11.06

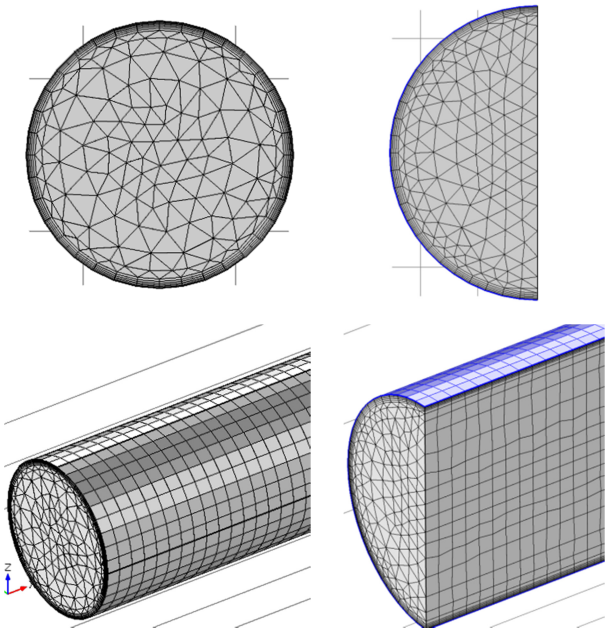

Figure 6.9 – Finite Element Meshes used in the numerical studies for the KTH data.

Boundary Conditions

Additionally, the following boundary conditions (described in detail in Section 4.6.3) were enforced on the numerical studies:

i. at the inlet, the initial velocities (see Table 6.2) were imposed in the direction perpendicular to the pipe section and the turbulence intensity and length scales used are defined by Equations 6.9 and 6.10. A value of 0.05 was assumed for the turbulence intensity scale, similarly to previous studies for solid-liquid horizontal flows (Ling et al. 2003) and the turbulence length scale was assumed to be the same as the particle diameter (Kenning and Crowe 1997).

$$I_T = 0.05 \tag{6.9}$$

$$L_T = d_p \tag{6.10}$$

ii. At the outlet, the normal gradients of k and ε are fixed equal to zero as demonstrated by Equation 4.75. Moreover, a pressure value has to be assigned at the outlet which is typically fixed at zero; however, to avoid numerical instabilities that hinder numerical convergence a hydrostatic pressure profile (see Equation 6.11) was assigned.

$$p = -g(z + D)\left(\rho_f(1 - \phi_0) + \rho_s\phi_0\right) \tag{6.11}$$

iii. The Law of The Wall or Wall Function was used as depicted in Equation 4.84 for the near wall treatment of the flow. A value of 1.5 μm was imposed for the roughness height, k_s, which is typical for surfaces as drawn tubing, plastic pipes, etc. (COMSOL Multiphysics 2013).

6.4.4. EXPERIMENTAL AND NUMERICAL RESULTS

Water Calibration Tests

Initial tests were performed with water using the experimental conditions depicted in Table 6.2 which served to verify if both the pressure transducers and the MRI apparatus were suitably calibrated. The experimental data for

pressure gradients were compared with calculations obtained using Darcy-Weisbach Equation (see Equation 6.12) and the Moody Diagram for the friction factor (see Table 6.6 and Figure 6.12) (Peker and Helvaci 2011; Liu 2003).

$$\frac{\Delta P}{L} = f \frac{\rho V^2}{2D} \quad \textbf{(6.12)}$$

The experimental 1D MRI velocity profiles were compared with numerical results from CFD simulations using the High Reynolds k-ε turbulence model (Wilcox 2006). Single phase turbulence numerical models have already been verified as being capable of providing accurate depictions of simple flows (Pisarenco et al. 2011; Vasava 2007; Satish et al. 2013).

In Figures 6.10 and 6.11 the experimental MRI and CFD numerical velocity profiles for water testing in both the 34 and 50 mm internal diameter pipes are shown. The velocity profiles were normalized using the maximum velocity values for both experimental and numerical data.

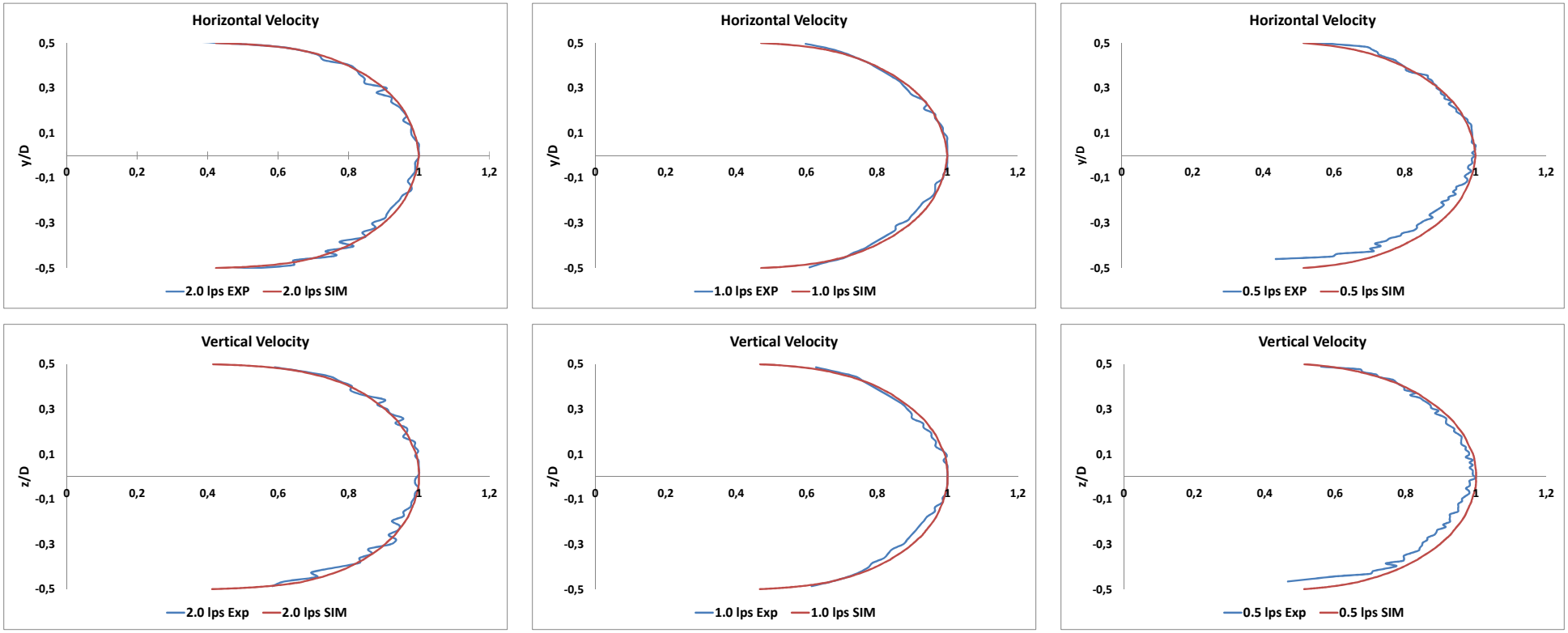

Figure 6.10 – Experimental MRI and Numerical *k-ε* normalized horizontal (Top) and vertical (Bottom) velocity profiles for flow rates of 2.0 (Left), 1.0 (Middle) and 0.5 $l.s^{-1}$ (Right) in a 34 mm ID pipe.

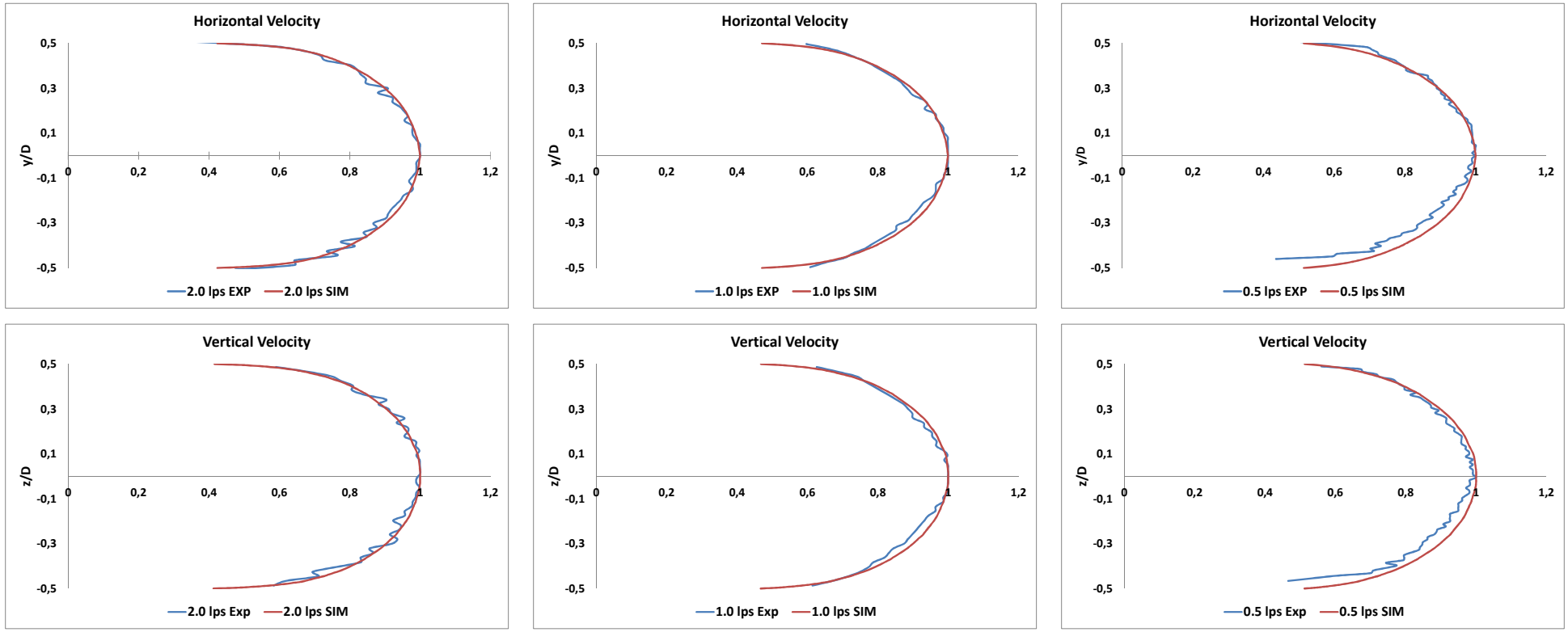

Figure 6.11 – Experimental MRI and Numerical *k-ε* normalized horizontal (Top) and vertical (Bottom) velocity profiles for flow rates of 2.0 (Left), 1.0 (Middle) and 0.5 $l.s^{-1}$ (Right) in a 50 mm ID pipe.

Regarding the friction factor in the pressure gradient calculation, using Darcy-Weisbach Equation (see Equation 6.12), the pipe equivalent roughness, ϵ, was assumed to be 0.0015 mm, which is a typical value in most textbooks for PVC, Glass or Other Drawn Tubing (F. M. White 1998).

Table 6.6 – Comparison of Experimental, Numerical and Darcy-Weisbach pressure gradients profiles for water flow in 34 and 50 mm ID pipes (deviations from experimental are in bold).

	Pressure Gradient ($Pa.m^{-1}$) for 34 mm ID pipe		
Flow rate ($l.s^{-1}$)	**Experimental**	**Darcy-Weisbach**	**Numerical**
0.5	101.7	117.7 **(15.7%)**	113.3 **(11.4%)**
1.0	321.9	399.6 **(24.1%)**	379.4 **(17.9%)**
2.0	1360.2	1378.1 **(1.31%)**	1227.2 **(-9.78%)**
	Pressure Gradient ($Pa.m^{-1}$) for 50 mm ID pipe		
Flow rate ($l.s^{-1}$)	**Experimental**	**Darcy-Weisbach**	**Numerical**
1.0	60.8	63.9 **(5.09%)**	56.6 **(-6.91%)**
2.0	208.5	218.1 **(4.60%)**	189.7 **(-9.02%)**
4.0	727.8	755.9 **(3.86%)**	613.6 **(-15.7%)**

With Table 6.6 and Figures 6.10 to 6.12 it was shown that the experimental and calculated velocity profiles are congruent, displaying small deviations. The highest deviation, 24.1%, occurs between the experimental and Darcy-Weisbach results for the 34 mm ID pipe with a flow rate of 1.0. Although this deviation value seems considerable, further inspection of the Table 6.6 actually shows an absolute difference of 77.7 $Pa.m^{-1}$ which, realistically, is negligible. Overall, the experimental pressure gradient was matched by both numerical and Darcy-Weisbach calculations.

These results allowed us to demonstrate the correct calibration of both the MRI and pressure transducers since both the Darcy-Weisbach and the High

Reynolds *k-ε* turbulence model have already been extensively validated for water flows.

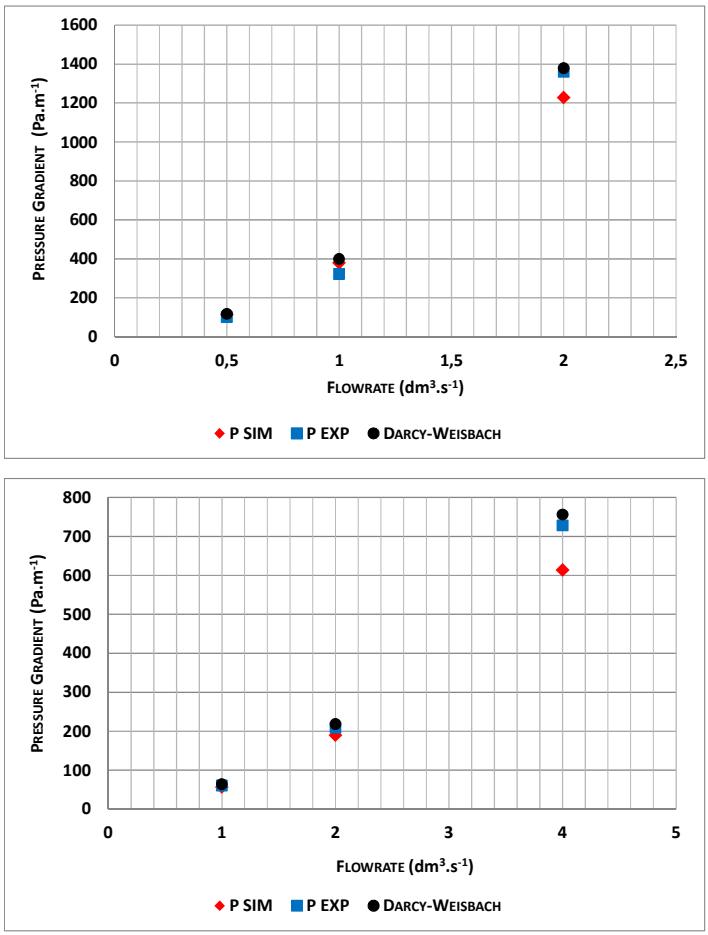

Figure 6.12 – Experimental, Numerical and Darcy-Weisbach pressure gradients profiles for water flow in 34 (Top) and 50 mm ID (Bottom) pipes.

Beyond the initial testing with the MRI apparatus to attain 1D velocity profiles it also became possible to attain 2D cross-section velocity profiles. As this was a newly implemented routine (MRI GRE2D), some preliminary testing was done with water before moving to the solid-liquid suspensions tests. The 2D velocity profiles from both the MRI and the High Reynolds *k-ε* turbulence model are shown in Figure 6.13, for the water flow case, where the numerical results were converted to flow velocity to match the dimensions presented by the MRI data. The correspondence between flow rate and flow velocity values can be seen in Table 6.2.

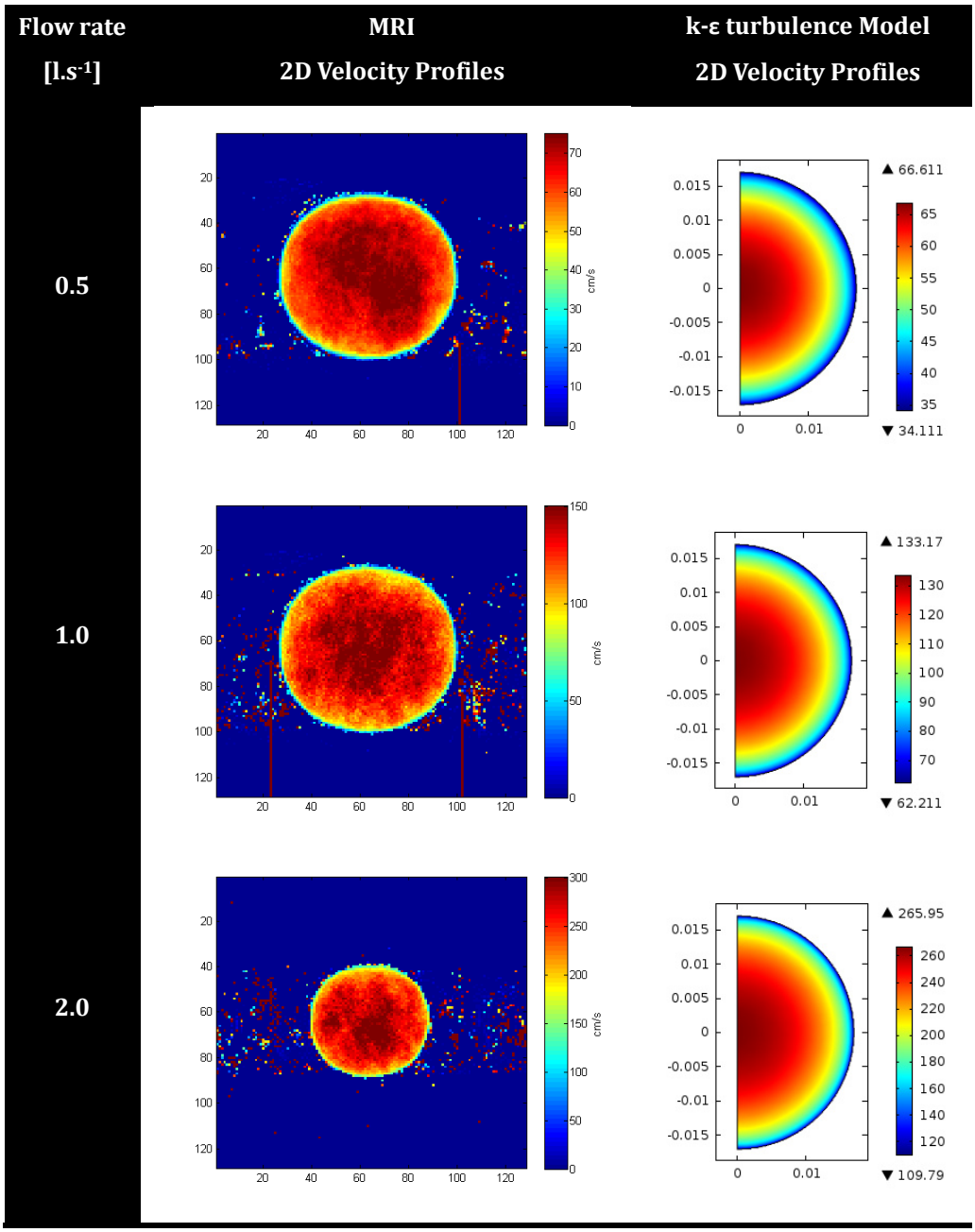

Figure 6.13 – MRI and Numerical 2D velocity profiles for water at the flow rates of 2.0 (Bottom), 1.0 (Middle) and 0.5 l. s^{-1} (Top) in a 34 mm ID pipe.

Although there are some small deviations between the maximum value between the MRI and numerical results, overall, the profiles appear to be concordant in spite of differences among the colour scales of the images. An interesting result is the similarity of the values for the velocity closer to the wall, between the numerical and MRI results.

0.1-0.2 mm particles in 34 mm ID pipe

After the initial tests with the MRI apparatus using water, small spherical particles with size between 0.1-0.2 mm were introduced in the flow loop. As described in Table 6.2 the volumetric concentrations studied were 0.5, 1.0 and 3.0 % (v/v) for flow rates of 0.5, 1.0 and 2.0 $\mathrm{l.s^{-1}}$. The numerical and experimental results, from both MRI and UPV, match quite well with negligible deviations as presented in Figures 6.14 to 6.17. The UPV and MRI profiles, representing the velocities of the dispersed and continuous phases, respectively, are concordant with what was expected, since the Stokes Numbers for these particles is smaller than one for all flow velocities (see Table 6.4), indicating that the particles follow the fluid streamlines; in other words, the particle motion is tightly coupled with the motion of the fluid since, locally, there is very little motion between the phases.

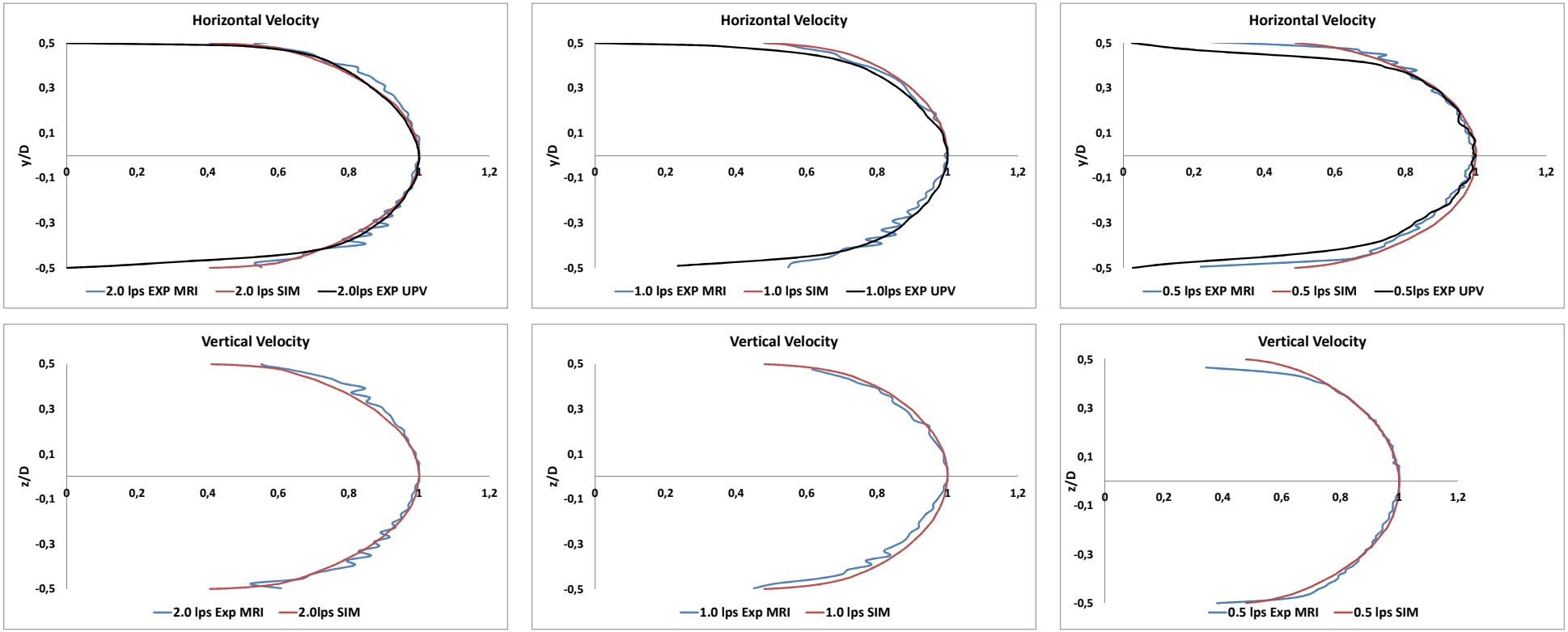

Figure 6.14 – Experimental MRI, UPV and Numerical normalized horizontal (Top) and vertical (Bottom) velocity profiles for flow rates of 2.0 (Left), 1.0 (Middle) and 0.5 $l.s^{-1}$ (Right) in a 34 mm ID pipe for a solids volumetric concentration of 0.5 % (v/v).

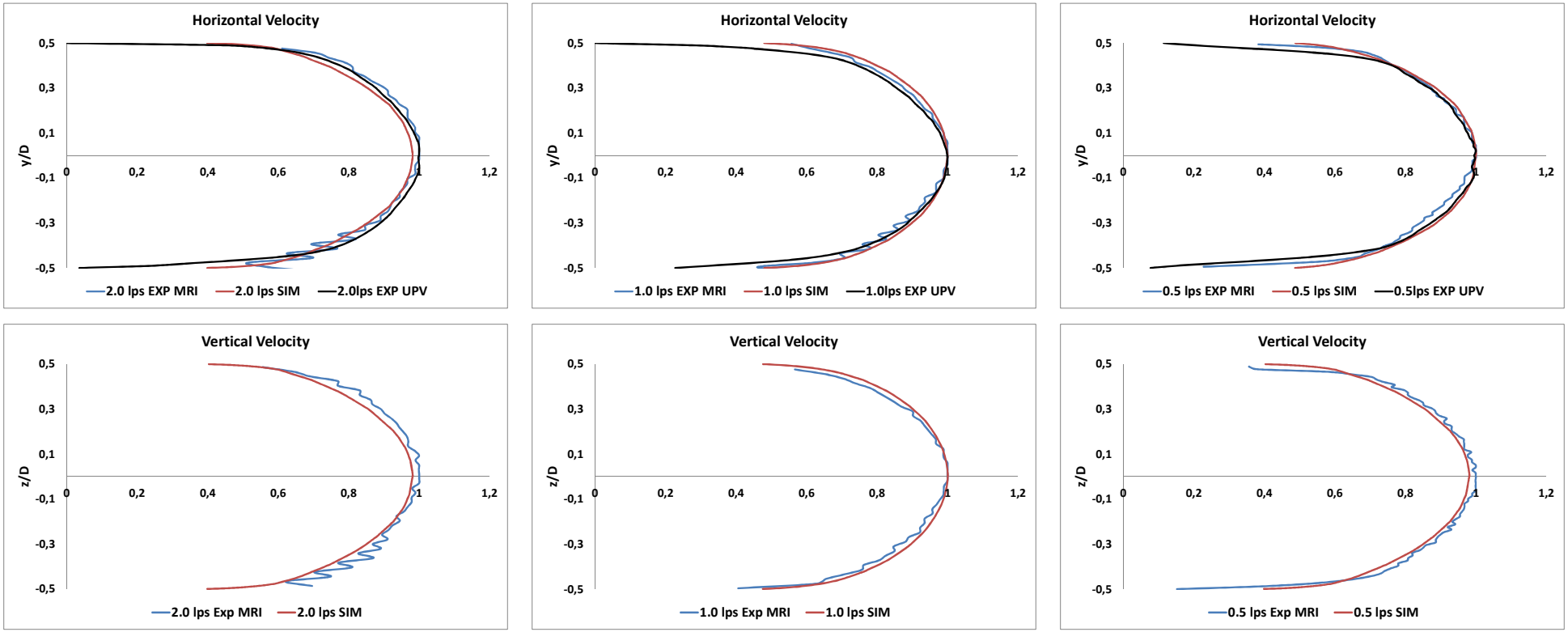

Figure 6.15 – Experimental MRI, UPV and Numerical normalized horizontal (Top) and vertical (Bottom) velocity profiles for flow rates of 2.0 (Left), 1.0 (Middle) and 0.5 $l.s^{-1}$ (Right) in a 34 mm ID pipe for a solids volumetric concentration of 1.0 % (v/v).

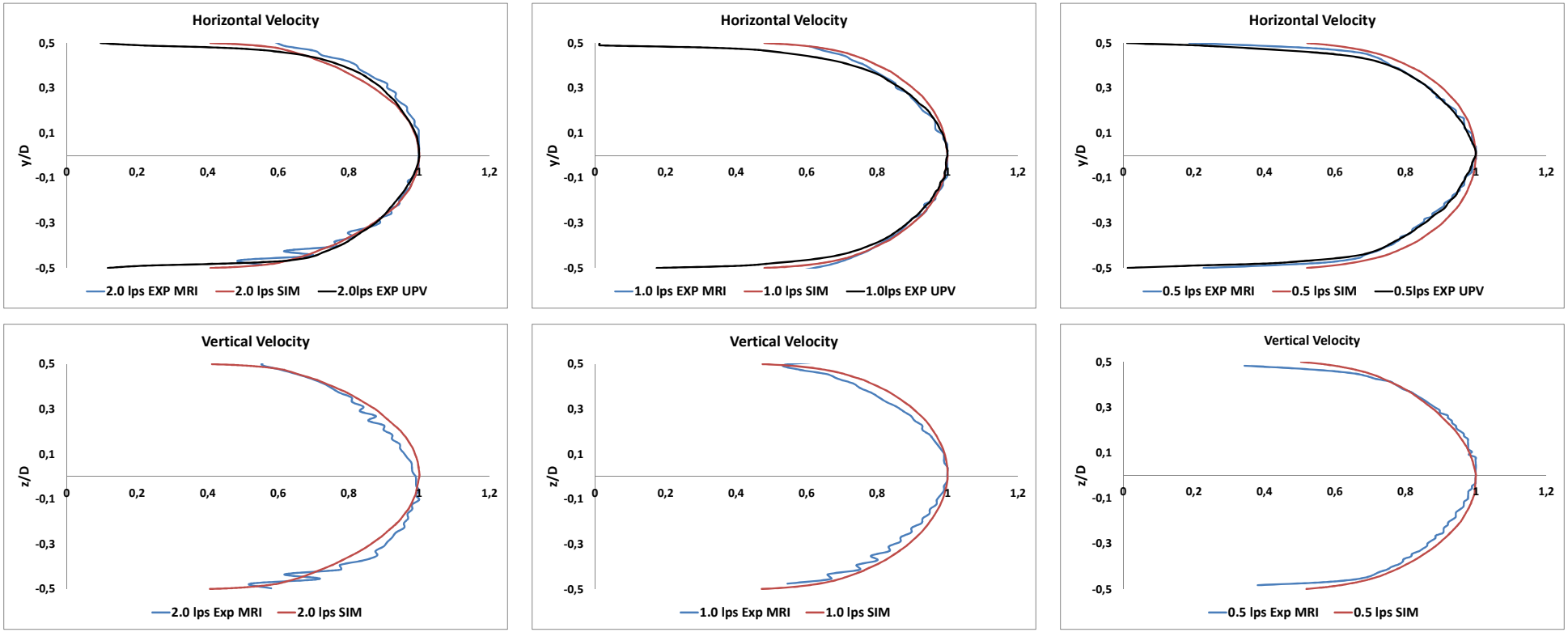

Figure 6.16 – Experimental MRI, UPV and Numerical normalized horizontal (Top) and vertical (Bottom) velocity profiles for flow rates of 2.0 (Left), 1.0 (Middle) and 0.5 $l.s^{-1}$ (Right) in a 34 mm ID pipe for a solids volumetric concentration of 3.0 % (v/v).

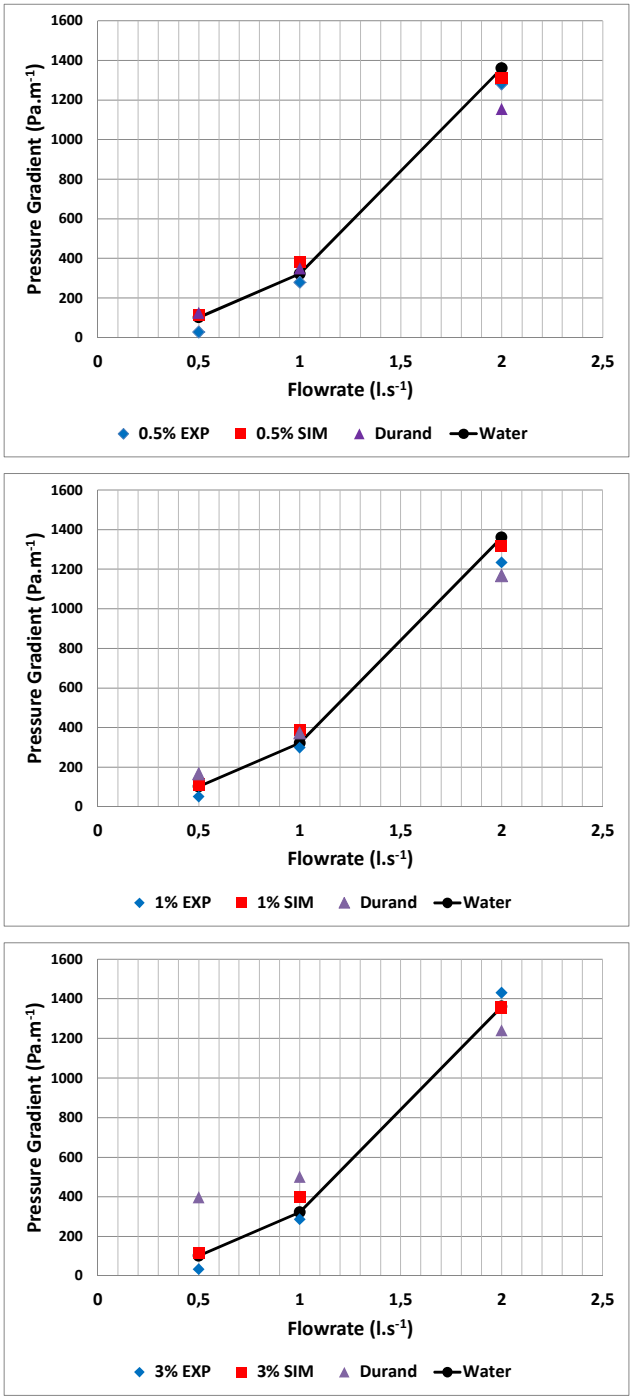

Figure 6.17 – Experimental, Numerical and Durand-Condolios pressure gradients profiles for solid-liquid suspensions of 0.1-0.2 mm particles for 0.5 (Top), 1.0 (Middle) and 3.0 % (v/v) (Bottom) solids volumetric concentration in a 34 mm ID pipe.

Regarding the pressure gradient for these tests, a comparison was done between the experimental and numerical results. Additionally, the pressure drops using the Durand-Condolios correlation, one of the most widely used correlations for pressure drops of solid-liquid mixtures, were computed to

serve as reference. In this particular study the modified version (see Equations 6.13 and 6.14) of the Durand-Condolios by Hayden & Stelson (Hayden and Stelson 1968; Abulnaga 2002), which is based on the terminal velocity, was employed.

$$\frac{i_m - i_w}{\phi_s i_w} = 100\left[\frac{gD\left(\frac{\rho_m - \rho_L}{\rho_L}\right)V_T}{U^2\sqrt{gd_p\left(\frac{\rho_m - \rho_L}{\rho_L}\right)}}\right]^{1.3} \quad \textbf{(6.13)}$$

$$i_w = f_D\,\frac{U^2}{2gD} \quad \textbf{(6.14)}$$

Overall, for the 0.5 and 1.0 % (v/v) volumetric fractions of particles, the pressure gradients matched quite well considering the Mixture Model, Durand-Condolios correlation and experimental measurements for all flow velocities studied. However, for the 3.0 % (v/v) volumetric fraction there was an overshoot in pressure gradient estimation, for the lower flow velocities, using the Durand-Condolios correlation. The numeric and experimental values also matched quite well for this particle concentration.

Additionally, the 2D velocity profiles obtained with the MRI and the Mixture Model, shown in Figures 6.18 to 6.20, also display, in spite of small deviations, similar maximum velocity values at the pipe centre, and minimum velocity values close to the wall of the pipe.

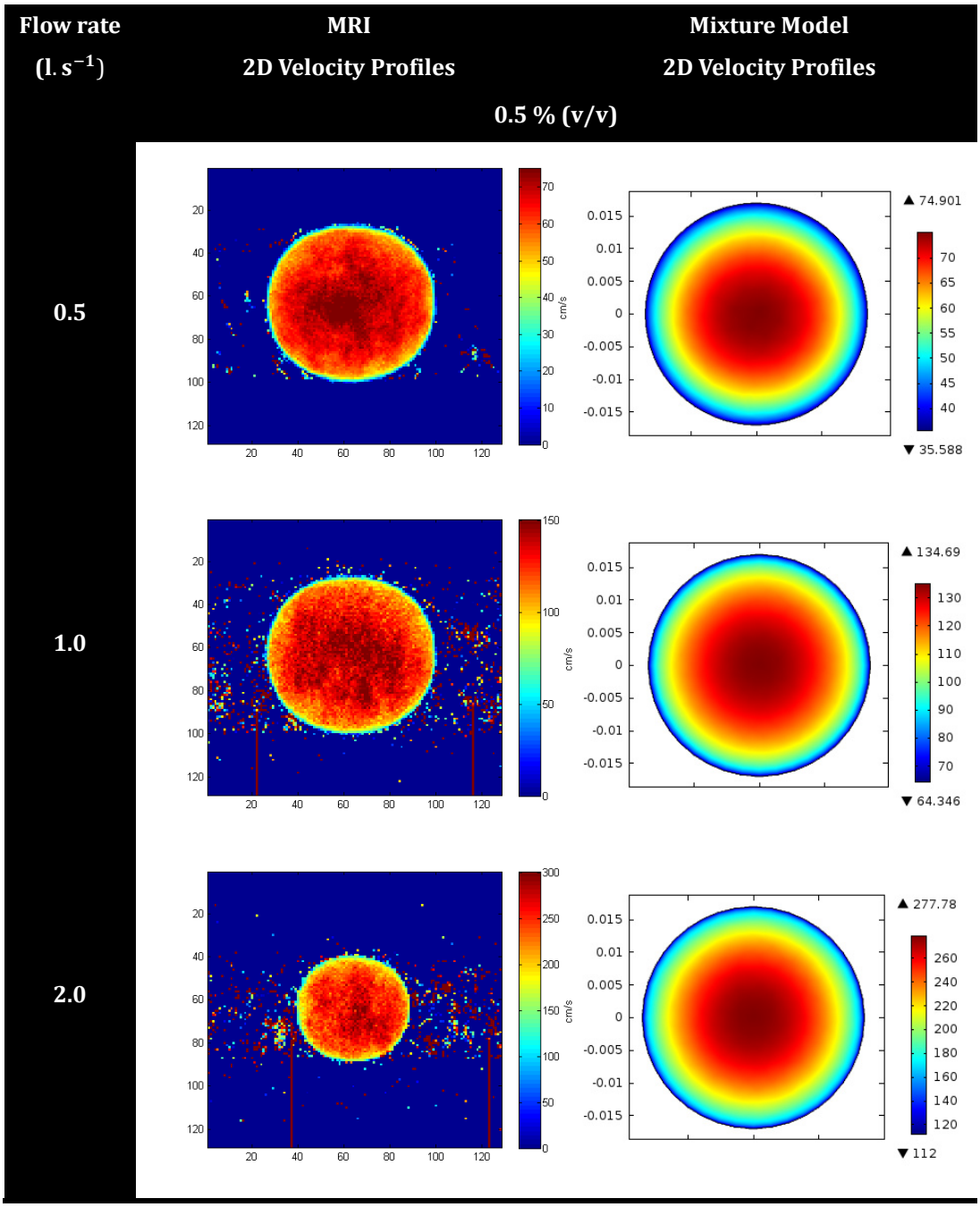

Figure 6.18 – MRI and Numerical 2D velocity profiles for solid-liquid suspensions of 0.1-0.2 mm particles with flow rates of 2.0 (Bottom), 1.0 (Middle) and 0.5 $l.s^{-1}$ (Top) in a 34 mm ID pipe for a solids volumetric concentration of 0.5 % (v/v).

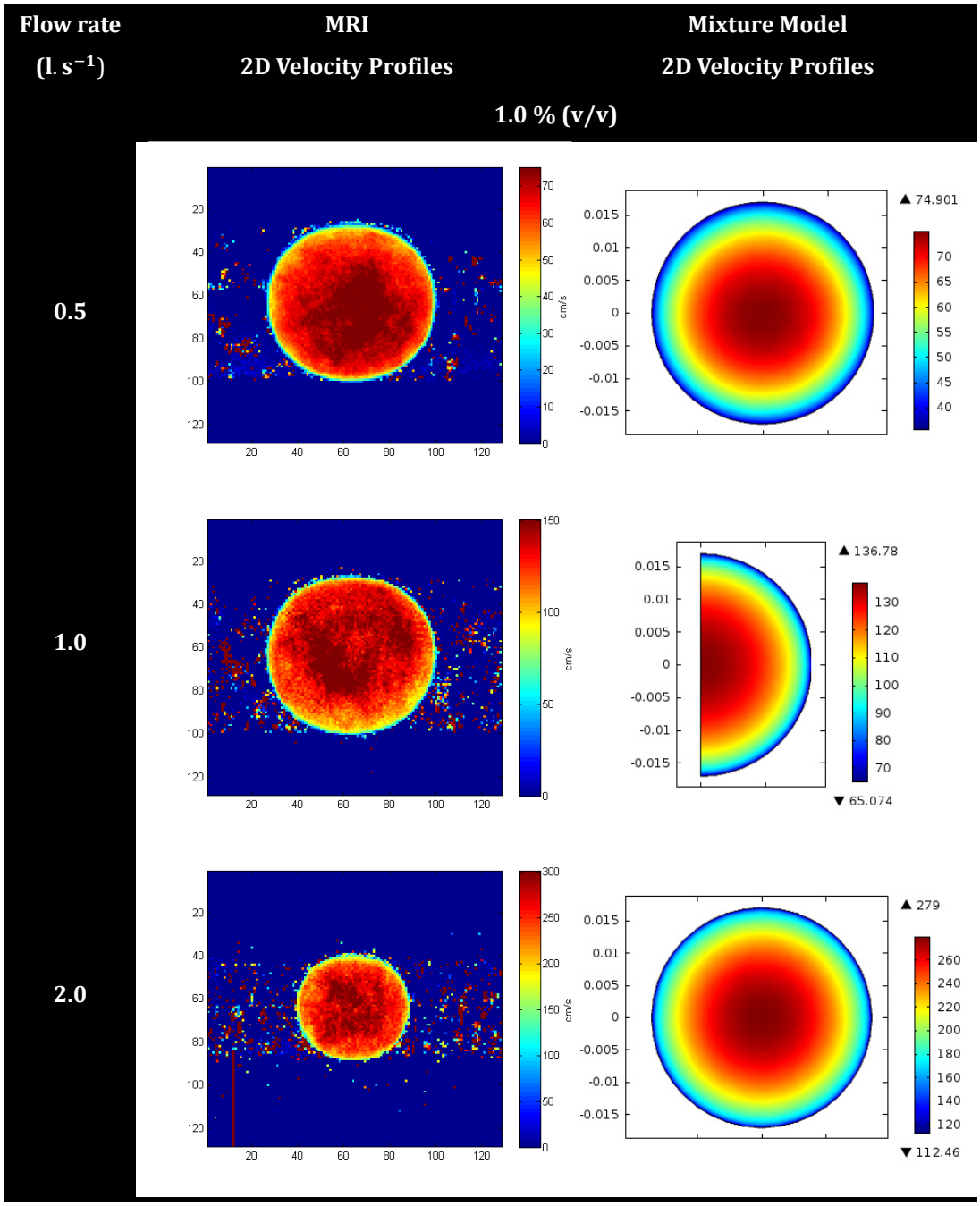

Figure 6.19 – MRI and Numerical 2D velocity profiles for solid-liquid suspensions of 0.1-0.2 mm particles with flow rates of 2.0 (Bottom), 1.0 (Middle) and 0.5 l. s^{-1} (Top) in a 34 mm ID pipe for a solids volumetric concentration of 1.0 % (v/v).

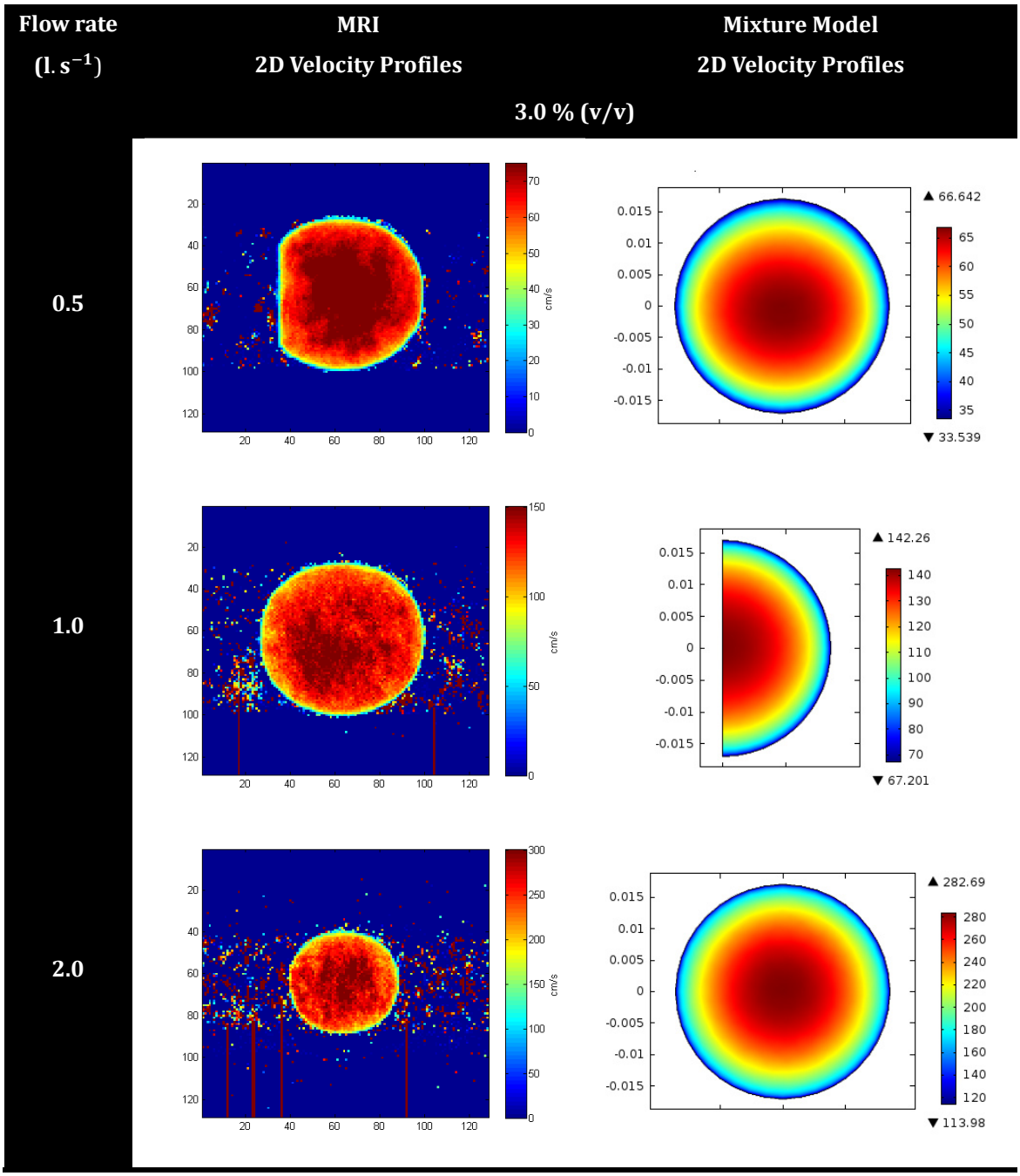

Figure 6.20 – MRI and Numerical 2D velocity profiles for solid-liquid suspensions of 0.1-0.2 mm particles with flow rates of 2.0 (Bottom), 1.0 (Middle) and 0.5 l. s^{-1} (Top) in a 34 mm ID pipe for a solids volumetric concentration of 3.0 % (v/v).

0.4-0.6 mm particles in 34 mm ID pipe

Following the tests with the 0.1-0.2 mm particles, similar testing was performed with bigger particles with a size range of 0.4-0.6 mm, with a mean particle diameter of 0.5 mm (see Appendix C). The same solids volumetric

fractions and flow rates used for the 0.1-0.2 mm particles testing were employed for these trials. With these bigger particles, it can be seen from Figures 6.21 to 6.23 that the numerical and experimental velocity profiles seem to concur for the MRI and numeric results. The UPV data, however, deserves some considerations as there are asymmetries, which should not occur for horizontal profiles, which, rather than depicting a physical phenomenon, can result from the following reasons: first, a faulty alignment of the ultrasound probes ensuing from a slight manufacture error which is detrimental to accurate data acquisition (Wiklund and Stading 2008; T. Wang et al. 2003); secondly, and more plausible, in the posterior probe occurred some particles accumulation, thus, causing an obstruction in the signal generation and acquisition for this probe (which is located in the right side of the flow direction as depicted in Figure 3.27). Nevertheless, if the offset in the lower half of the aforementioned Figures is disregarded, and only the first half of the UPV velocity profiles is considered, then it becomes apparent that the velocity profiles now match the MRI and Mixture Model numerical profiles. For the larger velocities, with a Stokes Number of 2.20, it was assumed that the Mixture Model application was still valid and the velocity profiles seem to further validate the assumption.

An additional validation of this assumption comes from Figure 6.24, where the experimental and numerical pressure gradients match with small deviation. The pressure gradients using Durand-Condolios correlations (see Equations 6.13 and 6.14) were also computed, and similarly to the previous studies with the 0.1-0.2 mm particles, a deviation for the higher particle concentration occurs at the lower flow velocities.

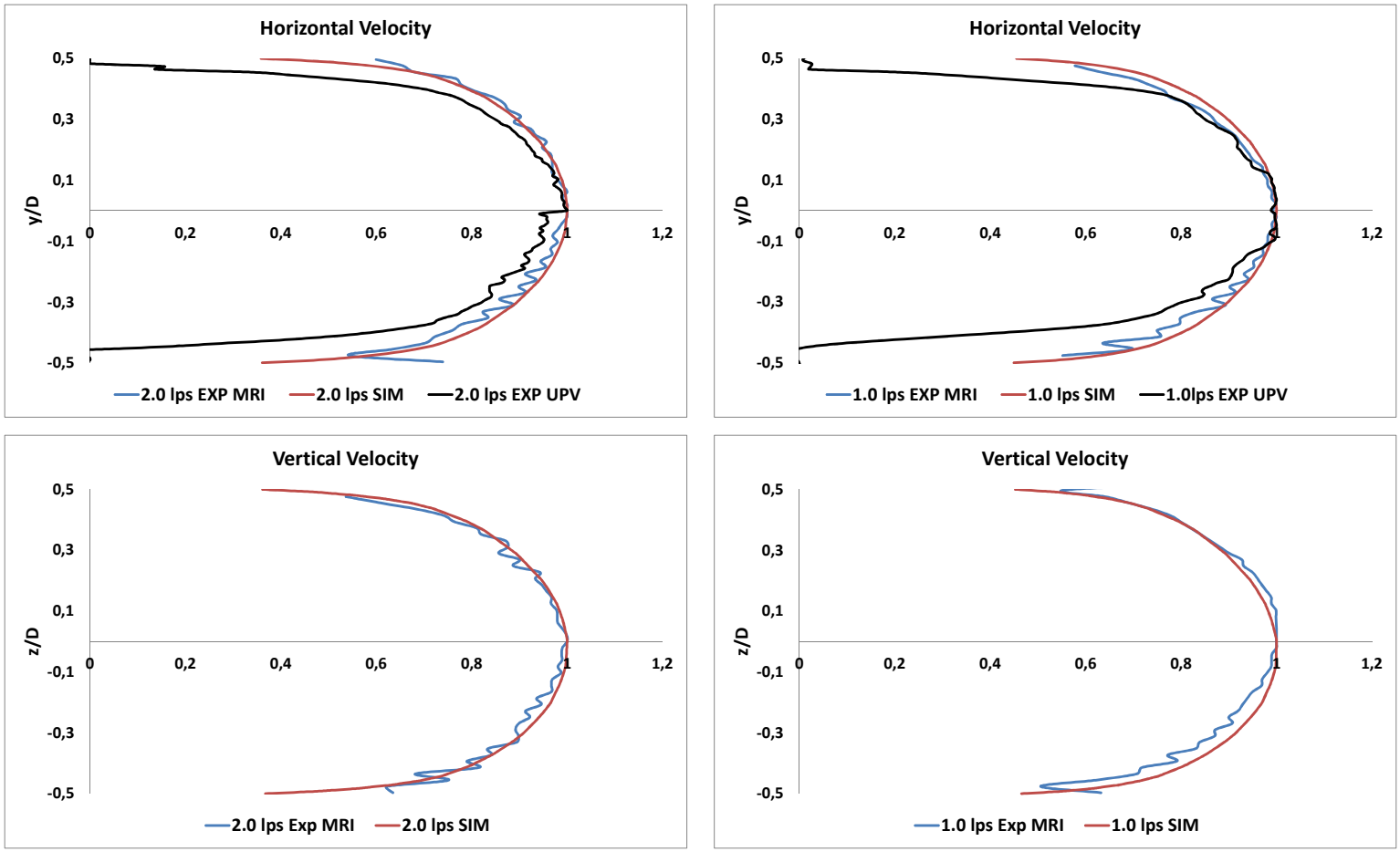

Figure 6.21 – Experimental MRI, UPV and Numerical normalized horizontal (Top) and vertical (Bottom) velocity profiles for solid-liquid suspensions of 0.4-0.6 mm particles with flow rates of 2.0 (Left) and 1.0 $l.s^{-1}$ (Right) in a 34 mm ID pipe for a solids volumetric concentration of 0.5 % (v/v).

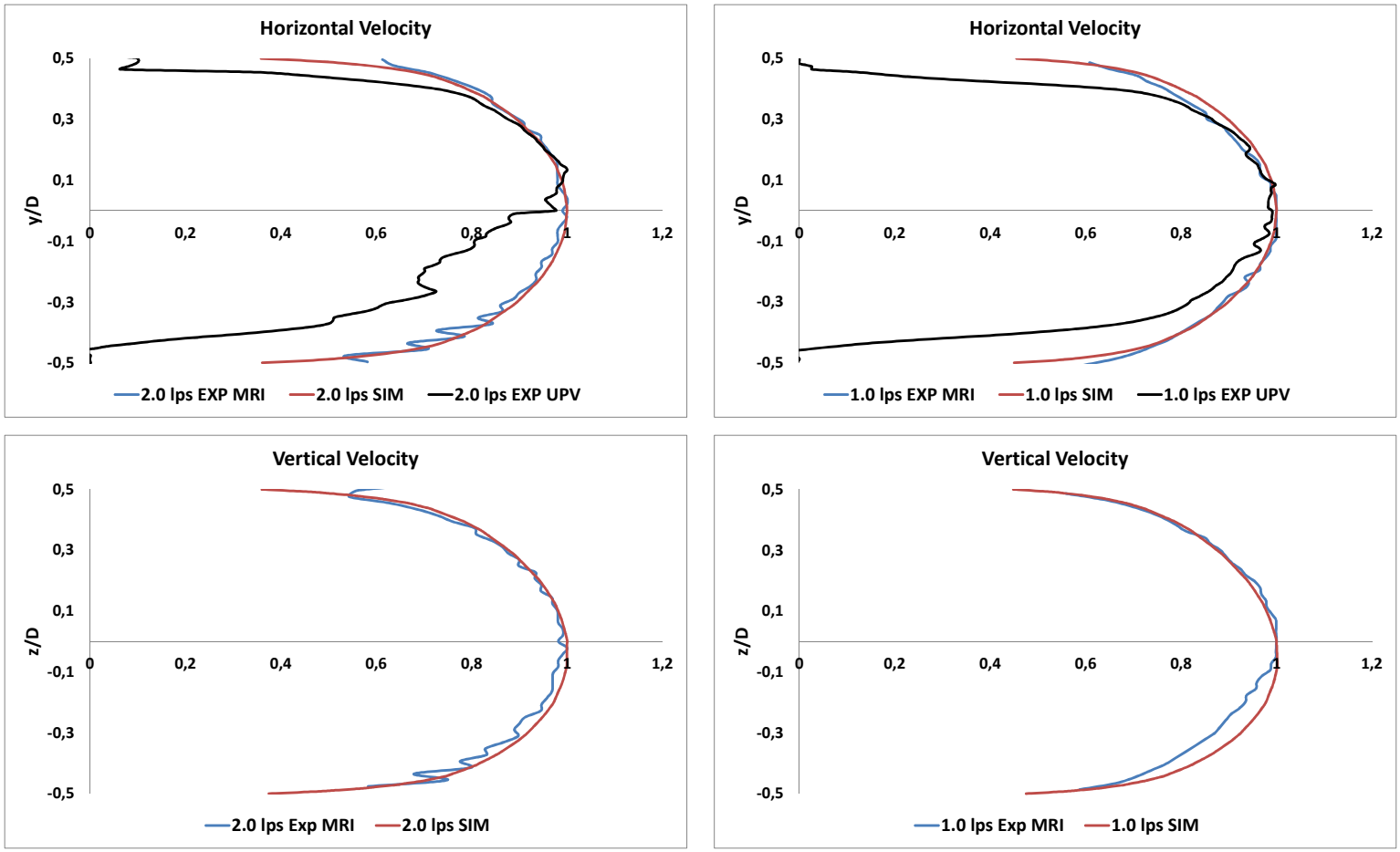

Figure 6.22 – Experimental MRI, UPV and Numerical normalized horizontal (Top) and vertical (Bottom) velocity profiles for solid-liquid suspensions of 0.4-0.6 mm particles with flow rates of 2.0 (Left) and 1.0 $l.s^{-1}$ (Right) in a 34 mm ID pipe for a solids volumetric concentration of 1.0 % (v/v).

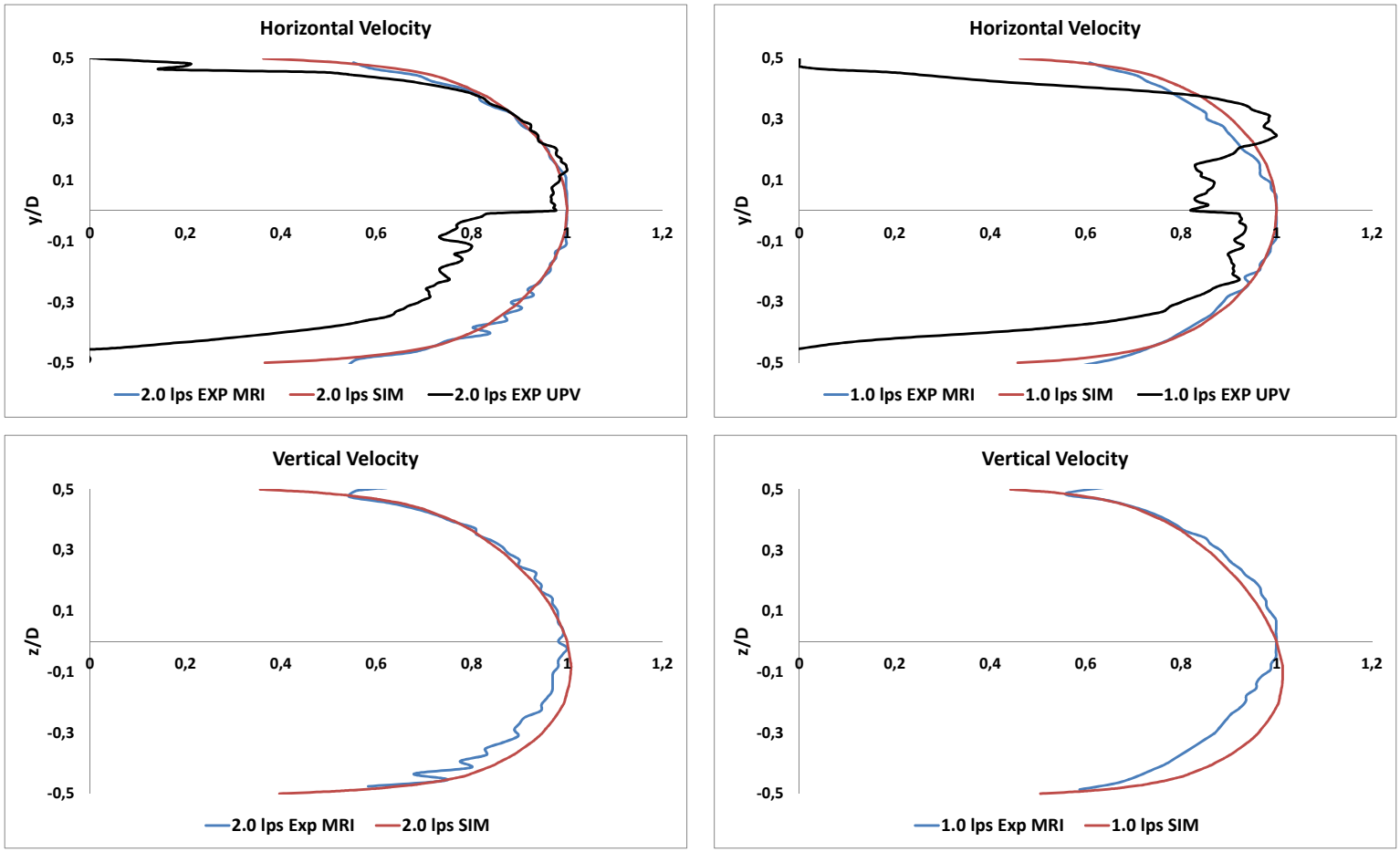

Figure 6.23 – Experimental MRI, UPV and Numerical normalized horizontal (Top) and vertical (Bottom) velocity profiles for solid-liquid suspensions of 0.4-0.6 mm particles with flow rates of 2.0 (Left) and 1.0 $l.s^{-1}$ (Right) in a 34 mm ID pipe for a solids volumetric concentration of 3.0 % (v/v).

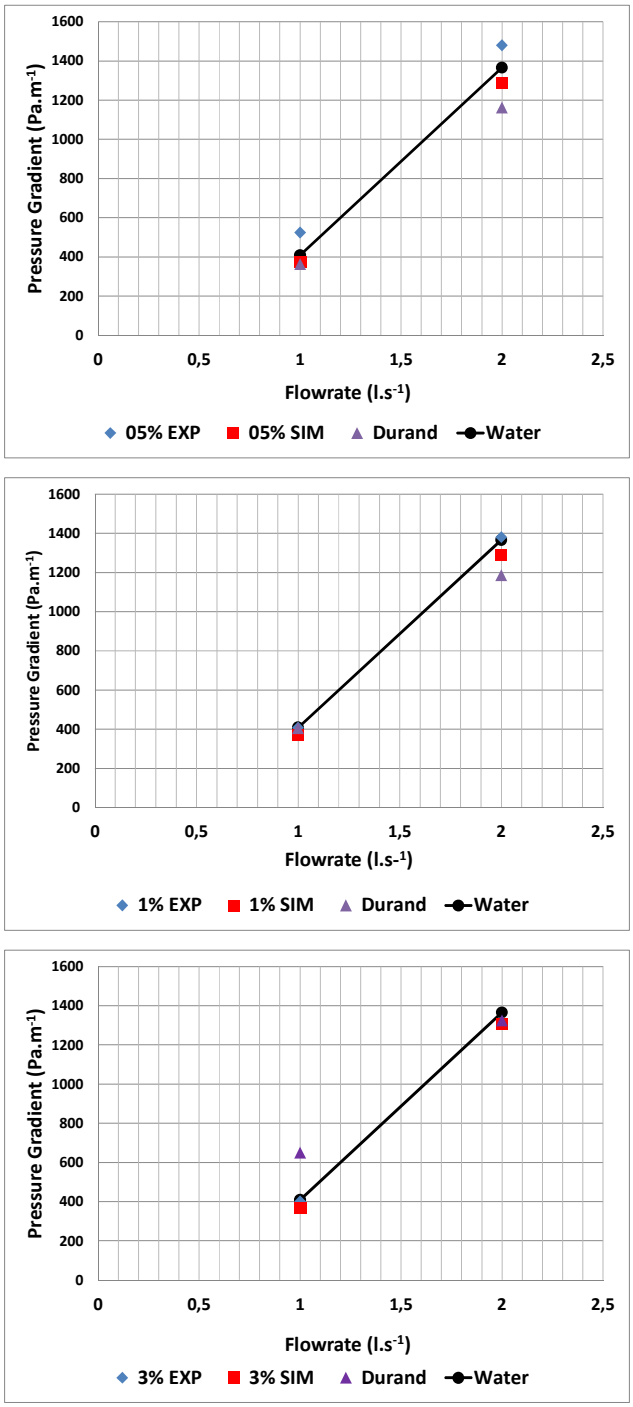

Figure 6.24 – Experimental, Numerical and Durand-Condolios pressure gradients profiles for solid-liquid suspensions of 0.4-0.6 mm particles with 0.5 (Top), 1.0 (Middle) and 3.0 % (v/v) (Bottom) solids volumetric concentration in a 34mm ID pipe.

Similarly to the smaller particles, 0.1-0.2 mm, 2D MRI velocity profiles were also acquired for the 0.4-0.6 mm particles. The results are shown below in Figures 6.25 to 6.27. Although the colorbar for the MRI and Mixture Model velocity profiles displays different ranges, it can still be observed that, overall,

these profiles are in agreement. Similarly to the results for the smaller particles, displayed in Figures 6.18 to 6.20, the maximum flow velocity value observed at the pipe centre is similar for both the MRI and Mixture Model profiles, as well as the minimum flow velocity value at the pipe wall.

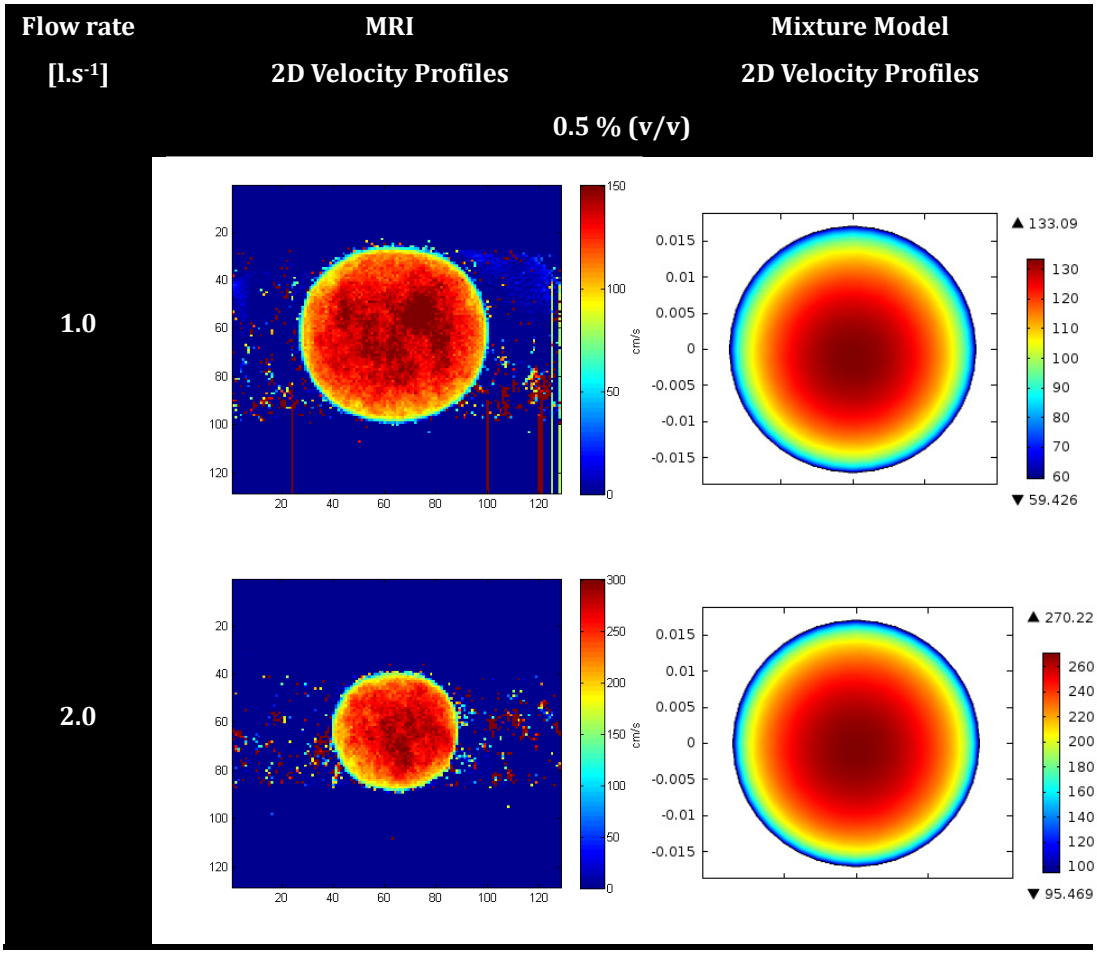

Figure 6.25 – MRI and Numerical 2D velocity profiles for solid-liquid suspensions of 0.4-0.6 mm particles with flow rates of 2.0 (Bottom) and 1.0 l. s^{-1} (Top) in a 34 mm ID pipe for a solids volumetric concentration of 0.5 % (v/v).

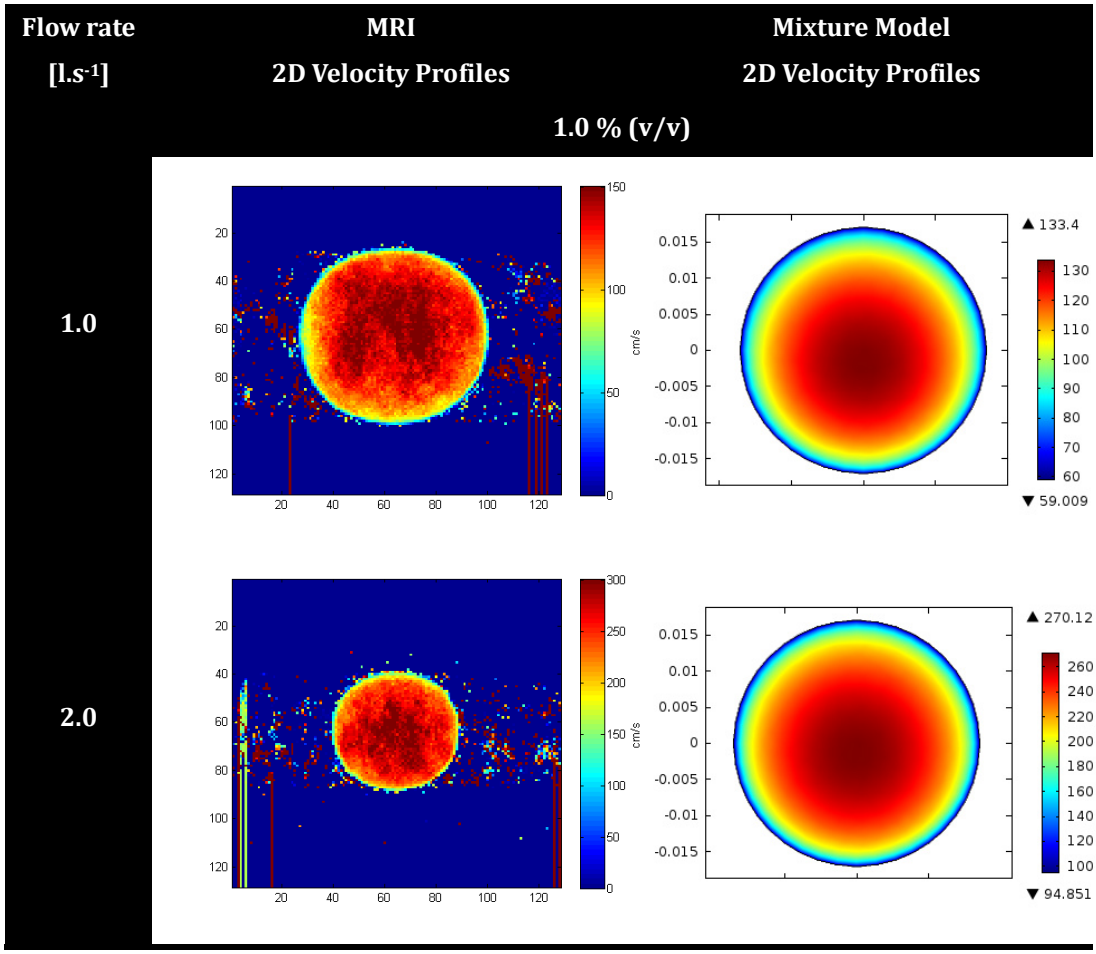

Figure 6.26 – MRI and Numerical 2D velocity profiles for solid-liquid suspensions of 0.4-0.6 mm particles with flow rates of 2.0 (Bottom) and 1.0 l. s^{-1} (Top) in a 34 mm ID pipe for a solids volumetric concentration of 1.0 % (v/v).

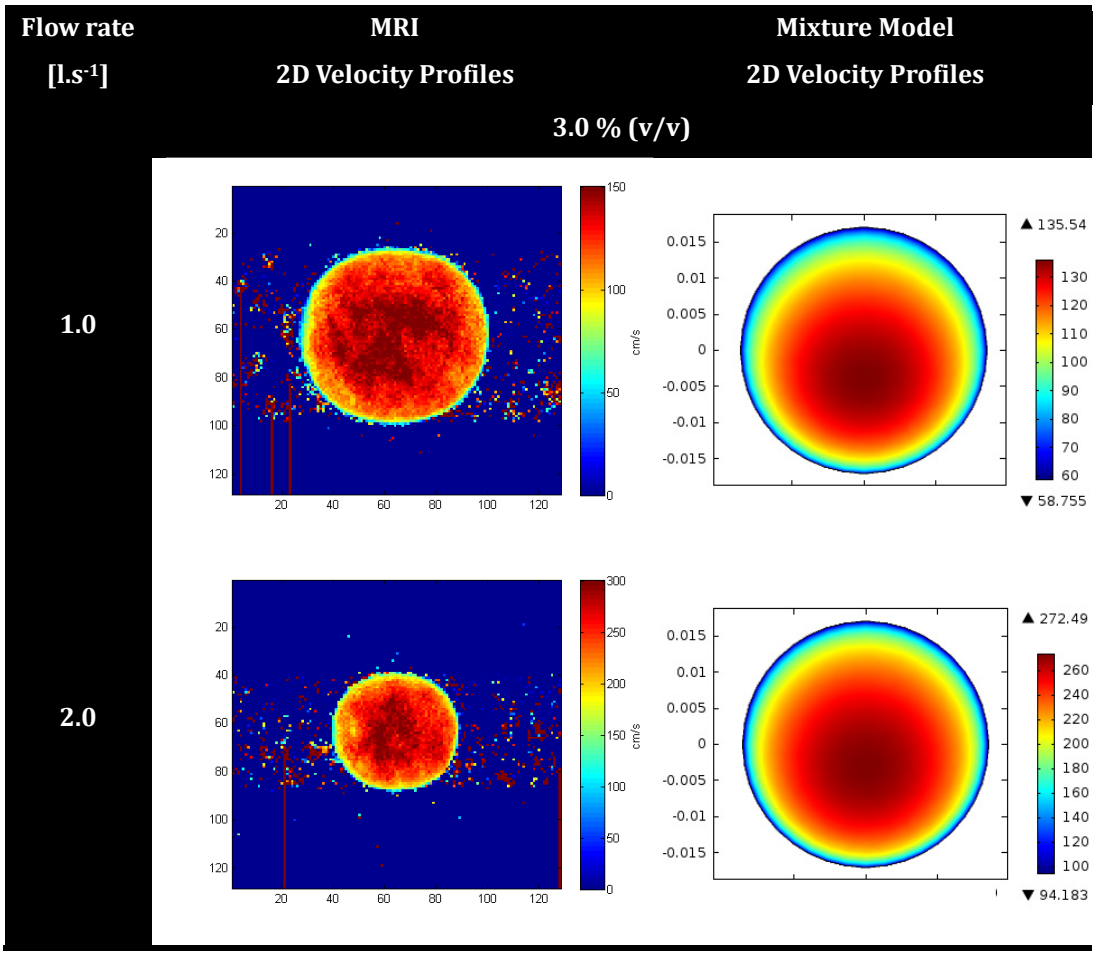

Figure 6.27 – MRI and Numerical 2D velocity profiles for solid-liquid suspensions of 0.4-0.6 mm particles with flow rates of 2.0 (Bottom) and 1.0 l. s^{-1} (Top) in a 34 mm ID pipe for a solids volumetric concentration of 3.0 % (v/v).

0.4-0.6 mm particles in 50 mm ID pipe

At the KTH Mekanics laboratory, it was also possible to study solid-liquid suspensions using a pipe with a bigger internal diameter. The particles used were the bigger particles with a size range of 0.4-0.6 mm with a mean particle diameter of 0.5 mm (see Appendix C). The solids volumetric fractions and flow rates are depicted in Table 6.2.

For a brief period of time it was also possible to use the EIT system developed at DEQ-Coimbra to acquire vertical normalized distributions of conductivity to infer on the distribution of particles in the pipe section. For this technique to retrieve adequate images, NaCl was added to the flow rig in order to attain a flowing solution with an electrical conductivity of 1200 mS. cm^{-1}. The

reference measurements were done without any particles in the flow rig.

The reconstructed 2D images shown in Figure 6.28 represent normalized conductivity measurements, η. The normalization is done using the reference measurements for the 1200 mS. cm^{-1} NaCl solution without particles, as described by Equation 6.15, where σ_0 represents the reference electrical conductivity and $\sigma_m$is the mixture electrical conductivity.

$$\eta = \frac{\sigma_0 - \sigma_m}{\sigma_0} \tag{6.15}$$

From the information in Figure 6.28 it is possible to observe the effect of particle concentration on the conductivity gradient. For 1.0 and 3.0 % (v/v) particle concentration at 2 l. s^{-1} the colour change towards blue in the bottom, where the concentration increased up to 3.0 % (v/v), indicates a shift to higher particle concentration along the bottom of the pipe. The regions with a more intense red colour represent the areas where there is little change in the electrical conductivity, thus, meaning, little or no particles presence. Also, the effect of the flow velocity increase in the turbulent dispersion of particles is discernible by comparison of the left and right columns, demonstrated by the shift in the colour profiles towards the top of the colourbar, i.e., indicating a lower normalized electrical conductivity difference between the mixture and the reference measurements. At 5.0 % (v/v) particle concentration it would be expected that the lower part of the image would be of similar blue colour as the 3.0 % (v/v) reconstructed images, but corresponding to an even greater area, denoting a higher particle concentration at the bottom, due to the effect of gravity.

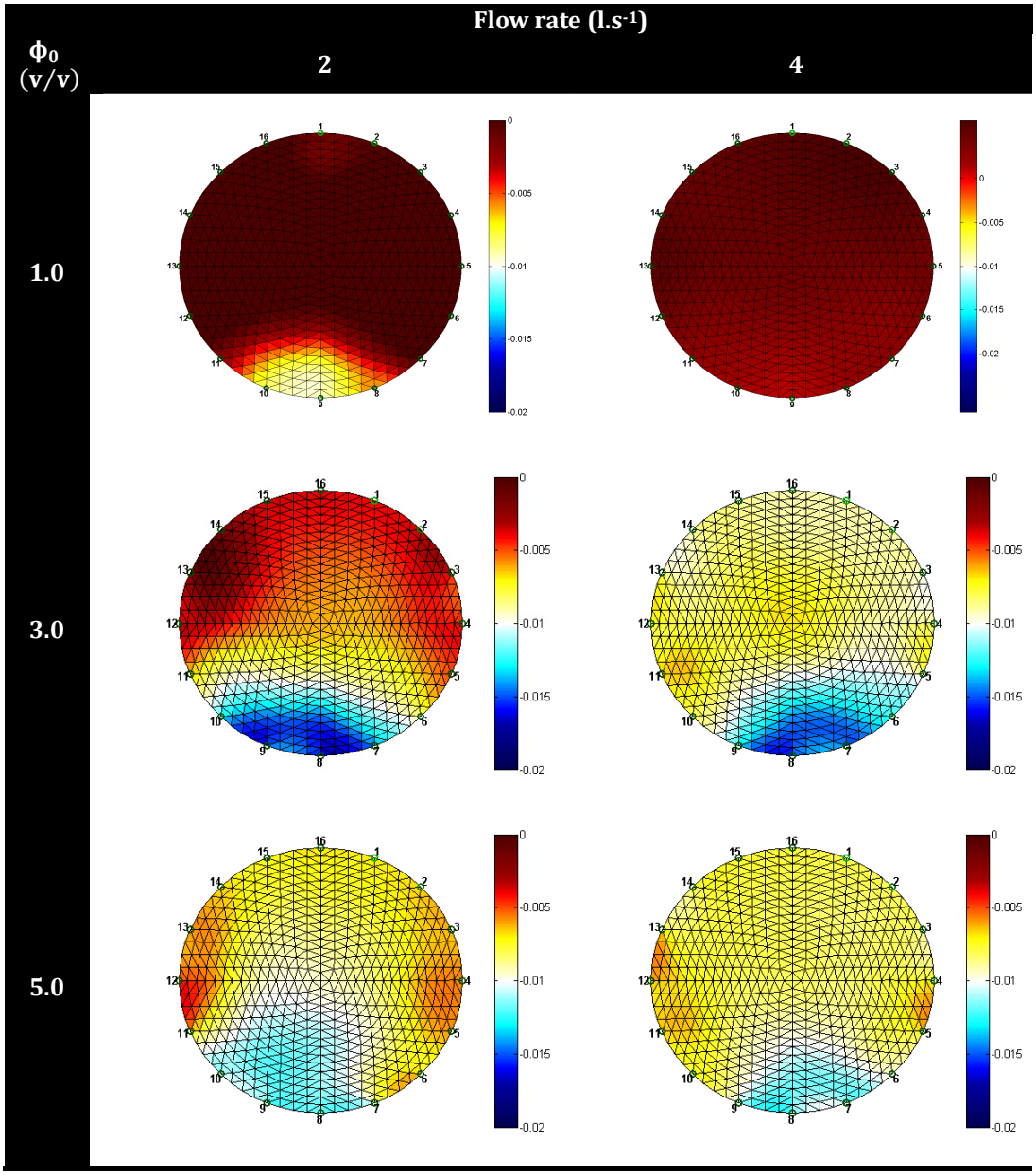

Figure 6.28 – Reconstructed 2D images of the pipe cross-section using EIT normalized conductivity measurements for solid-liquid suspensions of 0.4-0.6 mm particles for 1.0 (Top), 3.0 (Middle) and 5.0 % (v/v) (Bottom) solids volumetric concentration in a 50 mm ID pipe.

This is, however, not the case when the two bottom reconstructed images in Figure 6.28 are inspected in detail. In this case the particles seem to be more fluidized as denoted by wider white and yellow areas. This colour arrangement, particularly at the lower flow velocities, appears to indicate the presence of particle-particle interaction, due to increased particle concentration, which is augmented with an increase in the flow velocity.

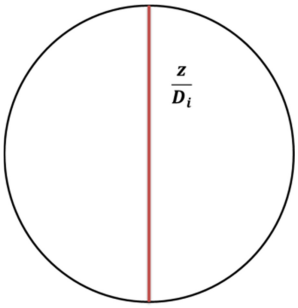

Figure 6.29 – 1D vertical slice schematics for both reconstructed EIT 2D images of the pipe cross-section and numerical data with the Mixture Model in a 50 mm ID pipe.

For the purpose of comparing the reconstructed EIT 2D images and numerical data with the Mixture Model, a 1D vertical distribution was computed as is schematically represented in Figure 6.29. This vertical 1D profile is presented in Figure 6.30, where a comparison is made between the normalized electrical conductivity and the numerical concentration profiles resulting from the Mixture Model. The normalized electrical conductivity profiles for both 1.0 and 3.0 % (v/v) at 2 and 4 $\mathrm{l.s^{-1}}$, respectively, display a higher difference at the top of the pipe section ($z/D = 0.5$), which can wrongfully appear as a higher particle concentration. Based on a physical understanding of the flow phenomena for these flow velocities, with this particle to fluid density ratio, and taking into account the flow regime considerations made in Section 6.3.2, then it is straightforward to assume that this is inaccurate. The increased normalized electrical conductivity is more likely due to small air bubbles present near the EIT data acquisition section. In the remaining profiles higher differences are observed, between the reference and the mixture normalized electrical conductivities, for the lower flow velocities, which were expected since the particle concentrations at the pipe bottom were higher. However, at first glance and making a comparison between similar vertical positons, it would appear that for some normalized electrical conductivity profiles at lower flow velocities the particle concentration (inferred from the normalized electrical conductivity difference) is always higher for most of the pipe cross-section, which is not the case.

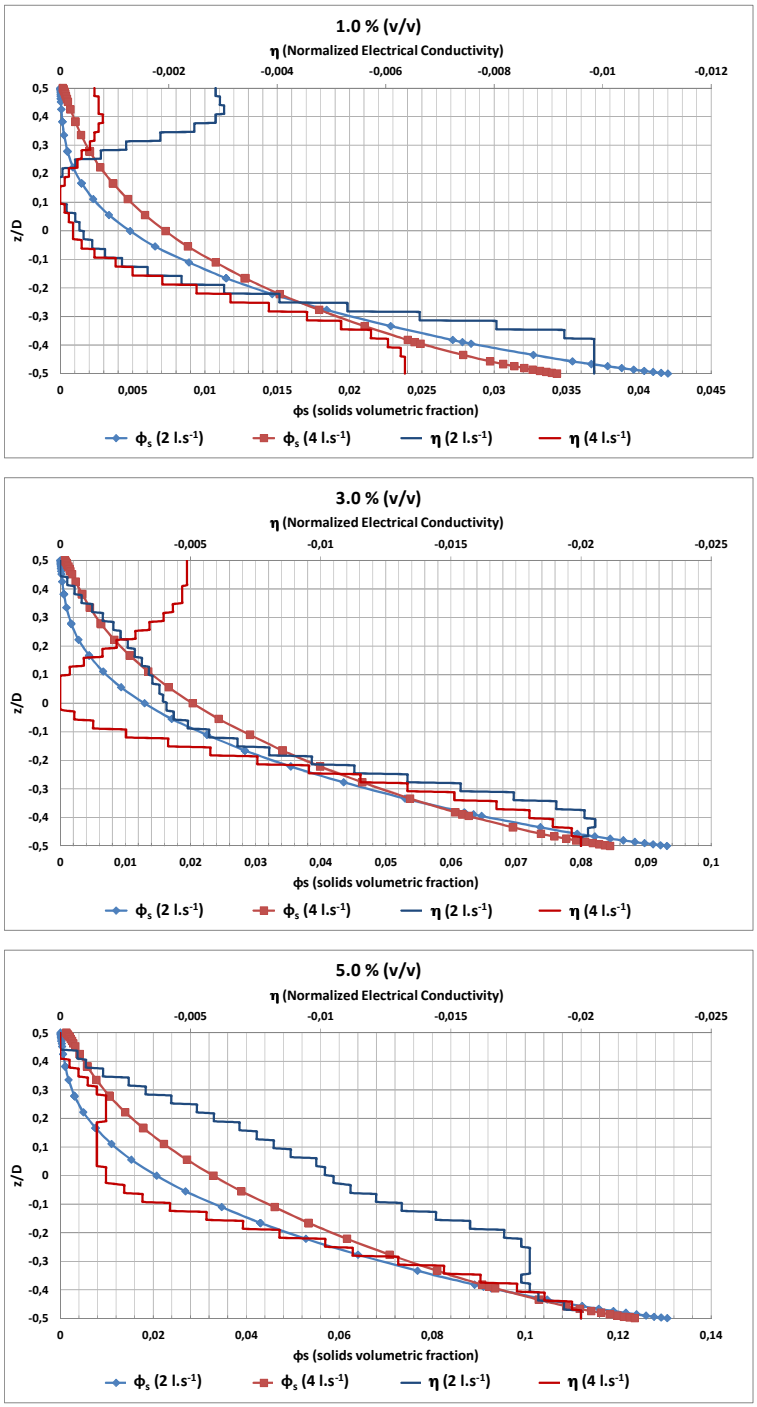

Figure 6.30 – 1D vertical normalized electrical conductivity profiles (η) with EIT and particle concentrations profiles (ϕ_s) with the Mixture Model in a 50 mm ID pipe.

Considering the physical phenomena involved and flow regimes considerations in Section 6.3.3, a careful inspection of the profiles in Figure 6.30 indicates that the normalized electrical conductivities for the higher flow velocities are closer to zero above the pipe bottom, which in turn signifies

that the mixture is more fluidized and thus the differences in the normalized electrical conductivities are reduced.

With this study and with the simultaneous use of the EIT apparatus the aim was to have actual vertical concentration profiles rather than inferring through the normalized electrical conductivity. To accomplish the proposed endeavour two approaches were used to attain the vertical particle distributions.

The first approach was based on the Maxwell Equation, which is one of the most widely used equations that correlates the electrical conductivity with particle concentration, and has shown great promise in deposition recognition (Fangary et al. 1998) and depicting the asymmetry in swirling flows (M. Wang, Jones, and Williams 2003). Other Equations have been employed for particle migration of buoyant particles (Norman, Nayak, and Bonnecaze 2005). Since all particles involved in this study are non-conducting settling particles, one of the approaches to achieve vertical particle distributions will be to use the Maxwell Equation (see Equation 6.16).

$$\sigma_m = \sigma_w \left(\frac{2 - 2\,\phi_0}{2 + \phi_0} \right) \tag{6.16}$$

Using the studies by Giguère et al. (2008) as the basis, where the normalized electrical conductivity, η, is combined with Equation 6.16, and through algebraic manipulation, Equation 6.17 is obtained for the apparent solids concentration, ϕ_{ap}:

$$\phi_{ap} = \frac{2 - 2\big((1+\eta)(\sigma_0/\sigma_{s0})\big)}{2 - \big((1+\eta)(\sigma_0/\sigma_{s0})\big)} \tag{6.17}$$

where the σ_0/σ_{s0} quantity is achieved using the known initial concentration of solids, ϕ_0, as the initial condition in Equation 6.16. This assumes a homogenous particle distribution which is contrary to the observed experimental flow regimes. In order to avoid the homogeneous particle

distribution and provide a more accurate description of the particle distribution, based on the normalized electrical conductivity profiles, the following assumption was made where the initial concentration of solids is multiplied by the normalized electrical conductivity as shown in Equation 6.18:

$$\sigma_m = \sigma_w \left(\frac{2 - 2\,\eta\,\phi_0}{2 + \eta\,\phi_0} \right) \tag{6.18}$$

and with Equation 6.18 the new σ_0/σ_{s0} quantity is calculated and then used in Equation 6.17.

The second approach was to calculate the area under the normalized electrical conductivity curve, A_σ, and obtain the vertical particle distribution according to Equation 6.19.

$$\phi(z) = \frac{\phi_0}{A_\sigma}\eta \tag{6.19}$$

The calculated vertical particle distribution profiles, using both approaches and the numerical vertical particle distribution profiles from the Mixture Model are presented in Figure 6.31. The modified Maxwell Equation (see Equation 6.17), by comparison with the Mixture Model's numerical values, undershoots the particle concentration values for most of the lower bottom half of the pipe section. This happens for all concentrations and flow velocities.

With the second approach, Equation 6.19, the particle concentration values are similar between the Mixture Model and the calculated values using EIT electrical conductivity data, with the exception for the 5.0 % (v/v) concentration profile at $4\,\mathrm{l.s^{-1}}$. This can be attributed to the ratio between the initial particle concentration and the area under the curve in Equation 6.19. As described above, a more fluidized mixture will result in a reduced normalized electrical conductivity profile, therefore, resulting in a smaller area under the curve. For area values below one, this ratio will result in an

overshoot of the concentration profile as seen for 1.0 and 5.0 % (v/v) particle concentrations for a 4 l. s^{-1} flow rate, albeit more noticeable for 5.0 % (v/v) particle concentration.

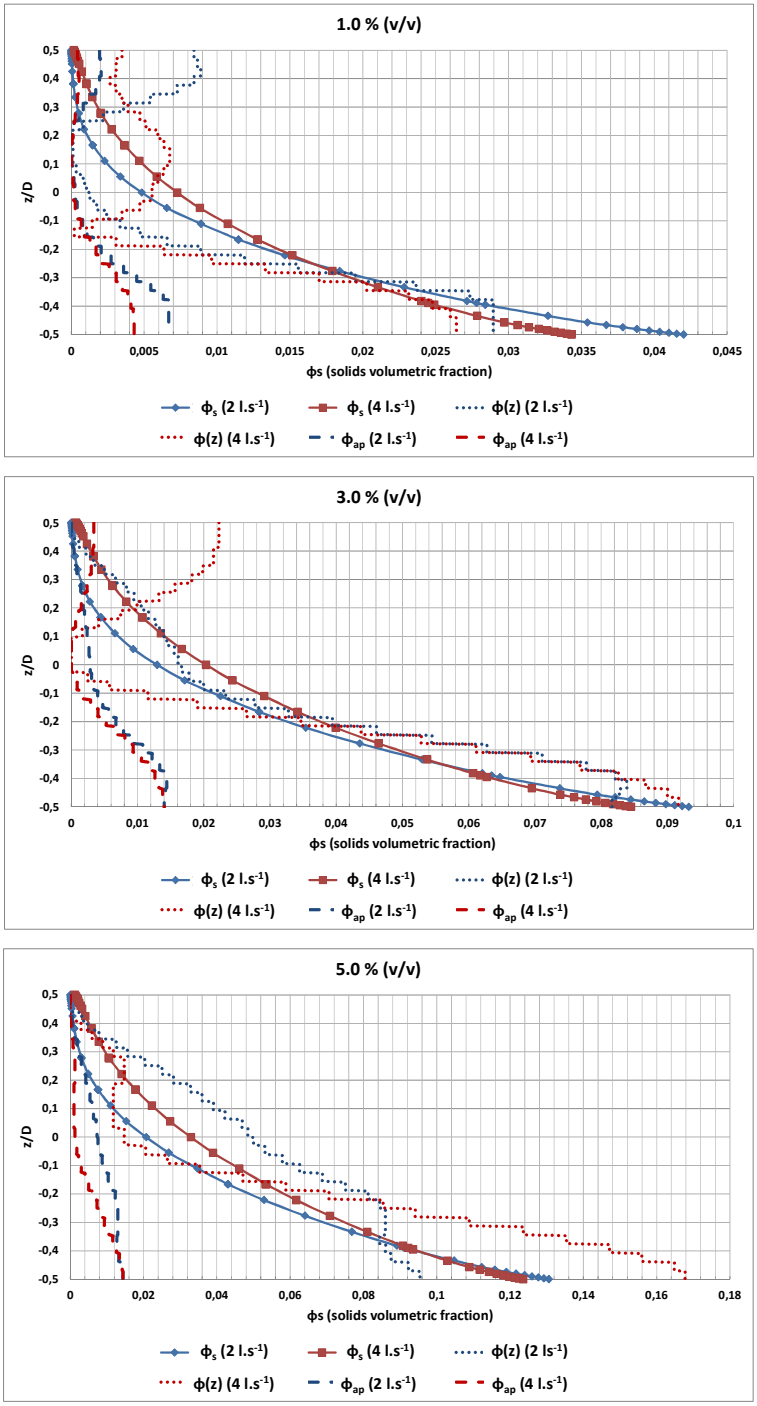

Figure 6.31 – Comparison between 1D calculated vertical particle distribution profiles with EIT, $\phi(z)$, and Maxwell Equation, ϕ_{ap}, with the particle concentrations profiles from the Mixture Model in a 50 mm ID pipe.

The MRI, UPV and numerical velocity profiles are presented in Figures 6.32 to 6.34 and, overall, the normalized profiles seem to match for the UPV, MRI and numerical data sets. For these experiments the UPV probes were vertical for most of the experiments, and due to particle settling, the bottom probe acquisition was hindered considerably failing to provide any data. For the highest particle concentration (5.0 % (v/v)) UPV data was obtained in both vertical and horizontal positions, as seen in Figure 6.34. The UPV profiles seem to become unreliable at the pipe centre area where the data is riddled with noise which can be attributed to the fact that only the probe on top of the pipe section was acquiring data. In spite of the aforementioned noisy data, the vertical positioning of the probes did provide an opportunity to use UPV to recognize the effect of the flow velocity on the particle distribution gradients which seem to be concordant, in almost all the tests, with both the MRI and the numerical data. The vertical asymmetry, which is more notorious for the higher concentration of particles, resulting from particle settling, is matched between the normalized experimental and the numerical profiles, although at the pipe bottom there are some differences. Considering the data from the Deposition Velocities in Table 6.3 and by visual inspection of the flows, the differences between the MRI and UPV profiles at the pipe bottom can be further explained by the presence of a moving bed where the particles slow the water velocity. The bigger offset at the pipe bottom from the UPV profiles can be explained by the lack of data from the bottom probe and the increased impedance in the signal propagation due to increasing particle concentration.

Similarly to the previous studies, it was assumed that, for a Stokes Number of 1.66 (see Table 6.4), the Mixture Model application was still valid and again the velocity profiles seem to further validate the assumption, as seen in Figures 6.32 to 6.34. Further corroboration comes from Figure 6.35 where the experimental and numerical pressure gradients match with small deviation, particularly when the results using the Durand-Condolios correlations show increasing offsets with increasing particle concentration.

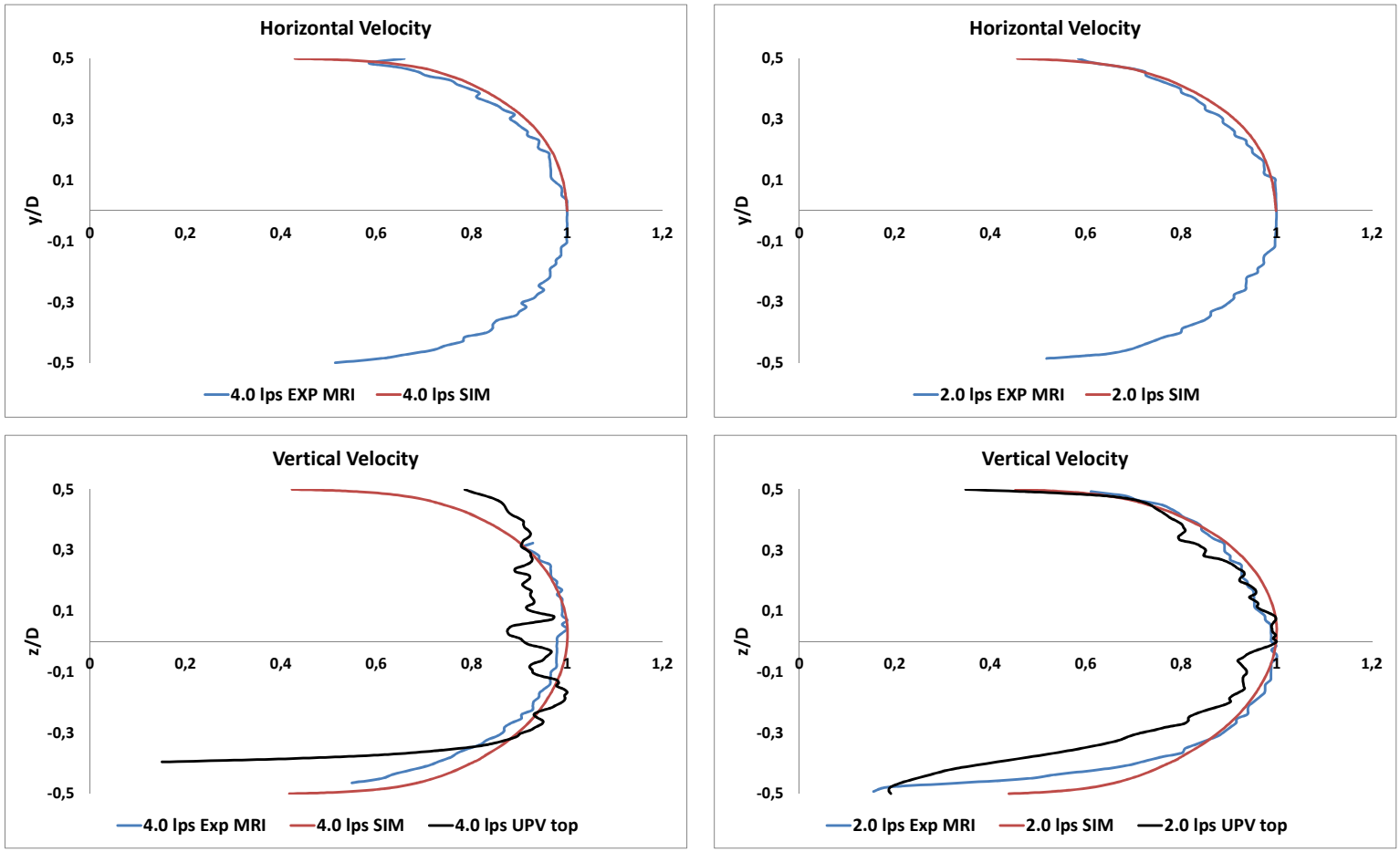

Figure 6.32 – Experimental MRI, UPV and Numerical normalized horizontal (Top) and vertical (Bottom) velocity profiles for solid-liquid suspensions of 0.4-0.6 mm particles with flow rates of 4.0 (Left) and 2.0 $l.s^{-1}$ (Right) in a 50 mm ID pipe for a solids volumetric concentration of 1.0% (v/v).

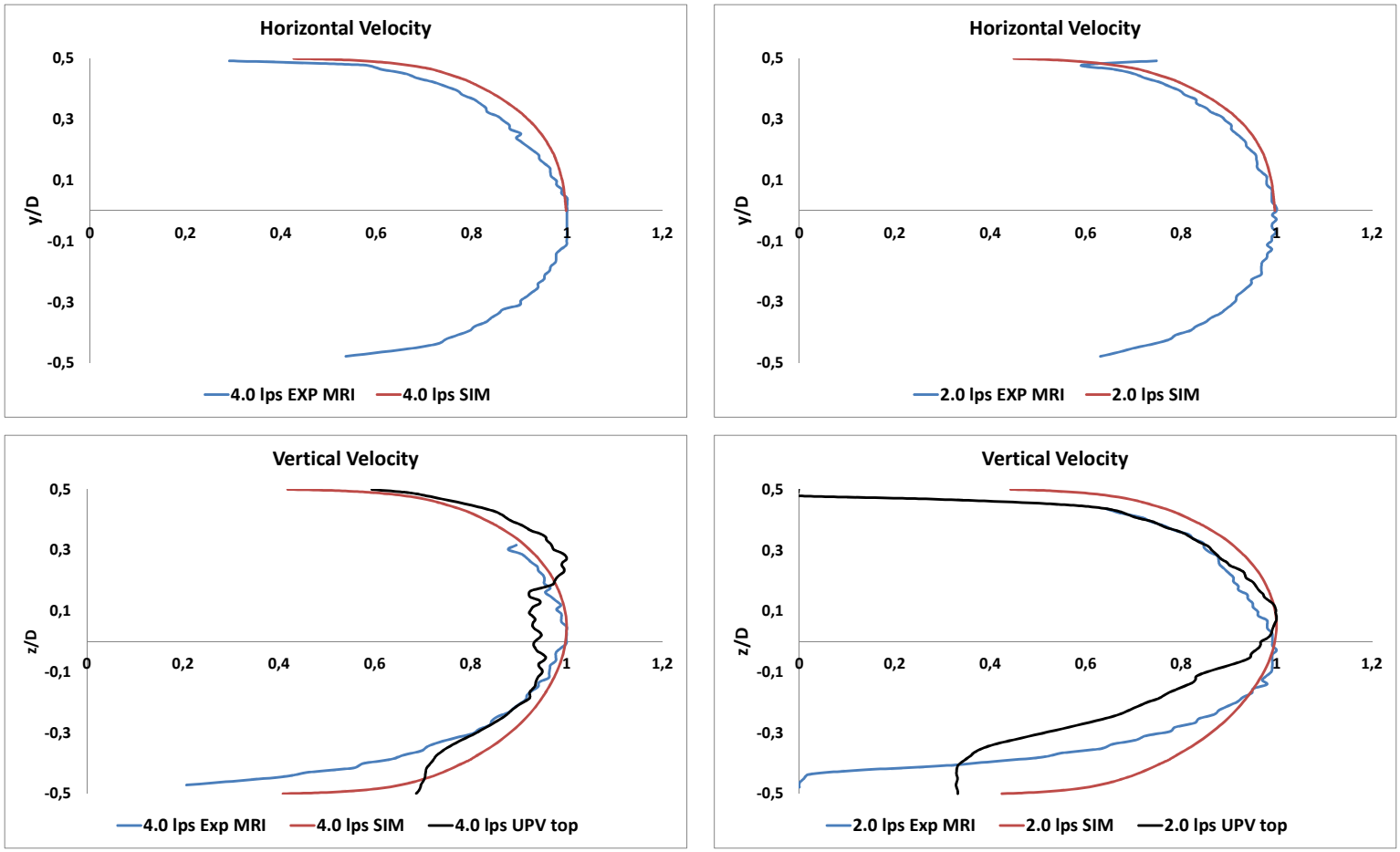

Figure 6.33 – Experimental MRI, UPV and Numerical normalized horizontal (Top) and vertical (Bottom) velocity profiles for solid-liquid suspensions of 0.4-0.6 mm particles with flow rates of 4.0 (Left) and 2.0 $l.s^{-1}$ (Right) in a 50 mm ID pipe for a solids volumetric concentration of 3.0% (v/v).

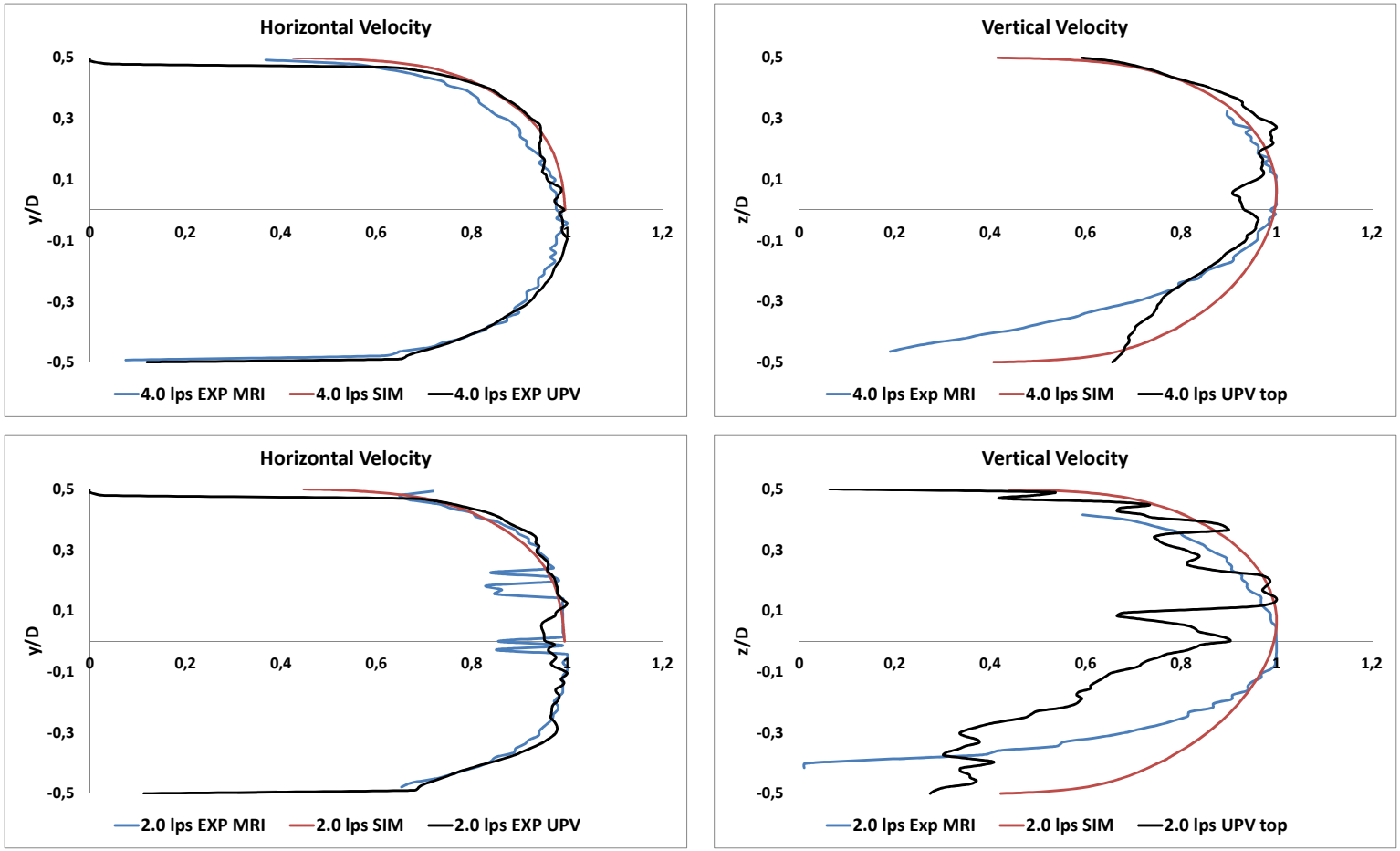

Figure 6.34 – Experimental MRI, UPV and Numerical normalized horizontal (Top) and vertical (Bottom) velocity profiles for solid-liquid suspensions of 0.4-0.6 mm particles with flow rates of 4.0 (Left) and 2.0 $l.s^{-1}$ (Right) in a 50 mm ID pipe for a solids volumetric concentration of 5.0% (v/v).

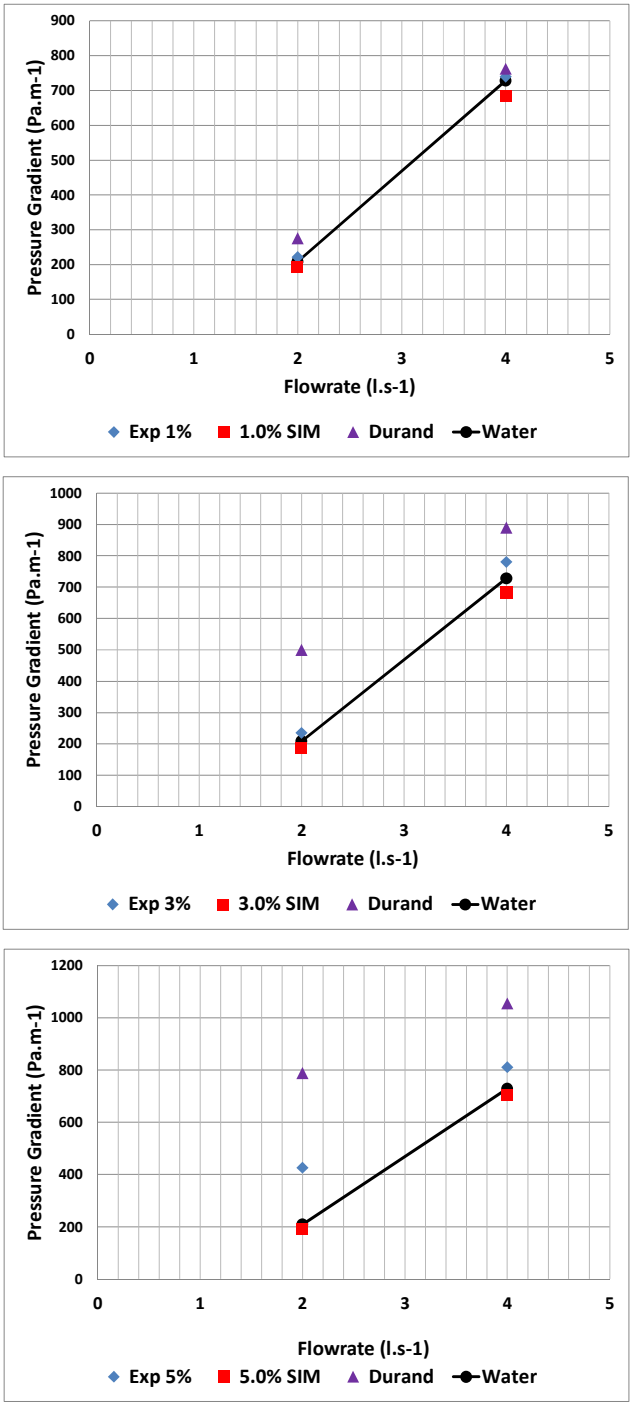

Figure 6.35 – Experimental, Numerical and Durand-Condolios pressure gradients profiles for solid-liquid suspensions of 0.4-0.6 mm particles for 1.0 (Top), 3.0 (Middle) and 5.0% (v/v) (Bottom) solids volumetric concentration in a 50 mm ID pipe.

The biggest deviation occurs for 5.0 % (v/v) at 2 $\mathrm{l.s^{-1}}$ where a considerable moving bed was observed. As documented by previous authors (Ling et al. 2003) the Mixture Model can provide a better prediction of pressure gradients if the solid-liquid suspension mean velocity is higher than the

critical deposition velocity. When the flow rate is $2\ \mathrm{l.s^{-1}}$, corresponding to a flow velocity of $1\ \mathrm{m.s^{-1}}$, that is below the critical deposition velocity, thus resulting in a numeric overshoot of the pressure gradient. As the particle concentration increases this effect becomes even more noticeable for the $2\ \mathrm{l.s^{-1}}$ flow rate.

6.4.5. TURBULENCE MODULATION ANALYSIS

The results obtained using Equation 4.104 from the Tanaka & Eaton study (Tanaka and Eaton 2008) to analyse the effect on the turbulence modulation of the two different particle sizes used in the KTH experiments, are presented in Table 6.7.

Table 6.7 – Stokes Number (St) based Particle Moment Number (Pa_{St}) values for the KTH tests.

		34 mm ID pipe				50 mm ID pipe
	d_p	0.1-0.2 mm	0.4-0.6 mm		d_p	0.4-0.6 mm
Pa_{St}	$0.5\ \mathrm{l.s^{-1}}$	6.72	--------	Pa_{St}		--------
	$1.0\ \mathrm{l.s^{-1}}$	18.99	211.09		$2.0\ \mathrm{l.s^{-1}}$	154.81
	$2.0\ \mathrm{l.s^{-1}}$	53.74	597.04		$4.0\ \mathrm{l.s^{-1}}$	437.86

Comparing the calculated values in Table 6.7 with the data from Figure 4.7 it seems that for the 34 mm ID pipe flows and smaller particles, their Pa_{St} values appear to place them in the area of turbulence augmentation in water. Using the pressure gradient as the evaluation variable for the turbulence modulation and looking at Figure 6.17, it would seem that the smaller particles attenuate the turbulence, since their pressure gradient is equal or lesser than the pressure gradient of single-phase water flow under the same conditions. However, for such small concentrations it is expected that the influence of the particles will be small. The biggest particles showed also augment the turbulence in both the 34 and 50mm pipes flows.

In Figure 6.36, the influence of the particle size on the numerical turbulence kinetic, k, and turbulence dissipation rate, ε, are shown. The turbulence variables with the water flows were attained using a High Reynolds k-ε

Turbulence model and the remanding profiles with the Mixture Model coupled with High Reynolds *k*-*ε* Turbulence model and a SN drag correlation. With all these profiles the highest flow velocity was tested (2 m. s^{-1}, see Table 6.2), and with the exception for the water profiles, all the other profiles are for a particle concentration of 3.0 % (v/v) since it was the common particle concentration for the studies in both pipe diameters. For the 34 mm ID pipe the influence of the 0.1-0.2 mm particle sizes with 3.0 % (v/v) is practically negligible, thus further validating the observations by several authors (Druzhinin and Elghobashi 1999; Druzhinin 2001) that for small *St* and *Pa* Numbers (see Tables 6.4 and 6.7) the particles have little effect on the flow. Also, it further validates the assumption by other authors (Rizk and Elghobashi 1989; Hsu 2003; Kartushinsky et al. 2010; Roco and Shook 1984) to use a single-phase numerical model to characterize these dilute suspensions with the smaller particles. The turbulence variables for larger particles, in the 34 mm pipe, showed a slight increase, when compared with the smaller particles, which can be attributed to the a higher degree of heterogeneity in the particle distribution in the pipe cross-section. This can be observed by comparing the turbulent kinetic energy profiles between the two particles sizes in the 34 mm ID pipe, where the *k* profile for the bigger particles indicates a displacement towards the bottom of the pipe.

The influence of the bigger particles in the turbulence variables, when compared to the water flow in the 50 mm ID pipe, point to an increase in both the *k* and *ε* maximum values, although not that significant. What is noticeable in these profiles is the displacement of the turbulence production towards the lower part of the pipe cross–section denoting an even higher degree of particle heterogeneity in this area of the pipe. This was expected since the amount of particles is now higher (even though the volumetric concentration is the same) due to the rise in total volume of the flow loop owing to the increased pipe diameter. Also, comparing the *k* profiles for the bigger particles, in both pipe configurations, points to an increase in the turbulence production near the pipe wall for the 34 mm ID pipe which can be attributed

to the presence of a higher amount of particles fluidised as pointed out by the Deposition Velocities in Table 6.3.

So, in all the studied cases, there appears to be amplification of the turbulence production resulting from the introduction of the particles and as expected from the parameters in Table 6.7 and Figure 4.7.

34 mm ID pipe			50 mm ID pipe	
Water	**0.1-0.2 mm**	**0.4-06 mm**	**Water**	**0.4-0.6 mm**
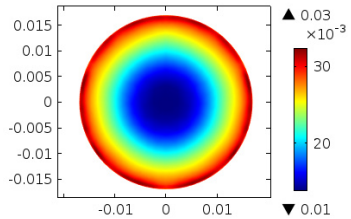	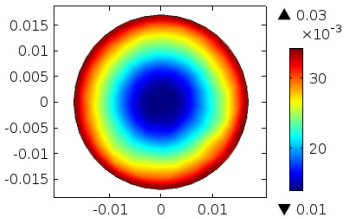	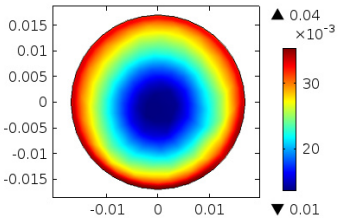	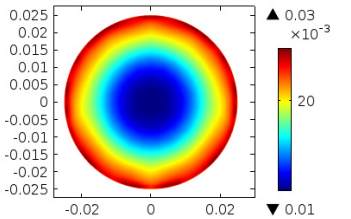	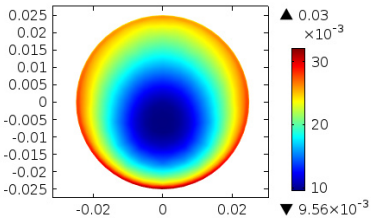
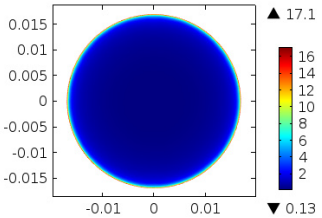	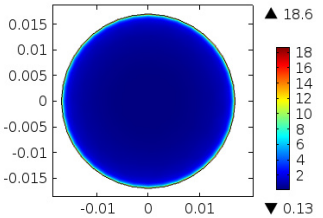	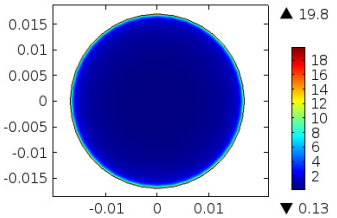	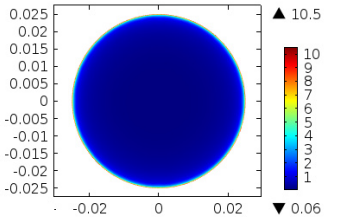	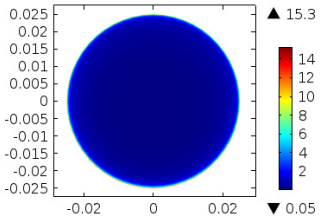

Figure 6.36 – Comparison of the numerical turbulent kinetic energy, k, (Top Row) and turbulent dissipation rate, ε, (Bottom Row) profiles for the studied flows at KTH for a flow velocity of 2 m. s^{-1} between water and solid-liquid suspensions with 3.0 % (v/v) solids volumetric concentration for both 34 and 50 mm ID pipes.

6.5. CONCENTRATED SOLID-LIQUID SUSPENSIONS FLOWS – DEQ-FCTUC

With the studies presented in this section the aim was to go beyond the solids concentrations studied at KTH Mekanics by using the same particle sizes with increasing concentrations until a maximum of 11.0 % (v/v) was achieved. Above this particle concentration there were some issues switching on the pumping system so further tests could not be performed. Additionally, EIT and probe sampling were employed to obtain vertical solids concentration profiles to compare with the numerical results obtained using the Mixture Model and different drag correlations.

6.5.1. EXPERIMENTAL CONDITIONS

The experimental conditions for the flow and particle data are depicted in Table 6.8. Contrarily to the studies at KTH, the experimental tests conducted at DEQ only employed a single 100 mm internal diameter (ID) pipe configuration.

Table 6.8 – Conditions for the DEQ experiments.

	FLOW DATA	
PIPE ID [mm]	100	
$Q\ [m^3.h^{-1}]$	28.0 56.0 84.0	
$A\ [m^2]$	0.007854	
$U\ [m.s^{-1}]$	0.99 1.98 2.97	
$\rho_F\ [kg.m^{-3}]$	998**	
$\mu_F\ [Pa.s]$	1.02×10^{-3}**	
Re	96894 193788 290681	
	PARTICLE DATA	
$\rho_P\ [kg.m^{-3}]$	2500	2500
$d_p\ [mm]$	0.15*	0.5*
$\phi\ [v/v]$	0.008 0.02 0.05 0.08 0.11	

*** Averaged values, see Appendix C for additional details.**
**** Values at 20ºC.**

6.5.2. FLOW REGIME CONSIDERATIONS

Similarly to the previous tests on dilute solid-liquid suspensions, different flow regimes were imposed with the experiments at DEQ's pilot rig. The same two sizes of particles were employed with increasing particle concentrations and higher flow rates.

0.1-0.2 mm Particles

In this 100 mm pipe configuration the 0.1-0.2 mm particles, at a flow rates of 28 $m^3.h^{-1}$, displayed a sliding or moving bed regime (see Figure 6.37) with

practically no or little particle fluidization. At the remaining flow velocities of 56 and 84 $m^3.h^{-1}$ heterogeneous flow regimes were observed. Furthermore, as the particle concentration increased the amount of fluidized particles also increased, mainly due to particle-particle interactions, particularly for the heterogeneous flow regimes.

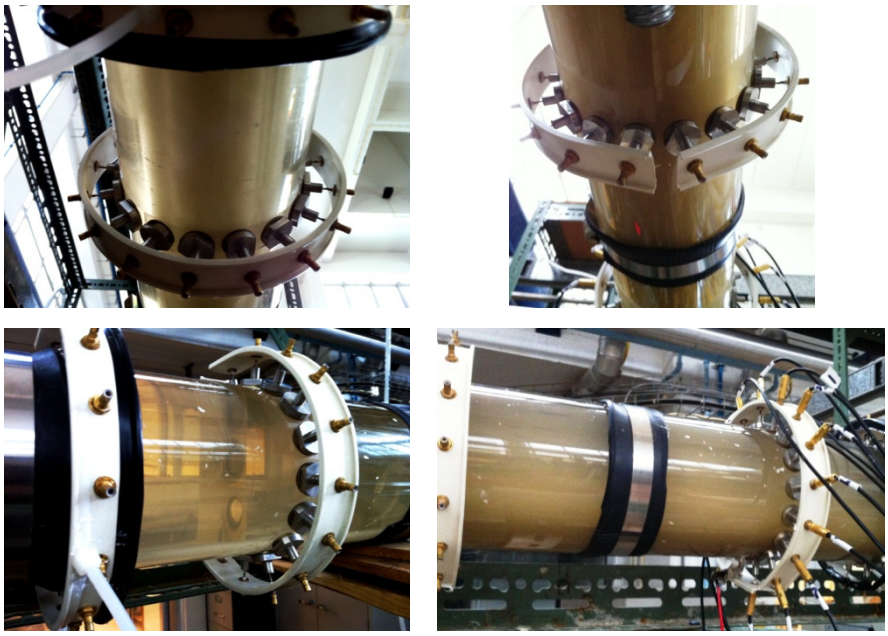

Figure 6.37 – Pictures of the observed flow regimes for the 0.1-0.2 mm sized particles with particle concentrations of 0.8 % (v/v) at 28 $m^3.h^{-1}$ (Left) and 5.0 % (v/v) at 84 $m^3.h^{-1}$ (Right).

0.4-0.6 mm Particles

For the bigger particles, with a flow rate of 28 $m^3.h^{-1}$, a dune formation was observed which become more evident with the increase in the concentration of the particles (see Figure 6.38).

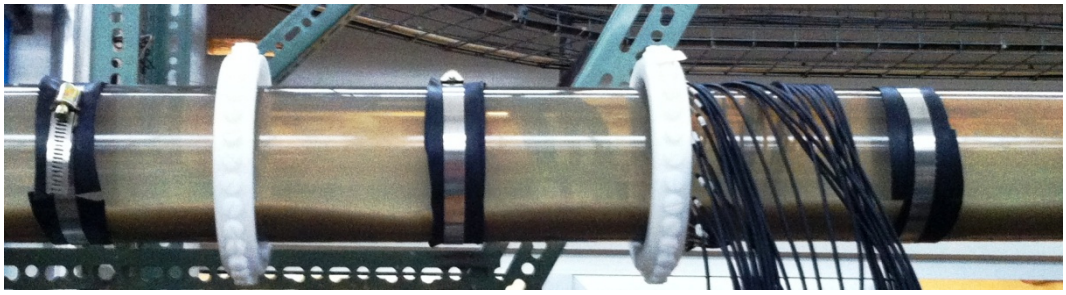

Figure 6.38 – Picture of the dune formation observed at a 28 $m^3.h^{-1}$ flow rate with the 0.4-0.6 mm particles at 5.0 % (v/v) particle concentration in the 100 mm ID pipe tests.

A moving or sliding bed was the flow regime observed for a flow rate of 56 $m^3.h^{-1}$, which displayed increasingly amounts of fluidized particles as the particle concentration was larger, seemingly related with increased particle-particle interaction. Lastly, for a flow rate of 84 $m^3.h^{-1}$, the highest achieved in this flow loop with this pumping system, the flow regime was heterogeneous (see Figure 6.39).

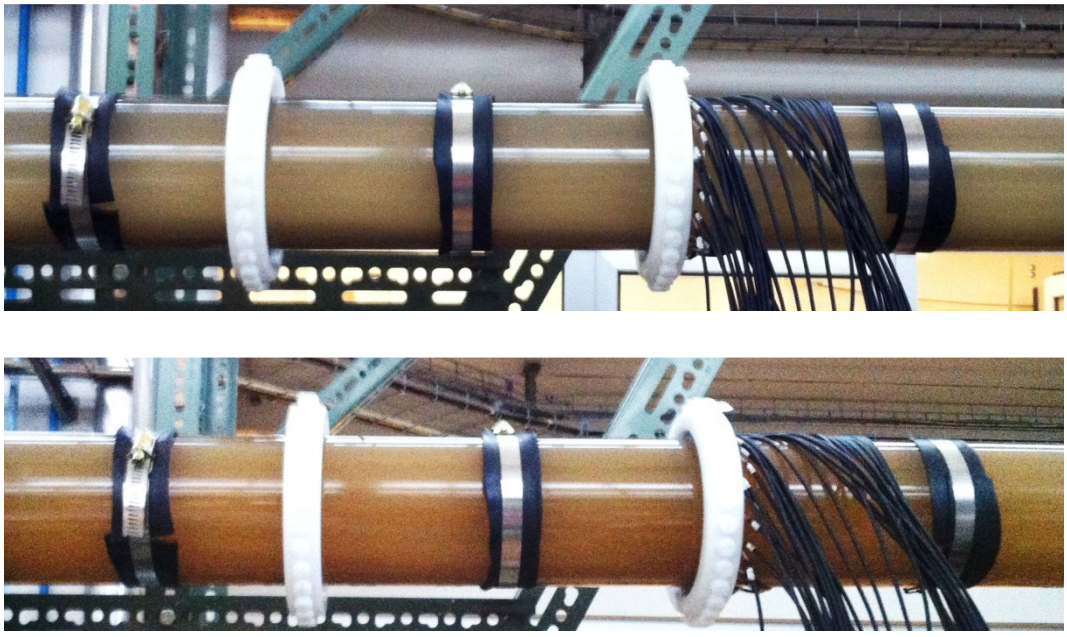

Figure 6.39 – Pictures of the moving bed regime (Top) and heterogeneous flow (Bottom) regimes with the 0.4-0.6 mm particles at 5.0 % (v/v) particle concentration in the 100 mm ID pipe tests.

Deposition Velocities

The calculated Deposition Velocity values, for both sizes of particles, were obtained using the same correlations defined in Section 6.4.2 and are summarized in Table 6.9. The values obtained with Correlation III (see Section 6.4.2) seem to provide a more accurate depiction of the flow velocity at which the 0.1-0.2 mm particles start to fluidize and Correlation I offers the best approximation to the deposition velocity for the 0.4-0.6 mm particles. This was confirmed by visual inspection as seen in Figures 6.37 to 6.39.

Table 6.9 – Deposition velocities for the DEQ tests.

			Correlation I				Correlation II	Correlation III	
	d_p (mm)	ϕ	AR	Δ	F_L	V_D ($m.s^{-1}$)	V_D ($m.s^{-1}$)	F_L	V_D ($m.s^{-1}$)
100 mm pipe	0.125	0.008	63.6	0.705	1.96	1.96	1,09	0,46	0,79
		0.02	63.6	0.705	1.96	1.96	1,06	0,51	0,88
		0.05	63.6	0.705	1.96	1.96	1,28	0,58	0,99
		0.08	63.6	0.705	1.96	1.96	1,40	0,61	1,05
		0.11	63.6	0.705	1.96	1.96	1,50	0,64	1,09
	0.50	0.008	2355.69	---	1.2	2.06	1,33	0,69	1,18
		0.02	2355.69	---	1.2	2.06	1,30	0,77	1,33
		0.05	2355.69	---	1.2	2.06	1,56	0,87	1,49
		0.08	2355.69	---	1.2	2.06	1,72	0,92	1,58
		0.11	2355.69	---	1.2	2.06	1,83	0,96	1,64

6.5.3. NUMERICAL STUDIES CONDITIONS

The numerical results continued to be produced using the Mixture Model coupled with the High Reynolds *k-ε* Turbulence Model, as depicted in Sections 4.3 and 4.7.1 considering that we are still in the low particle concentration regime. The initial conditions for the numerical studies were as described in Table 6.8.

Validity of the Mixture Model

Table 6.10 presents the calculated values for the Particle Stokes Number, Particle Reynolds Number and Terminal Velocity. The Re_p values are higher than one, and since the studied solid-liquid suspensions go from dilute to concentrated, two drag correlations were used: the Schiller-Naumann (SN) and Haider-Levenspiel (HL) drag correlations. These drag correlations were chosen based on their superior performance in previous numerical studies. The St_p values validate the application of the Mixture Model in these studies (Manninen, Taivassalo, and Kallio 1996; Hiltunen et al. 2009).

Table 6.10 – Particle data for the DEQ experiments.

Particle Data	**100 mm ID Pipe**	
$\boldsymbol{\rho_P}$ $[\boldsymbol{kg.m^{-3}}]$	2500	2500
$\boldsymbol{d_p}$ $[\boldsymbol{mm}]$	0.15*	0.5*
$\boldsymbol{U}$ $[\boldsymbol{m.s^{-1}}]$	0.99 1.98 2.97	0.99 1.98 2.97
$\boldsymbol{\phi}$ $[\boldsymbol{v/v}]$	0.008 0.02 0.05 0.08 0.11	0.008 0.02 0.05 0.08 0.11
$\boldsymbol{St_p}$	0.03 0.06 0.09	0.34 0.67 1.01
$\boldsymbol{V_T}$ $[\boldsymbol{m.s^{-1}}]$	0.018	0.200
$\boldsymbol{Re_p}$	2.65	98.2

*** Averaged values, see Appendix C for additional details**

Geometry

The flow geometry consisted of a horizontal pipe with a diameter of 100 mm as shown in Table 6.8. According to Equation 6.8 for this pipe internal diameter a minimum entrance length of 5.0 m is necessary for assuring that the numerical studies are conducted under fully developed flow conditions.

The numerical data retrieved came from an additional 0.25 m long section that was introduced after the entrance length of 5.0 m.

Finite Element Mesh

The finite element mesh images and characteristics, employed in these numerical studies, are shown in Figure 6.40 and Table 6.11, respectively. For the 100 mm ID pipe mesh the numerical studies were conducted until mesh independent results were attained.

Table 6.11 – Finite Element Mesh characteristics for the numerical studies with the DEQ data.

	100 mm ID Pipe
Number of Elements	164 348
Number of Boundary Layers	6
Wall Lift off in Viscous Units (y^+)	11.06

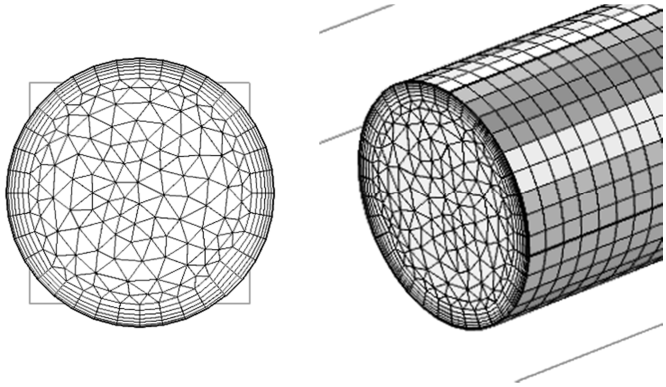

Figure 6.40 – Finite Element Swept Mesh used in the numerical studies for the DEQ data.

Boundary Conditions

For the numerical studies emulating the experimental data at DEQ's flow loop, the enforced boundary conditions are described below:

i. As for the KTH numerical studies, the initial velocities at the inlet (see Table 6.8) were imposed in the direction perpendicular to the pipe-cross section area and the turbulence intensity and length scales were equal to those depicted in Equations 6.9 and 6.10 in Section 6.4.3.

ii. The normal gradients of k and ε, at the outlet, were again fixed to zero as demonstrated by Equation 4.75, and the hydrostatic pressure profile (see Equation 6.11) was assigned.

iii. Wall Functions (see Equation 4.80) were once again employed to the numerical depiction of the near wall treatment of the flow. The roughness height imposed was equal to the one utilised in the KTH numerical studies, 1.5 μm, typical value for surfaces as drawn tubing, plastic pipes, etc. (COMSOL Multiphysics 2013).

6.5.4. EXPERIMENTAL AND NUMERICAL RESULTS

Water Calibration Tests

The calibration of pressure transducers was checked through a series of single-phase flows using water under the conditions depicted in Table 6.8. The Darcy-Weisbach Equation (see Equation 6.12) with the Moody Diagram for the friction factor (see Table 6.12 and Figure 6.41) (Peker and Helvaci 2011; Liu 2003), were again compared against experimental results and numerical results using the High Reynolds k-ε turbulence model (Wilcox 2006) in a similar way as described in Section 6.4.4, where the pipe equivalent roughness, ϵ, was also assumed to be 0.0015 mm (F. M. White 1998).

Table 6.12 – Comparison of Experimental, Numerical and Darcy-Weisbach pressure gradients profiles for water flow in the 100 mm ID pipes.

	Pressure Gradient (Pa.m^{-1}) for 100 mm ID pipe		
$Q\ [m^3.h^{-1}]$	**Experimental**	**Darcy-Weisbach**	**Numerical**
28	90	89 **(-0.98%)*****	80 **(-10.6%)**
56	308	309 **(0.52%)**	276 **(-10.2%)**
84	640	647 **(1.13%)**	576 **(-10.0%)**

*****deviations from experimental are in bold.**

The validation of an accurate calibration of the pressure transducers comes

from Table 6.12 and Figure 6.41. The highest deviation, $-10.6\,\%$, occurs between the experimental and numerical results for the 100 mm ID pipe with a flow rate of $28\,m^3.h^{-1}$. Considering that this deviation represents a difference of $9\,Pa.m^{-1}$ and that the highest absolute difference occurs between the experimental and numerical results for the highest flow rate, $84\,m^3.h^{-1}$, then it is acceptable to assume that the experimental pressure gradient was matched by both numerical and Darcy-Weisbach calculations.

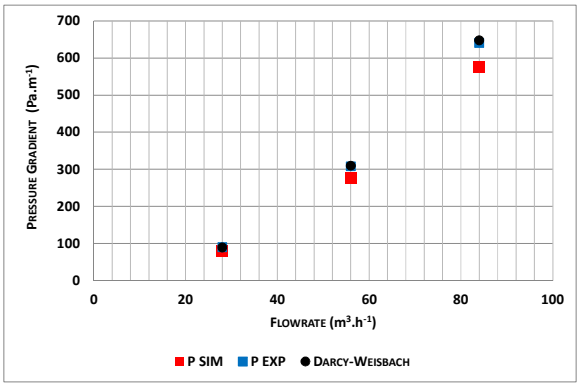

Figure 6.41 – Experimental, Numerical and Darcy-Weisbach pressure gradients profiles for water flow in a 100 mm ID pipe.

0.1-0.2 mm spherical particles in 100mm ID pipe

Similarly to the previous experiments performed at KTH Mekanics for dilute solid-liquid suspensions, small spherical particles with size between 0.1-0.2 mm were introduced to the flow loop with concentrations ranging from 0.08 to 11.0 % (v/v). Data acquisition occurred at flow rates of 28, 56 and $84\,m^3.h^{-1}$, as shown in Table 6.8, using, simultaneously, an Electrical Impedance Tomography (EIT) apparatus (see Section 3.2) coupled with a Perspex section embed with electrode rings to attain electrical distribution profiles in the pipe cross-section. A Sampling Probe (SP) (see Figure 3.3) to acquire vertical distribution of particles in the pipe cross-section was also inserted. The EIT's 2D reconstructed images of the normalized electrical conductivity measurements (see Equation 6.15) are displayed in Figure 6.42 using as reference measurement a NaCl solution with an electrical

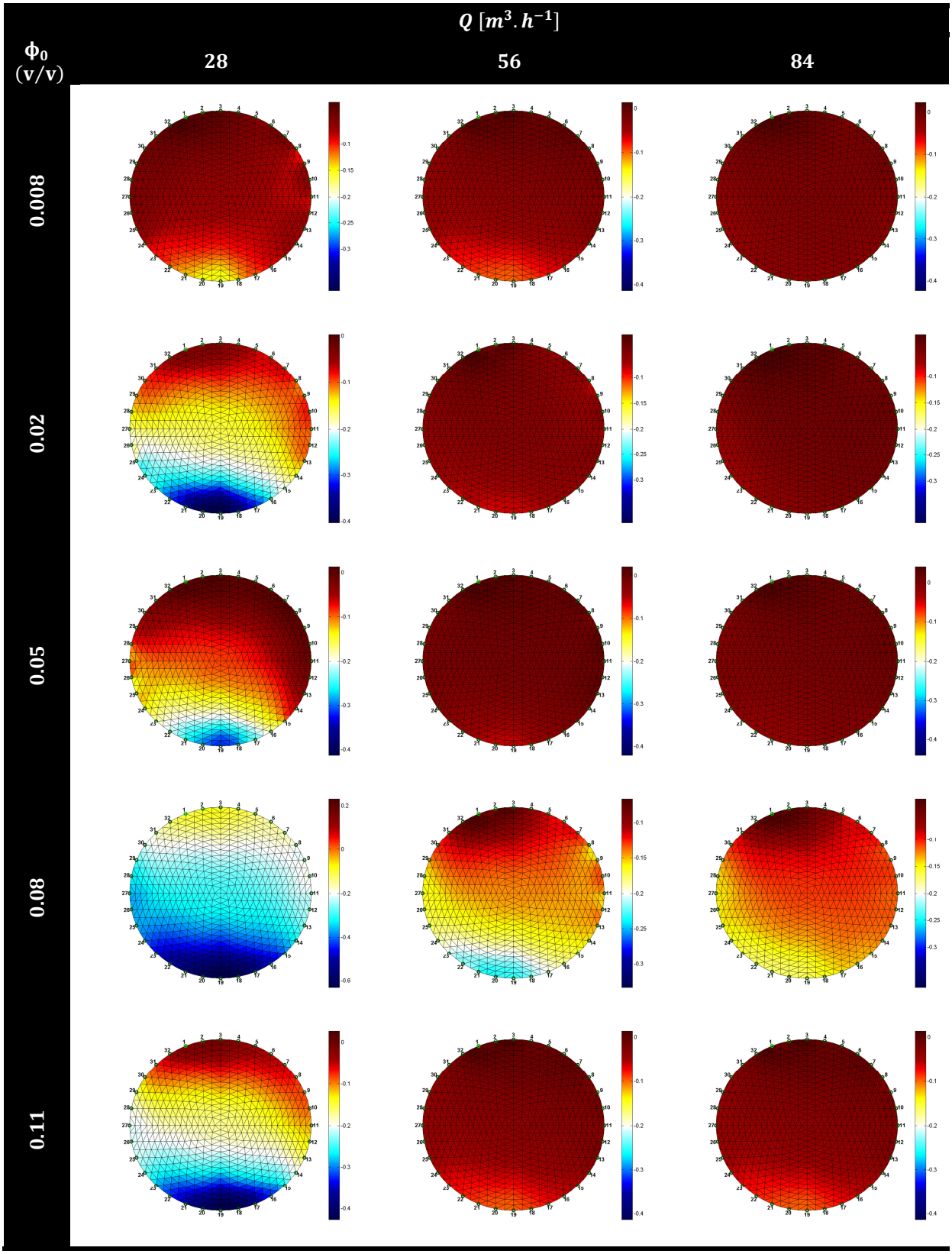

Figure 6.42 – Reconstructed 2D images of the pipe cross-section using EIT normalized conductivity measurements for solid-liquid suspensions of 0.1-0.2 mm particles in a 100 mm ID pipe.

conductivity of 696 $\mu S.cm^{-1}$. Overall, the effect of particle concentration ranging between 0.8 to 11 % (v/v) on the conductivity gradient is apparent, particularly for the lowest flow rate 28 $m^3.h^{-1}$. The effect of the increase in flow rate on the turbulent dispersion of particles is also noticeable by comparison of the columns for the three studied flow rates.

As for the case of the EIT results obtained at KTH Mekanics, the bottom area with a more intense blue colour denotes a higher concentration of particles and a more intense red colour represents the area where there is little change in the electrical conductivity, thus, meaning little or no particles being present.

The described behaviour in the previous paragraph is not followed in all the reconstructed images, however. This is more noticeable and unexpected at the lowest flow rate in the transitions between the particle concentrations of 2.0 to 5.0 % (v/v) and 8.0 to 11.0 % (v/v) where a more intense blue area was expected for the 5.0 and 11.0 % (v/v) in the bottom of the pipe cross section. In the studies on solid-liquid suspensions flows described in this thesis there was a concern to maintain the temperature constant, which became a very difficult task as the particle concentration and flow rate increased. So a rise in temperature was recorded, and observable in Table 6.13, which led to an increase in the suspension's electrical conductivity that was responsible for the unforeseen diminished blue areas, both in size and intensity, in the EIT's 2D normalized electrical conductivity reconstructed images.

This rise in temperature, during testing, in spite of a heat exchanger present in the DEQ's flow loop, was caused not only by an increased particle-wall and particle-particle friction, but also and mainly due to energy transfer from the pumping system to the continuous phase.

Table 6.13 – Operating experimental temperatures and final electrical conductivity of the suspension measured during data acquisition for the 0.1-0.2 mm particles in the 100 mm ID pipes.

	T (ºC) for 100 mm ID pipe			σ_m $(\mu S.cm)$ for 100 mm ID pipe
ϕ_0 (v/v)	28 $m^3.h^{-1}$	56 $m^3.h^{-1}$	84 $m^3.h^{-1}$	
0.000	26.0	26.2	26.6	696
0.008	22.6	23.8	24.9	679
0.02	26.6	26.4	26.1	688
0.05	27.6	27.2	26.6	714
0.08	27.4	26.8	26.2	666
0.11	30.1	29.2	28.5	734

After testing with the particle concentration of 5.0 % (v/v) was done, and prior to initiating the 8.0 % (v/v) tests, the water level had to be corrected, due to losses associated with samples removal through the sampling probe (SP), and small amounts of NaCl were introduced in the flowing solution to approach the measured electrical conductivity of the reference measurements with water. As pointed out in the literature (M. Wang, Jones, and Williams 2003; Giguère et al. 2008) any variations of temperature and/or flowing electrical conductivity resulting from particle introduction or flow loop operation will influence the image reconstruction based on the water reference values. Optimally, these variations should be introduced in the software to adequately compensate the reference profile in order to match the flowing conditions of the suspension being studied. Since the EIDORS software (Nick Polydorides and Lionheart 2002) was used, it was not possible to implement the necessary corrections to the MATLAB® subroutines to compensate the reference profiles for the 0.1-0.2 mm particles studies.

In spite of these deviations in the 2D image reconstruction, the EIT vertical 1D concentration profiles attained, as demonstrated by Figure 6.29 and Equations 6.16 to 6.19, seem to match well against the Sampling Probe (SP) data and the Mixture Model vertical solids distribution profiles which can be observed in Figures 6.43 and 6.44. Considering the vertical solids

concentration profiles for the highest flow rate, 84 $m^3.h^{-1}$, the EIT calculated solids concentration, $\phi(z)$, seem to agree for the highest solids concentrations although there are some overshoots, particularly at the pipe bottom. The increase in the solution's electrical conductivity, due to the rise in temperature inside the flow loop, for the 5.0 % (v/v) solids volumetric fraction explains the upper part of the profile, where the solids concentrations based on Equation 6.19 is practically null, which is incorrect, once an heterogeneous flow regime was observed. The small amount of particles, for the 0.8 % (v/v) solids volumetric fraction, at the highest flow rate, will have an almost negligible effect on the electrical potential differences measurements acquired with the EIT, as demonstrated by the 2D reconstructed image in Figure 6.42. So, overall, for the highest flow rate, 84 $m^3.h^{-1}$ and with these smaller particles, the EIT calculated solids concentration, $\phi(z)$, seems to provide a better agreement with the Sampling Probe data for the higher particle concentrations due to the increased influence over the electrical conductivity measurements.

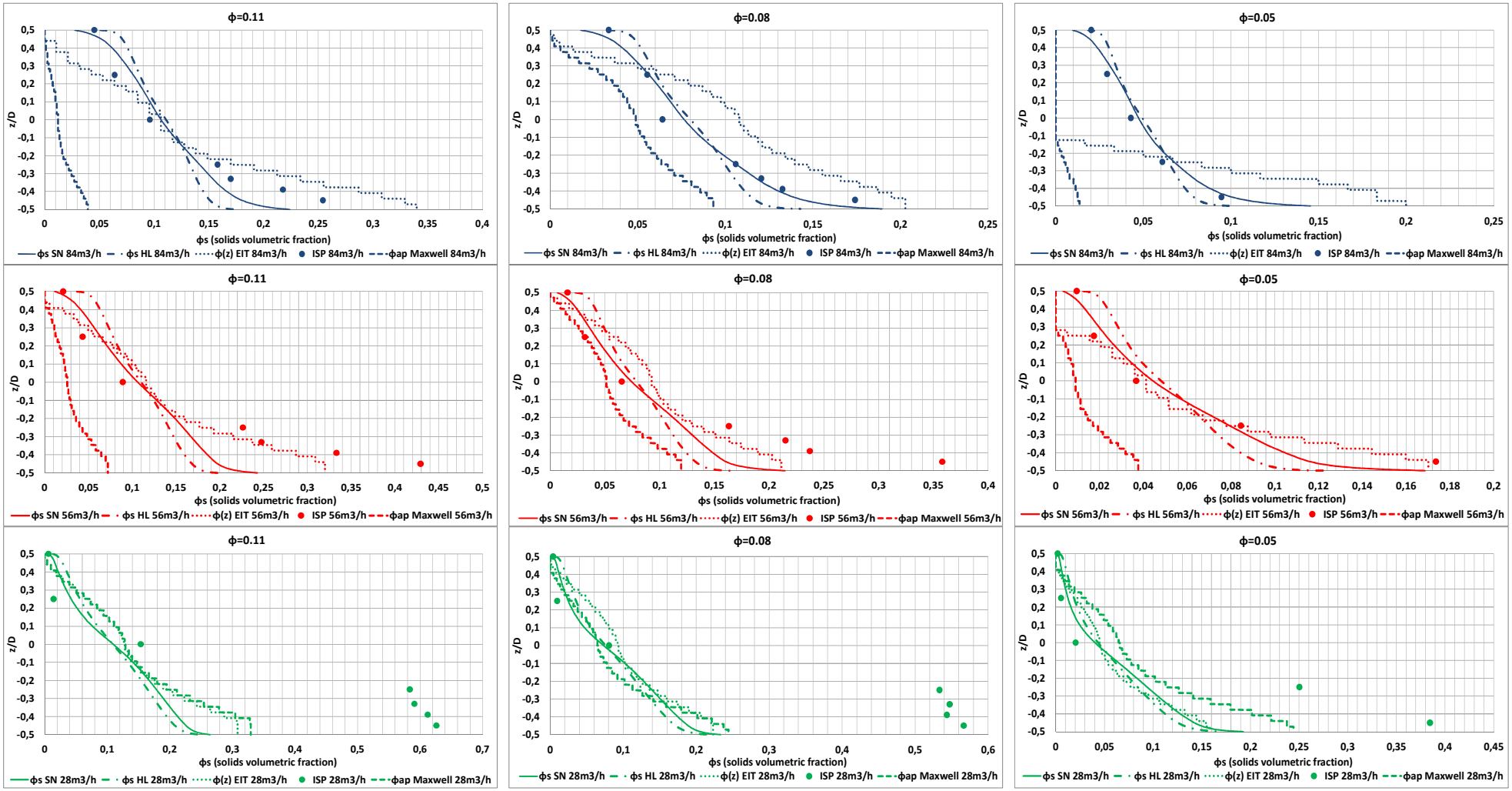

Figure 6.43 – Comparison between the experimental 1D vertical particle concentrations profiles from the (SP) with the calculated profiles using the EIT, Maxwell Equation, and the Mixture Model (using the Schiller-Naumann (SN) and Haider-Levenspiel (HL) drag correlations) in a 100 mm ID pipe for 0.1-0.2 mm particle concentrations of 11.0 (Left Column), 8.0 (Middle Column) and 5.0 % (v/v) (Right Column) and for 28 (Bottom Line), 56 (Middle Line) and 84 $m^3.h^{-1}$ (Top Line) flow rates.

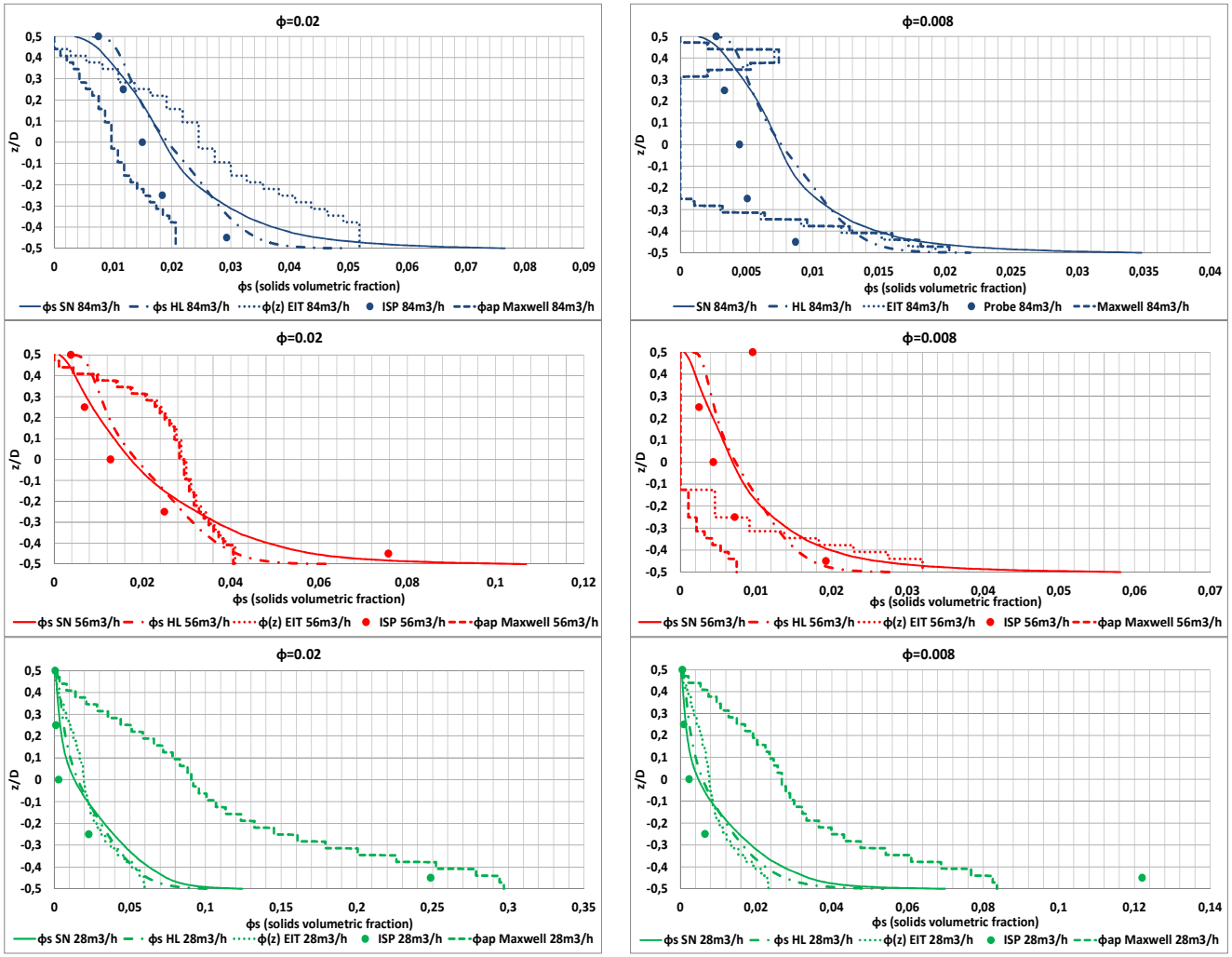

Figure 6.44 – Comparison between the experimental 1D vertical particle concentrations profiles from the (SP) with the calculated profiles using the EIT, Maxwell Equation, and the Mixture Model (using the Schiller-Naumann (SN) and Haider-Levenspiel (HL) drag correlations) in a 100 mm ID pipe for 0.1-0.2 mm particle concentrations of 2.0 (Left Column) and 0.8 % (v/v) (Right Column) and for 28 (Bottom Line), 56 (Middle Line) and 84 m3/h (Top Line) flow rates.

The numerical profiles attained using the Mixture Model and the Schiller-Naumann drag correlation, ϕ_sSN, seem to provide the most accurate representation of the data obtained using the Sampling Probe (SP), while the Haider-Levenspiel drag correlation data, ϕ_sHL, does not portrait the experimental data as accurately for the higher particle concentrations. The calculated vertical concentration profiles using the modified Maxwell Equation (see Equation 6.17) seem to loose accuracy as the solids concentration in the flow loop increases, for the highest flow rate. This can be attributed to the fact that the Maxwell Equation was initially developed for homogeneous flows and with increasing particle concentration of settling particles the vertical concentration gradient will be significant for this flow rate, as shown by the Sampling Probe data.

For the intermediate flow rate, $56\ m^3.h^{-1}$ and with the highest particle concentrations, namely 11.0 and 8.0 % (v/v), became cumbersome to acquire the samples with the SP, since the probe became obstructed by the amount of particles due to the low flow velocity near the pipe bottom, so there is some uncertainty associated with the last measured samples. Regardless, apart from the measurements near the pipe bottom for the 11.0 and 8.0 % (v/v) particle concentrations, the EIT calculated solids concentration, $\phi(z)$, follow the SP probe data with little deviation, falling short only at the pipe bottom which can be attributed to the aforementioned blockage issues with the sampling probe. The SN drag correlation displays a better accuracy for the highest particle concentration flows, while the HL drag correlation has a more accurate representation of the solids distribution profiles for the lower concentrations, although these differences are not substantial. The Maxwell Equation shows a better agreement with the SP data for this flow rate, when compared with the highest flow rate; however, the trend observed for the highest flow rate data is still present, i.e., it loses accuracy as the solids concentration increases in the flow loop.

At the lowest studied flow rate, $28\ m^3.h^{-1}$, the blockage issue with the SP became even more noticeable. The validation of the sliding or moving bed can

be observed in the vertical concentration profiles in Figures 6.43 and 6.44, although the concentration values attained near the pipe bottom, using SP, seem quite high for the studied concentrations. Nevertheless, the EIT calculated solids concentration, $\phi(z)$, display agreement with most of the sampling points, for all particle concentrations, being the exception the region near the pipe bottom. The numerical concentration profiles provided by the Mixture Model display a similar behaviour as the EIT solids concentrations profiles, i.e., they match up with the SP data to most points, but not at the pipe bottom. Overall, the drag correlations show similar behaviour. Still, the HL drag correlation shows a slight better representation of the SP data for the lowest particle concentrations. Contrarily to the behaviour displayed with the higher flow rates, the Maxwell Equation demonstrates a better agreement with the SP data as the particle concentration in the flow loop increases. This can be explained by the intensification in the fluidization of particles, resulting from increased particle-particle interactions, and thus, resulting in small volumetric fraction of particles in the upper of the pipe section; where the Maxwell Equation has shown, for the higher flow rates, to provide better agreements with the Sampling Probe data.

Apart from the vertical solids distribution data, the experimental pressure gradients were also acquired for all particle concentrations and flow rates studied. Its comparison with numerical data resulting from simulations with the Mixture Model, using both the SN and HL drag correlations, are presented in Figure 6.45 together with the results obtained with the Durand-Condolios correlation (see Equations 6.13 and 6.14). Overall, and as observed for the pressure gradient results (see Section 6.4) attained in the KTH Mekanics flow loop, the Durand-Condolios correlation displays a persistent overshoot, when compared to the experimental pressure gradient data. As the particle concentration increases so does the overshoot, particularly for the lowest studied flow rate. The numerical pressure gradients attained with the Mixture Model indicate an overall agreement with the experimental pressure

gradient data, with the exceptions being the highest particle concentration and lowest flow rates. This is due to the Mixture Model inability to accurately depict the behaviour of concentrated suspensions at velocities lower than the Deposition Velocity (Ling et al. 2003), i.e., when a sliding or moving bed is present. This was also observed for the KTH Mekanics results depicted in Section 6.4.4. Considering Table 6.9, it can be seen that the Deposition Velocity for the 0.8 and 2.0 % (v/v) solids volumetric fraction is below the operating flow velocity, considering a flow rate of 28 $m^3.h^{-1}$, and, thus, the Mixture Model performs well under these conditions.

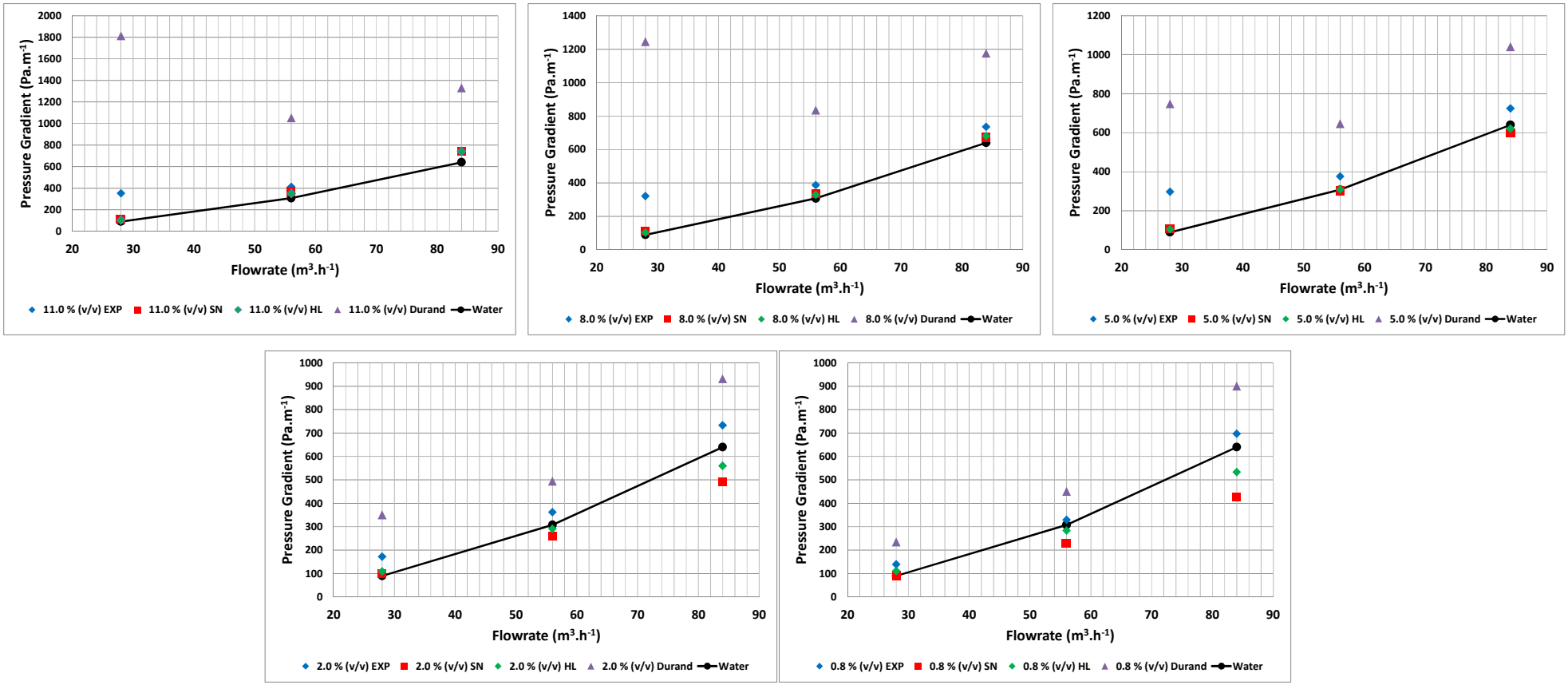

Figure 6.45 – Experimental, Numerical and Durand-Condolios pressure gradients profiles for solid-liquid suspensions of 0.1-0.2 mm particles for 11.0 to 0.8 % (v/v) solids volumetric concentration with 28, 56 and 84 $m^3.h^{-1}$flow rates in a 100 mm ID pipe.

For a particle concentration higher than 2.0 % (v/v) the Deposition Velocity is now equal to or higher than the flow velocity for the operating flow rate of 28 $m^3.h^{-1}$, and so the observed Mixture Model results undershoot the pressure gradient. Regarding the Drag Correlations, the differences between the results using the Schiller-Naumann and the Haider-Levenspiel are only observable at the highest flow rates, and for 0.8 and 2.0 % (v/v) concentrations, where the pressure gradient results, with the HL drag correlation, are closer to the experimental values.

0.4-0.6 mm spherical particles in 100 mm ID pipe

The same experimental approach was pursued for the bigger particles, 0.4-0.6 mm in size, again employing the particle concentrations and flow rates depicted in Tables 6.8 and 6.10. With these tests, and considering the temperature and electrical conductivity issues observed with the smaller particles, additional attention was dedicated in maintaining both, as constant as possible as can be seen in Table 6.14.

Table 6.14 – Operating experimental temperatures and final electrical conductivity of the suspension measured during data acquisition for the 0.4-0.6 mm particles in the 100 mm ID pipes.

	T (ºC) for 100 mm ID pipe			σ_m ($\mu S.cm$) for 100 mm ID pipe
ϕ_0 (v/v)	28 $m^3.h^{-1}$	56 $m^3.h^{-1}$	84 $m^3.h^{-1}$	
0.000	29.2	29.3	30.0	621
0.008	29.5	29.8	30.1	625
0.02	29.5	29.4	29.1	633
0.05	29.2	29.5	29.7	640
0.08	27.4	27.2	27.9	619
0.11	28.5	28.4	28.1	626

Comparatively to the previous results with the 0.1-0.2 mm particles, the EIT's 2D reconstructed images portray more adequately the expected effect of particle concentration on the conductivity gradient as seen in Figure 6.46.

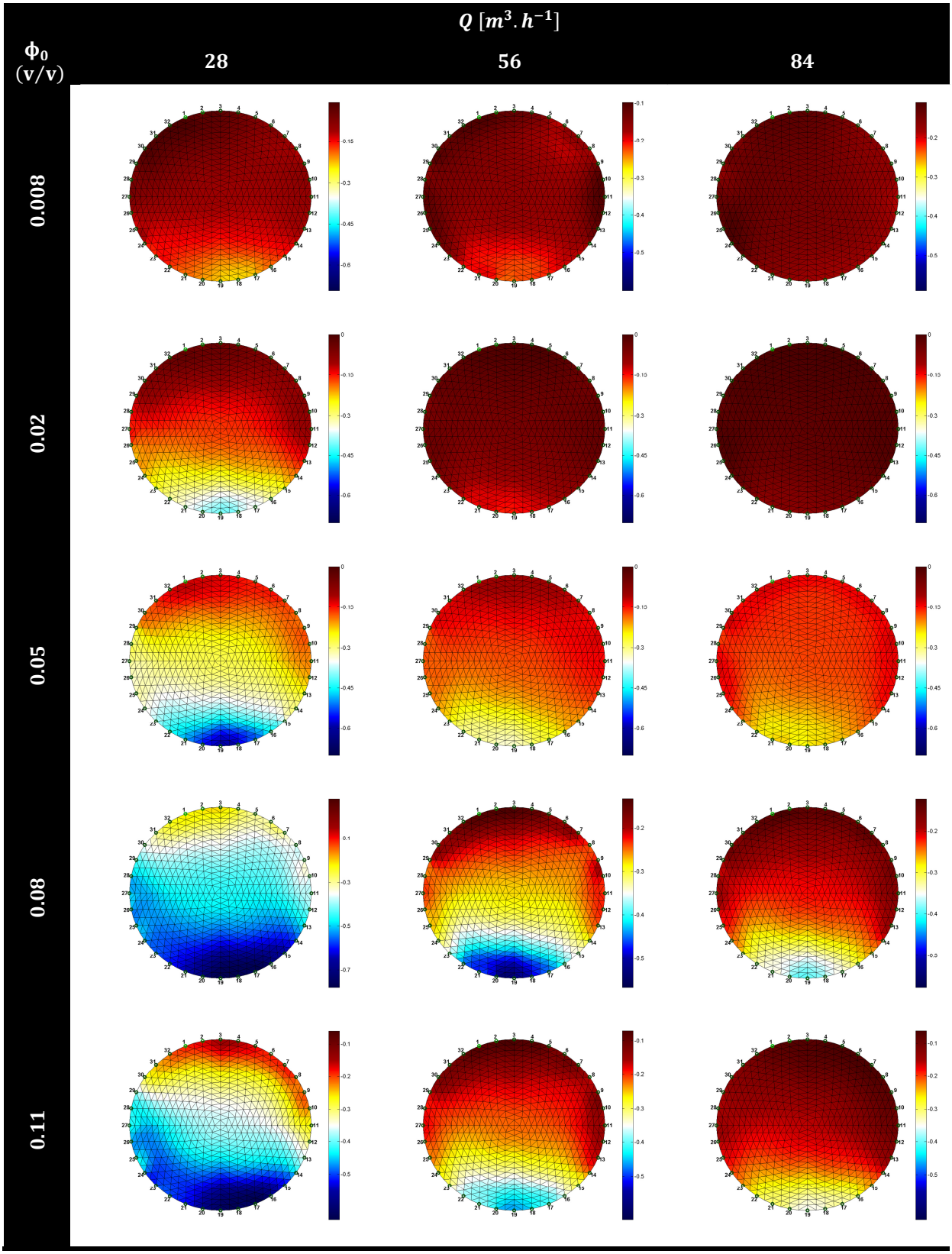

Figure 6.46 – Reconstructed 2D images of the pipe cross-section using EIT normalized conductivity measurements for solid-liquid suspensions of 0.4-0.6 mm particles in a 100 mm ID pipe.

The only exception occurred for the transition between the particle concentrations of 5.0 to 8.0 % (v/v) where an overestimated blue area occurs for the bottom region of the pipe section for the 8.0 % (v/v) concentration and for all flow rates. A look at Table 6.14 shows the difference between the reference measurements and the 8.0 % (v/v) operating temperatures. The reason why the temperatures are lower was a consequence of both 8.0 and 11.0 % (v/v) measurements having been done consecutively on the same day. The pumping system could not be turned off as particles were being introduced to the flow loop to achieve 11.0 % (v/v), since turning off the pump for this concentration for the 0.4-0.6 mm particles compromised the pumping capability, when switched on, and would require disassembly of the pumping system. So, the measurements had to start at a lower temperature with the 8.0 % (v/v) solids concentration, since the temperature rise with the 11.0 % (v/v) would be considerable, as it was observed for the same particle concentration for the 0.1-0.2 mm particles (see Table 6.13). The variation of electrical conductivity observed for the 8.0 % (v/v) further points to the influence of operating temperature in the electrical conductivity, as seen previously for the 0.1-0.2 mm particles. This also stresses the necessity and importance of having a database of reference measurements, for a range of temperatures and electrical conductivities. Employing an alternative injection protocol to the Adjacent Pattern such as an Opposite Pattern or a combination of both, could also increase the accuracy of the electrical conductivity, and consequently the solids concentration profiles.

The effect of particle concentration on the conductivity gradient is even more pronounced since these particles are bigger and the result is a higher moving or sliding bed. Based on the deposition velocities, as described in Section 6.5.2 and confirmed by the observed flow regimes, the particles will be mostly gathered at the pipe bottom with increased particle fluidization proportional to the flow rate. This is corroborated in Figure 6.46 where the intensity and size of the blue areas decreased as the particle concentrations and flow rate are smaller, with the aforementioned exception of the 8.0 %

(v/v) particle concentration.

The SP experimental data, for the 2.0 and 0.8 % (v/v) solids concentration and lowest flow rate, appears somehow high at the pipe bottom. This is most likely a result of the already mentioned blockage issues of the probe combined with the lower flow velocity near the pipe bottom that introduced an error in the sampling data.

The EIT vertical 1D concentration profiles can be observed in Figures 6.47 and 6.48. The numerical profiles using the Mixture Model and the HL drag correlation, ϕ_sHL, overall seem to better describe the SP data for the highest flow rate, 84 $m^3.h^{-1}$ and for all solids volumetric fractions. For the 56 $m^3.h^{-1}$ flow rate, for all solids volumetric fractions, there are no significant differences between the studied drag correlations and all appear to be congruent with the SP experimental data. And for the last studied flow rate, 28 $m^3.h^{-1}$, a reversal is perceived between the drag correlations, with the SN drag correlation providing a more accurate portrayal of the SP data. The HL drag correlation was developed to account for particle-particle interaction in more concentrated flows, so it was expected that it would behave better for the highest flow rate since the amount of fluidized particles is higher. The SN drag correlation is an extension on the single sphere drag Stokes Law (Yilmaz and Gundogdu 2009) and it does not depict account particle-particle interaction accurately, thus, making it more adequate for flows where particle interaction is small, i.e., in the upper part of the pipe with the lowest flow rate, 28 $m^3.h^{-1}$ where particle fluidization is small.

The EIT's calculated solids concentration profiles, $\phi(z)$, agreement with the SP data appears to be better for the highest flow rates for all particle concentrations, when compared with the ones obtained using Maxwell Equation (see Equation 6.17). This tendency seems to hold for the remaining flow rates and particle concentrations being the exception the region near the pipe bottom for the lower particle concentrations. At the pipe bottom the concentration profiles calculated using Maxwell's Equation are closer to the

SP data, for the lower particle concentrations, but for the remaining pipe section the EIT's calculated solids concentration, $\phi(z)$, approaches considerably better the SP data, particularly in the region closer to the top of the pipe. Due to the small amount of larger particles present in the flow, for the lower particle concentrations, the EIT measurements will resemble almost as a homogeneous particle distribution (see Figure 6.46), thus, resulting in bigger area under the electrical conductivity curve (see Equation 6.19) which will undershoot the EIT's calculated solids concentration, $\phi(z)$.

Analysis of the pressure data in Figure 6.49 shows that the numerical pressure gradient attained with the Mixture Model undershoots the experimental pressure gradient for the lowest and intermediate flow rates, 28 and 56 $m^3.h^{-1}$, respectively. This deviation becomes larger increases as solids concentration increases due to the rise in dune size or moving bed observed. As already stated, the Mixture Model fails to properly account the pressure gradient in the presence of a stationary or moving bed (Ling et al. 2003), due to the model's inability to correct the available flow area in the pipe, which is reduced for flow rates below the deposition velocity, causing an increase in the friction loss. Nevertheless, for the higher flow rates and higher particle concentrations, which are typically the favoured operating conditions in industrial environments, the Mixture Model with the HL drag correlation provides a more accurate representation of the pressure gradient since it accounts for particle-particle interaction as explained above. The SN drag correlations numerical results show a better agreement with the experimental pressure gradient at low solids volumetric fraction and lowest flow rate where particle fluidization is lower.

The Durand-Condolios correlation displays a similar behaviour as the one found for the 0.1-0.2 mm particles, i.e., it fails to properly depict the pressure gradients, moreover, its results deviate considerably as the solids concentration increases.

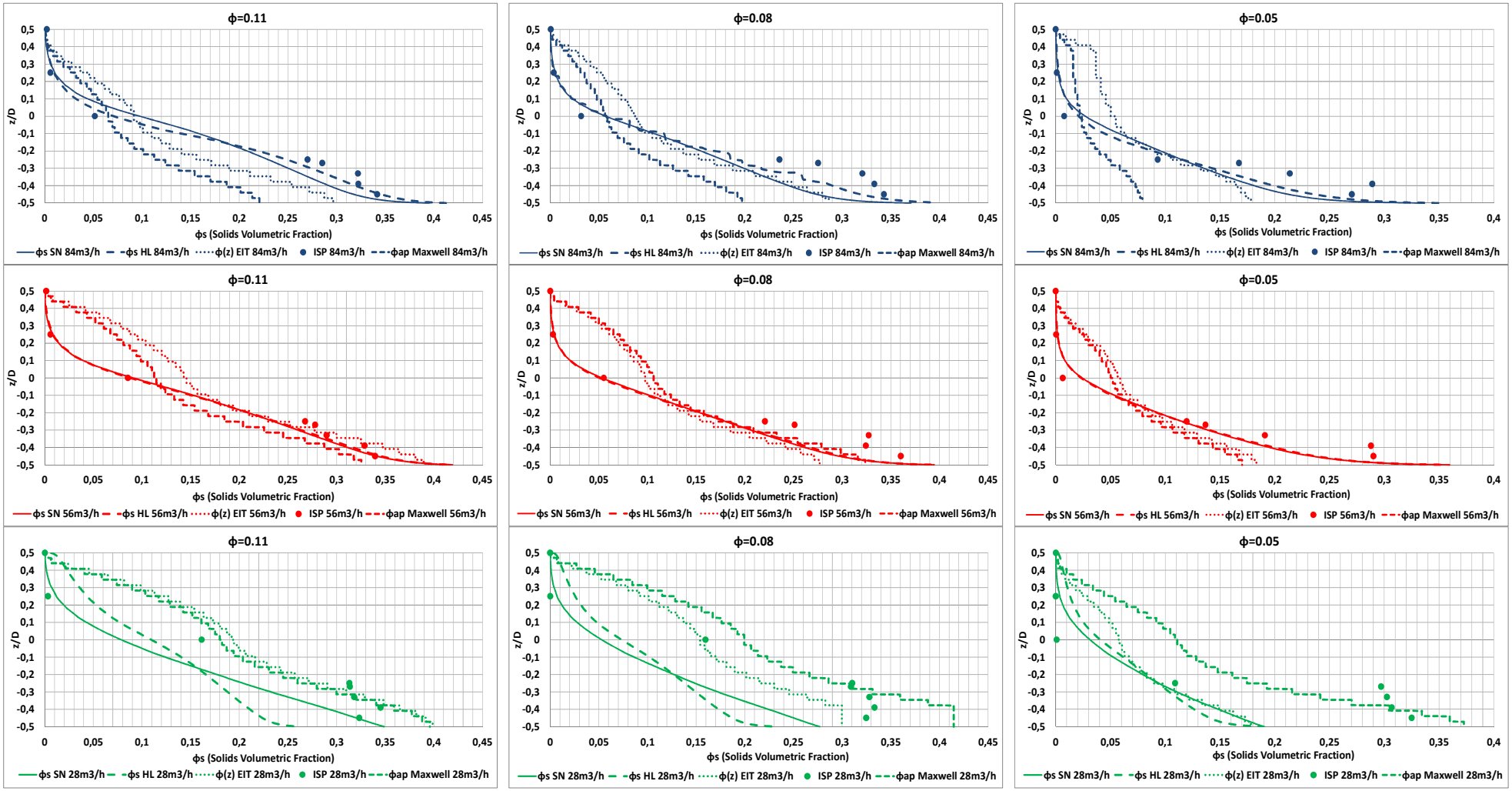

Figure 6.47 – Comparison between the experimental 1D vertical particle concentrations profiles from the (SP) with the calculated profiles using the EIT, Maxwell Equation, and the Mixture Model (using the Schiller-Naumann (SN) and Haider-Levenspiel (HL) drag correlations) in a 100 mm ID pipe for 0.4-06 mm particle concentrations of 11.0 (Left Column), 8.0 (Middle Column) and 5.0 % (v/v) (Right Column) and for 28 (Bottom Line), 56 (Middle Line) and 84 $m^3.h^{-1}$ (Top Line) flow rates.

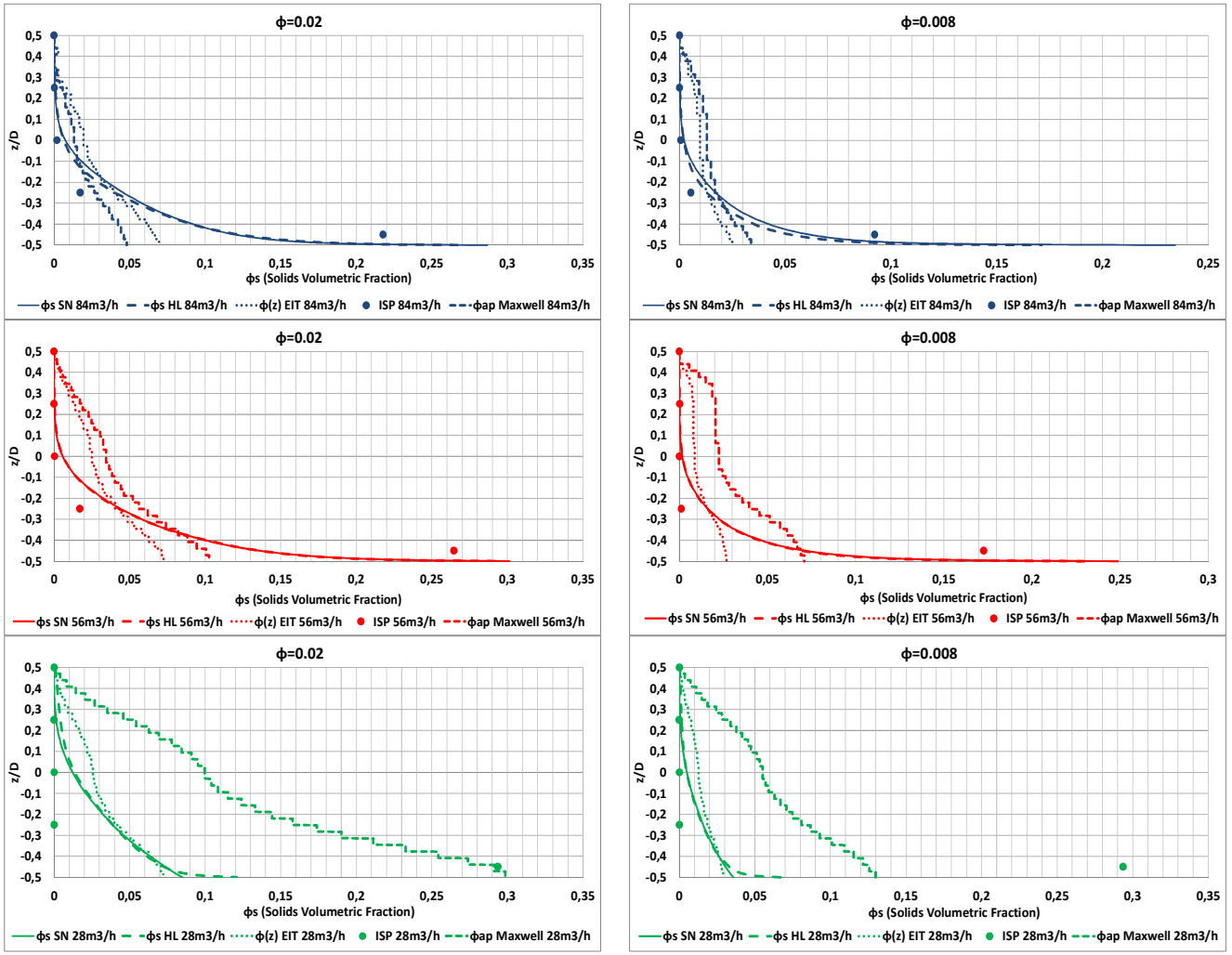

Figure 6.48 – Comparison between the experimental 1D vertical particle concentrations profiles from the (SP) with the calculated profiles using the EIT, Maxwell Equation, and the Mixture Model (using the Schiller-Naumann (SN) and Haider-Levenspiel (HL) drag correlations) in a 100 mm ID pipe for 0.4-0.6 mm particle concentrations of 2.0 (Left Column) and 0.8 % (v/v) (Right Column) and for 28 (Bottom Line), 56 (Middle Line) and 84 $m^3.h^{-1}$ (Top Line) flow rates.

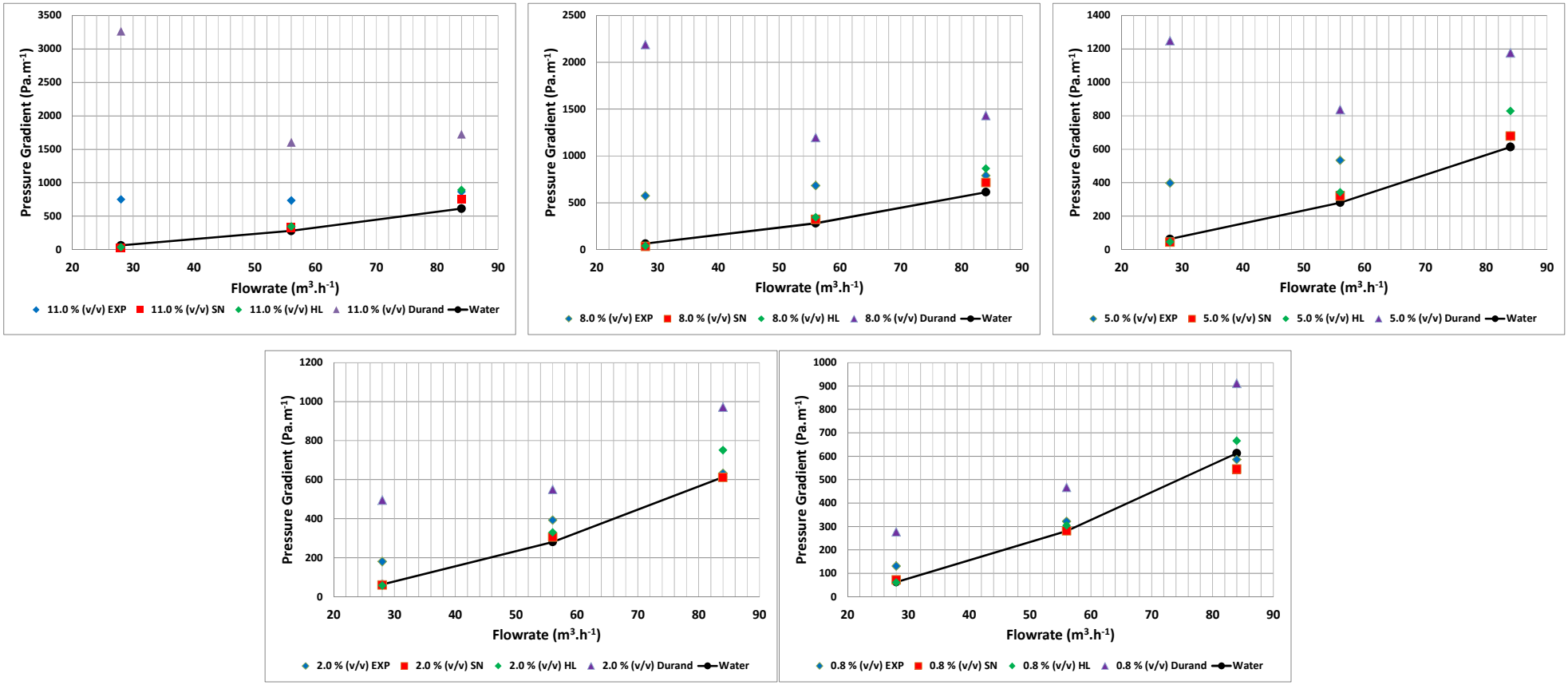

Figure 6.49 – Experimental, Numerical and Durand-Condolios pressure gradients profiles for solid-liquid suspensions of 0.4-0.6 mm particles for 11.0 to 0.8 % (v/v) solids volumetric concentration with 28, 56 and 84 $m^3.h^{-1}$flow rates in a 100 mm ID pipe.

6.5.5. TURBULENCE MODULATION ANALYSIS

The effect of particles on the modulation of turbulence was analysed similarly to the way the KTH Mekanics results for the dilute solid-liquid suspensions were tested, using Equation 4.104. The effect, from the two sizes of particles tested at DEQ, are depicted in Table 6.15 and analysed below.

Table 6.15 – Stokes Number (St) based Particle Moment Number (Pa_{St}) values for the DEQ tests.

		100 mm ID pipe	
	$Q\ [m^3.h^{-1}]$	0.1-0.2 mm	0.4-0.6 mm
Pa_{St}	**28**	9.44	104.9
	56	26.71	296.8
	84	49.07	597.3

The Pa_{St} values for both particle sizes appear to place them in the area of turbulence augmentation in water. Using the pressure gradient as the evaluation variable for the turbulence modulation it appears that the values are congruent with Tanaka's data in Figure 4.7 (Tanaka and Eaton 2008). In Figure 6.50, the influence of the particle size is analysed on the numerical turbulence kinetic, k, and turbulence dissipation rate, ε. The turbulence variables with the water flows were obtained using a High Reynolds k-ε Turbulence model and the remaining profiles with the Mixture Model coupled High Reynolds k-ε Turbulence model and a SN drag correlation. With all these profiles the highest flow velocity tested was adopted, 2.97 m. s^{-1} (see Table 6.8), and with the exception for the water profiles, all the other profiles are for particle concentration of 5.0 and 11.0 % (v/v) for both particle sizes studied.

For the smaller particles, 0.1-0.2 mm, the turbulence variables should possess similar or higher values than the water flows based on the pressure gradients in Figure 6.45 since the *St* Numbers are lower than one (see Table 6.10); however, the profiles attained with the Mixture Model depicted lower values than expected which can be attributed to the drag correlation employed, also

observable in Figure 6.45, where the numerical pressure gradient shows a consistent slight undershoot. The numerical pressure gradient values with HL drag correlation display closer values to the experimental data, thus indicating the importance of accurate drag modelling for turbulent flows of settling particles. Nonetheless, overlooking the numerical values momentarily and focusing on the shape of the *k* profiles, for the smaller particles, it is noticeable the higher area of turbulence near the bottom of the pipe which is consistent with a heterogeneous flow regime. Considering just the experimental data for both water and smaller particle flows, from Figure 6.45, and comparing it to Table 6.15, it would seem to be an amplification of the turbulence production introduced by the particles which is consistent with the Pa_{St} values obtained with Tanaka's equations.

The bigger particles influence in the turbulence variables is more perceptible (see Figure 6.50), as expect from the St Numbers depicted in Table 6.10, which are one order of magnitude higher than for the smaller particles. This is also the case for the Pa_{St} Number in Table 6.15. The heterogeneous flow regimes are also quite clear from Figure 6.50 where the main contribution to the turbulence production comes from the bottom of the pipe due to particle-particle and particle-wall stresses, rather than the pipe wall as was the case for the smaller particles. Comparing the turbulent kinetic energy profiles, between the 5.0 and 11.0 % (v/v) particle concentrations, there is an apparent decrease of the turbulent production near the pipe bottom for the 11.0 % (v/v) particle concentration. This is due to the increase in fluidized particles ensuing from the increase particle-particle interaction as a result of the increase in the number of particles, as can be perceived by the rise in the minimum value for the k values in Figure 6.50. The turbulence profiles in Figure 6.50, in spite of being higher than for the water flows, are lower than expected if the pressure gradients in Figure 6.49 are taken into consideration. This, similarly as for the smaller particles, is due to the drag correlations effect on the numerical turbulence production. Also, similarly as for the smaller particles the Pa_{St} values obtained with Tanaka's equations in Table

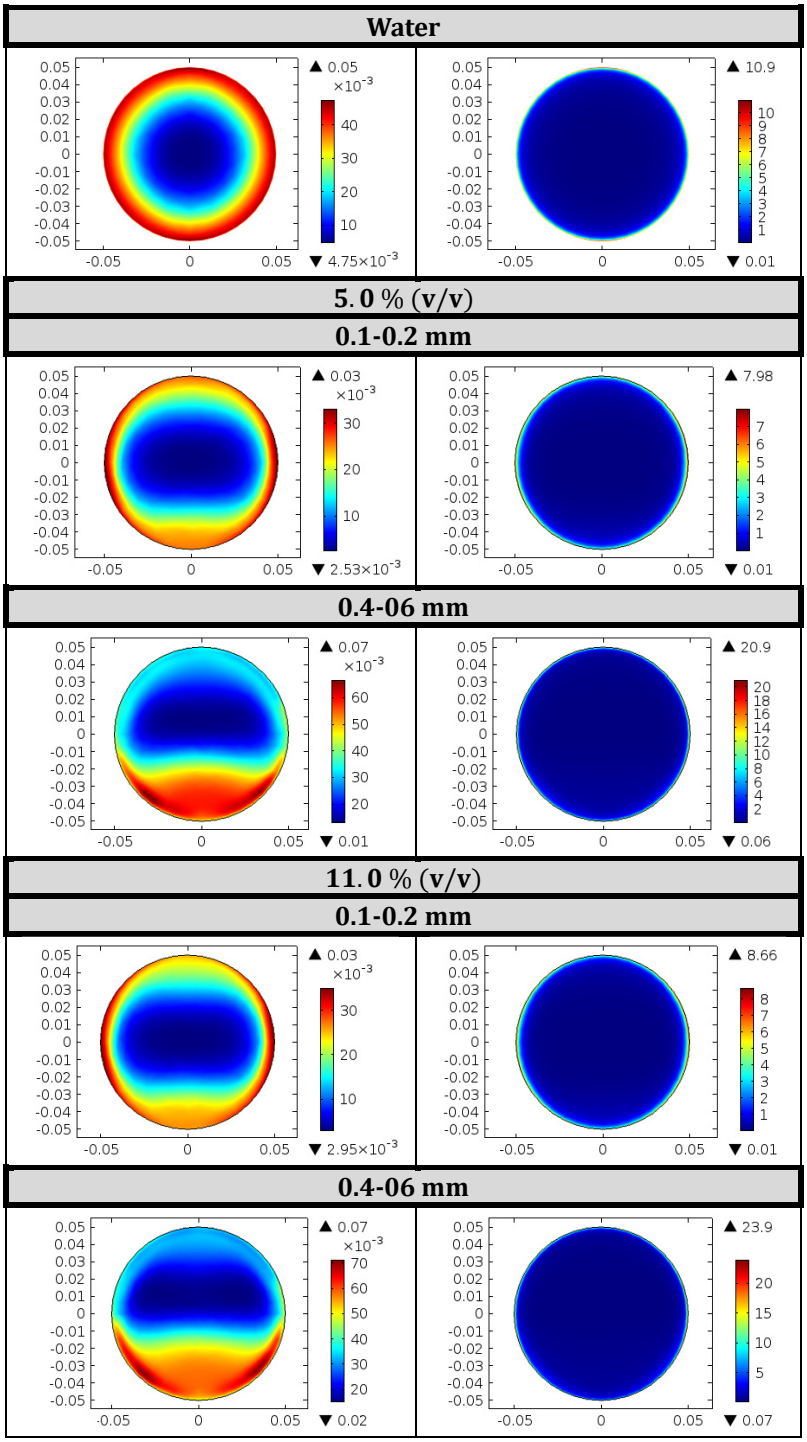

Figure 6.50 – Comparison of the numerical turbulent kinetic energy, k, (Left Column) and turbulent dissipation rate, ε, (Right Column) profiles for the studied flows at DEQ for a flow velocity of 3 m. s^{-1} between water and solid-liquid suspensions with 5.0 and 11.0 % (v/v) solids volumetric concentration for a 100 mm ID pipes.

6.15 also point to an augmentation of the turbulence production introduced by the particles which seems to match the experimental data from Figure

6.45.

6.6. CONCLUDING REMARKS

Following the experimental results depicted in this Chapter, these main conclusions can be drawn:

1. Preliminary testing with the developed EIT apparatus showed the ability to detect objects at different locations in Static Imaging. Also, it displayed the capability of recognizing different flow regimes in Dynamic Imaging using solid-liquid suspensions flows;
2. For the dilute flows, in both 34 and 50 mm ID pipes at KTH laboratory, the attained flow velocity profiles using the MRI and UPV techniques matched well with the numerical velocity profiles from the Mixture Model, coupled with a High Reynolds k-ε Turbulence Model, validating this model application. The UPV technique appears to loose accuracy as the particle size and concentration increases. Furthermore, the calculated EIT particle distribution profiles using Equation 6.19 seem to match well with the numerical concentrations profiles attained with the Mixture Model;
3. For the tests with concentrated flows at DEQ-FCTUC the calculated EIT particle distribution profiles, $\phi(z)$, using Equation 6.19, matched better with the Sampling Probe (SP) data, particularly for the higher particle concentrations and flow rates, which are the preferred conditions for industrial applications. The modified Maxwell Equation (see Equation 6.17) performed well for dilute concentrations and low flow rate;
4. The experimental pressure drops, both KTH and DEQ tests, were matched well by the numerical pressure drops from the Mixture Model for flow velocities above the critical deposition velocity;

CHAPTER VII

CONCLUSIONS AND FUTURE WORK

7. CHAPTER VII – CONCLUSIONS AND FUTURE WORK

In this last Chapter the most pertinent conclusions from the present study have been drawn. Finally, recommendations for future work are proposed.

7.1. CONCLUSIONS

The main objective of this thesis was to study the behaviour of solid-liquid suspensions pipeline conveying by means of experimental and numerical techniques.

In order to acquire particle distribution profiles in the pipe cross-section an Electrical Impedance Tomography (EIT) system was developed. This newly built portable and low cost system was used to infer on particle distribution profiles using the distribution of electrical field inside the 2D domain under inspection. Additional experimental data was also acquired in the form of velocity profiles for both the liquid and solid phases employing Magnetic Resonance Imaging (MRI) and Ultrasonic Pulse Velocimetry (UPV). With these techniques, the flows were characterized for two different sized particles and increasing volumetric concentrations. The obtained conclusions were as follows:

1. Preliminary static testing with the EIT system showed the ability to recognize the presence of multiple objects through their interference in the distribution of the electrical field across the pipe section. A shift in the objects position was also successfully described by this technique;
2. EIT 2D imaging of flow regimes solid-liquid suspensions flows were accomplished for different particle sizes and concentrations;
3. Additionally, the concentration profiles attained using the normalized electrical conductivity profiles from EIT showed good agreement with the sampling probe and numerical data sets, particularly for higher concentrations of particles. In spite of some deviations, the method used in this thesis to calculate particle distributions from the

normalized electrical distribution showed a better accuracy than the Maxwell Equation;

4. The EIT results were highly sensitive to temperatures changes as confirmed by other authors (M. Wang, Jones, and Williams 2003; Giguère et al. 2008);
5. The 1D velocity profiles acquired with both the MRI and UPV techniques showed good agreement with each other and with the numerical results from the Mixture Model although the UPV data exhibited some of these technique shortcomings: a small deviation in the angle between the probes can affect the data acquisition considerably, and the acquired information with the probe placed further downstream was, at times, affected by the presence of particle accumulation in the probe socket. This was visible by the increased noise in the UPV data with increasing particle concentration in Chapter VI;
6. The 2D velocity profiles also acquired using the MRI, overall, matched well the Mixture Model numerical results.

With the numerical studies in this thesis the goal was to have a numerical model that would provide accurate representations of solid-liquid suspensions flows and would serve as an alternative to empirical or semi-empirical correlations. To that end, data from the literature was chosen for both buoyant and settling particles, which were simulated using the Mixture Model. From the numerical studies with the Mixture Model the following conclusions were reached:

7. For concentrated flows with buoyant particles and homogeneous distribution of particles, the Mixture Model showed good agreement with data from the literature, for both 2D and 3D studies, further demonstrating that 2D studies revealed to be sufficient for these types of flows;
8. Additionally, for the buoyant particles, the study on the influence of turbulence scales and closure coefficients demonstrated that the

turbulence scales of a fully developed flow was negligible. The closure coefficients have been studied extensively in the literature (Bardow et al. 2008; Lai and Yang 1997; Rizk and Elghobashi 1989; Costa, Oliveira, and Blay 1999; Wilcox 2006) and with the present work it was demonstrated that for homogeneous flows of buoyant particles the closure values used for single-phase flows are still adequate;

9. For settling particles, the numerical results obtained with the Mixture Model combined with a High Reynolds *k-ε* Turbulence Model showed, in overall, good agreement for the 10 % (v/v) and highest flow velocity of $5\ \mathrm{m.s^{-1}}$. For the remaining particle concentrations and flow velocities, considerable deviations arose for the pressure gradient estimation, particularly for the highest particle concentrations, which are the conditions of interest in industrial environments. Additionally, this model failed to depict the turbulence attenuation observed for the highest particle concentration, 40 % (v/v) at the highest flow velocity of $5\ \mathrm{m.s^{-1}}$. These deviations were attributed to the use of the Wall Function to describe the behaviour of the suspensions near the pipe wall;
10. Incorporating a Low Reynolds Jones-Lauder *k-ε* Turbulence Model into the Mixture Model resulted in an improvement of both the pressure gradient and the particle distribution estimation for the higher particle concentrations of, 30 and 40 % (v/v), and for the flow velocities of, 3 and $5\ \mathrm{m.s^{-1}}$. In the latter flow velocity, where turbulence attenuation occurred, the Low Reynolds Turbulence closure provided accurate numerical results. For the particle concentration of 10% (v/v) the Mixture Model coupled with High Reynolds Turbulence closure numerical results were a better match;
11. For lower flow velocities of, 1 and $2\ \mathrm{m.s^{-1}}$ both the High and Low Reynolds implementations of the Mixture Model, for higher particle concentrations, were not adequate; however, for these flow velocities a stationary or a moving/sliding bed regime was observed which is

not desirable in most industrial environments and where higher flow velocities are often adopted;

12. For an intermediate flow velocity of $3\ \mathrm{m.s^{-1}}$, and higher particle concentrations of, 30 and 40 % (v/v), one of the main turbulence contributions is assumed to come from particle-wall stresses. To account for these stresses, an expression was added to the wall stresses to include the influence of the particle-wall interaction, in the Low Reynolds implementations of the Mixture Model. This resulted in an improvement of the pressure gradient;
13. Finally, from the drag correlations studied with the settling particles data, it was demonstrated that for the high flow velocities of $5\ \mathrm{m.s^{-1}}$, the SN drag correlation seems to depict more accurately the experimental particle distribution profiles, while the HL drag correlation performs better for medium flow velocities, such as $3\ \mathrm{m.s^{-1}}$. The GSN drag correlation seems to provide a more adequate numerical representation of the concentration profiles, specifically for lower flow velocities, for instance $2\ \mathrm{m.s^{-1}}$. These numerical results showed that further research is needed for drag correlations which at this point are still case specific.

7.2. FUTURE WORK

Recommendations for further research, either numerical or experimental, on solid-liquid suspensions conveying are posed in the following paragraphs:

Regarding the EIT experimental technique, additional measurements using water or NaCl solutions flows need to be carried out in order to gather additional information on the electrical conductivity variation with temperature, thus, allowing for temperature compensation in the EIT profiles. Moreover, further testing involving solid-liquid suspensions flows with increasing particle sizes and concentrations should be done, allowing to the creation of a database containing reference data, which would let particle concentration estimation to be carried out without prior knowledge of the

amount of particles in the system. Lastly, further MATLAB® and LabVIEW® coding is wanted in order to permit optimization of the data generation and acquisition with the EIT system, and consequently allowing on-line image reconstruction (instead of the present status, that for using higher sampling rate data acquisition, image reconstruction as to be executed offline).

In this study, velocity profiles were attained using a MRI apparatus. For future testing it would be interesting to attain turbulence intensity profiles for solid-liquid suspensions flows, based on the velocity fluctuations, and to compare these profiles with both High and Low Reynolds Turbulence closures estimated data. Varying the particles size and concentrations would provide valuable data for numerical model validation and/or improvement.

As mentioned in Chapter II there is a lack of data for turbulence attenuation due to the presence of particles. On this subject, a few studies (Messa, Malin, and Malavasi 2014; Václav Matoušek 2005; D.R. Kaushal and Tomita 2007) attribute this phenomena to, possibility, and possibly, a hydrodynamic Lift Force. Further testing, both experimental and numerical, under the conditions depicted in the literature by several authors (S. Lahiri and Ghanta 2010; D.R. Kaushal and Tomita 2007) is pivotal. This additional data will permit the refinement, using Tanaka's study (Tanaka and Eaton 2008), of the areas where turbulence attenuations with solid-liquid suspensions flows occurs. This, in turn, will allow for the design of more efficient pipelines and pumping systems.

Finally, and regarding numerical testing, DNS studies could be extended to turbulent flows with higher Reynolds Number, once computational structures are developing rapidly (the need of larger computational resources are the major limitation of its usage), and help improve drag correlations.

APPENDICES

APPENDIX A – ELECTRICAL IMPEDANCE TOMOGRAPHY THEORY

A.1. EIT GOVERNING EQUATION IN DOMAIN Ω

The equations depicting EIT's physical model are obtained taking Maxwell's basic equations of electromagnetism as a starting point (M. Vauhkonen 1997; N. Polydorides 2002; Noor 2007).

In a conductive isotropic domain, Ω, possessing a boundary, $\partial\Omega$, that is considered an ideal insulator and having a finite number of electrodes placed around that same perimeter, taken as ideal conductors, the following laws hold true:

I. The differential form of Ampère's' Law with Maxwell's extension (Villate 1999):

$$\nabla \times \boldsymbol{H} = \boldsymbol{J} + \frac{\partial \boldsymbol{D}}{\partial t} \tag{A.1}$$

II. The differential form of the Induction Law by Faraday (Villate 1999)

$$\nabla \times \boldsymbol{E} = -\frac{\partial \boldsymbol{B}}{\partial t} \tag{A.2}$$

in these Equations $\boldsymbol{E}$ is the electric field, $\boldsymbol{H}$ is the magnetic field, $\boldsymbol{D}$ represents the electric flux density, $\boldsymbol{B}$ the magnetic flux density and $\boldsymbol{J}$ the electric current density. Assuming that the excitation conditions for EIT are quasi-static (Noor 2007; Grootveld 1996), for each current injection pattern, the measurements are considered to be taken instantaneously and the current injection patterns are low frequency harmonic signals, ω, then

$$\frac{\partial \boldsymbol{D}}{\partial t} \approx 0 \text{ and } \frac{\partial \boldsymbol{B}}{\partial t} \approx 0 \tag{A.3}$$

turning Equations A.1 and A.2, respectively, into

$$\nabla \times \boldsymbol{H} = \boldsymbol{J} \tag{A.4}$$

$$\nabla \times \boldsymbol{E} = 0 \tag{A.5}$$

In vector calculus (Villate 1999), if the rotational of a vector $\boldsymbol{E}$ is zero then

there is a scalar φ whose gradient equals the aforementioned vector, and from the electric field equation,

$$\boldsymbol{E} = -\nabla\varphi \tag{A.6}$$

where φ is the electric potential in a point of domain Ω.

Ohm's Law conveys the relation between the electric current density and the electrical field for an isotropic medium, where σ stands for the electrical conductivity (see Equation A.7).

$$\boldsymbol{J} = \sigma\boldsymbol{E} \tag{A.7}$$

Taking the divergence operator on both sides of Equation A.4 and combining it with Equations A.6 and A.7 the following expression ensues

$$\nabla \cdot (\sigma\nabla\varphi) = 0 \tag{A.8}$$

Equation A.8 stands as the fundamental Equation for EIT.

A.2. CONDITIONS AT THE BOUNDARY $\partial\Omega$

There exists an infinite number of solutions for Equation A.8, thus it is quintessential to impose conditions at the boundary that ensure the existence of a unique solution.

Let us consider Figure A.1 where a cylindrical electrode with volume τ is placed, at the boundary of a domain Ω, so that the faces of the cylindrical object are parallel to the boundary $\partial\Omega$.

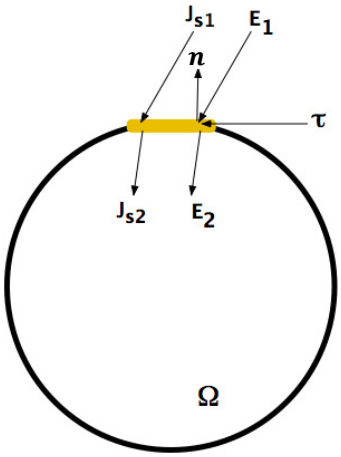

Figure A.1 – Neumann boundary condition derivation, where J_{s1} and J_{s2} are the electric current densities outsider and inside the volume τ, respectively. E_1 and E_2 are the corresponding electric fields (adapted from (M. Vauhkonen 1997)).

If $\Gamma_1 \subset \partial\Omega$ represents the area occupied by the cylinder in Figure A.1 then the electric current density is given by

$$\sigma \frac{\partial \varphi}{\partial \boldsymbol{n}} = j \; for \; \Gamma_1 \tag{A.9}$$

and in the remaining boundary

$$\sigma \frac{\partial \varphi}{\partial \boldsymbol{n}} = 0 \; for \; \Gamma_2 = \partial\Omega - \Gamma_1 \tag{A.10}$$

where $j = -J \cdot \boldsymbol{n}$ represents the applied electric current, and $\boldsymbol{n}$ is the normal unit towards the outside of the cylinder.

A.3. ELECTRODE MODELS

Accurate modelling the electrodes placed at the domain boundary, in EIT, is essential due to the fact that the electrodes are the media by which the electric field is imposed and the resulting electric potentials are measured. The mathematical model must take into account several electrodes' characteristics such as location, dimension and contact impedance so to obtain a representation of the electric potential as closer to reality as possible.

Several electrode models have been developed in the literature (Cheng et al. 1989; M. Wang 2005b; Boyle and Adler 2010) for EIT. The first model, the

"Continuum Model" (Noor 2007; M. Vauhkonen 1997; Cheng et al. 1989), assumes the non-existence of any models and that the injected current is a continuous function.

$$j(\theta) = C\cos(k\theta) \tag{A.11}$$

with C as a constant and $\theta = 2\pi\, l/L$ where $l = 1, \dots, L$ and $k = 1, \dots, L/2$, and L represents the number of electrodes. The resistivity values attained with this model, using experimental data, are overestimated by 25% due to the fact that the "Continuum Model" ignores the existence of electrodes.

Another model found in the literature is the "Gap Model" (M. Vauhkonen 1997; Noor 2007; Cheng et al. 1989) that assumes that the injected current is given by:

$$j = \begin{cases} \frac{I_\ell}{|e_\ell|} & x \in e_\ell \;\; with \;\; \ell = 1, \dots, L \\ 0 & x \in \partial\Omega / \Phi_{\ell=1}^{L} e_\ell \end{cases} \tag{A.12}$$

Being e_ℓ, I_ℓ and L the area of the electrode, the injected current on electrode ℓ and the total number of electrodes, respectively. Comparatively to the "Continuum Model", the "Gap Model" showed some improvements but still overestimates the resistivity values obtained with experimental data. Both these models ignore the "Shunt Effect" (Cheng et al. 1989; M. Wang 2005b) of the electrodes and the contact impedance ensuing from the interface electrode/medium. This "Shunt Effect" is a phenomenon resulting from the presence of metallic electrodes with high conductivity at the boundary $\partial\Omega$, which allow for a short-circuit of the injected current and thus occurring a reduction of the electric current density inside the domain Ω.

The "Shunt Model" (M. Vauhkonen 1997; Noor 2007; Cheng et al. 1989) takes into account the above-mentioned "shunt effect" as well as the electric potential of each electrode. To that effect, the expression for the electric current density is redefined as:

$$j = \begin{cases} \int_{e_\ell} \sigma \frac{\partial \varphi}{\partial \boldsymbol{n}} dS = I_\ell & x \in e_\ell \; with \; \ell = 1, \dots, L \\ \sigma \frac{\partial \varphi}{\partial \boldsymbol{n}} & x \in \partial\Omega / \Phi_{\ell=1}^{L} e_\ell \end{cases} \quad \textbf{(A.13)}$$

and the "Shunt Effect" is incorporated through the following equation

$$\varphi = \Phi_\ell \quad x \in e_\ell \; with \; \ell = 1, \dots, L \quad \textbf{(A.14)}$$

with Φ_ℓ representing the voltage measured in electrode ℓ.

Contrasting with the previous iterations for the electrode model, this model undershoots the resistivity values using experimental values. This is a result of failing to introduce the contact impedance, which is a function of the electrode geometry and electrode/medium interface, into the model.

The last model found in the literature belongs to Cheng, designated as the "Complete Electrode Model" (Cheng et al. 1989; M. Vauhkonen 1997; Noor 2007; P. J. Vauhkonen et al. 1999), which incorporates the "shunt effect" (Equation A.16) and the contact impedance at the electrode/medium interface (Equation A.15). Introducing the contact impedance, z_ℓ, at electrode ℓ into Equation A.14 the following expression results:

$$\varphi + z_\ell \, \sigma \frac{\partial \varphi}{\partial \boldsymbol{n}} = \Phi_\ell \quad x \in e_\ell \; with \; \ell = 1, \dots, L \quad \textbf{(A.15)}$$

$$j = \begin{cases} \int_{e_\ell} \sigma \frac{\partial \varphi}{\partial \boldsymbol{n}} dS = I_\ell & x \in e_\ell \; with \; \ell = 1, \dots, L \\ \sigma \frac{\partial \varphi}{\partial \boldsymbol{n}} & x \in \partial\Omega / \Phi_{\ell=1}^{L} e_\ell \end{cases} \quad \textbf{(A.16)}$$

In Equation A.16 the top term represents the Neumann boundary condition for the injection of the electric current, and the bottom term represents the space between electrodes. Equation A.15 represents the Dirichlet boundary condition, i.e., the measured electric potential difference or voltage in non-injecting electrodes.

To ensure the existence of a unique solution the theorem of conservation of electric charge (Equation A.17) and the choice of an electric potential of

reference (Equation A.18), being typically chosen the "ground potential" as reference, are imposed.

$$\int_{\partial\Omega} j = 0 \Leftrightarrow \sum_{\ell=1}^{L} \mathrm{I}_\ell = 0 \tag{A.17}$$

$$\int_{\partial\Omega} \varphi = 0 \Leftrightarrow \sum_{\ell=1}^{L} \Phi_\ell = 0 \tag{A.18}$$

In summation, Equations A.15 to A.18 in conjunction with Equation A.8 define the "Complete Electrode Model", considered as the most accurate electrode model employed in EIT (Noor 2007; Cheng et al. 1989) and henceforth will be utilized in the both Forward and Inverse Problems calculations in the next Sections.

A.4. FORWARD AND INVERSE PROBLEMS

In a circular geometry, with a homogeneous distribution of conductivity, the Forward problem is solved analytically.

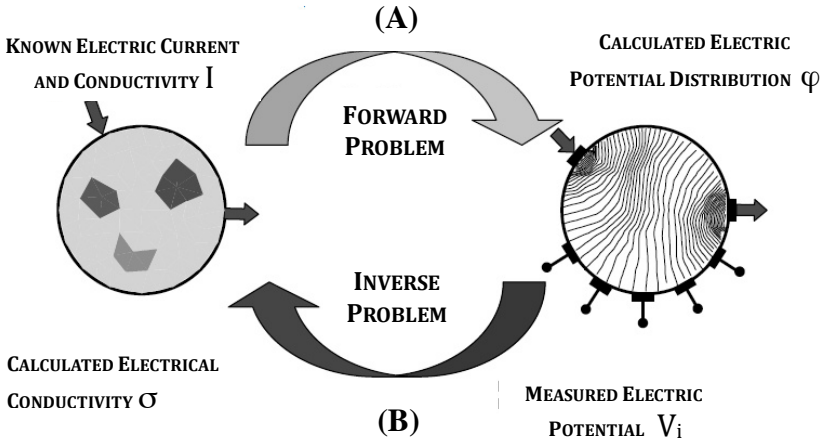

Figure A.2 – Forward Problem in EIT (A): the electrical conductivity and electric current are known and the electric potential distribution is calculated; Inverse Problem in EIT (B): the physical model is wanted based on the aforementioned electric potential distribution (Adapted from (Molinari 2003)).

However, the Inverse problem is more cumbersome and can only be solved by resorting to numerical methods. The Inverse problem is then solved using the Forward Problem as an estimate of the initial conductivity (see Figure A.2).

The classical forward problem consists in finding an effect for a particular cause through a physical/mathematical model. These sort of mathematical problems are usually well-defined which means that they have a unique solution and are relatively insensitive to small perturbations in the data (M. Vauhkonen 1997; Noor 2007; Molinari 2003). The forward problem in EIT, defined using Maxwell Laws (Noor 2007; M. Vauhkonen 1997; N. Polydorides 2002), determines the electric potentials in the boundary using an initial estimation of the conductivity/resistivity distribution. The most common approach to solve the forward problem is the Complete Electrode Model (CEM), based on a Finite Element Method (FEM) formulation (Cheng et al. 1989). As pointed out in Section A.3., this model incorporates the shunt effect and the contact impedance in the electrode/domain interface. The FEM procedure starts with the Galerkin formulation of the problem, also known as weak form of the problem (M. Vauhkonen 1997; Zienkiewicz and Cheung 1965). This continuous formulation is converted into a discrete one using the Finite Element Method (FEM) (M. Vauhkonen 1997; Tossavainen 2007; Segerlind 1984). This method is the appropriate for the work developed in this study due to its' ability to solve ODEs in complex geometries and with non-trivial boundary conditions (M. Vauhkonen 1997).

In 2D, using the Complete Electrode Model, Equation A.8 is multiplied by an arbitrary function ϑ (Borsic, Lionheart, and Polydorides 2004; Zienkiewicz and Cheung 1965; Segerlind 1984; Tossavainen 2007) and integrated in the domain Ω imposing that for all arbitrary functions the following expression holds true

$$\int_{\Omega} \vartheta \, \nabla \cdot (\sigma \nabla \varphi) dx = 0 \tag{A.19}$$

Applying Green's First Identity to Equation A.19 (Tossavainen 2007)

$$\int_{\Omega} \vartheta \, \nabla \cdot (\sigma \nabla \varphi) \, dx = - \int_{\Omega} \sigma \, \nabla \varphi \cdot \nabla \vartheta \, dx + \int_{\Omega} \sigma \frac{\partial \varphi}{\partial \nu} \vartheta \, dS = 0 \tag{A.20}$$

and combining with Equation A.19

$$\int_{\Omega} \vartheta \, \nabla \cdot (\sigma \nabla \varphi) \, dx$$

$$= -\int_{\Omega} \sigma \, \nabla\varphi \cdot \nabla\vartheta \, dx + \int_{\partial\Omega / \Phi_{\ell=1}^{L} e_\ell} \sigma \overbrace{\frac{\partial \varphi}{\partial \nu}}^{0} \vartheta \, dS + \sum_{\ell=1}^{L} \int_{e_\ell} \sigma \frac{\partial \varphi}{\partial \nu} \vartheta \, dS \quad \textbf{(A.21)}$$

Equation A.15 can then be rearranged into the following form

$$\sigma \frac{\partial \varphi}{\partial \nu} = \frac{1}{z_\ell} (\Phi_\ell - \varphi) \quad x \in e_\ell \; with \; \ell = 1, \dots, L \quad \textbf{(A.22)}$$

Replacing Equation A.22 in Equation A.21

$$-\int_{\Omega} \sigma \, \nabla\varphi \cdot \nabla\vartheta \; dx + \sum_{\ell=1}^{L} \int_{e_\ell} \frac{1}{z_\ell} (\Phi_\ell - \varphi) \, \vartheta \, dS = 0 \quad \textbf{(A.23)}$$

Now, returning to Equation A.15 and multiplying it by V_ℓ followed by the integral calculation over the surface of electrode e_ℓ

$$\int_{e_\ell} V_\ell \left(\varphi + z_\ell \sigma \frac{\partial \varphi}{\partial \nu} \right) dS = \int_{e_\ell} V_\ell \, \Phi_\ell \, dS \quad \ell = 1, \dots, L \quad \textbf{(A.24)}$$

Assuming that z_ℓ is constant for each electrode ℓ and dividing Equation A.24 by it

$$\frac{1}{z_\ell} \int_{e_\ell} V_\ell \, \varphi \, dS + \int_{e_\ell} V_\ell \, \sigma \frac{\partial \varphi}{\partial \nu} dS = \frac{1}{z_\ell} \int_{e_\ell} V_\ell \, \Phi_\ell \, dS \quad \ell = 1, \dots, L \quad \textbf{(A.25)}$$

Now using Equation A.16, Equation A.25 can be rewritten

$$\frac{1}{z_\ell} \int_{e_\ell} V_\ell \, \varphi \, dS + V_\ell I_\ell = \frac{1}{z_\ell} \int_{e_\ell} V_\ell \, \Phi_\ell \, dS \quad \ell = 1, \dots, L \quad \textbf{(A.26)}$$

Adding Equations A.26 and A.23 ensues

$$\int_{\Omega} \sigma \nabla\varphi \cdot \nabla\vartheta \; dx - \sum_{\ell=1}^{L} \frac{1}{z_\ell} \int_{e_\ell} \left((\Phi_\ell - \varphi)\vartheta + \varphi V_\ell\right) dS = \sum_{\ell=1}^{L} V_\ell I_\ell \; - \sum_{\ell=1}^{L} \int_{e_\ell} V_\ell \; \Phi_\ell \; dS \tag{A.27}$$

And, with a little reorganization, Equation A.27 becomes

$$\int_{\Omega} \sigma \nabla\varphi \cdot \nabla\vartheta \; dx + \sum_{\ell=1}^{L} \frac{1}{z_\ell} \int_{e_\ell} (\vartheta\varphi - \vartheta\Phi_\ell - \varphi V_\ell + V_\ell\Phi_\ell) \, dS = \sum_{\ell=1}^{L} V_\ell I_\ell \tag{A.28}$$

or

$$\int_{\Omega} \sigma \, \nabla\varphi \cdot \nabla\vartheta \, dx + \sum_{\ell=1}^{L} \frac{1}{z_\ell} \int_{e_\ell} (\varphi - \Phi_\ell)(\vartheta - V_\ell) \, dS = \sum_{\ell=1}^{L} I_\ell V_\ell \tag{A.29}$$

where σ is the electrical conductivity, φ is the approximated voltage using FEM, Φ_ℓ the voltage measured at electrode ℓ , z_ℓ is the impedance at the electrode ℓ, ϑ is the function of the Galerkin formulation, V_ℓ is the vector of the measured voltages on all the electrodes and I_ℓ is the current injected on the electrode ℓ.

To attain a solution employing FEM as a starting point, the discretization of the domain Ω into elements is necessary, in this case triangles whose vertices are designated as nodes. This assembly of elements is designated as finite element mesh with K elements and N nodes (Borsic, Lionheart, and Polydorides 2004; Zienkiewicz and Cheung 1965; Segerlind 1984; Tossavainen 2007).

The approximate solution, known as weak solution, φ, obtained from FEM, can be written

$$\varphi = \sum_{i=1}^{N} \Phi_i w_i \tag{A.30}$$

being Φ_i the voltage in node i to be determined, N the number of nodes in the finite element mesh and w_i the shape function. The voltage at the electrode is calculated using the approximation

$$\varphi^E = \sum_{j=1}^{L-1} \beta_j \eta_j \tag{A.31}$$

in which

$$\eta_1 = [-1,1,\cdots,0]^{\mathbb{T}}, \eta_2 = [0,-1,1,\cdots,0]^{\mathbb{T}} \in \mathcal{R}^L, \text{ etc.} \tag{A.32}$$

In Equation A.31, L is the number of electrodes and β_j represents the voltage at electrode j. This ensures that the choice for a reference voltage in Equation A.32 is valid. Associating these approximations in the variational form and using $\vartheta = w_i$ and $\mathrm{V} = \eta_j$, a matricial equation is formed,

$$\boldsymbol{Ab} = \boldsymbol{f} \tag{A.33}$$

where

$$b = (\boldsymbol{\Phi}, \boldsymbol{\beta})^{\mathbb{T}} \in \mathcal{R}^{(N+L-1)} \text{ with } \boldsymbol{\Phi} = (\Phi_1, \Phi_2, \cdots, \Phi_N)^{\mathbb{T}} \text{ and } \boldsymbol{\beta} = (\beta_1, \beta_2, \cdots, \beta_{L-1})^{\mathbb{T}} \tag{A.34}$$

represent the coefficients (nodal potentials) to be determined. The sparse matrix A has a structure $\boldsymbol{A} \in \mathcal{R}^{(N+L-1)\times(N+L-1)}$

$$\boldsymbol{A} = \begin{pmatrix} B & C \\ C^{\mathbb{T}} & D \end{pmatrix} \tag{A.35}$$

in which

$$B(i,j) = \int_{\Omega} \sigma \, \nabla w_i \cdot \nabla w_j \, dx + \sum_{\ell=1}^{L} \frac{1}{z_\ell} \int_{e_\ell} w_i w_j \, dS \quad i,j = 1,2,\cdots,N \tag{A.36}$$

$$C(i,j) = -\left(\frac{1}{z_1} \int_{e_1} w_i \, dS - \frac{1}{z_{j+1}} \int_{e_{j+1}} w_i \, dS \right) \quad i = 1,2,\cdots,N \text{ and } j = 1,2,\cdots,L-1 \tag{A.37}$$

$$D(i,j) = \sum_{\ell=1}^{L} \frac{1}{z_\ell} \int_{e_\ell} (\eta_i)_\ell (\eta_j)_\ell \, dS = \begin{cases} \dfrac{|e_1|}{z_1} & i \neq j \\ \dfrac{|e_1|}{z_1} + \dfrac{|e_{j+1}|}{z_{j+1}} & i = j \end{cases} \quad i,j = 1,2,\cdots,L-1 \tag{A.38}$$

Here, $|e_j|$ represents the size of electrode j (diameter in this particular case).

The vector f, from Equation A.33 is given by

$$\boldsymbol{f} = \begin{pmatrix} \mathbf{0} \\ \sum_{\ell=1}^{L} I_\ell(\eta_i)_\ell \end{pmatrix} = \begin{pmatrix} \mathbf{0} \\ \tilde{\boldsymbol{I}} \end{pmatrix} \tag{A.39}$$

with $\mathbf{0} = (0,0,\cdots,0)^{\mathbb{T}} \in \mathcal{R}^N$ and $\tilde{\mathbf{I}} = (I_1 - I_2, I_2 - I_3, \cdots, I_{L-1} - I_L)^{\mathbb{T}} \in \mathcal{R}^{L-1}$: the last vector is the injected currents vector. Solving with respect to b, Equation A.33 becomes

$$\boldsymbol{b} = \boldsymbol{A}^{-1}\boldsymbol{f} \tag{A.40}$$

The electrodes voltages φ_h^ℓ are obtained using Equation A.40

$$\begin{aligned} \varphi_h^1 &= -\sum_{\ell=1}^{L-1} \beta_\ell \\ \varphi_h^2 &= \beta_1 \\ \varphi_h^3 &= \beta_2 \\ &\vdots \\ \varphi_h^L &= \beta_{L-1} \end{aligned} \tag{A.41}$$

or in the form of matrix

$$\boldsymbol{\varphi_h^E} = \boldsymbol{\eta\beta} \tag{A.42}$$

where $\boldsymbol{\eta} \in \mathcal{R}^{L\times(L-1)}$ is a sparse matrix which the form

$$\boldsymbol{\eta} = \begin{pmatrix} 1 & 1 & 1 & 1 & \dots & 1 \\ & -1 & & & & \\ & & -1 & & & \\ & & & -1 & & \\ & & & & \ddots & \\ & & & & & -1 \end{pmatrix} \tag{A.43}$$

and $\boldsymbol{\beta} = (\beta_1, \beta_2, \cdots, \beta_{L-1})^{\mathbb{T}}$. The relation between the injected electric current and the measured electric potentials can be displayed in the form of matrix

$$\varphi_h^E = \eta\beta = \eta\check{R}(\sigma)\eta^{\mathbb{T}} I = R(\sigma)I \tag{A.44}$$

where $\check{R}(\sigma) \in \mathcal{R}^{(L-1)\times(L-1)}$is the inverse part of A, $R(\sigma) = \eta\check{R}(\sigma)\eta^{\mathbb{T}} \in \mathcal{R}^{L\times L}$ and $I = (I_1, I_2, \cdots, I_L)^{\mathbb{T}} \in \mathcal{R}^L$ is the vector with the injected electric currents also called the "current pattern" (M. Vauhkonen 1997).

The solution of the Forward Problem, using the Finite Element Method, was attained with either one of the meshes depicted on Figure A.3. The structured mesh (see Figure A.3(a)) had 2304 linear elements and 1201 nodes, while the non-structured mesh (see Figure A.3(b)) had 415 linear elements and 241 nodes.

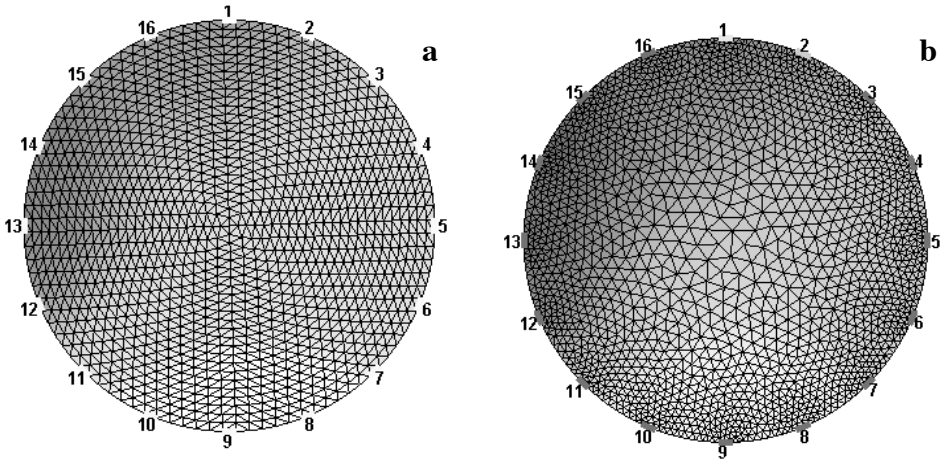

Figure A.3 – Meshes utilized in the 2D EIT image reconstruction.

Traditionally is assumed that all physical problems could be modelled using well-defined mathematical formulations; however, today it is known that several problems in science and engineering fields are not well-defined and are ill-conditioned. These particular type of problems are designated as Inverse Problems and are, as the name suggests, inverse to classical problems which may not possess a stable solution and small variations in the data can affect significantly the solution (M. Vauhkonen 1997; Noor 2007; Molinari 2003).

Inverse problems are utilized in the determination of causes to observed and/or warranted effects, or in calibrating parameters of mathematical models to match observations (M. Vauhkonen 1997). These particular kind of mathematical problems fail to comply to Jacques Hadamard postulates for a well-posed problem (Molinari 2003), which are:

I. Existence of a solution – existence;
II. The solution is unique – unicity;
III. The solution depends continuously on the data – Stability of Solution;

The Inverse Problem is the core issue when dealing with Electrical Impedance Tomography, more precisely, the inverse problem of the physical model identification: given the injected currents (causes) and the respective electric potential that ensues at the electrodes (effects) the goal is to obtain the electrical conductivity distribution (physical model) inside the domain Ω.

The methods to solve Inverse Problems can be segregated into two groups: deterministic methods (M. Vauhkonen 1997; M. Vauhkonen et al. 1998) and statistical methods (M. Vauhkonen 1997; P. J. Vauhkonen et al. 2000). For the work developed in this study only deterministic methods will be considered.

Let us consider a physical model

$$\mathbb{z} = \hbar(\theta) \tag{A.45}$$

where $\mathbb{z} \in \mathcal{R}^M$ is the observation, and $\theta \in \mathcal{R}^N$ is the parameter to be estimated. If the model is linear then Equation A.45 can be rewritten as

$$\mathbb{z} = \mathcal{H}(\theta), \mathcal{H} \in \mathcal{R}^{M \times N} \tag{A.46}$$

In the previous Equations A.45 and A.46, if either $\hbar(\theta)$ or $\mathcal{H}(\theta)$ are known, the result or effect $\mathbb{z}$ can be calculated. It's a classic problem, which is normally stable and has a unique solution. In the inverse problem $\mathbb{z}$ is measured/observed and the parameter θ is determined. Since $\mathbb{z}$ is a measured/observed quantity it is liable to observation errors. This is a potential issue due to the ill-conditioning, typical in inverse problems, quite susceptible to observation errors.

An inverse problem, in reality, does not possess a classic solution typically because $\mathbb{z} \notin \mathcal{R}(\mathcal{H})$ with (Molinari 2003; M. Vauhkonen 1997)

$$\mathcal{R} = \{\mathbb{z} \in \mathcal{R}^M | \mathbb{z} = \mathcal{H}x \quad for\ any\ x \in \mathcal{R}^N\} \tag{A.47}$$

For this reason a generalized solution is explored to minimize the difference between the observations and measurements obtained with the numerical method. In the case that the number of measurements, M, equals the number of variables, N, a simple inversion of the matrix $\mathcal{H}$ is sufficient to determine θ. If the problem is over-determined ($M > N$) or under-determined ($M < N$), then the solution that presents the best fit is chosen (Molinari 2003; M. Vauhkonen 1997).

A method that can be used to obtain the solution is the Least Squares Method (M. Vauhkonen 1997; Zienkiewicz and Emeritus 2000). The vector θ is called the least squares solution of the problem.

$$\theta = \min_{\theta} \|L\mathbb{z} - L\mathcal{k}(\theta)\|^2 \tag{A.48}$$

or

$$\theta = \min_{\theta} \|L\mathbb{z} - L\mathcal{H}(\theta)\|^2 \tag{A.49}$$

with $L^T L = \mathcal{W}$, and where $\mathcal{W}$ is called the weighting matrix.

If $\mathcal{k}(\theta)$ is a non-linear function, then there exist infinite solutions to Equation A.49. The problem can be linearized around θ_o using a Taylor Series Expansion.

$$\mathcal{k}(\theta) = \mathcal{k}(\theta_o) + \frac{\partial \mathcal{k}}{\partial \theta}(\theta_o)(\theta - \theta_o) + O(\|\theta - \theta_o\|) \tag{A.50}$$

The term $\frac{\partial \mathcal{k}}{\partial \theta}(\theta_o)$ represents the Jacobian , $\mathcal{J}$, of $\mathcal{k}(\theta)$ at the point θ_o.

Ignoring the higher order terms and rearranging

$$\mathcal{k}(\theta) - \mathcal{k}(\theta_o) = \mathcal{J}(\theta - \theta_o) \tag{A.51}$$

with $\Delta\mathcal{k} = \mathcal{k}(\theta) - \mathcal{k}(\theta_o)$ and $\Delta\theta = \theta - \theta_o$ Equation A.51 becomes

$$\Delta\hbar = \mathcal{J}\Delta\theta \tag{A.52}$$

Equation A.52 represents the linearized relation between a variation in parameter θ and a variation $\Delta\hbar$ in the observation around the point θ_o. The least squares method solution for the linearized form of Equation A.49 is only attainable through the Moore-Penrose Inverse or pseudo-inverse of $\mathcal{H}$

$$\Delta\hbar = \mathcal{H}^{+}\Delta\theta \tag{A.53}$$

In the last equation $\mathcal{H}^{+}$ represents

$$\mathcal{H}^{+} = (\mathcal{J}^{\mathbb{T}}\mathcal{W}\mathcal{J})^{-1}\mathcal{J}^{\mathbb{T}}\mathcal{W} \tag{A.54}$$

The solution to the non-linear problem can be achieved through iterative methods, as is the case with the Gauss-Newton algorithm, which was used in this study. In this algorithm the objective function $o(\theta) = \|L\mathbb{z} - L\mathcal{H}(\theta)\|^2$ is approximated by a second order Taylor Series Expansion for the initial point θ_o.

$$\begin{aligned} o(\theta) \approx o(\theta_o) + \left(\frac{\partial o}{\partial\theta}(\theta_o)\right)^{\mathbb{T}}(\theta-\theta_o) \\ + \frac{1}{2}(\theta-\theta_o)^{\mathbb{T}}\left(\frac{\partial^2 o}{\partial\theta^2}(\theta_o)\right)^{\mathbb{T}}(\theta-\theta_o) = f(\theta) \end{aligned} \tag{A.55}$$

The gradient of o is given by $\frac{\partial o}{\partial\theta}$ and the Hessian by $\frac{\partial^2 o}{\partial\theta^2}$. The approximation $f(\theta)$ reaches a minimum at $\theta = \bar{\theta}$ when

$$\frac{\partial f}{\partial\theta}(\bar{\theta}) = \left(\frac{\partial o}{\partial\theta}(\theta_o)\right) + \left(\frac{\partial^2 o}{\partial\theta^2}(\theta_o)\right)(\bar{\theta}-\theta_o) \tag{A.56}$$

Then, solving for $\bar{\theta}$

$$\bar{\theta} = \theta_o - \left(\frac{\partial^2 o}{\partial\theta^2}(\theta_o)\right)^{-1}\left(\frac{\partial o}{\partial\theta}(\theta_o)\right) \tag{A.57}$$

The gradient of o becomes

$$\frac{\partial o}{\partial \theta}(\theta_o) = -2\left(\frac{\partial \hbar}{\partial \theta}(\theta_o)\right)^{\mathbb{T}} \mathcal{W}(\mathbb{z} - \hbar(\theta_o)) \tag{A.58}$$

and consequently the Hessian becomes

$$\frac{\partial^2 o}{\partial \theta^2}(\theta_o) = -2\left(\sum_{j=1}^{M}\left(\mathbb{z}_j - \hbar_j(\theta_o)\right)\mathcal{W}\frac{\partial^2 \hbar_j}{\partial \theta^2}(\theta_o)\right) + 2\left(\frac{\partial \hbar}{\partial \theta}(\theta_o)\right)^{\mathbb{T}} \mathcal{W}\left(\frac{\partial \hbar}{\partial \theta}(\theta_o)\right) \tag{A.59}$$

With the Gauss-Newton algorithm the Hessian is approximated by the second term in the right side of Equation A.55. Gauss-Newton formulation is defined by

$$\bar{\theta}_{i+1} = \bar{\theta}_i + \left(\mathcal{J}_i{}^{\mathbb{T}}\mathcal{W}\mathcal{J}_i\right)^{-1}\left(\mathcal{J}_i^{\mathbb{T}}\mathcal{W}\left(\mathbb{z} - \hbar(\bar{\theta}_i)\right)\right) \tag{A.60}$$

Where the term $\mathcal{J}_i = \frac{\partial \hbar}{\partial \theta}(\theta_i)$ represents the Jacobian of the model $\hbar(\theta)$ at the point θ_i.

The previous mathematical deduction of the Gauss-Newton algorithm assumes that the problem is well-defined. This, however, is not the case for EIT since it's characterized as an inverse problem and thus ill-conditioned. For the application of the Gauss-Newton algorithm to the EIT inverse problem, i.e. to obtain reconstructed images of the conductivity distribution in the domain, a modification is required to obtain a stable solution.

This modification is designated Regularization and consists of the substitution of an ill-conditioned problem by a well-defined one. This is achieved by extending the least mean squares method

$$o_\alpha(\theta) = \left\|L_1\left(\mathbb{z} - \hbar(\theta)\right)\right\|^2 + \alpha\|L_2(\theta - \theta_o)\|^2 \tag{A.61}$$

θ_o is the initial estimate for θ, $\alpha > 0$ is the regularization parameter, L_1 is the square root of the pondered matrix $\mathcal{W} = {L_1}^{\mathbb{T}}L_1$ and L_2 is the regularization matrix.

For the work described in this manuscript the regularization technique employed was Tikhonov's General Regularization and applying it to the Gauss-Newton algorithm results

$$\bar{\theta}_{i+1} = \bar{\theta}_i + \left(\mathcal{J}_i{}^{\mathbb{T}}\mathcal{J}_i - \alpha R^{\mathbb{T}}R\right)^{-1}\left(\mathcal{J}_i^{\mathbb{T}}\left(\mathbb{z} - \hbar(\bar{\theta}_i)\right) - \alpha R^{\mathbb{T}}R\bar{\theta}_i\right) \quad \textbf{(A.62)}$$

With the Regularization Matrix, R, the nearest three elements are considered and pondered in regards to the inverse of the distance between their centers (see Figure A.4). The parameter α is fine-tuned empirically a posteriori by visual inspection.

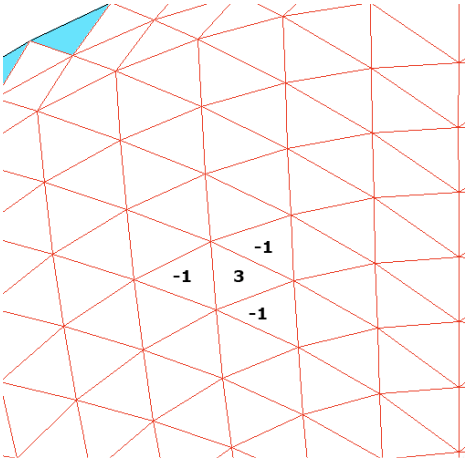

Figure A.4 – Regularization application to a mesh element.

APPENDIX B – MATLAB® AND LABVIEW® CODES

MATLAB® Codes

The following MATLAB® scripts are used in coupled with the EIDORS software package. Initial versions of these codes were implemented by the author and here are presented the optimized and improved final versions by Bruno Branco at the DEQ laboratory.

This first script load all the necessary subroutines and calls the necessary functions for the image reconstruction.

```
function run()
%%%%%%%%%%%%%%%%%%%%%%%%%%%%%%%%%%%%%%%%%%%%%%%%%%%%%%%%%%%%%%%%%%%
%%%%%%%%
%definir a quantidade de dados a simular. imagem unica ou
multiplas%%%%%%%
%imagens. Em caso de uma imagem singular,q_imagens=0 caso
contrario%%%%%%%
q_imagens=0;%q_imagens=1.%%%%%%%%%%%%%%%%%%%%%%%%%%%%%%%%%%%%%%%%%%
%%%%%%%%
n_ele=32;%definir n_electrodos 16 ou
32%%%%%%%%%%%%%%%%%%%%%%%%%%%%%%%%%%%
inj=1;%definir protocolo implementado (inj=1) adjacente, (inj=2)
oposto %%
brancos=1;%definir quantas condutividades de
branco%%%%%%%%%%%%%%%%%%%%%%%
concentracoes=1;%definir o numero de concentracoes
%%%%%%%%%%%%%%%%%%%%%%%
graf_saida=0;%definir grafico de
saida.%%%%%%%%%%%%%%%%%%%%%%%%%%%%%%%%%%%
%graf_saida==0 imagem
recontruida%%%%%%%%%%%%%%%%%%%%%%%%%%%%%%%%%%%%%%%%%
%graf_saida==1 perfis
radiais%%%%%%%%%%%%%%%%%%%%%%%%%%%%%%%%%%%%%%%%%%%%%
%%%%%%%%%%%%%%%%%%%%%%%%%%%%%%%%%%%%%%%%%%%%%%%%%%%%%%%%%%%%%%%%%%%
%%%%%%%%
%%


dirname=pwd;
parentdir = fileparts(dirname);
 if q_imagens==0
     i=1;
     j=1;
     sp=1;
     nh=1;
     h=1;

     simul(n_ele,inj,i,j,sp,h,nh,parentdir,q_imagens,graf_saida)
```

```
 else

for h=1:1:brancos  %percorre todas pastas  de sets homogeneos
    for nh=1:1:concentracoes  %percorre todos as pastas de sets
não homogeneos

for sp=14:14:84 % Caudal. Define o caudal para reconstruir imagens
do mesmo caudal/velodidade dos sets homogeneos e não homogeneos.
28=1m/s
nfiles_h=dir([parentdir
'\dados\simulacao\imagens_multiplas\set_homogeneo\B' num2str(h)
'\' num2str(sp) '\*.txt']);
nfiles_nh=dir([parentdir
'\dados\simulacao\imagens_multiplas\set_naohomogeneo\C'
num2str(nh) '\' num2str(sp) '\*.txt']);
nfiles_h_size=size(nfiles_h);
nfiles_nh_size=size(nfiles_nh);
h_s=nfiles_h_size(1,1)/2;
nh_s=nfiles_nh_size(1,1)/2;

%h_s e nh_s numero total de pares de ficheiros (coseno e seno).
%\h_s  na pasta com ficheiros do set homogeneo.
%\nh_s na pasta com ficheiro do set de data não homogeneo.

%os ciclos for são para simular todos as combinaçoes posiveis
entre sets
%homogeneos e sets não homogenos

for i=1:h_s% set homogeneo escolhido a cruzar
   for j=1:nh_s   % set nao homogeneo a cruzar
       close all
       simul(n_ele,inj,i,j,sp,h,nh,parentdir,q_imagens,graf_saida)

   end

end

end
    end
end
 end
```

The second script creates the mesh and solves both forward and inverse problems.

```
function simul(n_ele,inj,aa,bb,sp,h,nh,parentdir,q_imagens,
graf_saida)
close all

switch inj%definicao do tipo de injecao e do hyperparameter
    case 1
        opt1='{ad}';
        opt2='{ad}';
```

```
        hyper=5;% definicao do hyperparameter para injecção
adjacente [4 a 6]tipicamente..
    case 2
        opt1='{op}';
        opt2='{ad}';

        hyper=3;%definicao do hyperparameter para injecção oposta
[1 a 4]tipicamente.

end

clc

[Vh,Vi,VV]=data_read(n_ele,inj,aa,bb,sp,h,nh,parentdir,q_imagens);


imdl_2D= mk_common_model('d2c',n_ele);% 2D Model using distmesh
Nel= n_ele; % Number of elecs
Nplanes=1; % Number of planes
Zc = 0.011; % Contact impedance
curr = 22; % applied current mA
options={'no_meas_current','no_rotate_meas','do_redundant'}; %
Custom settings of our electrodes
stimulation=mk_stim_patterns( Nel, Nplanes, opt1,opt2, options,
curr ); % New stimulation data
imdl_2D.fwd_model.stimulation = stimulation; % Replace model
stimulation data with new custom one

for i =1:Nel
    imdl_2D.fwd_model.electrode(i).z_contact=Zc;
end
imdl_2D.fwd_model.electrode =
imdl_2D.fwd_model.electrode([2,3:1:n_ele,1]); % Para colocar o
electrodo 16/32 no topo

%% Show mesh design
%show_fem(imdl_2D.fwd_model,[0,1,0]);
% Reconstruct Image
%imdl_2D.fwd_model= imdl_2D.fwd_model.stimulation;
% Guass-Newton solvers
imdl_2D.solve= @aa_inv_solve;%define o algoritmo usando na
reconstrução
imdl_2D.fwd_model.normalize_measurements=1;
imdl_2D.hyperparameter.value=hyper;
% Tikhonov prior
%imdl_2D.RtR_prior= @tikhonov_image_prior;
imdl_2D.fwd_model.meas_select=VV;
% imdl_2D.meas_icov = meas_icov_rm_elecs( imdl_2D,[ 6]);% remove
os electrodos da reconstrução
rec_img= inv_solve(imdl_2D, Vh, Vi);
rec_img.calc_colours.npoints = 512;%numero de pontos da matrix
slice usada nos
%rec_img.calc_colours.backgnd=[0,0,0];
%rec_img.calc_colours.ref_level=0;%valor atribuida à cor branca na
escala de cores
```

```
%rec_img.calc_colours.clim=0.07;%Limite da escala de cores. no
caso de ref_level=0 os limites da escala sao iguais ao .clim.



figure
if graf_saida==0% se graf_saida ==0 a figura gravada é a imagem
rescontruida.

    h=show_fem(rec_img,[1,-1]);
    axis off

    if q_imagens==0
        saveas(h,[parentdir
'\dados\resultados\imagem_unica_reconstruidas\'
num2str(aa*1000+bb) ], 'png')

    else

        saveas(h,[parentdir
'\dados\resultados\imagens_multiplas_reconstruidas\B' num2str(h)
'\C' num2str(nh) '\' num2str(sp) '\' num2str(aa*1000+bb) ], 'png')
    end

else %se graf_saida ==1 a figura gravada é o perfil da imagem
reconstruida.

    npoints=rec_img.calc_colours.npoints;
    nlimite=rec_img.calc_colours.clim;
    hh=show_slices(rec_img);
    figuras=graf_in(hh,npoints,nlimite,sp,nh);
    if q_imagens==0 % se q_imagens==0 apenas 1 imagem ou perfil e
gravado, cosrrespondente ao conjunto de dados simulados. 1 set
homogeneio com 1 set não homogeneo

        saveas(figuras,[parentdir
'\dados\resultados\imagem_unica_reconstruidas\perfil_'
num2str(aa*1000+bb) ],'png')
    else
        saveas(figuras,[parentdir
'\dados\resultados\imagens_multiplas_perfis\B' num2str(h) '\C'
num2str(nh) '\' num2str(sp) '\perfil_' num2str(aa*1000+bb)
],'png')
    end
end

close all
```

The third, and final script by Bruno Branco, is a subroutine that reads all the data acquired with the EIT and introduces it to the previous script.

```
function [Vh,Vi,VV]=dataread(xx,opcao,a,b,speed,hh,nnh)

tic
write=0;
xon=0;
%speed;
n_elect=4;

infodata=struct('cosenos',[], 'senos',[],'cosenosbranco',[],
'senosbranco',[]);
h=dir(['C:\Users\deqadmin\Desktop\123\h\' num2str(hh) '\'
num2str(speed) '\*.txt']);
nh=dir(['C:\Users\deqadmin\Desktop\123\nh\' num2str(nnh) '\'
num2str(speed) '\*.txt' ]);

c=a*2;
d=b*2;




inc=0;
for i=1:xx

    if xx<20



infodata(i).cosenos=dlmread(['C:\Users\deqadmin\Desktop\123\nh\'
num2str(nnh) '\' num2str(speed) '\' nh(d).name ],'\t', ['B'
num2str(6+inc) '..N' num2str(15+inc)]);

infodata(i).senos=dlmread(['C:\Users\deqadmin\Desktop\123\nh\'
num2str(nnh) '\' num2str(speed) '\' nh(d-1).name ],'\t', ['B'
num2str(6+inc) '..N' num2str(15+inc)]);

infodata(i).cosenosbranco=dlmread(['C:\Users\deqadmin\Desktop\123\
h\' num2str(hh) '\' num2str(speed) '\' h(c).name],'\t', ['B'
num2str(6+inc) '..N' num2str(15+inc)]);

infodata(i).senosbranco=dlmread(['C:\Users\deqadmin\Desktop\123\h\
' num2str(hh) '\' num2str(speed) '\' h(c-1).name],'\t', ['B'
num2str(6+inc) '..N' num2str(15+inc)]);
    else

infodata(i).cosenos=dlmread(['C:\Users\deqadmin\Desktop\123\nh\'
num2str(nnh) '\' num2str(speed) '\' nh(d).name ],'\t', ['B'
num2str(6+inc) '..AD' num2str(15+inc)]);

infodata(i).senos=dlmread(['C:\Users\deqadmin\Desktop\123\nh\'
num2str(nnh) '\' num2str(speed) '\' nh(d-1).name ],'\t', ['B'
num2str(6+inc) '..AD' num2str(15+inc)]);

infodata(i).cosenosbranco=dlmread(['C:\Users\deqadmin\Desktop\123\
h\' num2str(hh) '\' num2str(speed) '\' h(c).name],'\t', ['B'
num2str(6+inc) '..AD' num2str(15+inc)]);
```

```
infodata(i).senosbranco=dlmread(['C:\Users\deqadmin\Desktop\123\h\
' num2str(hh) '\' num2str(speed) '\' h(c-1).name],'\t', ['B'
num2str(6+inc) '..AD' num2str(15+inc)]);


    end

    inc=inc+16;

end


mediasenos=zeros(xx,xx-3);
mediacosenos=zeros(xx,xx-3);
mediasenosbrancos=zeros(xx,xx-3);
mediacosenosbrancos=zeros(xx,xx-3);

modulo3=zeros(xx+1,xx-3);
modulobrancos3=zeros(xx+1,xx-3);

for j=1:xx
    for k=1:xx-3
        mediacosenos(j,k)=mean(infodata(j).cosenos(6:end,k));
        mediasenos(j,k)=mean(infodata(j).senos(6:end,k));

mediacosenosbrancos(j,k)=mean(infodata(j).cosenosbranco(6:end,k));

mediasenosbrancos(j,k)=mean(infodata(j).senosbranco(6:end,k));



modulo(j,k)=abs(complex(mediacosenos(j,k),mediasenos(j,k)));

modulobrancos(j,k)=abs(complex(mediacosenosbrancos(j,k),mediasenos
brancos(j,k)));
    end
end

     modulo(:,27)= modulo(:,3);
     modulobrancos(:,27)=modulobrancos(:,3);
     modulo(:,28)= modulo(:,2);
     modulobrancos(:,28)=modulobrancos(:,2);
     modulo(:,18)= modulo(:,12);
     modulobrancos(:,18)=modulobrancos(:,12);

if xon==1




%    modulo(:,1:14)=fliplr(modulo(:,16:29));
```

```
% %
%   modulobrancos(:,1:14)=fliplr(modulobrancos(:,16:29));
%


 %modulo(:,1:14)=fliplr(modulo(:,16:29));
%
 %modulobrancos(:,1:14)=fliplr(modulobrancos(:,16:29));
%  B=mean(modulo);
% C=mean(modulobrancos);
%
% for kkl=1:32
%
% modulobrancos(kkl,:)=C;
%
% modulo(kkl,:)=B;
%
%
% end


else
end









%modulobrancos(:,5)=0.0001;
%xlswrite('mediagfdgfcdg.xlsx',modulos,'Folha4','A1')
%xlswrite('mo.xlsx',modulobrancos,'Folha5','A18')
%#########################################################
%#########################################################
matriz=zeros(xx,xx);
matrizbranco=zeros(xx,xx);
VV=zeros(xx*xx,1);
%xlswrite('media.xlsx',modulo,'Folha1')
%xlswrite('media.xlsx',modulobrancos,'Folha2')
%xlswrite('media.xlsx',modulo-modulobrancos,'Folha3')
for tt=1:n_elect


    modulo3(1:xx,:)=modulo;
    modulo3(xx+1,:)=modulo(1,:);
    modulo=modulo3(2:end,:);

    modulobrancos3(1:xx,:)=modulobrancos;
    modulobrancos3(xx+1,:)=modulobrancos(1,:);
    modulobrancos=modulobrancos3(2:end,:);


end
```

```
switch opcao
    %case Injecção adjacente - Medidas adjacentes
    case 1
        disp( 'Injecção adjacente - Medidas adjacentes');
        disp( opcao);

        q=0;
        for n=1:xx
            p=0;
            for m=1:xx-3
                if(q+m+2+p>xx)
                    p=p-xx;
                end
                matriz(q+m+2+p,n)=modulo(n,m);
                matrizbranco(q+m+2+p,n)=modulobrancos(n,m);


            end
            q=q+1;

        end
        %matriz de selelecção meas_select VV
        for i=1:xx
            for j=1:xx
                if abs(matriz(j,i))> 0

                    VV(j+(i-1)*xx)=1;
                else
                end

            end
        end

        Vi=matriz(matriz>0);
        Vh=matrizbranco(matrizbranco>0);


        %case 2 Injecção Oposta - Medidas adjacentes
    case 2
        disp( 'Injecção Oposta - Medidas adjacentes');
        disp( opcao);

        modulo2=zeros(xx,xx-4);
        modulobrancos2=zeros(xx,xx-4);

        modulo2(:,1:(xx/2)-2)=modulo(:,1:(xx/2)-2);

        modulo2(:,(xx/2)-1:xx-4)=modulo(:,(xx/2):xx-3);

        modulobrancos2(:,1:(xx/2)-2)=modulobrancos(:,1:(xx/2)-2);

        modulobrancos2(:,(xx/2)-1:xx-4)=modulobrancos(:,(xx/2):xx-
3);
```

```
        q=0;
        for n=1:xx
            p=0;


            act=0;
            for m=1:xx-2
                if(q+m+1+p>xx)
                    p=p-xx;
                end

                if m==((xx/2)-1)
                    % matriz(q+m+1+p,n)=0;
                    %matrizbranco(q+m+1+p,n)=0;
                    act=act+1;

                elseif m==(xx/2)

                    % matriz(q+m+1+p,n)=0;
                    %matrizbranco(q+m+1+p,n)=0;
                    act=act+1;
                else


                    matriz(q+m+1+p,n)=modulo2(n,m-act);
                    matrizbranco(q+m+1+p,n)=modulobrancos2(n,m-
act);

                end
            end

            q=q+1;

        end


        %matriz de selelecção meas_select VV
        for i=1:xx
            for j=1:xx
                if abs(matriz(j,i))> 0

                    VV(j+(i-1)*xx)=1;
                else
                end

            end

        end

        Vi=matriz(matriz>0);
        Vh=matrizbranco(matrizbranco>0);


end % end switch case
```

```
if write==0

   % xlswrite('dados_entrada.xlsx',matriz,'Folha2')
    %xlswrite('dados_entrada.xlsx',matrizbranco,'Folha3')
  %  xlswrite('dados_entrada.xls',Vi,'Folha1','B2')
   % xlswrite('dados_entrada.xls',Vh,'Folha1','C2')
    %xlswrite('dados_entrada.xls',Vi-Vh,'Folha1','D2')
   % xlswrite('dados_entrada.xlsx',matriz-
matrizbranco,'Folha4','B2')
else
end


toc
end
```

LabVIEW® Codes

Similarly to the MATLAB® codes the LabVIEW® code present here are an improved version by Bruno Branco on the initial code by the author of this thesis.

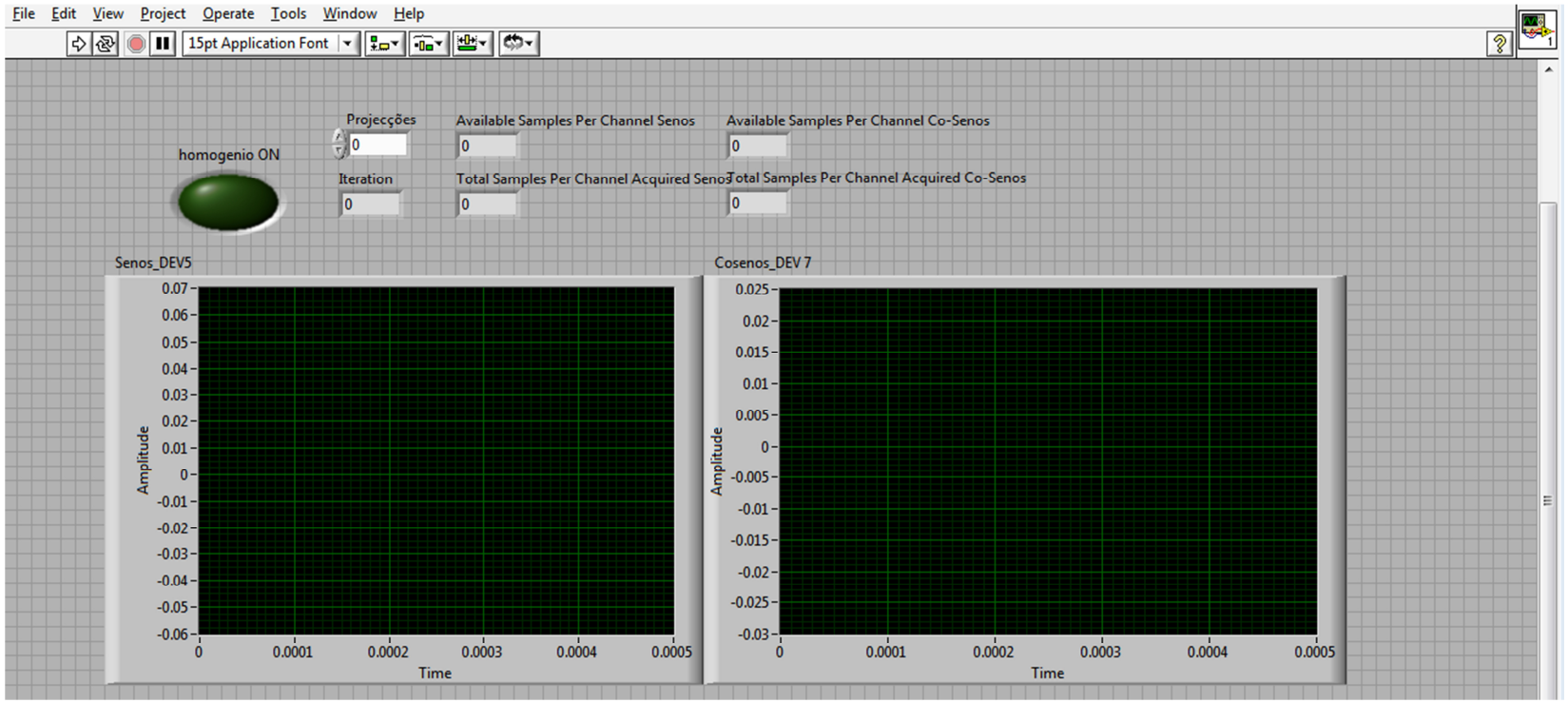

Figure B1 – Front Panel image.

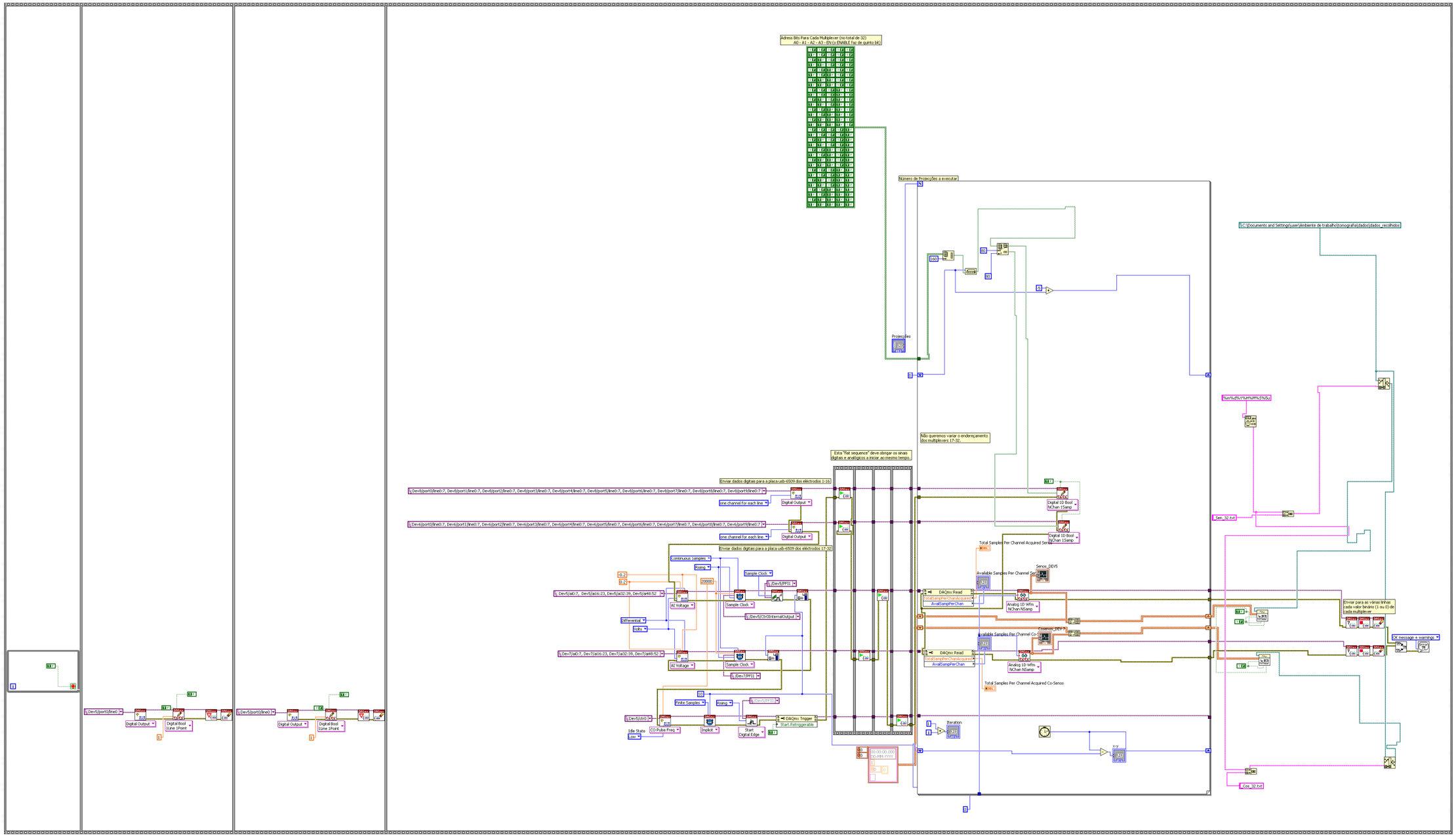

Figure B2 – Block Diagram code.

APPENDIX C – PARTICLE SIZE ANALYSIS

In the numerical studies depicted in this thesis using the Mixture Model it was assumed that the particle size distributions were very narrow and thus a discrete value would suffice. So for the numerical studies involving the 0.1-0.2 and 0.4-0.6 mm particles mean values of 0.15 and 0.5 mm were assumed, respectively. To ascertain on the validity of this assumption, a Mastersizer 2000 provided by Malvern Instruments®, was applied in the particle size characterization depicted in this supplementary material. The analysis from the Mastersizer 2000 for both 0.1-0.2 and 0.4-0.6 mm particles are presented below.

0.1-02 mm particles

The 148.771 μm value shown in Figure C.1 validates the mean value assumption of about 0.15 mm value in the numerical studies for the 0.1-0.2 mm particles.

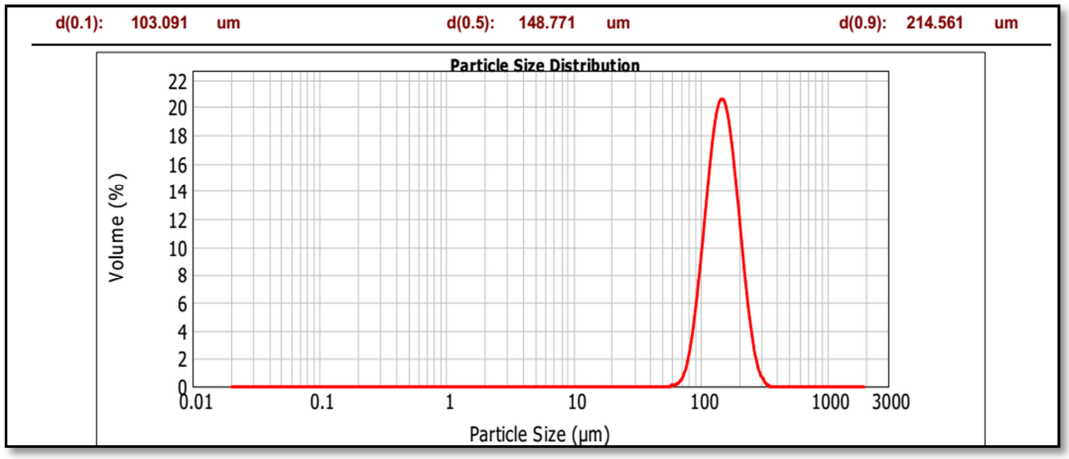

Figure C.1 – Mastersizer 2000 profile for the 0.1-0.2 mm particles.

Additionally, in Table C.1 it can be seen that the distribution of particles is centred on the 150 μm value.

Table C.1 – Volume fraction per particle sizes for the 0.1-0.2 mm particles.

Size (µm)	Volume In %	Size (µm)	Volume In %
11.482	0.00	120.226	16.68
13.183	0.00	138.038	18.61
15.136	0.00	158.489	17.01
17.378	0.00	181.970	12.63
19.953	0.00	208.930	7.52
22.909	0.00	239.883	3.36
26.303	0.00	275.423	0.93
30.200	0.00	316.228	0.02
34.674	0.00	363.078	0.00
39.811	0.00	416.869	0.00
45.709	0.00	478.630	0.00
52.481	0.00	549.541	0.00
60.256	0.11	630.957	0.00
69.183	0.80	724.436	0.00
79.433	3.08	831.764	0.00
91.201	7.04	954.993	0.00
104.713	12.21	1096.478	0.00
120.226		1258.925	0.00

0.4-06 mm particles

The 495.636 µm value shown in Figure C.2 validates the mean value assumption of about 0.5 mm value in the numerical studies for the 0.4-0.6 mm particles.

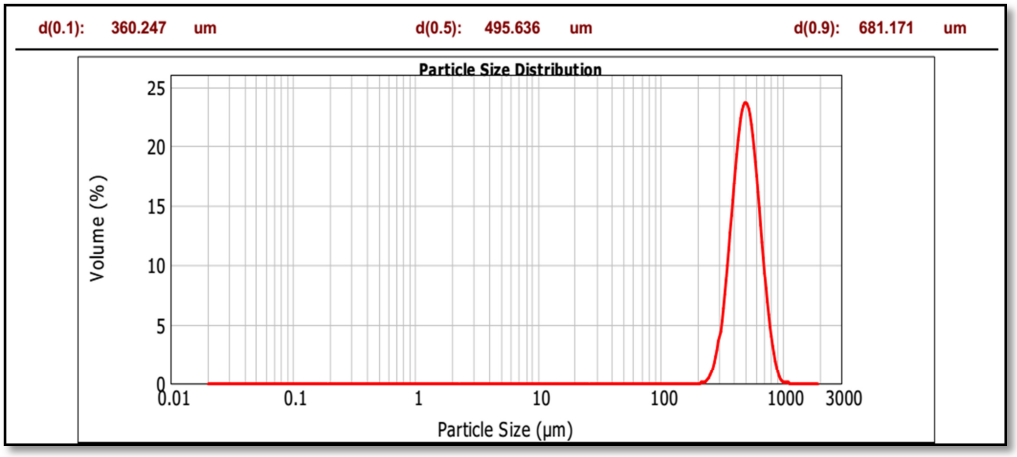

Figure C.2 – Mastersizer 2000 profile for the 0.4-0.6 mm particles.

Additionally, in Table C.2 it can be seen that the distribution of particles is centred on the 500 µm value.

Table C.2 – Volume fraction per particle sizes for the 0.4-0.6 mm particles

Size (µm)	Volume In %
120.226	0.00
138.038	0.00
158.489	0.00
181.970	0.00
208.930	0.02
239.883	0.52
275.423	2.64
316.228	7.42
363.078	14.10
416.869	19.83
478.630	21.22
549.541	17.41
630.957	10.75
724.436	4.75
831.764	1.23
954.993	0.08
1096.478	0.00
1258.925	

APPENDIX D – BUOYANT PARTICLES 3D SIMULATIONS

TURBULENCE SCALES ANALYSIS

3D Numerical Results

Analogously to the 2D study, the turbulence scales influence on a 3D fully developed homogenous flow was evaluated by calculating pressure drop (deviations from experimental values are displayed in parenthesis, ΔExp), mixture velocity, turbulent kinetic energy and turbulent dissipation rate.

The results are grouped in Table D1:

Table D1 – Influence of the different turbulence scales on the numerical turbulence variables and comparison between the experimental and numerical pressure drops for the 3D numerical studies

			1 m. s^{-1}			**4 m. s^{-1}**		
Case	I_T	L_T	ΔP (Pa) ΔExp	k (m^2.s^{-2})	ε (m^2.s^{-3})	ΔP (Pa) ΔExp	k (m^2.s^{-2})	ε (m^2.s^{-3})
1	0.04126	0.0036560	755.14 (4.10%)	0.00890	0.5721	8151.7 (-11.63%)	0.0965	66.401
2	0.04000	0.0003000	757.07 (3.86%)	0.00900	0.5721	8152.0 (-11.63%)	0.0966	66.927
3	0.04000	0.0000464	765.03 (2.85%)	0.00890	0.5857	8152.2 (-11.63%)	0.0968	66.740

Similarly to the two dimensional studies in Section 5.5, for all the three Cases the sharpest variations in k and in ε occur at the pipe wall. The corresponding profiles are presented in Figures D1 to D3, for two flow velocities. Figure D4 represents cross-sectional images of the turbulent parameters profiles, k and ε, for a flow velocity of 4 m. s^{-1}.

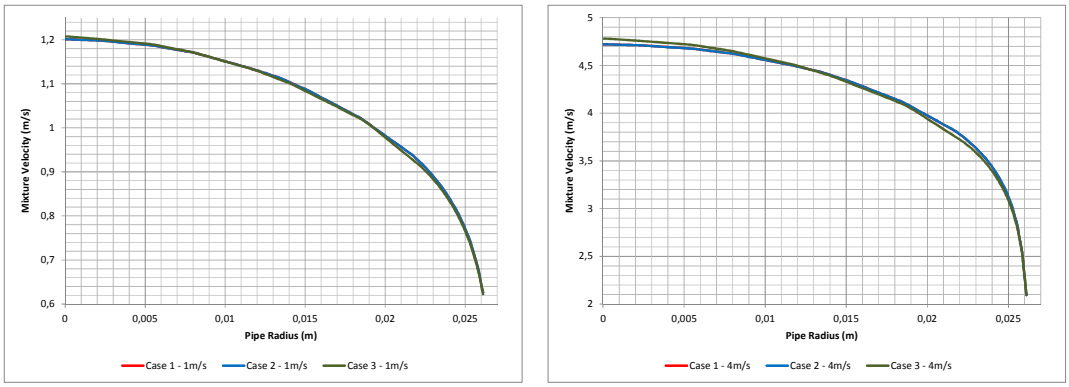

Figure D1 – 3D mixture velocity for Case 1, 2 and 3 along the pipe radius for a flow velocity of 1 m. s^{-1} (Left) and 4 m. s^{-1} (Right).

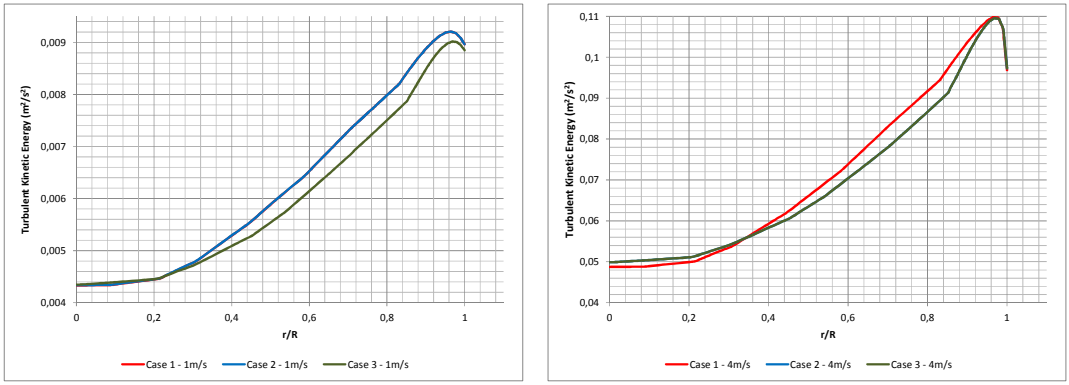

Figure D2 – 3D turbulent kinetic energy for Case 1, 2 and 3 along the pipe radius for a flow velocity of 1 m. s^{-1} (Left) and 4 m. s^{-1} (Right).

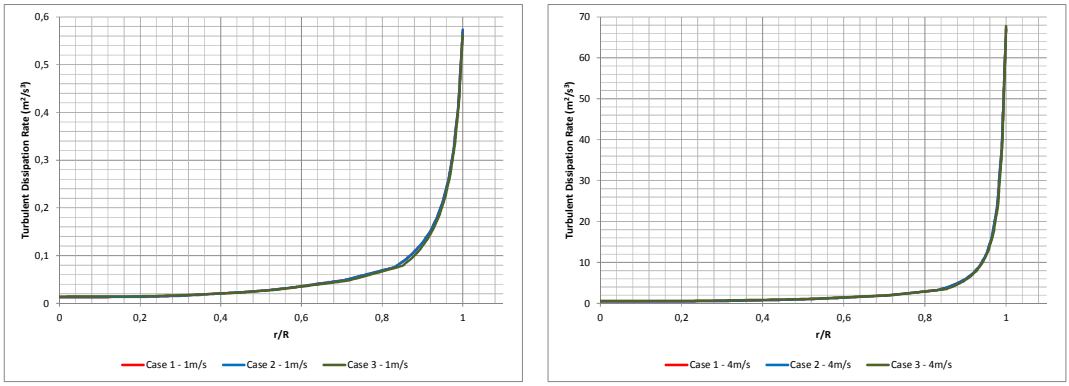

Figure D3 – 3D turbulent dissipation rate for Case 1, 2 and 3 along the pipe radius for a flow velocity of 1 m. s^{-1} (Left) and 4 m. s^{-1} (Right).

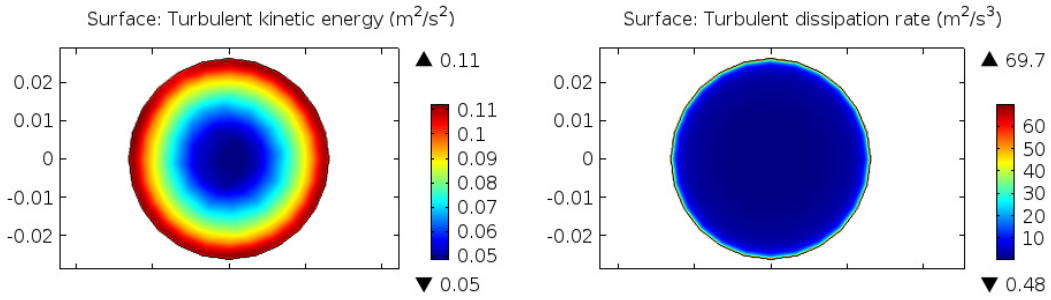

Figure D4 – Cross sectional images of the 3D turbulent kinetic energy (Left) and turbulent dissipation rate for Case 2 for a flow velocity of 4 m. s^{-1}.

From Table D1 it can be observed that the influence on the calculated pressure drop with varying the turbulence scales is almost negligible. Comparing the pressure drop values obtained with the two and three dimensional simulations for a flow velocity of 1 m. s^{-1} it can verified that the values are very similar, but for a flow velocity of 4 m. s^{-1} a slight increase of about 560 Pa occurs for the 3D study. This increase, 7.4%, is negligible and can be attributed both to the vertical pressure gradient resultant from the gravity force inclusion in the three dimensional numerical studies and to additional numerical diffusion, which is typical for higher velocities flows where turbulence also increases.

The differences between the turbulent kinetic energy values are very small for the two and three dimensional studies, for both flow velocities. The energy dissipation rate values are also similar for the two simulation strategies, for a flow velocity of 1 m. s^{-1}, but a larger difference is noted when comparing the results for the flow velocity of 4 m. s^{-1}, where an increase of about 20% is observable between the two dimensional and the three dimensional simulations. This is in-line with the calculated pressure drop increase witnessed, for the three dimensional simulations, for the higher velocity, and can be attributed to the aforementioned causes.

CLOSURE COEFFICIENTS ANALYSIS

3D Numerical Results

In a similar fashion to the 2D study, the influence of an increase of 20% in the

Table D2 – Comparison between the simulated 3D results for Case 2 and for a 20% increase in the closure coefficients.

	$1\ m.s^{-1}$					
	ΔP (Pa) ΔExp	**ΔP (Pa)** $\Delta Case2$	k **(m².s⁻²)**	k **(m².s⁻²)** $\Delta Case2$	ε**(m².s⁻³)**	ε**(m².s⁻³)** $\Delta Case2$
Case 2	777.07 (1.32)	--	0.009899	--	0.5476	--
$C_{\varepsilon 1}$**+ 20%**	638.01 (18.98)	17.90	0.008097	18.20	0.3679	32.82
$C_{\varepsilon 2}$**+ 20%**	888.64 (12.85)	14.36	0.011400	15.16	0.7242	32.25
σ_ε**+ 20%**	811.93 (3.11)	4.490	0.010300	4.050	0.5989	9.370
σ_k**+ 20%**	788.53 (0.14)	1.470	0.010100	2.030	0.5662	3.400
C_μ**+ 20%**	798.29 (1.38)	2.730	0.009954	0.550	0.5652	3.210
σ_t**+ 20%**	787.8 (0.05)	1.380	0.010000	1.020	0.5641	3.010
	$4\ m.s^{-1}$					
	ΔP (Pa) Dev_{Exp} **(%)**	**ΔP (Pa)** Dev_{Case2} **(%)**	k **(m².s⁻²)**	k **(m².s⁻²)** Dev_{Case2} **(%)**	ε**(m².s⁻³)**	ε**(m².s⁻³)** Dev_{Case2} **(%)**
Case 2	8151.7 (11.62)	--	0.0966	--	66.927	--
$C_{\varepsilon 1}$**+ 20%**	6474.8 (11.34)	20.57	0.0783	18.94	35.289	47.27
$C_{\varepsilon 2}$**+ 20%**	9753.5 (33.56)	19.65	0.1131	17.08	89.929	34.37
σ_ε**+ 20%**	8330.7 (14.08)	2.196	0.0969	0.311	66.938	0.016
σ_k**+ 20%**	8170.1 (11.88)	0.226	0.0954	1.242	64.919	3.000
C_μ**+ 20%**	8427.0 (15.40)	3.377	0.0971	0.518	66.747	0.268
σ_t**+ 20%**	8152.0 (11.63)	0.004	0.0953	1.346	62.367	6.813

standard value of the closure coefficients was evaluated for a 3D fully

developed homogenous flow and the results are presented in Table D2, where the pressure drop values and their deviation from the experimental values (ΔExp) are presented in the second column and the pressure drop, turbulent kinetic energy and turbulent dissipation rate deviations from the reference case ($\Delta Case2$), Case 2, are presented in columns 3, 5 and 7 respectively.

The behaviour observed for the 3D simulation closure coefficient analysis, is consistent with the previous two dimensional studies. Comparison of Table 5.7 and Table D2 shows that the effect of the closure coefficients $C_{\varepsilon 1}$ and $C_{\varepsilon 2}$ is more notorious on the pipe wall values of k and ε. As was the case for the two-dimensional study, the production and production-dissipation terms of Equations 4.67 and 4.68 dominate over the remaining terms, for the same pipe flows. Still, at the lower velocity, the influence of changes on the other closure coefficients (σ_ε, σ_k, $C_\mu$and σ_t) on the flow parameters, is more pronounced for the 3D simulation than for the 2D simulation. Observing Equations 4.67 and 4.68, it can be seen that the closure coefficients, σ_ε, σ_k, C_μ are directly related with the gradient operator which, jointly with the aforementioned inclusion of the gravity force and additional numerical diffusion could, support the observable differences between the two and three-dimensional studies. The turbulent Schmidt Number, σ_T, is linked to the turbulent eddy viscosity, to the mixture density and to spatial variation of the solid volumetric concentration (Equation 4.49); although for homogeneous flows the mixture density and distribution of particles may not be significant, the turbulent eddy viscosity will vary throughout the pipe section and thus could be the reason for the discrepancies between the two and three-dimensional studies. From Figures 5.9 and D5, and for both 2D and 3D studies, the boundary layer has increased substantially when increasing $C_{\varepsilon 1}$. Moreover, when $C_{\varepsilon 2}$ increases the absolute values of k and ε in the boundary layer increase as well.

In a similar way to the 2D study, an increase in the σ_ε value influences the diffusive term and the turbulent dynamic viscosity, causing a slight increase in the production and dissipation of turbulence (see Figure D6).

The 2D and 3D results regarding the Schmidt Turbulent number (σ_T) variation are consistent. This is the parameter with an overall lower influence on the flow parameters (see Figure D7).

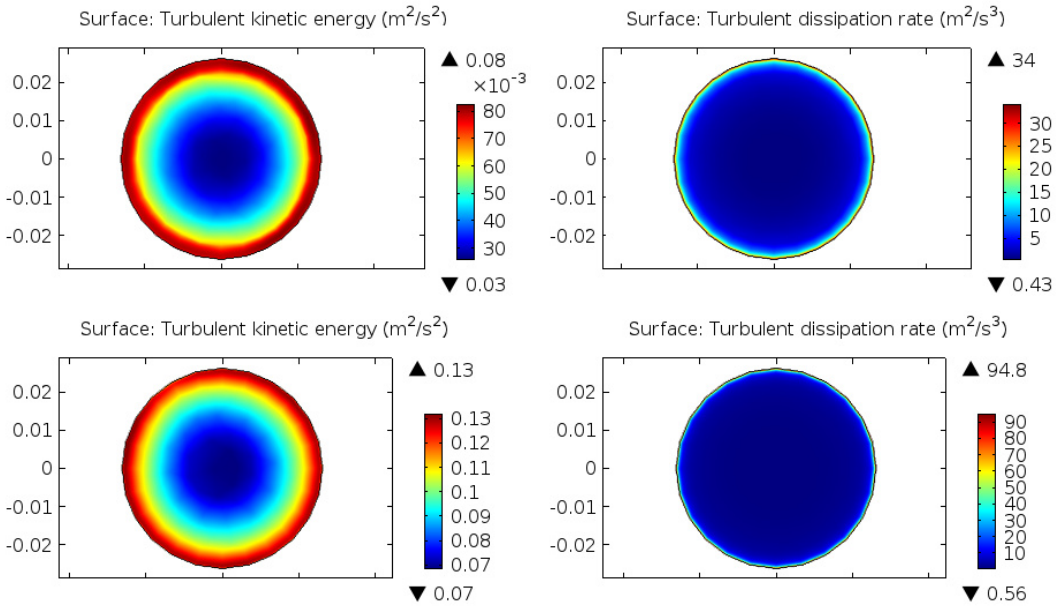

Figure D5 – Pipe cross section profile of the 3D Turbulent Kinetic Energy (Left) and Turbulent Dissipation Rate (Right) for an increase of 20% in the standard value of $C_{\varepsilon 1}$ (Top) and $C_{\varepsilon 2}$ (Bottom) for a flow velocity of 4 m. s^{-1}.

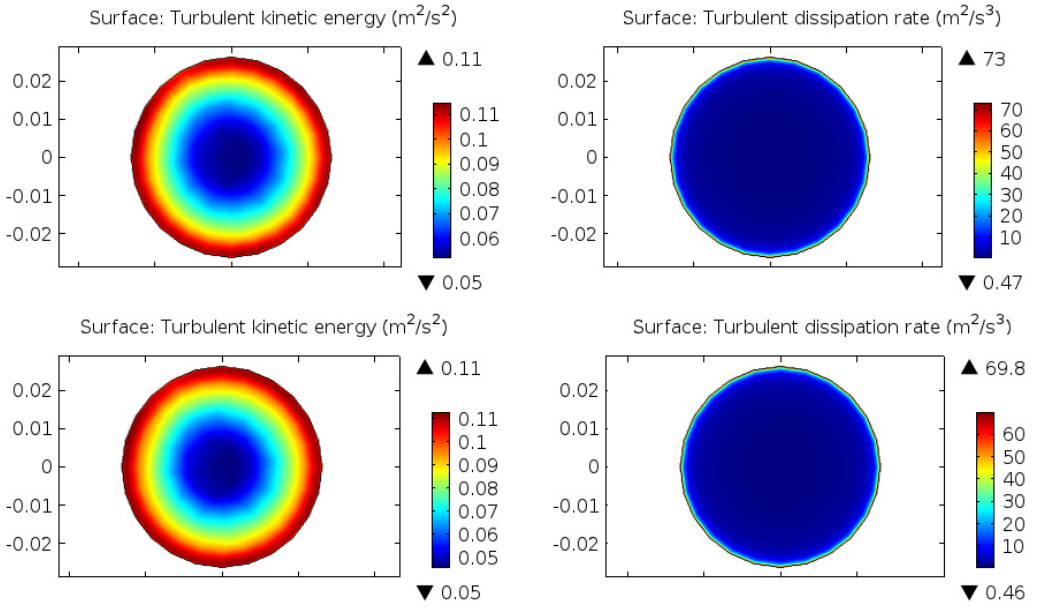

Figure D6 – Pipe cross section profile of the 3D Turbulent Kinetic Energy (Left) and Turbulent Dissipation Rate (Right) for an increase of 20% in the standard value of σ_ε (Top) and σ_k (Bottom) for a flow velocity of 4 m. s^{-1}.

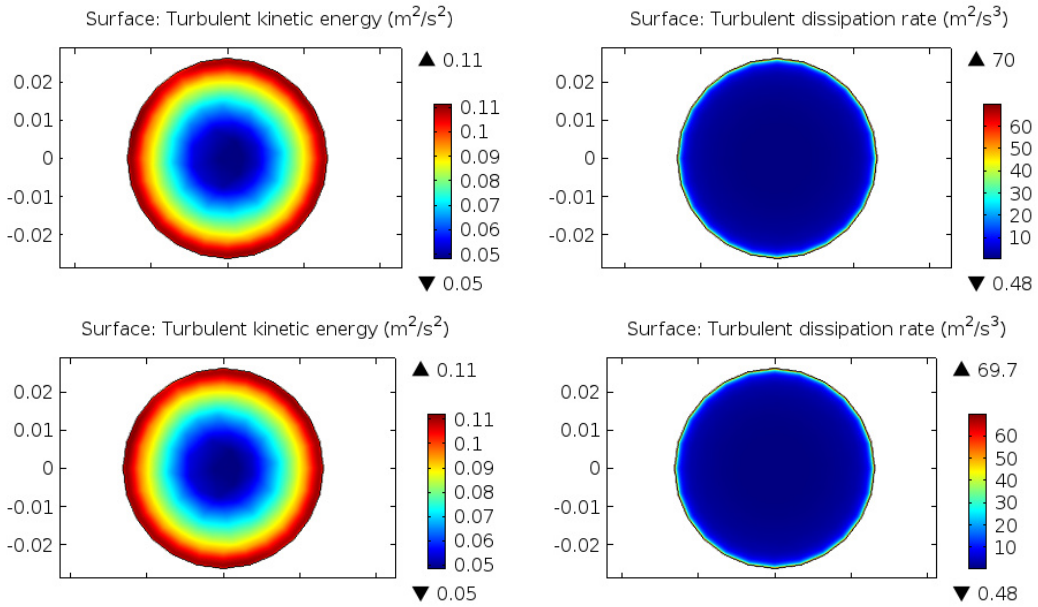

Figure D7 – 3D Turbulent Kinetic Energy (Left) and Turbulent Dissipation Rate (Right) for an increase of 20% in the standard value of C_μ (Top) and σ_t (Bottom) for a flow velocity of 4 m. s^{-1}.

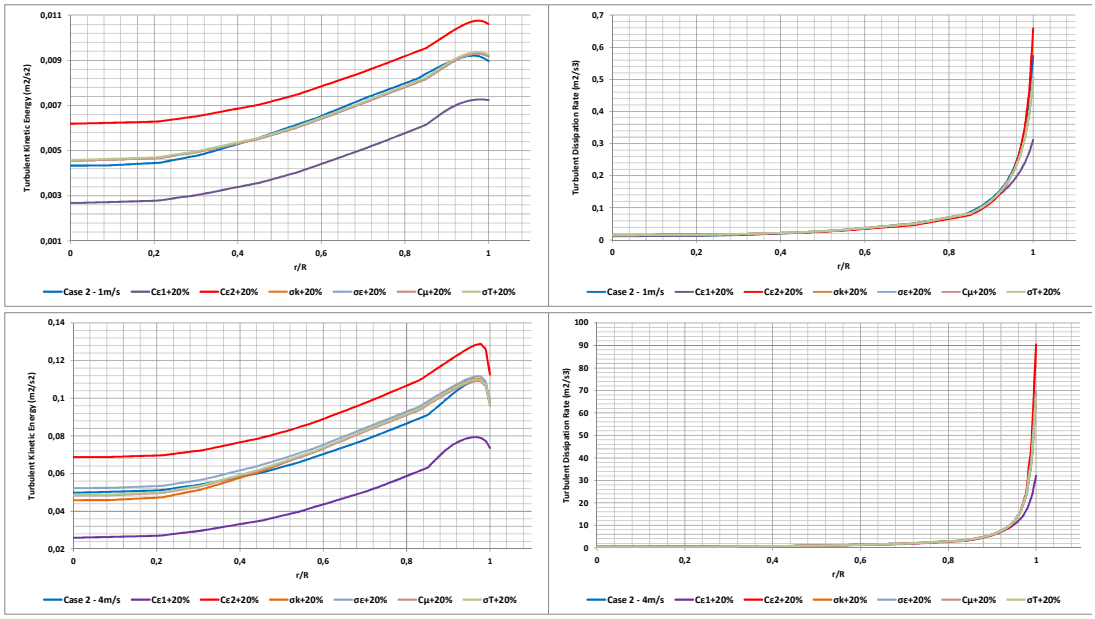

Figure D8 – 3D Turbulent Kinetic Energy (Left) and Turbulent Dissipation Rate (Right) for all closure coefficients for a flow velocity of 1 m. s^{-1} (Top) and 4 m. s^{-1} (Bottom).

Analogously to the 2D numerical results, the increase of 20% in the closure coefficients was studied, for the 3D numerical studies and presented in Table D2 and Figures D5 to D8, for the flow velocity of 1 m. s^{-1} it is shown that

increasing $C_{\varepsilon 1}$ and $C_{\varepsilon 2}$ deviates the pressure drop values (our control variable) further from the experimental results. For this velocity the impact of the closure coefficients, σ_ε, σ_k, C_μ and σ_t was also negligible. Again, and as observed for the 2D studies, for $4\,\mathrm{m.s^{-1}}$ the deviation on the calculated pressure drop, when the values of all closure coefficients were larger, increased, with the exception of the calculations with a higher $C_{\varepsilon 1}$ which maintained roughly the same pressure drop value. This can be explained by Figure D8, where we can see that the kinetic energy nearly tripled its values with the variation of $C_{\varepsilon 2}$, while the dissipation rate also increased at the wall: bearing in mind the connection between $C_{\varepsilon 2}$ and the ratio ε^2/k described by Equation 4.68, the observed increase is not a surprise. Overall, it does seem that the standard closure coefficients values, which were initially optimized for single phase-flows, are the adequate choice for homogeneous solid-liquid flows as previously observed in the 2D studies.

APPENDIX E – CONFERENCE AND JOURNAL PUBLICATIONS

In this Appendix are presented the scientific conference and journal publications resulting from the study depicted in this thesis.

Conferences Presentations

(2014) Comparison of Mixture Model Simulations with Experimental Solid-liquid Suspension Flow Data, R.Silva, Fernando A.P. Garcia, Pedro Faia, Maria Graça Rasteiro, IFPSS 15 - 15th International Freight Pipeline Society Symposium 2014, Prague, Czech Republic.

(2014) Using COMSOL Multiphysics to Describe Solid/Liquid Flows, M G Rasteiro, F A P Garcia, P M Faia, R Silva, Iberian COMSOL Multiphysics Conference 2014, Málaga, Spain.

(2014) Application of different low-Reynolds k-ε turbulence models to model the flow of concentrated pulp suspensions in pipes, Carla Cotas, Rui Silva, Fernando Garcia, Pedro Faia, Dariusz Asendrych, Maria Graça Rasteiro, WCPT 7 - 7th World Congress on Particle Technology (WCPT7), Beijing, China.

(2014) Particle Distribution Studies in Highly Concentrated Solid-Liquid Flows in pipes using the Mixture Model, R Silva, C Cotas, F A P Garcia, P M Faia, M G Rasteiro, WCPT 7 - 7th World Congress on Particle Technology (WCPT7), Beijing, China.

(2013) Numerical Studies of Solid-Liquid Turbulent Pipe Flow of Settling Suspensions, R. Silva, F. A. P. Garcia, P. M. Faia, M. G. Rasteiro, 9th World Congress of Chemical Engineering (WCCE9), 18-23 August 2013, Coex, Seoul, Korea.

(2012) Modelling Solid-Liquid Flow in Pipes Using CFD: Study of the Effect of Turbulence Modification, R. Silva, F. A. P. Garcia, M. Faia, M. G. Rasteiro, 07th International Conference for Conveying and Handling of Particulate Solids (CHoPS 2012) 10 – 13 September 2012, Friedrichshafen/Germany.

(2011) Imagens Tomográficas de Impedância Eléctrica para Avaliação da Distribuição de Fases em Escoamentos Sólido-Líquido, R. Silva, P. M. Faia, M. G. Rasteiro, F. A. P. Garcia, A. R. Ferreira, M. J. Santos, J. B. Santos, A. P. Coimbra,

Congresso de Métodos Numéricos em Engenharia - CMNE 2011, Coimbra, Portugal 14 – 17 Junho.

(2010) Imaging particulate multiphase flow with Electrical Impedance Tomography, P. Faia, R. Silva, M. G. Rasteiro, A. R. Ferreira, J. B. Santos, M. J. Santos, F. A. P. Garcia, A. P. Coimbra, WCPT6 – World Congress Of Particle Technology, Nuremberg, Germany 26.-29. April 2010.

(2009) Models for complex slurry data prediction based on Electrical Impedance Imaging, R. Silva, P.M. Faia, M.G. Rasteiro, F.A. Garcia, A.R. Ferreira, M.J. Santos, J.B. Santos, A.P. Coimbra, Congreso de Métodos Numéricos en Ingeniería, Barcelona, pg.243.

(2009) Sistema Automático de Tomografia de Impedância Complexa para Estudo de Escoamento de Suspensões Sólido-Líquido, R. Silva, H. Costa, P.M. Faia, M.G. Rasteiro, F.A. Garcia, A.R. Ferreira, M.J. Santos, J.B. Santos, Fórum END - 1ª Conferência Nacional em Ensaios Não Destrutivos, Tema: Aplicações de END na Indústria e Desenvolvimentos Tecnológicos Emergentes, 4 de Dezembro de 2009, Instituto de Soldadura e Qualidade -Auditório do Edifício A Taguspark - Avª Prof. Dr. Cavaco Silva, nº 33, Porto Salvo, Portugal.

Journal Publications

(2015) Particle Distribution Profiles of Settling Suspensions Pipe Flow using EIT: comparison with numerical data from the Mixture Model., R. Silva, F. A. P. Garcia, P. Faia, M. G. Rasteiro, Flow Measurement and Instrumentation **(in Preparation).**

(2015) Validating Settling Suspensions Numerical Data through MRI, UPV and EIT measurements., R. Silva, F. A. P. Garcia, P. Faia, M. G. Rasteiro, Paul Krochak, Fredrik Lundell, Measurement Science and Technology **(in Preparation).**

(2015) Evaluating the performance of the Mixture Model coupled with a High and a Low Reynolds Turbulence Closure in the numerical descriptionn of Concentrated Solid-Liquid Flows of Settling Particles, R. Silva, F. A. P. Garcia, P. Faia, M. G. Rasteiro, International Journal of Multiphase Flow **(in Preparation).**

(2015) Validation of Mixture Model Simulations of Settling Suspensions with

Experimental Solid-Liquid Flow Data, R. Silva, F. A. P. Garcia, P. Faia, M. G. Rasteiro, Journal of Hydrology and Hydromechanics/IFPSS 15 Special Issue **(In Review)**

(2015) Modelling solid-liquid homogeneous turbulent flow of neutrally buoyant particles using the Mixture Model: a study on the length scales and closure coefficients, R. Silva, F. A. P. Garcia, P. Faia, M. G. Rasteiro, Multiphase Science and Technology **(in Press)**

(2015) Particle Distribution Studies in Highly Concentrated Solid-Liquid Flows in Pipe using the Mixture Model, R. Silva, F. A. P. Garcia, P. Faia, M. G. Rasteiro, Procedia Engineering /WCPT7 Special Issue **(In Press)**

(2015) Settling Suspensions Flow Modelling: A Review, Rui Silva, Fernando A. P. Garcia, Pedro M. G. M. Faia, Maria G. Rasteiro, KONA Powder and Particle Journal No.32 (2015)

(2012) Imaging particulate two-phase flow in liquid suspensions with Electric Impedance Tomography, P. M. Faia, R. Silva, M. G. Rasteiro, F. A. P. Garcia, A. R. Ferreira, M. J. Santos, J. B. Santos, A. P. Coimbra, Particulate Science and Technology, 30: 329–342, 2012

(2011) Electrical Tomography: a review of configurations and applications to particulate processes, M. G. Rasteiro, R. Silva, F. A. P. Garcia, P. M. Faia, KONA Powder and Particle Journal No.29, pp. 67-80.

BIBLIOGRAPHY

Abbott, JR, N Tetlow, AL Graham, SA Altobelli, E Fukushima, LA Mondy, and TS Stephens. 1991. "Experimental Observations of Particle Migration in Concentrated Suspensions: Couette Flow." *Journal of Rheology* 35 (5): 773.

Abouelwafa, MSA, and EJM Kendall. 1979. "Optimization of Continuous Wave Nuclear Magnetic Resonance to Determine in Situ Volume Fractions and Individual Flow Rates in Two Component Mixtures." *Review of Scientific Instruments* 50 (12): 1545–49.

Abulnaga, B. 2002. *Slurry Systems Handbook*. 1st ed. New York: McGraw-Hill Professional.

Adams, JFW, M Fairweather, and J Yao. 2011. "Modelling and Simulation of Particle Re-Suspension in a Turbulent Square Duct Flow." *Computers & Chemical Engineering*. Elsevier Ltd.

Aidun, CK, and JR Clausen. 2010. "Lattice-Boltzmann Method for Complex Flows." *Annual Review of Fluid Mechanics* 42 (1): 439–72.

Altobelli, S, R Givler, and E Fukushima. 1991. "Velocity and Concentration Measurements of Suspensions by Nuclear Magnetic Resonance Imaging." *Journal of Rheology* 35: 721.

Amundson, KR, JA Reimer, and MM Denn. 1991. "Investigation of Microstructure in Poly[(p-Hydroxybenzoic Acid)-Co-(ethylene Terephthalate)] Using Nuclear Magnetic Resonance Spectroscopy." *Macromolecules* 24 (11): 3250–60.

Andersson, HI. 1996. "Flows Dominated by Centrifugal and Coriolis Forces - A Survey of EUROMECH 336." *Fluid Dynamics Research*.

Ariyaratne, C. 2005. "Design and Optimisation of Swirl Pipes and Transition Geometries for Slurry Transport." University of Nottingham.

Arko, A, R Waterfall, M Beck, T. Dyakowski, P Sutcliffe, and M Byars. 1999. "Development of Electrical Capacitance Tomography for Solids Mass Flow Measurement and Control of Pneumatic Conveying Systems." In *1st World Congress on Industrial Process Tomography*, 140–46. Buxton, Greater Manchester.

Arnesen, AJ. 2010. "Comparison of Finite Element Methods for the Navier-Stokes Equations." University of Oslo.

Aziz, A Al, and H Mohamed. 2013. "A Study of the Factors Affecting Transporting Solid-Liquid Suspension through Pipelines." *Open Journal of Fluid Dynamics* 2013 (September): 152–62.

Bagnold, R. 1954. "Experiments on a Gravity-Free Dispersion of Large Solid Spheres in a Newtonian Fluid under Shear." *Proceedings of the Royal Society A: Mathematical, Physical and Engineering Sciences* 225 (1160): 49–63.

Bagnold, RA. 1966. "An Approach to the Sediment Transport Problem from General Physics." In *The Physics of Sediment Transport by Wind and Water*, 231–91.

Bakker, A. 2006. "Lecture 5 - Solution Methods Applied Computational Fluid Dynamics."

Balachandar, S, and JK Eaton. 2010. "Turbulent Dispersed Multiphase Flow." *Annual Review of Fluid Mechanics* 42 (1): 111–33.

Banavar, JR, and LM Schwartz. 1989. "Probing Porous Media with Nuclear Magnetic Resonance." In *Molecular Dvnamics in Restricted Geometries*, 273. New York: Wiley.

Barber, D, and B Brown. 1984. "Applied Potential Tomography." *Journal of Physics. E. Scientific Instruments*, no. 17: 723.

Bardow, A, CH Bischof, H Martin Bücker, G Dietze, R Kneer, A Leefken, W Marquardt, U Renz, and E Slusanschi. 2008. "Sensitivity-Based Analysis of the K-Ep Model for the Turbulent Flow between Two Plates." *Chemical Engineering Science* 63 (19): 4763–75.

Barnes, HA. 2000. *A Handbook of Elementary Rheology*. University of Wales,Institute of Non-Newtonian Fluid Mechanics.

Bartosik, A. 2010. "Simulation of Turbulent Flow of a Fine Dispersive Slurry." *Chemical and Process Engineering* 31 (1): 67–80.

Bartosik, A. 2011. "Mathematical Modelling of Slurry Flow with Medium Solid Particles." In *2nd International Conference on Mathematical Models for Engineering Science*, 124–29.

Batchelor, G. 1982. "Sedimentation in a Dilute Polydisperse System of Interacting Spheres. Part 1. General Theory." *Journal of Fluid Mechanics* 119: 379–408.

Batchelor, G, and C Wen. 1982. "Sedimentation in a Dilute Polydisperse System of Interacting Spheres. Part 2. Numerical Results." *Journal of Fluid Mechanics* 124: 495–582.

Bayford, RH. 2006. "Bioimpedance Tomography (electrical Impedance Tomography)." *Annual Review of Biomedical Engineering* 8 (January): 63–91.

Beck, M, and R Williams. 1996. "Process Tomography: A European Innovation and Its Applications." *Measurement Science and Technology* 7: 215.

Beck, M, and RA Williams. 1995. *Process Tomography: Principles, Techniques and Applications*. Edited by Butterworth-Heinemann.

Beck, MS, E Campogrande, M Morris, RA Williams, and RC Waterfall. 1993. *Tomographic Techniques for Process Design and Operation*. Computational Mechanics Publications.

Bennett, MA, RM West, SP Luke, and RA Williams. 2002. "The Investigation of Bubble Column and Foam Processes Using Electrical Capacitance Tomography." *Minerals Engineering* 15 (4): 225–34.

Blümler, P, and B Blümich. 1992. "Magnetization Filters: Applications to NMR Imaging of Elastomers." *Magnetic Resonance Imaging* 10 (5): 779–88.

Bohnet, M, and O Triesch. 2003. "Influence of Particles on Fluid Turbulence in Pipe and Diffuser Gas-Solids Flow." *Chemie-Ingenieur-Technik* 75 (75): 850–57.

Bonn, D, S Rodts, M Groenink, S Rafaï, N Shahidzadeh-Bonn, and P Coussot. 2008. "Some Applications of Magnetic Resonance Imaging in Fluid Mechanics: Complex Flows and Complex Fluids." *Annual Review of Fluid Mechanics* 40 (1): 209–33.

Boonkhao, B, RF Li, XZ Wang, RJ Tweedie, and K Primrose. 2011. "Making Use of Process Tomography Data for Multivariate Statistical Process Control." *AIChE Journal* 57 (9): 2360–68.

Borhani, N. 2010. *ERCOFTAC Bulletin 82*. *ERCOFTAC*. Lausanne.

Borsic, A, W Lionheart, and N Polydorides. 2004. "Part 1 of Electrical Impedance Tomography: Methods, History and Applications." In *Electrical Impedance Tomography: Methods, History and Applications*, edited by DS Holder, 3–64.

Boyle, A, and A Adler. 2010. "Electrode Models under Shape Deformation in Electrical Impedance Tomography." *Journal of Physics: Conference Series* 224 (April): 012051.

Bredberg, J. 2000. *On the Wall Boundary Condition for Turbulence Models*. *Internal Report 00/4 Department of Thermo and Fluid Dynamics CHalmers University Of Technology. Goteborg, Sweden.*

Brennen, C. 2005. *Fundamentals of Multiphase Flow*. 1st Ed. Cambridge: Cambridge University Press.

Capecelatro, J, and O Desjardins. 2013. "Eulerian–Lagrangian Modeling of Turbulent Liquid–Solid Slurries in Horizontal Pipes." *International Journal of Multiphase Flow* 55 (October): 64–79.

Caprihan, A, and E Fukushima. 1990. "Flow Measurements by NMR." *Physics Reports* 198 (4): 195–235.

Cebeci, T. 2004. *Analysis of Turbulent Flows with Computer Programs*. Elsevier.

Chan Kim, M, K Youn Kim, K Jin Lee, Y Joo Ko, and S Kim. 2005. "Electrical Impedance Imaging of Phase Boundary in Two-Phase Systems with Adaptive Mesh Regeneration Technique." *International Communications in Heat and Mass Transfer* 32 (7): 954–63.

Chemloul, NS, K Chaib, and K Mostefa. 2009. "Simultaneous Measurements of the Solid Particles Velocity and Concentration Profiles in Two Phase Flow by Pulsed Ultrasonic Doppler Velocimetry." *Journal of the Brazilian Society of Mechanical Sciences and Engineering* 31 (4): 333–43.

Chen, L, Y Duan, W Pu, and C Zhao. 2010. "CFD Simulation of Coal-Water Slurry Flowing in Horizontal Pipelines." *Korean Journal of Chemical Engineering* 26 (4): 1144–54.

Chen, L, Q Kang, Y Mu, Y-L He, and W-Q Tao. 2014. "A Critical Review of the Pseudopotential Multiphase Lattice Boltzmann Model: Methods and Applications." *International Journal of Heat and Mass Transfer* 76 (September). Elsevier Ltd: 210–36.

Chen, P, MJ McCarthy, and R Kauten. 1989. "NMR for Internal Quality Evaluation of Fruits and Vegetables." *Transactions of the ASAE* 32 (5): 1747–53.

Chen, R. 1994. "Analysis of Homogeneous Slurry Pipe Flow." *Journal of Marine Science and Technology* 2 (1): 37–45.

Chen, S, and GD Doolen. 1998. "Lattice Boltzmann Method for Fluid Flows." *Annual Review of Fluid Mechanics* 30 (1). Annual Reviews 4139 El Camino Way, PO Box 10139, Palo Alto, CA 94303-0139, USA: 329–64.

Cheng, KS, D Isaacson, JC Newell, and DG Gisser. 1989. "Electrode Models for Electric Current Computed Tomography." *IEEE Transactions on Biomedical Engineering* 36 (9): 918–24.

Chmielewski, M, and M Gieras. 2013. "Three-Zonal Wall Function for K-E Turbulence Models." *Cmst.Eu* 19 (2): 107–14.

Chu, KW, B Wang, a. B Yu, and a. Vince. 2009. "CFD-DEM Modelling of Multiphase Flow in Dense Medium Cyclones." *Powder Technology* 193 (3). Elsevier B.V.: 235–47.

Chung, TJ. 2002. *Computational Fluid Dynamics*. Cambridge University Press.

Clift, R, J Grace, and M Weber. 2005. *Bubbles, Drops, and Particles*. Dover Publications.

COMSOL Multiphysics. 2012. "COMSOL Multiphysics User Guide Version 4.3.a." Stockholm, Sweden: COMSOL AB.

COMSOL Multiphysics. 2013. "COMSOL Multiphysics User Guide Version 4.4." Stockholm, Sweden: COMSOL AB.

Costa, J, L Oliveira, and D Blay. 1999. "Test of Several Versions for the K– E Type Turbulence Modelling of Internal Mixed Convection Flows." *International Journal of Heat and Mass Transfer* 42: 4391–4409.

Crowe, CT. 2000. "On Models for Turbulence Modulation in Fluid–particle Flows." *International Journal of Multiphase Flow* 26: 719–27.

Crowe, CT. 2005. *Multiphase Flow Handbook*. Edited by CT Crowe, E Michaelides, and JD Schwarzkopf. Boca Raton: CRC Press - Taylor & Francis Group.

Crowe, CT, TR Troutt, and JN Chung. 1996. "Numerical Models for Two-Phase Turbulent Flows." *Annual Review of Fluid Mechanics* 28 (1): 11–43.

Cundall, PA, and ODL Strack. 1979. "A Discrete Numerical Model for Granular Assemblies." *Géotechnique* 29 (1): 47–65.

Dickin, F, R Waterfall, and R Williams. 1992. "Tomographic Imaging of Industrial Process Equipment: Techniques and Applications." *Circuits, Devices and Systems, IEE Proceedings G* 139 (I): 72–82.

Donthi, S, and L Subramanyan. 2004. "Capacitance Based Tomography for Industrial Applications." In *M. Tech. Credit Seminar Report, Electronic Systems Group*, 1–19.

Doron, P, and D Barnea. 1995. "Pressure Drop and Limit Deposit Velocity for Solid-Liquid Flow in Pipes." *Chemical Engineering Science* 50 (10): 1595–1604.

Druzhinin, OA. 2001. "The Influence of Particle Inertia on the Two-Way Coupling and Modification of Isotropic Turbulence by Microparticles." *Physics of Fluids* 13 (2001): 3738–55.

Druzhinin, OA, and S Elghobashi. 1999. "On the Decay Rate of Isotropic Turbulence Laden with Microparticles." *Physics of Fluids* 11 (1999): 602.

Dyakowski, T, and AJ Jaworski. 2003. "Non-Invasive Process Imaging – Principles and Applications of Industrial Process Tomography." *Chemical Engineering & Technology* 26 (6): 697–706.

Dyakowski, T, G Johansen, BT Hjertaker, D Sankowski, V Mosorov, and J Wlodarczyk. 2006. "A Dual Modality Tomography System for Imaging Gas/Solids Flows." *Particle & Particle Systems Characterization* 23 (3-4): 260–65.

Dyverfeldt, P, A Sigfridsson, JE Kvitting, and T Ebbers. 2006. "Quantification of Intravoxel Velocity Standard Deviation and Turbulence Intensity by

Generalizing Phase-Contrast MRI." *Magnetic Resonance in Medicine : Official Journal of the Society of Magnetic Resonance in Medicine* 56 (4): 850–58.

Ekambara, K, RS Sanders, K Nandakumar, and JH Masliyah. 2009. "Hydrodynamic Simulation of Horizontal Slurry Pipeline Flow Using ANSYS-CFX." *Industrial & Engineering Chemistry Research* 48 (17): 8159–71.

Elghobashi, S, and GC Truesdell. 1993. "On the Two-Way Interaction between Homogeneous Turbulence and Dispersed Solid Particles. I: Turbulence Modification." *Physics of Fluids A: Fluid Dynamics* 5 (7): 1790.

Fangary, Y, R Williams, W Neil, J Bond, and I Faulks. 1998. "Application of Electrical Resistance Tomography to Detect Deposition in Hydraulic Conveying Systems." *Powder Technology*.

Felice, R Di, and R Kehlenbeck. 2000. "Sedimentation Velocity of Solids in Finite Size Vessels." *Chemical Engineering & Technology* 23: 1123–26.

Ferziger, J, and M Perić. 2002. *Computational Methods for Fluid Dynamics*. 3rd ed. Springer.

Fox, MD. 1978. "Multiple Crossed-Beam Ultrasound Doppler Velocimetry." *IEEE Transactions on Sonics and Ultrasonics* 25 (5): 281–86.

Fox, RO. 2012. "Large-Eddy-Simulation Tools for Multiphase Flows." *Annual Review of Fluid Mechanics* 44 (1): 47–76.

Fukushima, E. 1999. "Nuclear Magnetic Resonance as a Tool to Study Flow." *Annual Review of Fluid Mechanics* 31 (1): 95–123.

Gao, H, H Li, and L-P Wang. 2013. "Lattice Boltzmann Simulation of Turbulent Flow Laden with Finite-Size Particles." *Computers & Mathematics with Applications* 65 (2). Elsevier Ltd: 194–210.

Garrido, L, J Ackerman, WA Ellingson, and JD Weyand. 2008. "Determination of Binder Distribution in Green-State Ceramics by NMR Imaging." In *12th Annual Conference on Composites and Advanced Ceramic Materials, Part 2 of 2: Ceramic Engineering and Science Proceedings, Volume 9, Issue 9/10*. Hoboken, NJ, USA: John Wiley & Sons, Inc.

German, JB, and MJ McCarthy. 1989. "Stability of Aqueous Foams: Analysis Using Magnetic Resonance Imaging." *Journal of Agricultural and Food Chemistry* 37 (5): 1321–24.

Giguère, R, L Fradette, D Mignon, and P a. Tanguy. 2008. "Characterization of Slurry Flow Regime Transitions by ERT." *Chemical Engineering Research and Design* 86 (9): 989–96.

Gillies, RG, J Schaan, RJ Sumner, MJ McKibben, and CA Shook. 2000. "Deposition Velocities for Newtonian Slurries in Turbulent Flow." *The Canadian Journal of Chemical Engineering* 78 (4): 704–8.

Gillies, RG, CA Shook, and KC Wilson. 1991. "An Improved Two Layer Model for Horizontal Slurry Pipeline Flow." *The Canadian Journal of Chemical Engineering* 69 (1): 173–78.

Gillies, RG, CA Shook, and J Xu. 2004. "Modelling Heterogeneous Slurry Flows at High Velocities." *The Canadian Journal of Chemical Engineering* 82: 1060–65.

Gisser, DG, D Isaacson, and JC Newell. 1987. "Current Topics in Impedance Imaging." *Clinical Physics and Physiological Measurement* 8 (4A): 39–46.

Gladden, LF. 1994. "Nuclear Magnetic Resonance in Chemical Engineering: Principles and Applications." *Chemical Engineering Science* 49 (20): 3339–3408.

Goharian, M, M Soleimani, A Jegatheesan, K Chin, and GR Moran. 2008. "A DSP Based Multi-Frequency 3D Electrical Impedance Tomography System." *Annals of Biomedical Engineering* 36 (9): 1594–1603.

Graham, AL. 1991. "Note: NMR Imaging of Shear-Induced Diffusion and Structure in Concentrated Suspensions Undergoing Couette Flow." *Journal of Rheology*.

Grootveld, C. 1996. "Measuring & Modeling of Concentrated Settling Suspensions Using Electrical Impedance Tomography." Delft University Technology.

Guer, Y Le, P Reghem, I Petit, and B Stutz. 2003. "Experimental Study of a Buoyant Particle Dispersion in Pipe Flow." *Chemical Engineering Research ...* 81 (October): 1136–43.

Hadinoto, K. 2010. "Predicting Turbulence Modulations at Different Reynolds Numbers in Dilute-Phase Turbulent Liquid–particle Flow Simulations." *Chemical Engineering Science* 65 (19): 5297–5308.

Hadinoto, K, and JW Chew. 2010. "Modeling Fluid–particle Interaction in Dilute-Phase Turbulent Liquid–particle Flow Simulation." *Particuology* 8 (2). Chinese Society of Particuology: 150–60.

Hamidipour, M, and F Larachi. 2010. "Characterizing the Liquid Dynamics in Cocurrent Gas–liquid Flows in Porous Media Using Twin-Plane Electrical Capacitance Tomography." *Chemical Engineering Journal* 165 (1). Elsevier B.V.: 310–23.

Hansent, EW. 1988. "A Nonequilibrium Phase Diagram of the System HCI-H2O Determined by 1H NMR," no. 74: 99–104.

Harbottle, D, M Fairweather, and S Biggs. 2011. "The Minimum Transport Velocity of Colloidal Silica Suspensions." *Chemical Engineering Science* 66 (11). Elsevier: 2309–16.

Harikumar, R, R Prabu, and S Raghavan. 2013. "Electrical Impedance Tomography (EIT) and Its Medical Applications : A Review." *International Journal of Soft Computing and Engineering (IJSCE)* 3 (4): 193–98.

Hayden, JW, and TE Stelson. 1968. "Hydraulic Conveyance of Solids in Pipes." In *International Symposium on Solid–Liquid Flow in Pipes*. Philadelphia.

Heikkinen, LM, J Kourunen, T Savolainen, PJ Vauhkonen, JP Kaipio, and M Vauhkonen. 2006. "Real Time Three-Dimensional Electrical Impedance Tomography Applied in Multiphase Flow Imaging." *Measurement Science and Technology* 17: 2083–87.

Henderson, RP, and JG Webster. 1978. "An Impedance Camera for Spatially Specific Measurements of the Thorax." *IEEE Transactions on Bio-Medical Engineering* 25 (3): 250–54.

Hiltunen, K, A Jäsberg, S Kallio, H Karema, M Kataja, A Koponen, M Manninen, and V Taivassalo. 2009. *Multiphase Flow Dynamics: Theory and Numerics*. Espoo: VTT Publications.

Holliday, N, R a. Williams, and G Lucas. 2005. "A High-Performance EIT System." *IEEE Sensors Journal* 5 (2): 289–99.

Hosokawa, S, and A Tomiyama. 2004. "Turbulence Modification in Gas–liquid and Solid–liquid Dispersed Two-Phase Pipe Flows." *International Journal of Heat and Fluid Flow* 25 (3): 489–98.

Hrenya, C, E Bolio, D Chakrabarti, and JL Sinclair. 1995. "Comparison of Low Reynolds Number K–ε Turbulence Models in Predicting Fully Developed Pipe Flow." *Chemical Engineering Science* 50 (12): 1923–41.

Hsu, T-J. 2003. "On Two-Phase Sediment Transport: Dilute Flow." *Journal of Geophysical Research* 108 (C3): 3057.

Hunt, ML, R Zenit, CS Campbell, and CE Brennen. 2002. "Revisiting the 1954 Suspension Experiments of R. A. Bagnold." *Journal of Fluid Mechanics* 452: 1–24.

Hunter, TN, J Peakall, and SR Biggs. 2011. "Ultrasonic Velocimetry for the in Situ Characterisation of Particulate Settling and Sedimentation." *Minerals Engineering* 24 (5). Elsevier Ltd: 416–23.

Ishii, M, and T Hibiki. 2011. *Thermo-Fluid Dynamics of Two-Phase Flow*. *NASA STI/Recon Technical Report A*. 2nd Ed. New York: Springer.

Jha, SK, and FA Bombardelli. 2009. "Two-Phase Modeling of Turbulence in Dilute Sediment-Laden, Open-Channel Flows." *Environmental Fluid Mechanics* 9 (2): 237–66.

Jia, J, M Wang, HI Schlaberg, and H Li. 2010. "A Novel Tomographic Sensing System for High Electrically Conductive Multiphase Flow Measurement." *Flow Measurement and Instrumentation* 21 (3). Elsevier Ltd: 184–90.

Jiang, YY, and P Zhang. 2012. "Numerical Investigation of Slush Nitrogen Flow in a Horizontal Pipe." *Chemical Engineering Science* 73 (May): 169–80.

Jones, W., and B. Launder. 1972. "The Prediction of Laminarization with a Two-Equation Model of Turbulence." *International Journal of Heat and Mass Transfer* 15: 301–14.

Kalitzin, G, G Medic, G Iaccarino, and P Durbin. 2005. "Near-Wall Behavior of RANS Turbulence Models and Implications for Wall Functions." *Journal of Computational Physics* 204: 265–91.

Karhunen, K, A Seppänen, A Lehikoinen, PJM Monteiro, and JP Kaipio. 2010. "Electrical Resistance Tomography Imaging of Concrete." *Cement and Concrete Research* 40 (1). Elsevier Ltd: 137–45.

Kartushinsky, A, EE Michaelides, Y Rudi, and G (Gus) Nathan. 2010. "RANS Modeling of a Particulate Turbulent Round Jet." *Chemical Engineering Science* 65 (11). Elsevier: 3384–93.

Kaushal, D., Y Tomita, and R. Dighade. 2002. "Concentration at the Pipe Bottom at Deposition Velocity for Transportation of Commercial Slurries through Pipeline." *Powder Technology* 125 (1): 89–101.

Kaushal, DR, T Thinglas, Y Tomita, S Kuchii, and H Tsukamoto. 2012. "CFD Modeling for Pipeline Flow of Fine Particles at High Concentration." *International Journal of Multiphase Flow* 43 (July). Elsevier Ltd: 85–100.

Kaushal, DR, and Y Tomita. 2007. "Experimental Investigation for near-Wall Lift of Coarser Particles in Slurry Pipeline Using Γ-Ray Densitometer." *Powder Technology* 172 (3): 177–87.

Kenning, V, and C Crowe. 1997. "On the Effect of Particles on Carrier Phase Turbulence in Gas-Particle Flows." *International Journal of Multiphase Flow*, 403–8.

Kiger, K, and C Pan. 2002. "Suspension and Turbulence Modification Effects of Solid Particulates on a Horizontal Turbulent Channel Flow." *J. Turbulence* 5248 (02): 1–21.

Kose, K, K Satoh, T Inouye, and H Yasuoka. 1985. "NMR Flow Imaging." *Journal of the Physical Society of Japan* 54 (1): 81–92.

Kourunen, J, R Käyhkö, J Matula, J Käyhkö, M Vauhkonen, and LM Heikkinen. 2008. "Imaging of Mixing of Two Miscible Liquids Using Electrical Impedance Tomography and Linear Impedance Sensor." *Flow Measurement and Instrumentation* 19 (6). Elsevier Ltd: 391–96.

Kromkamp, J, D van den Ende, D Kandhai, R van der Sman, and R Boom. 2006. "Lattice Boltzmann Simulation of 2D and 3D Non-Brownian Suspensions in Couette Flow." *Chemical Engineering Science* 61 (2): 858–73.

Kuzmin, D, O Mierka, and S Turek. 2007. "On the Implementation of the K-E Turbulence Model in Incompressible Flow Solvers Based on a Finite Element Discretisation." *International Journal of Computing Science and Mathematics* 1 (2): 193.

Lahiri, S, and KC Ghanta. 2010. "Slurry Modelling by CFD." *Chemical Industry and Chemical Engineering Quarterly* 16 (4): 295–308.

Lahiri, SK, and KC Ghanta. 2008. "Prediction of Pressure Drop of Slurry Flow in Pipeline by Hybrid Support Vector Regression and Genetic Algorithm Model." *Chinese Journal of Chemical Engineering* 16 (6): 841–48.

Lai, J, and C Yang. 1997. "Numerical Simulation of Turbulence Suppression: Comparisons of the Performance of Four K-Epsilon Turbulence Models." *International Journal of Heat and Fluid Flow* 18 (6): 575–84.

Landau, L. 2014. "Abel, Niels Henrik (1802-1829)." http://scienceworld.wolfram.com/biography/Abel.html.

Lareo, C, PJ Fryer, and M Barigou. 1997. "The Fluid Mechanics of Two-Phase Solid-Liquid Food Flows: A Review." *Food and Bioproducts Processing* 75: 73–105.

Levy, DH, KK Gleason, M Rothschild, and JHC Sedlacek. 1993. "The Role of Hydrogen in Excimer-Laser-Induced Damage of Fused Silica." *Journal of Applied Physics* 73 (6): 2809.

Li, QH, and J Wang. 2013. "Weak Galerkin Finite Element Methods for Parabolic Equations." *Numerical Methods for Partial Differential Equations* 29 (6).

Lin, CX, and MA Ebadian. 2008. "A Numerical Study of Developing Slurry Flow in the Entrance Region of a Horizontal Pipe." *Computers & Fluids* 37 (8): 965–74.

Ling, J, PV Skudarnov, CX Lin, and MA Ebadian. 2003. "Numerical Investigations of Liquid–solid Slurry Flows in a Fully Developed Turbulent Flow Region." *International Journal of Heat and Fluid Flow* 24 (3): 389–98.

Liu, H. 2003. *Pipeline Engineering*. 1 edition. CRC Press.

Loth, E. 2010. *Particles, Drops and Bubbles: Fluid Dynamics and Numerical Methods*. Draft for. Cambridge University Press.

Majors, PD, DM Smith, and PJ Davis. 1991. "Effective Diffusivity Measurement in Porous Media via NMR Radial Imaging." *Chemical Engineering Science* 46 (12): 3037–43.

Malmivuo, J, and R Plonsey. 1995. *Bioelectromagnetism: Principles and Applications of Bioelectric and Biomagnetic Fields*. New York: Oxford University Press.

Mandø, M, MF Lightstone, L Rosendahl, C Yin, and H Sørensen. 2009. "Turbulence Modulation in Dilute Particle-Laden Flow." *International Journal of Heat and Fluid Flow* 30 (2). Elsevier Inc.: 331–38.

Manninen, M, V Taivassalo, and S Kallio. 1996. *On the Mixture Model for Multiphase Flow*. Edited by V Publications. Espoo: VTT Publications.

Mashayek, F, and RVR Pandya. 2003. "Analytical Description of Particle/droplet-Laden Turbulent Flows." *Progress in Energy and Combustion Science* 29 (4): 329–78.

Massoudi, M. 2010. "A Mixture Theory Formulation for Hydraulic or Pneumatic Transport of Solid Particles." *International Journal of Engineering Science* 48 (11). Elsevier Ltd: 1440–61.

Matoušek, V. 2002. "Pressure Drops and Flow Patterns in Sand-Mixture Pipes." *Experimental Thermal and Fluid Science* 26 (6-7): 693–702.

Matoušek, V. 2005. "Research Developments in Pipeline Transport of Settling Slurries." *Powder Technology* 156 (1): 43–51.

McCarthy, MJ. 1990. "Interpretation of the Magnetic Resonance Imaging Signal from a Foam." *AIChE Journal* 36 (2): 287–90.

Mehring, M. 1983. *Principles of High Resolution NMR in Solids*. *Springer, Berlin*. Springer Berlin Heidelberg.

Meng, Z, Z Huang, B Wang, H Ji, H Li, and Y Yan. 2010. "Air–water Two-Phase Flow Measurement Using a Venturi Meter and an Electrical Resistance Tomography Sensor." *Flow Measurement and Instrumentation* 21 (3). Elsevier Ltd: 268–76.

Messa, GV, M Malin, and S Malavasi. 2014. "Numerical Prediction of Fully-Suspended Slurry Flow in Horizontal Pipes." *Powder Technology* 256 (April). Elsevier B.V.: 61–70.

Miedema, S, E van Riet, and V Matoušek. 1995. "Reconstruction of and Numerical Sensitivity Analysis on Wilson Model for Hydraulic Transport of Solids in Pipelines." In *8th International Conference on Transport and Sedimentation of Solid Particles*, 15. Prague.

Miedema, SA. 2014. "Dredging Engineering." http://www.dredgingengineering.com/dredging/default.asp?id=1&mnu=1.

Molinari, M. 2003. "High Fidelity Imaging in Electrical Impedance Tomography." University of Southampton.

Murai, T, and Y Kagawa. 1985. "Electrical Impedance Computed Tomography Based on a Finite Element Model." *IEEE Transactions on Bio-Medical Engineering* 32 (2): 177–84.

Nakagawa, M, SA Altobelli, A Caprihan, E Fukushima, and E Jeong. 1993. "Experiments in Fluids Non-Invasive Measurements of Granular Flows by Magnetic Resonance Imaging." *Experiments in Fluids* 60 (1): 54–60.

Nicolay, K. 1992. "Applications of 31P NMR in the Study of Microbial Metabolism." *Trends in Food Science & Technology* 3 (January): 225–30.

Nobelprize.org. 2014. "The Nobel Prize in Physiology or Medicine 1979." *Nobel Media AB*. http://www.nobelprize.org/nobel_prizes/medicine/laureates/1979/.

Noor, J. 2007. "Electrical Impedance Tomography at Low Frequencies." University of New South Wales.

Norman, JT, H V. Nayak, and RT Bonnecaze. 2005. "Migration of Buoyant Particles in Low-Reynolds-Number Pressure-Driven Flows." *Journal of Fluid Mechanics* 523 (January): 1–35.

Nyström, B, ME Moseley, W Brown, and J Roots. 1981. "Molecular Motion of Small Molecules in Cellulose Gels Studied by NMR." *Journal of Applied Polymer Science* 26 (10): 3385–93.

Oevermann, M, S Gerber, and F Behrendt. 2008. "Euler-Euler and Euler-Lagrange Modeling of Wood Gasification in Fluidized Beds." In *9 thInternational Conference on Circulating Fluidized Beds (CFB-9)*. Hamburg.

Pakzad, L, F Ein-Mozaffari, and P Chan. 2008. "Using Electrical Resistance Tomography and Computational Fluid Dynamics Modeling to Study the Formation of Cavern in the Mixing of Pseudoplastic Fluids Possessing Yield Stress." *Chemical Engineering Science* 63 (9): 2508–22.

Pang, MJ, and JJ Wei. 2011. "Analysis of Drag and Lift Coefficient Expressions of Bubbly Flow System for Low to Medium Reynolds Number." *Nuclear Engineering and Design* 241 (6): 2204–13.

Peker, S, and S Helvaci. 2011. *Solid-Liquid Two Phase Flow*. *Vasa*. 1st Ed. Amsterdam: Elsevier Inc.

Pisarenco, M, B van der Linden, A Tijsseling, E Ory, and J Dam. 2011. "Friction Factor Estimation for Turbulent Flows in Corrugated Pipes with Rough Walls." *Journal of Offshore Mechanics and Arctic Engineering* 133 (1): 011101.

Polydorides, N. 2002. "Image Reconstruction Algorithms for Soft-Field Tomography." University of Manchester.

Polydorides, N, and WRB Lionheart. 2002. "A Matlab Toolkit for Three-Dimensional Electrical Impedance Tomography: A Contribution to the Electrical Impedance and Diffuse Optical Reconstruction Software Project." *Measurement Science and Technology* 13 (12): 1871–83.

Powell, RL. 2008. "Experimental Techniques for Multiphase Flows." *Physics of Fluids* 20 (4): 040605.

Qiu, L, and C Wu. 2014. "A Hybrid DEM/CFD Approach for Solid-Liquid Flows." *Journal of Hydrodynamics, Ser. B* 26 (1). Publishing House for Journal of Hydrodynamics: 19–25.

Ramadan, A, P Skalle, and A Saasen. 2005. "Application of a Three-Layer Modeling Approach for Solids Transport in Horizontal and Inclined Channels." *Chemical Engineering Science* 60 (10): 2557–70.

Rannacher, R. 2000. *Finite Element Methods for the Incompressible Navier-Stokes Equations*. Heidelberg, Germany.

Rasteiro, MG. 1988. "Transporte Hidráulico de Sólidos: Estudo Do Mecanismo de Suspensão." University of Coimbra.

Rasteiro, MG, MM Figueiredo, and H Franco. 1993. "Pressure Drop for Solid/Liquid Flow in Pipes." *Particulate Science and Technology* 11 (3-4): 147–55.

Rasteiro, MG, MM Rebola, and B Scarlet. 1988. "Simulation of Solid/Liquid Transport in Pipes." In *11th Internatinal Conference on the Hydraulic Transport of Solids in Pipes*. Stratford-upon-Avon.

Rasteiro, MG, R Silva, FAP Garcia, and PM Faia. 2011. "Electrical Tomography: A Review of Configurations and Applications to Particulate Processes." *KONA Powder and Particle Journal*, no. 29: 67–80.

Razzak, SA, S Barghi, and J-X Zhu. 2009. "Application of Electrical Resistance Tomography on Liquid–solid Two-Phase Flow Characterization in an LSCFB Riser." *Chemical Engineering Science* 64 (12): 2851–58.

Rhodes, M. 2008. *Introduction to Particle Technology: Second Edition*. Wiley.

Ricard, F, C Brechtelsbauer, XY Xu, and CJ Lawrence. 2005. "Monitoring of Multiphase Pharmaceutical Processes Using Electrical Resistance Tomography." *Chemical Engineering Research and Design* 83 (7): 794–805.

Richardson, JF, and WN Zaki. 1954. "Sedimentation and Fluidisation: Part I." *Trans. Inst. Chem. Eng.* 75 (3). Institution of Chemical Engineers: S82–100.

Rimpiläinen, V, M Kuosmanen, J Ketolainen, K Järvinen, M Vauhkonen, and LM Heikkinen. 2010. "Electrical Impedance Tomography for Three-Dimensional Drug Release Monitoring." *European Journal of Pharmaceutical Sciences : Official Journal of the European Federation for Pharmaceutical Sciences* 41 (2): 407–13.

Rizk, MA, and SE Elghobashi. 1989. "A Two-Equation Turbulence Model for Dispersed Dilute Confined Two-Phase Flows." *International Journal of Multiphase Flow* 15 (1): 119–33.

Robertson, T, S Schmidt, and B Klein. 1992. "Applications of NMR in Sensory Science." *Trends in Food Science & Technology* 3 (January): 236–40.

Roco, MC, and CA Shook. 1984. "A Model for Turbulent Slurry Flow." *Journal of Pipelines* 4: 3–13.

Rowe, P. 1987. "A Convenient Empirical Equation for Estimation of the Richardson-Zaki Exponent." *Chemical Engineering Science* 42 (11): 2795–96.

Salim, SM, and SC Cheah. 2009. "Wall Y+ Strategy for Dealing with Wall-Bounded Turbulent Flows." In *International MultiConference of Engineers and Computer Scientists*. Vol. II.

Satish, G, K Kumar, V Prasad, and S Pasha. 2013. "Comparison of Flow Analysys of a Sudden and Gradual Change of Pipe Diameter Using FLUENT Software." *International Journal of Research in Engineering and Technology* 2 (12): 41–45.

Schaan, J, RJ Sumner, RG Gillies, and C a Shook. 1997. "The Effect of Particle Shape on Pipeline Friction for Newtonian Slurries of Fine Particles." *The Canadian Journal of Chemical Engineering* 78: 717–25.

Schlaberg, HI, JH Baas, M Wang, JL Best, R a. Williams, and J Peakall. 2006. "Electrical Resistance Tomography for Suspended Sediment Measurements in Open Channel Flows Using a Novel Sensor Design." *Particle & Particle Systems Characterization* 23 (3-4): 313–20.

Schlichting, H, and K Gersten. 1979. *Boundary-Layer Theory*. *European Journal of Mechanics - B/Fluids*. 7th Editio. Vol. 20. McGraw-Hill.

Schramm, L. 2005. *Emulsions, Foams, and Suspensions: Fundamentals and Applications*. Weinheim, FRG: Wiley-VCH Verlag GmbH & Co. KGaA.

Segal, IA. 2012. *Finite Element Methods for the Incompressible Navier-Stokes Equations*. Delft.

Segerlind, LJ. 1984. *Applied Finite Element Analysis*. 2nd Editio. New York: Wiley.

Shardt, O, and JJ Derksen. 2012. "Direct Simulations of Dense Suspensions of Non-Spherical Particles." *International Journal of Multiphase Flow* 47 (December). Elsevier Ltd: 25–36.

Shimokawa, S, and E Yamada. 1985. "Simultaneous and Direct Measurement of Gas–liquid Density at High Temperature and High Pressure Using the Nuclear-Spin Projection Method." *Review of Scientific Instruments* 56 (6): 1220.

Shook, C. 1985. "Experiments with Concentrated Slurries of Particles with Densities near that of the Carrier Fluid." *The Canadian Journal of Chemical Engineering* 63 (December).

Shook, CA. 1976. "Developments in Hydrotransport." *The Canadian Journal of Chemical Engineering* 54 (1-2): 13–25.

Shook, CA, and AS Bartosik. 1994. "Particle—Wall Stresses in Vertical Slurry Flows." *Powder Technology* 81 (2): 117–24.

Shook, CA, and SM Daniel. 1965. "Flow of Suspensions of Solids in Pipelines: Part I. Flow with a Stable Stationary Deposit." *The Canadian Journal of Chemical Engineering* 43 (2): 56–61.

Shook, CA, SM Daniel, JA Scott, and JP Holgate. 1968. "Flow of Suspensions in Pipelines: Part II. Two Mechanisms of Particle Suspension." *The Canadian Journal of Chemical Engineering* 46 (4): 238–44.

Shook, CA, DB Has, W Husband, M Small, and R Gillies. 1981. "Pipeline Flow of Coarse Coal Slurries." *Journal of Pipelines* 1: 83–92.

Shook, CA, DB Has, WHW Husband, M Small, and R Gillies. 1982. "Flow of Coarse and Fine Sand Slurries in Pipelines." *Jounal of Pipelines* 3: 13–21.

Shukla, A, A Prakash, and S Rohani. 2007. "Particles Settling Studies Using Ultrasonic Techniques." *Powder Technology* 177 (2): 102–11.

Silva, R, C Cotas, FAP Garcia, PM Faia, and MG Rasteiro. 2014. "Particle Distribution Studies in Highly Concentrated Solid-Liquid Flows in Pipe Using the Mixture Model." In *The 7th World Congress on Particle Technology (WCPT7)*. Beijing: Elsevier Procedia Engineering (submitted for publication).

Silva, R, FAP Garcia, PM Faia, and MG Rasteiro. 2013. "Numerical Studies of Solid-Liquid Turbulent Pipe Flow of Settling Suspensions Using the Mixture Model." In *WCCE9 & APCChE 2013 Proceedings*, 65. Seoul.

Singh, G. 2009. *Short Introduction to Finite Element Method*. *Norwegian University of Science and Technology*.

Soldati, A, and C Marchioli. 2012. "Sediment Transport in Steady Turbulent Boundary Layers: Potentials, Limitations, and Perspectives for Lagrangian

Tracking in DNS and LES." *Advances in Water Resources* 48 (November). Elsevier Ltd: 18–30.

Sommerfeld, M, B van Wachem, and R Oliemans. 2008. *Best Practices Guidelines CFD Dispersed Multiphase Flows ERCOFTAC 2008*. Lausanne.

Stickel, JJ, and RL Powell. 2005. "Fluid Mechanics and Rheology of Dense Suspensions." *Annual Review of Fluid Mechanics* 37 (1): 129–49.

Stilbs, P. 1987. "Fourier Transform Pulsed-Gradient Spin-Echo Studies of Molecular Diffusion." *Progress in Nuclear Magnetic Resonance Spectroscopy* 19 (1): 1–45.

Stilbs, P, and B Lindman. 1984. "NMR Measurements on Microemulsions." *Progress in Colloid & Polymer Science* 69: 39–47.

Subramaniam, S. 2013. "Lagrangian–Eulerian Methods for Multiphase Flows." *Progress in Energy and Combustion Science* 39 (2-3): 215–45.

Sun, M, S Liu, Z LI, and J Lei. 2008. "Application of Electrical Capacitance Tomography to the Concentration Measurement in a Cyclone Dipleg." *Chinese Journal of Chemical Engineering* 16 (4): 635–39.

Sun, T, S Tsuda, K-P Zauner, and H Morgan. 2010. "On-Chip Electrical Impedance Tomography for Imaging Biological Cells." *Biosensors & Bioelectronics* 25 (5): 1109–15.

Sun, X, M Sakai, and Y Yamada. 2013. "Three-Dimensional Simulation of a Solid–liquid Flow by the DEM–SPH Method." *Journal of Computational Physics* 248 (September): 147–76.

Suryan, G. 1951. "Nuclear Resonance in Flowing Liquids." *Proceedings of the Indian Academy of Sciences - Section A* 33 (2): 107–11.

Takeda, Y. 1995. "Velocity Profile Measurement by Ultrasonic Doppler Method." *Experimental Thermal and Fluid Science* 1777 (94): 444–53.

Takeda, Y. 1999. "Ultrasonic Doppler Method for Velocity Profile Measurement in Fluid Dynamics and Fluid Engineering." *Experiments in Fluids* 26 (1): 177–78.

Tanaka, T, and J Eaton. 2008. "Classification of Turbulence Modification by Dispersed Spheres Using a Novel Dimensionless Number." *Physical Review Letters* 101 (11): 114502.

Tapp, HS, a. J Peyton, EK Kemsley, and RH Wilson. 2003. "Chemical Engineering Applications of Electrical Process Tomography." *Sensors and Actuators B: Chemical* 92 (1-2): 17–24.

Tapp, HS, and RH Wilson. 1997. "Developments in Low-Cost Electrical Imaging Techniques." *Process Control and Quality* 9: 7–16.

Toorman, EA. 2003. "Validation of Macroscopic Modelling of Particle-Laden Turbulent Flows." In *6th Belgian National Congress on Theoretical and Applied Mechanics*. Gent.

Tossavainen, O. 2007. "Shape Estimation in Electrical Impedance Tomography." *Environmental Sciences*. University of Kuopio.

Troshko, AA, and YA Hassan. 2001. "Law of the Wall for Two-Phase Turbulent Boundary Layers." *International Journal of Heat and Mass Transfer* 44 (4): 871–75.

Truesdell, GC, and S Elghobashi. 1994. "On the Two-Way Interaction between Homogeneous Turbulence and Dispersed Solid Particles. II. Particle Dispersion." *Physics of Fluids* 6 (3): 1405.

University of Leeds. 2014. "What Is Tomography?" *Industrial Process Tomography - Platform II*. http://www.leeds.ac.uk/olil/tomography/WhatIsTomography.php.

Vasava, PR. 2007. "Fluid Flow in T-Junction of Pipes." Lappeenranta University of Technology.

Vauhkonen, M. 1997. "Electrical Impedance Tomography and Prior Information."

Vauhkonen, M, D Vadász, PA Karjalainen, E Somersalo, and JP Kaipio. 1998. "Tikhonov Regularization and Prior Information in Electrical Impedance Tomography." *IEEE Transactions on Medical Imaging* 17 (2): 285–93.

Vauhkonen, PJ, M Vauhkonen, T Mäkinen, PA Karjalainen, and JP Kaipio. 2000. "Dynamic Electrical Impedance Tomography - Phantom Studies." *Inverse Problems in Engineering* 8 (14). Kuopio, Finland: 495–510.

Vauhkonen, PJ, M Vauhkonen, T Savolainen, and JP Kaipio. 1999. "Three-Dimensional Electrical Impedance Tomography Based on the Complete Electrode Model." *IEEE Transactions on Biomedical Engineering* 46 (9): 1150–60.

Ventura, C, FAP Garcia, P Ferreira, and MG Rasteiro. 2008. "Flow Dynamics of Pulp Fiber Suspensions." *Tappi Journal* 6 (7): 20–26.

Versteeg, H, and W Malalasekera. 2007. *An Introduction to Computational Fluid Dynamics: The Finite Volume Method*. 2nd ed. Prentice Hall.

Vilar, G, RA Williams, M Wang, and RJ Tweedie. 2008. "On Line Analysis of Structure of Dispersions in an Oscillatory Baffled Reactor Using Electrical Impedance Tomography." *Chemical Engineering Journal* 141 (1-3): 58–66.

Villate, J. 1999. *Electromagnetismo*. Lisboa: McGraw-Hill.

Visuri, O, GA Wierink, and V Alopaeus. 2012. "Investigation of Drag Models in CFD Modeling and Comparison to Experiments of Liquid–solid Fluidized Systems." *International Journal of Mineral Processing* 104-105 (March). Elsevier B.V.: 58–70.

Wang, J, S Wang, T Zhang, and Y Liang. 2013. "Numerical Investigation of Ice Slurry Isothermal Flow in Various Pipes." *International Journal of Refrigeration* 36 (1): 70–80.

Wang, J, and X Ye. 2013. "A Weak Galerkin Finite Element Method for Second-Order Elliptic Problems." *Journal of Computational and Applied Mathematics* 241 (March): 103–15.

Wang, M. 2005a. "Impedance Mapping of Particulate Multiphase Flows." *Flow Measurement and Instrumentation* 16 (2-3): 183–89.

Wang, M. 2005b. "Electrode Models in Electrical Impedance Tomography." *Journal of Zhejiang University SCIENCE A* 6A (12): 1386–93.

Wang, M, T Jones, and R Williams. 2003. "Visualization of Asymmetric Solids Distribution in Horizontal Swirling Flows Using Electrical Resistance Tomography." *Chemical Engineering Research and Design* 81 (8): 854–61.

Wang, SY, PC Wang, and M Faust. 1988. "Non-Destructive Detection of Watercore in Apple with Nuclear Magnetic Resonance Imaging." *Scientia Horticulturae* 35 (3-4): 227–34.

Wang, T, J Wang, F Ren, and Y Jin. 2003. "Application of Doppler Ultrasound Velocimetry in Multiphase Flow." *Chemical Engineering Journal* 92 (1-3): 111–22.

Watanabe, H, and M Fukuoka. 1992. "Measurement of Moisture Diffusion in Foods Using Pulsed Field Gradient NMR." *Trends in Food Science & Technology* 3 (January): 211–15.

West, RM, DM Scott, G Sunshine, J Kostuch, L Heikkinen, M Vauhkonen, BS Hoyle, HI Schlaberg, R Hou, and RA Williams. 2002. "In Situ Imaging of Paste Extrusion Using Electrical Impedance Tomography." *Measurement Science and Technology* 13 (12): 1890–97.

White, F. 1991. *Viscous Fluid Flow*. McGraw-Hill.

White, FM. 1998. *Fluid Mechanics*. Edited by JP Holman and J Lloyd. *Refrigeration And Air Conditioning*. 4th Editio. Vol. 6. Dover Classics of Science and Mathematics. Mcgraw-Hill College.

Wiklund, J, and M Stading. 2008. "Application of in-Line Ultrasound Doppler-Based UVP–PD Rheometry Method to Concentrated Model and Industrial Suspensions." *Flow Measurement and Instrumentation* 19 (3-4): 171–79.

Wilcox, DC. 2006. *Turbulence Modeling for CFD*. 3rd Ed. DCW Industries, Inc.

Wilkinson, AJ, EW Randall, TM Long, and A Collins. 2006. "The Design of an ERT System for 3D Data Acquisition and a Quantitative Evaluation of Its Performance." *Measurement Science and Technology* 17 (8): 2088–96.

Williams, R, X Jia, and SL McKee. 1996. "Development of Slurry Mixing Models Using Resistance Tomography." *Powder Technology* 87 (1): 21–27.

Wilson, KC. 1970. "Slip Point of Beds in Solid-Liquid Pipeline Flow." *Journal of the Hydraulics Division* 96 (1): 1–12.

Xia, Y, PT Callaghan, and KR Jeffrey. 1992. "Imaging Velocity Profiles: Flow through an Abrupt Contraction and Expansion." *AIChE Journal* 38 (9): 1408–20.

XiaoWei, H, and G LieJin. 2010. "Numerical Investigations of Catalyst–liquid Slurry Flow in the Photocatalytic Reactor for Hydrogen Production Based on Algebraic Slip Model." *International Journal of Hydrogen Energy* 35 (13). Elsevier Ltd: 7065–72.

Yang, WYW. 2007. "Tomographic Imaging Based on Capacitance Measurement and Industrial Applications." In *2007 IEEE International Workshop on Imaging Systems and Techniques*, 7–12.

Yilmaz, F, and MY Gundogdu. 2009. "Analysis of Conventional Drag and Lift Models for Multiphase CFD Modeling of Blood Flow." *Korea-Australia Rheology Journal* 21 (3): 161–73.

York, T. 2001. "Status of Electrical Tomography in Industrial Applications." *Journal of Electronic Imaging*, no. 10: 608–19.

Yu, Z, and L-S Fan. 2010. "Lattice Boltzmann Method for Simulating Particle–fluid Interactions." *Particuology* 8 (6). Chinese Society of Particuology: 539–43.

Zhang, H, Y Tan, D Yang, FX Trias, S Jiang, Y Sheng, and A Oliva. 2012. "Numerical Investigation of the Location of Maximum Erosive Wear Damage in Elbow: Effect of Slurry Velocity, Bend Orientation and Angle of Elbow." *Powder Technology* 217 (February). Elsevier B.V.: 467–76.

Zhang, S, G Xu, H Wu, D Geng, and W Yan. 2006. "Multi-Frequency EIT Hardware System Based on DSP." In *Annual International Conference of the IEEE Engineering in Medicine and Biology - Proceedings*, Suppl:6677–80.

Zhou, L. 2010. "Advances in Studies on Turbulent Dispersed Multiphase Flows." *Chinese Journal of Chemical Engineering* 18 (6). Chemical Industry and Engineering Society of China (CIESC) and Chemical Industry Press (CIP): 889–98.

Zhu, HP, ZY Zhou, and RY Yang. 2008. "Discrete Particle Simulation of Particulate Systems: A Review of Major Applications and Findings." *Chemical Engineering Science* 63 (23): 5728–70.

Zhu, K, S Madhusudana Rao, C-H Wang, and S Sundaresan. 2003. "Electrical Capacitance Tomography Measurements on Vertical and Inclined Pneumatic Conveying of Granular Solids." *Chemical Engineering Science* 58 (18): 4225–45.

Zielínski, TG. 2013. *Introduction to the Finite Element Method: Introductory Course on Multiphysics Modelling*.

Zienkiewicz, OC, and YK Cheung. 1965. "Finite Elements in the Solution of Field Problems." *The Engineer*, 507–10.

Zienkiewicz, OC, and F Emeritus. 2000. *The Finite Element Method Fifth Edition Volume 3 : Fluid Dynamics*. Vol. 3.

Zienkiewicz, OC, RL Taylor, and P Nithiarasu. 2014. *The Finite Element Method for Fluid Dynamics*. Seventh Ed. Elsevier.

Zimmerman, JRJ, and WEW Brittin. 1957. "Nuclear Magnetic Resonance Studies in Multiple Phase Systems: Lifetime of a Water Molecule in an Adsorbing Phase on Silica Gel." *The Journal of Physical Chemistry* 61 (10): 1328–33.